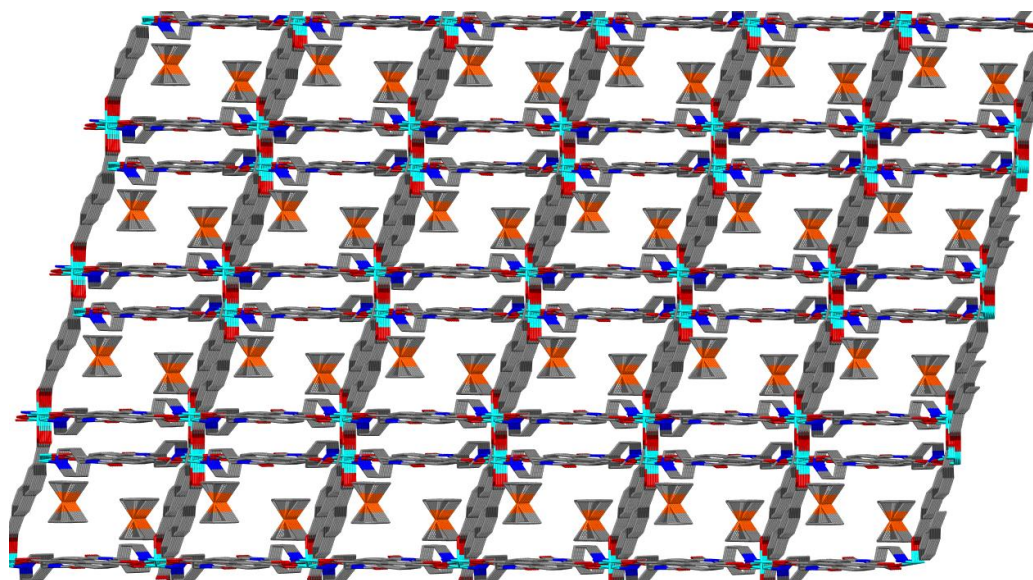![University of Nottingham logo — UK | CHINA | MALAYSIA]

Redox-active Metal-Organic Frameworks
constructed using novel Rylene Diimides

Joseph Ochocheowoni Ogar

Redox-active Metal-Organic Frameworks
constructed using novel Rylene Diimides

Thesis submitted to the University of Nottingham for the Degree of
Doctor of Philosophy

Joseph Ochocheowoni Ogar, MSc

September 2021

Declaration

Apart from where specific reference is made to other sources, the work presented in this report is the original work of the author. It has not been submitted, either in whole or in part, for any other degree.

Signed:

Date: 30|09|2021

Abstract

The synthesis and characterisation of three rylene diimides – N,N'-bis(2,6-diisopropyl-4-(pyridin-4-yl)phenyl)-1,4,5,8-naphthalenetetracarboxydiimide (DPPNDI), N,N'-bis(dinicotinic acid)-1,4,5,8-naphthalenetetracarboxydiimide (DNNDI) and N,N'-bis(2,6-diisopropyl-4-(pyridin-4-yl)phenyl)-3,4:9,10-perylenetetracarboxydiimide (DPPPDI) are reported here alongside the metal-organic frameworks (MOFs) prepared with them. Another linker used in this study is the widely studied N,N'-di-(4-pyridyl)-1,4,5,8-naphthalenetetracarboxydiimide or DPNDI. Each of the materials contains a redox-active functionalised naphthalenediimide (NDI) or perylenediimide (PDI). A total of 14 MOFs (**1** – **14**) are reported herein. The frameworks **1** – **7** were constructed using either DPNDI/DPPNDI or DPPPDI (acting as pillars) in conjunction with carboxylate linkers (acting as sheets) all of which are coordinated to either a Co^{2+} or Ni^{2+} centre. Frameworks **8** – **14** were constructed utilising DNNDI linker and seven lanthanides (Lanthanide = Dy **8**, Ce **9**, Pr **10**, Gd **11**, Ho **12**, La **13** and Nd **14**). The MOFs were all made by a straight-forward solvothermal method and characterised using SCXRD, PXRD, TGA ancyclic voltammetry and Uv-Vis spectroscopy. All the frameworks containing DPNDI, DPPNDI or DPPPDI **2** – **7** are two-fold interpenetrated except **1** which is non-interpenetrated. In terms of dimensionality, **1** and **6** is two-dimensional all the other materials are three-dimensional. The secondary building units (SBUs) are $\{[M(k^2-O_2NO)]_2(\mu^2-O_2CR)_2\}$ paddle wheel SBU for **1**, $M_2(\mu_2-O_2CR)_4$ paddle-wheel SBU for **2** – **7** and M-O-C rod SBUs with MO_8 polyhedra for **8** – **14**. Host-guest experiments involving the encapsulation of molecular ferrocene are also reported. The solid state electrochemistry of all the MOFs indicate that the

electrochemical behaviours of the rylene linker were exhibited by the MOFs constructed from them. Due to the presence of the redox-active ligands, these MOFs hold great potential for the entrapment of other electron-rich species which can in turn lead to new and exciting chemical properties.

Acknowledgements

I will like to cease this opportunity to express my profound gratitude to Prof. Neil R. Champness for painstakingly supervising this research and for all his encouragement, support, guidance and understanding during this academic sojourn. You are truly an inspiration and a role model to me. I am also very grateful to Prof. David Amabilino for accepting to be my supervisor after Prof. Neil Champness left the University of Nottingham.

My unquantifiable thanks to my beloved wife Margaret, son Emmanuel and daughter Camilla for their unwavering love, understanding and support throughout this journey. So much gratitude to the Niger Delta Development Commission (NDDC) for providing the tuition fees.

I also want to express my profound gratitude to the management of the University of Calabar for approving my study leave which has made it possible for me to come the University of Nottingham for this programme. Not forgetting Prof. Ayi, Prof. Offiong, Prof. Okafor and all my colleagues in UNICAL for their mentorship and support prior to my departure for this programme. I am truly grateful to you all.

This appreciation will not be complete without thanking all the members of the Champness Group especially for their reliable support. I especially thank Nicholas Pearce for untiringly putting me through in my moments of difficulty in the laboratory and for his invaluable suggestions which have given this thesis a major boost. I could not have wished for a better research group than the Champness' Group. So much thanks to Dr William Lewis and Stephen Argent for their help with crystallography, Dr Ana Ramos Geer for assistance with air-sensitive techniques.

To God in whom I live, move and have my being be all glory, honour and adoration forever.

List of Symbols and Abbreviations

DNNDI   N,N'-bis(dinicotinic   acid)-1,4,5,8-
               naphthalenetetracarboxydiimide (DNNDI)

DPNDI   N,N'-di-(4-pyridyl)-1,4,5,8-naphthalenetetracarboxydiimide

DPPNDI   N,N'-bis(2,6-diisopropyl-4-(pyridin-4-yl)phenyl)-1,4,5,8-
               naphthalenetetracarboxydiimide

DPPPDI   N,N'-bis(2,6-diisopropyl-4-(pyridin-4-yl)phenyl)-3,4:9,10-
               perylenetetracarboxydiimide

$E_{1/2}$ Redox potential

E_{pa} Peak Anodic Potential

Fc^+/Fc Ferrocenium/Ferrocene

g_{iso} Isotropic g-factor

λ   Wavelength

CIF   Crystallographic Information File

CV   Cyclic Voltammetry

DCTB   trans-2-[3-(4-tert-butylphenyl)-2-methyl-2-
               propenylidene]malonitrile

DMF   N,N-Dimethylformamide

DEF   N,N-Diethylformamide

EPR   Electron Paramagnetic Resonance

ESI   Electrospray Ionisation

H_2NDC 2,6-Naphthalenedicarboxylic acid

H_2BPDC Biphenyl-4,4′-dicarboxylic acid

IR   Infrared

MALDI   Matrix Assisted Laser Desorption Ionisation

MOF	Metal-organic framework
MS	Mass Spectrometry
MTV	Multivariant MOF
NDI	Naphthalene diimide
NMR	Nuclear Magnetic Resonance
PDI	Perylene diimide
QY	Quantum Yield
RDMOF	Rylene diimide metal-organic framework
UV	Ultraviolet
vis	Visible
vs	Versus

Contents

Chapter One   An Overview of Metal-Organic Frameworks

1.1 Introduction to metal-organic frameworks

Metal–organic frameworks (MOFs), also commonly referred to as porous coordination polymers (PCPs), are an interesting class of porous materials. They are constructed from metal-containing nodes (also called the secondary building units or SBUs) and organic linkers (also known as ligands).[1-4] Much attention has been drawn to this class of compounds due their prospects in the areas of gas adsorption and separation, catalysis, chemical sensing and other related applications.[128] A considerable number of known MOFs have displayed significant capacity and specific selectivity in gas adsorption.[5] When comparison is made between MOFs and the conventionally used microporous inorganic materials like zeolites, the former have the potential for more flexibility in terms of rational design, via control of the architecture and functionalization of the pores.[6,7]

Different geometries are produced by various metal ions and oxidation states,[8] making it possible to construct a near infinite library of framework structures and topologies. Furthermore, the feasibility of post-synthetically modifying these hybrid materials provides further routes to access other novel architectures.[9] Figure 1.1 illustrates the building blocks of metal organic frameworks whereby metal ions are connected with organic ligands.
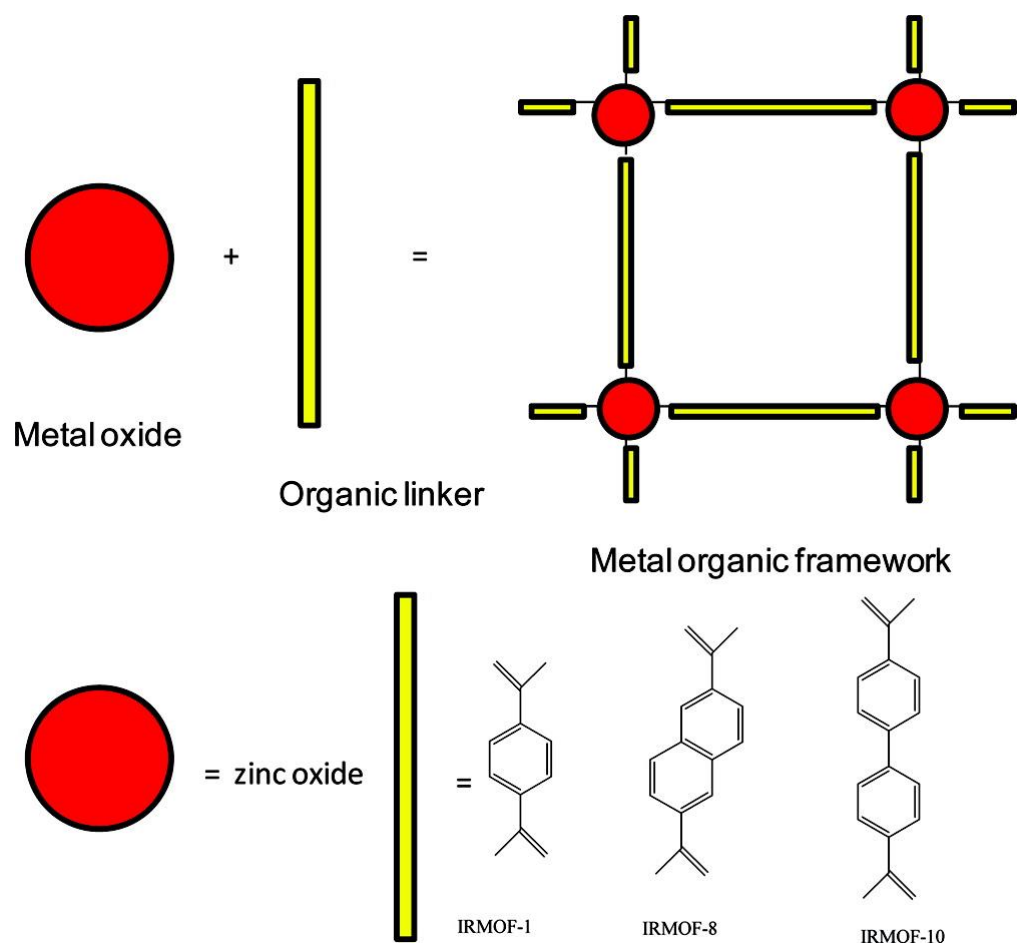
Figure 1.1 Typical building blocks of metal organic frameworks showing the combination of metal nodes with organic linkers.[10]

In 1965, some 30 years before the commonly assumed birth of what would be called MOFs, Tomic mentioned this class of materials and called them metal-organic polymers or supramolecular structures.[11] The frameworks were formed by coordinating bi- and trivalent aromatic carboxylic acids with metal ions such as zinc, nickel, iron, aluminium, thorium, uranium, etc. Some interesting features of MOFs, like high thermal stability and high metal content were already reported.[11]

It was Hoskins *et al* in 1989 who proposed this class of inorganic materials when they described the synthesis and structure of "the first example of a deliberately designed and constructed infinite framework".[12] In their work, Cu(I) centres were coordinated with 4,4',4'',4'''-tetracyanotetraphenylmethane (TCTPM),

producing a network with a diamond-like topology. The metal ion and the tetratopic organic linker both adopt a tetrahedral geometry shown in Figure 1.2.
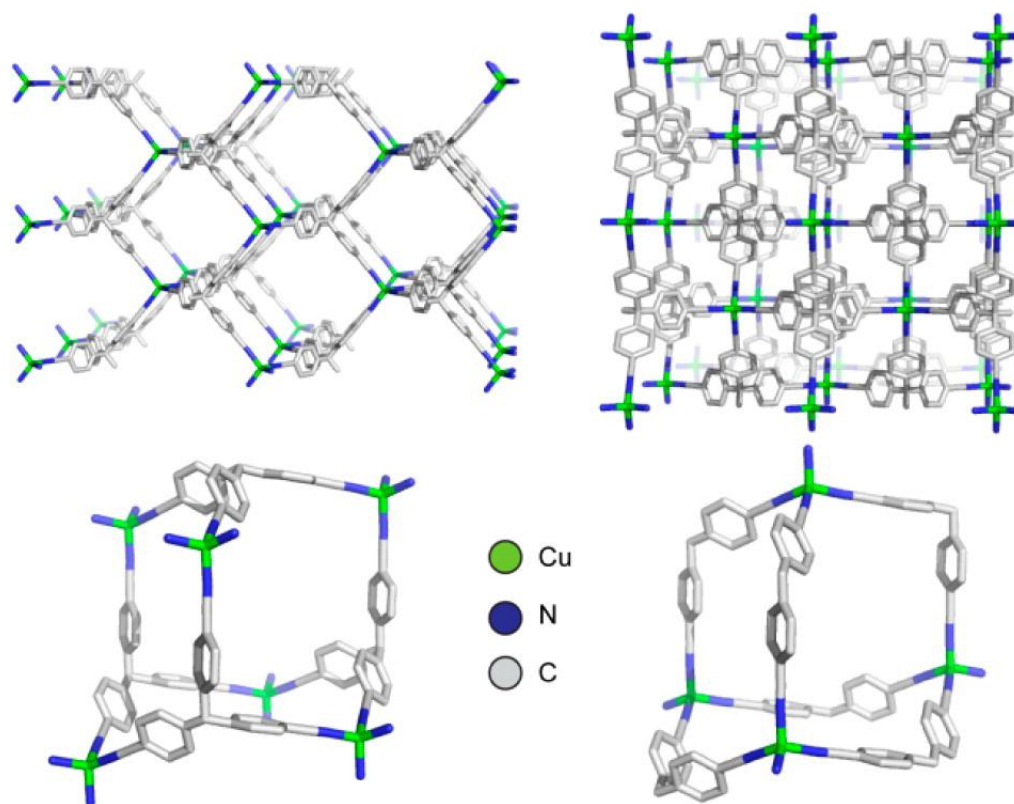
Figure 1.2: "The slow evaporation of a solution of a tetranitrile ligand with a Cu(I) precursor deposits a coordination polymer containing tetrahedral metal nodes with tetrahedral tetratopic spacers. Two views are shown (top) with hydrogen atoms omitted for clarity revealing a diamond-like network comprised of repeating adamantanoid units (bottom)".[12,13]

Since the discovery of this class of materials, a huge number of publications have been made. In 2010 alone, for instance, Web of Science – a scientific database, indexed well over 30 000 papers published on MOFs,[14-16] and in 2020, a publication by Fairen-Jimenez and co-workers indicated there exist about 99,075 MOFs in the Cambridge Structural Database (CSD) MOF subset.[17] This is indubitably a remarkable feat for a field that had commenced in earnest two decades ago. This field remains an exciting research area going by the number of research outputs with MOFs being investigated extensively for the adsorptive removal of various toxic pollutants (such as toxic gases, organic pollutants and

heavy metals) from the environment.[129] Very recently, Yaghi and Xu have successfully utilised MOFs for harvesting water from air.[18] Properties like ultra-huge porosity, pore geometry, and surface charge have made these applications possible.[19]

1.2 Terms associated with MOF chemistry
1.2.1 Secondary building unit

Secondary building units (SBUs) as a concept was adopted from the chemistry of zeolite as a means of predicting and describing the structure of MOFs. They are simple geometric figures which represent the inorganic clusters or coordination spheres (usually referred to as primary building units) which are coordinated together by the organic ligands to form a framework. Figure 1.3 presents some SBUs commonly found in metal carboxylate metal organic frameworks (a) the triangle, (b) the square paddle-wheel, (c) the tetrahedron, (d) the octahedral zinc acetate cluster and (e) the trigonal prismatic oxo-centred trimer. The SBUs are linked into MOFs by joining the carboxylate carbons with organic units. They could also be linked by replacement of terminal ligands with those that are non-terminal.
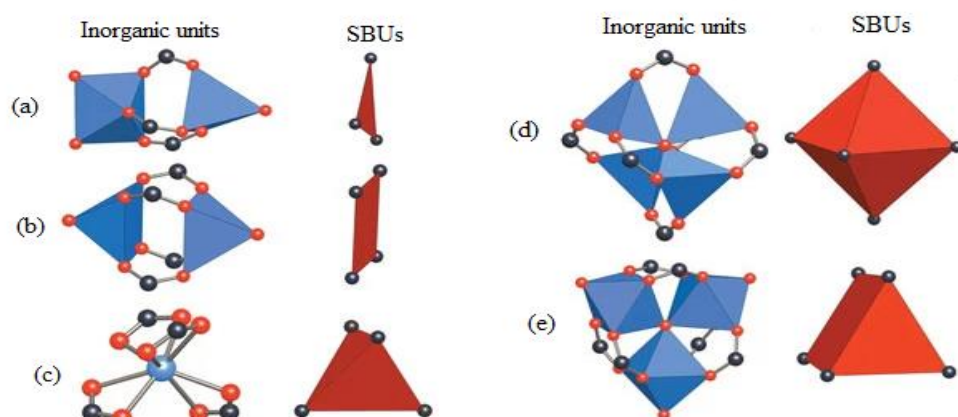
Figure 1.3 Examples of SBUs from carboxylate MOFs. O = red; C = black. In the inorganic units, the metal ion is inside the polyhedron (shown in blue) which bridges the coordinating oxygens, and the polygon or polyhedron defined by carboxylate carbon atoms (SBUs) are red.[20]

To further illustrate the concept of SBUs, the framework material, $Cr_3F(H_2O)_2O(1,4\text{-bdc})_3$ (1,4-bdc = benzene-1,4-dicarboxylate), given the name MIL-101 is shown in Figure 1.4. The MOF was constructed from the corner-sharing of tetrahedral SBUs, made up of chromium trimers and 1,4-bdc anions. The structure of this material exhibits several unusual features which include: large free aperture (12 Å for pentagonal windows and 16 Å × 14.5 Å for hexagonal windows), mesoporous cages (29 Å and 34 Å), and a very high nitrogen sorption capacity ($S_{Langmuir} \sim 5900$ m^2/g).[21, 22]
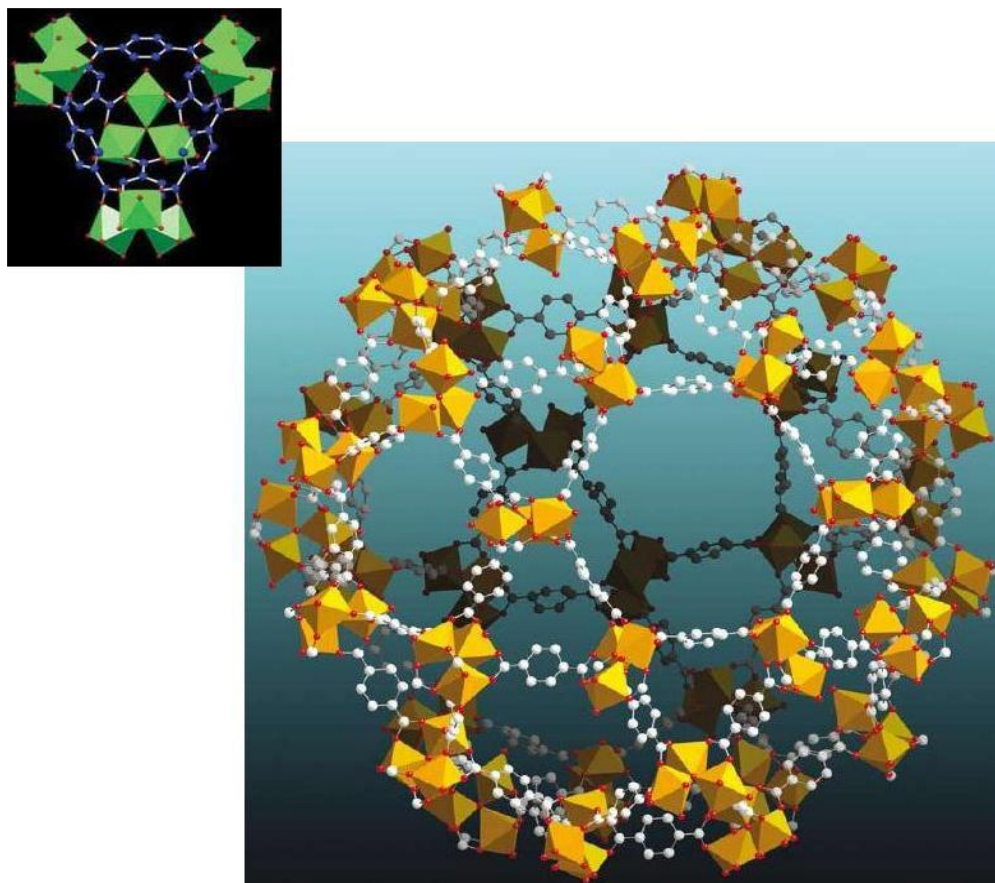
Figure 1.4 Structure of MIL-101 Indicating: (left) SBU and (right) fragment of the giant pore. Cr = orange polyhedron; C = white; O = red. For clarity, hydrogen atoms are omitted.[21]

1.2.2 Interpenetration

Interpenetration (also known by other names such as interlocking, interweaving and entanglement) is a natural phenomenon usually encountered in MOFs[23]. Interpenetration has been called the entwining of multiple lattices in MOFs.[24] Interpenetration was considered, in the early days of MOFs, as a threat to permanent porosity and different measures have been adopted in order to control this phenomenon. The reason for this fear is that when dealing with porous frameworks, the primary focus used to be on the pore size of the crystalline materials.[25] However, in a bid to increase the pore size, the system usually undergoes interpenetration so as to achieve a final structure that is architecturally

stable. This, of course, happens at the expense of the much-desired pore space. In order to minimise and/or prevent such interpenetration, a commonly employed strategy is the erection of steric restrictions by incorporating bulky substituents or moieties into organic tectons.[26,27] However, recent literature reports have shown that interpenetration is important in several material properties especially in storage and separation of small gas molecules. Researchers have also actively explored possible ways of installing this feature in MOFs. For instance, Barbour and co-workers have shown, using $[Co_2(ndc)_2(bpy)]$, that by increasing the temperature, the degree of interpenetration can be increased as illustrated in Figure 1.5. It also worth mentioning that the degree of interpenetration can be altered by factors such as temperature, solvent type, reaction time and steric hindrances.[28,29]
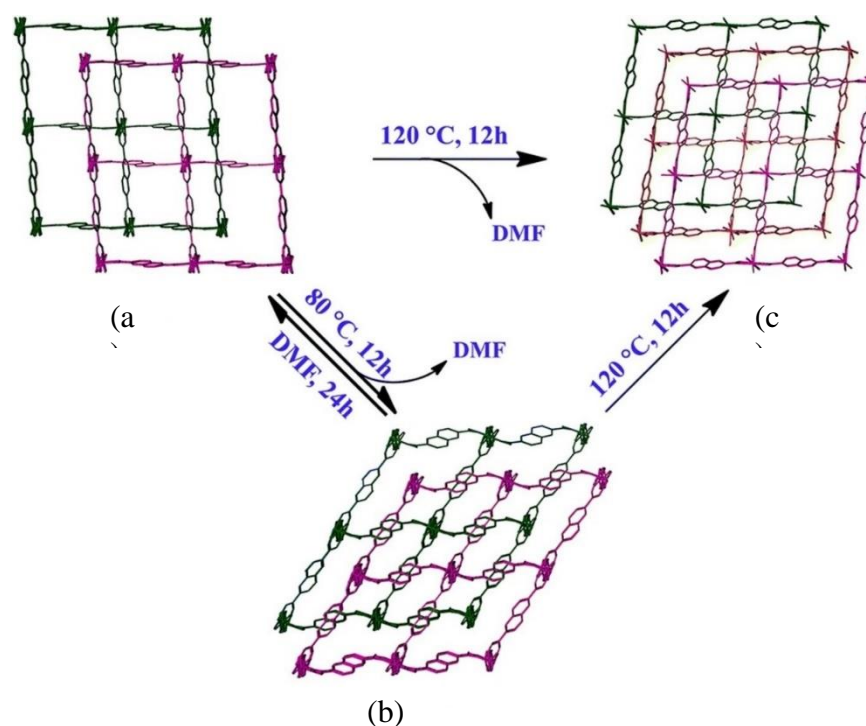
Figure 1.5 Schematic representation of interpenetration transformation in $[Co_2(ndc)_2(bpy)]$ as a function of temperature. (a) The as-synthesized $[Co_2(ndc)_2(bpy)]$; (b) Bent structure of the MOF upon heating to 80 °C; (c) Triply-interpenetrated MOF at 120 °C.[28]

Polyknotting or self-penetration is also possible in coordination polymers. This is a phenomenon in which a single coordination polymer net contains rings through which another component of the same network passes. The study into interpenetration and similar phenomena, with the aim of comprehending the design and prediction of these complex self-assembly processes, is important because of the influence they have on the properties of the coordination polymer materials.[30,31] Different kinds of interpenetration have been reported in the literature[26, 32] and are summarised in the next paragraph thus:

a) 1D nets: In this case the interpenetration could be parallel (meaning the direction of propagation of the chains are parallel) or inclined (meaning the direction of propagation of the chains are inclined); b) 2D nets: Parallel (meaning the planes are parallel) or inclined (meaning the planes are inclined); c) Borromean interpenetration: this interpenetration arises in which any two nets are not interpenetrated but addition of a third net makes the nets inseparable without breaking a bond; d) 3D nets: Here different topologies are possible; e) Interpenetration of nets with different dimensions: 1D/2D, 1D/3D, 2D/3D; f) Interpenetration of nets with different topologies; g) Self-penetration (discussed above) 0D nets: Polycatenanes.

Figure 1.6 represents some of the interpenetrations directed by the void spaces that have been reported for 2D materials.
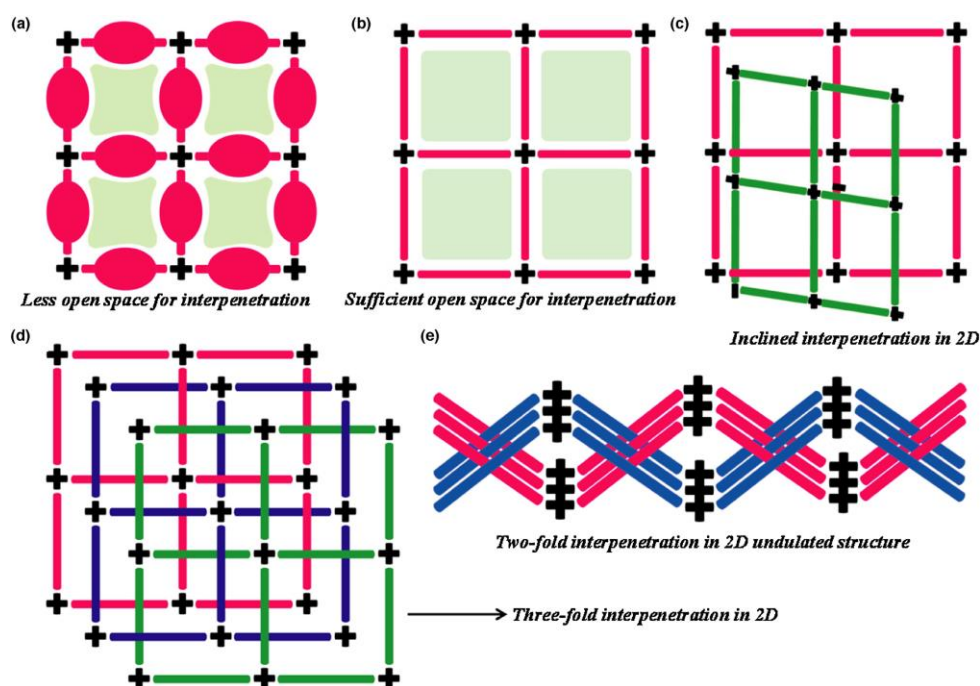
Figure 1.6 Schematic representation of 2D nets: (a) 2D network with no interpenetration, (b) A 2D network with sufficient two-dimensional open space, (c, d, e) Different types of interpenetration in 2D networks as indicated. [23]

1.2.3 Isoreticular MOFs

This was a term introduced into MOF chemistry by Yaghi *et al*.[20] Reticular synthesis is a conceptual approach whereby a MOF is designed and assembled. It is based upon identification of how a net is formed when the building blocks come together. The reticular synthesis approach has been used to prepare the first isoreticular series of MOFs (IRMOFs)[33] in which octahedral-shaped metal-containing SBUs were joined with a variety of linear ditopic carboxylate linkers to form 16 distinct MOFs which share the same cubic topology as IRMOF-1 (or MOF-5 as it is sometimes called). These 16 IRMOFs (see Figure 1.7) were formulated as $Zn_4O(link)_3(DEF)_x$. The links differ both in terms of functionality of the pendent groups (IRMOF-1 to IRMOF-7) and in length (IRMOF-8 to IRMOF-16). Expansion of the links leads to an increase in the internal void space (represented by yellow spheres in Figure 1.7). This expansion, however, allows

the formation of catenated/interpenetrated phases (IRMOF-9, IRMOF-11, IRMOF-13 and IRMOF-15). IRMOF-1was used to show that its 3-D porous framework can be functionalized with the organic groups -Br, -NH$_2$, -OC$_3$H$_7$, -OC$_5$H$_{11}$, -C$_2$H$_4$, and -C$_4$H$_4$ and that its void space can be expanded with the long linkers: biphenyl, tetrahydropyrene, pyrene, and terphenyl.
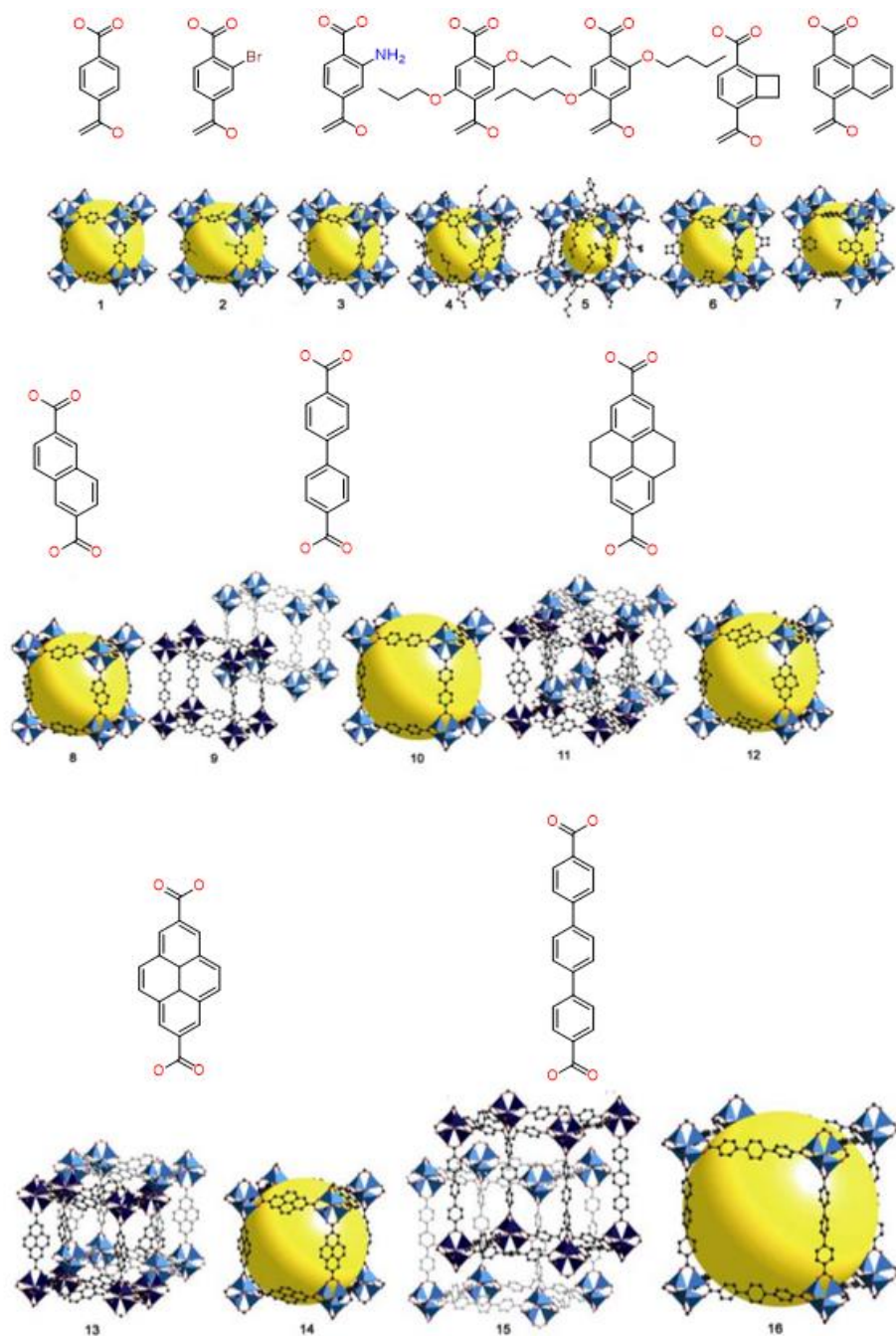
Figure 1.7 Organic linkers (top) and IRMOF series (bottom). The internal void space isrepresented by yellow spheres.[34]

Many other examples of isoreticular MOFs have been reported in the literature. Prominent among them was a review by Yaghi and co-workers in 2011[35] for various tritopic carboxylates and Cu_2 paddlewheel units as presented in Figure 1.8. Expansion from btc^{3-} (1,3,5-benzenetricarboxylate) to bbc^{3-} (4,4',4''-benzene-1,3,5-tryil-tribenzoate) led to enlargement of unit cell length to 68.31 Å in MOF-399 from 26.34 Å in HKUST-1 (MOF-199), resulting in an increase in volume by a factor of 17. Accordingly, MOF-399 had the highest porosity (94 %) and lowest density (0.126 $g \cdot cm^{-3}$) of any recorded MOF at the time it was reported in 2011. They consider that "the isoreticular expansion is one of the promising approaches to achieve the high surface area materials".
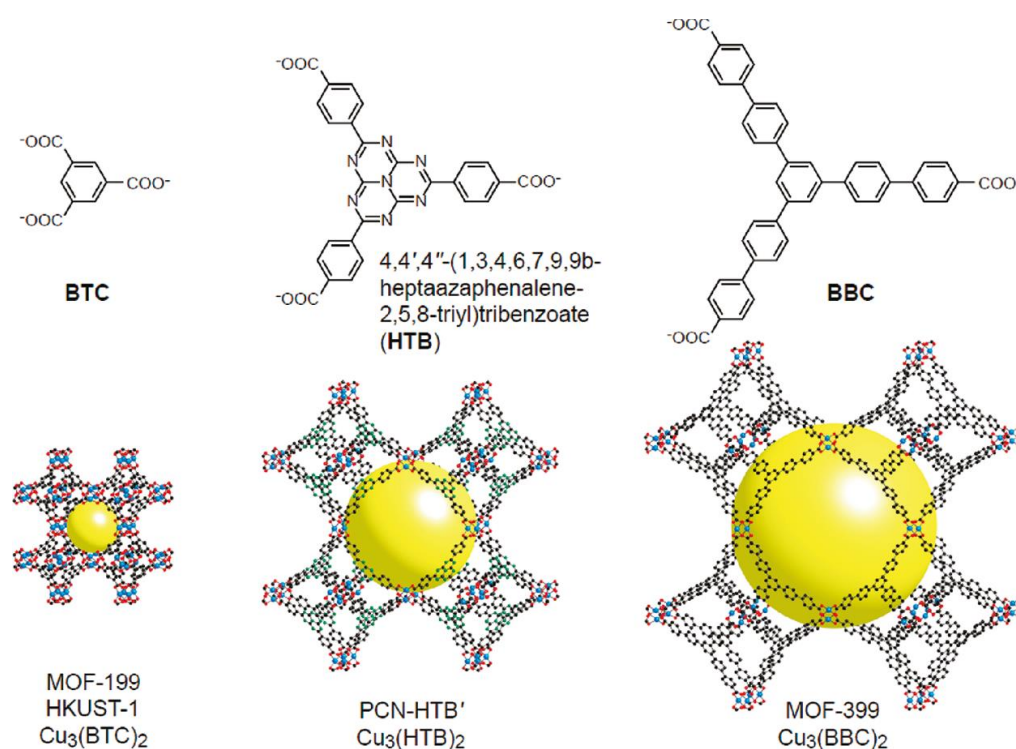
Figure 1.8. Molecular structures of organic linkers (top). Single crystal structures of MOF-199, PCN-HTB', and MOF-399 (bottom). The internal void space is represented by yellow spheres. Cu, blue; C, black; O, red; and N, green. Hydrogen atoms are omitted for clarity. [35]

1.3 Ligands used in MOFs synthesis
1.3.1. Carboxylate Ligands

The majority of metal-organic frameworks are made from multitopic ligands possessing the carboxylate functionality. Most of these classes of ligands are either commercially available, such as naphthalene-2,6-dicarboxylic acid (H_2NDC) and 1,3,5-benzenetricarboxylic acid or can be made easily using well defined and high yielding synthetic routes. The attractiveness of carboxylic acids as ligands is based on their high acidity (pKa ~ 4) which allows for facile *in situ* deprotonation. In addition, the metal–carboxylate bond formation is reversible under relatively mild conditions, which is probably responsible for the formation of well-ordered, crystalline MOFs. The negative charges on the carboxylates are countered by the positive charge of the metal centre once coordination takes place in a framework structure. This helps to eliminate any counter ions in the pores of the frameworks. However, it should be noted all frameworks achieve charge balance.

Figure 1.9 presents different varieties of ways in which a typical carboxylate linker (1,4-benzenedicarboxylic acid) could coordinate to the metal ions in MOFs. This coordination modes could also be observed with 1,3,5-benzenetricarboxylic acid as highlighted in Figure 1.10.
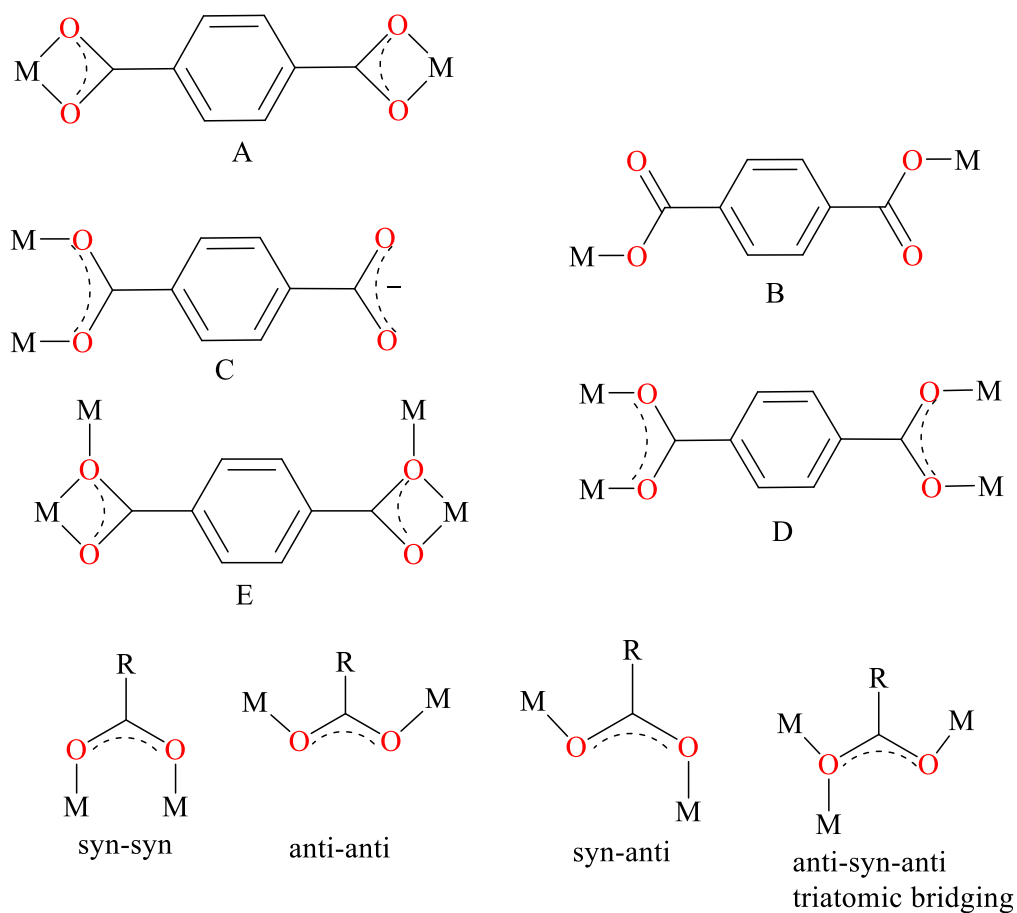
Figure 1.9 Possible coordination modes of 1,4-benzenedicarboxylic acid in MOFs: (A) chelating bis-bidentate, (B) isomonodentate, (C) mono-syn-syn bridging/bidentate, (D) syn-syn bridging bis-bidentate, (E) chelating/bridging bis-bidentate. The bottom row illustrates other possibilities with the respective terms used to describe the coordination modes.[36]
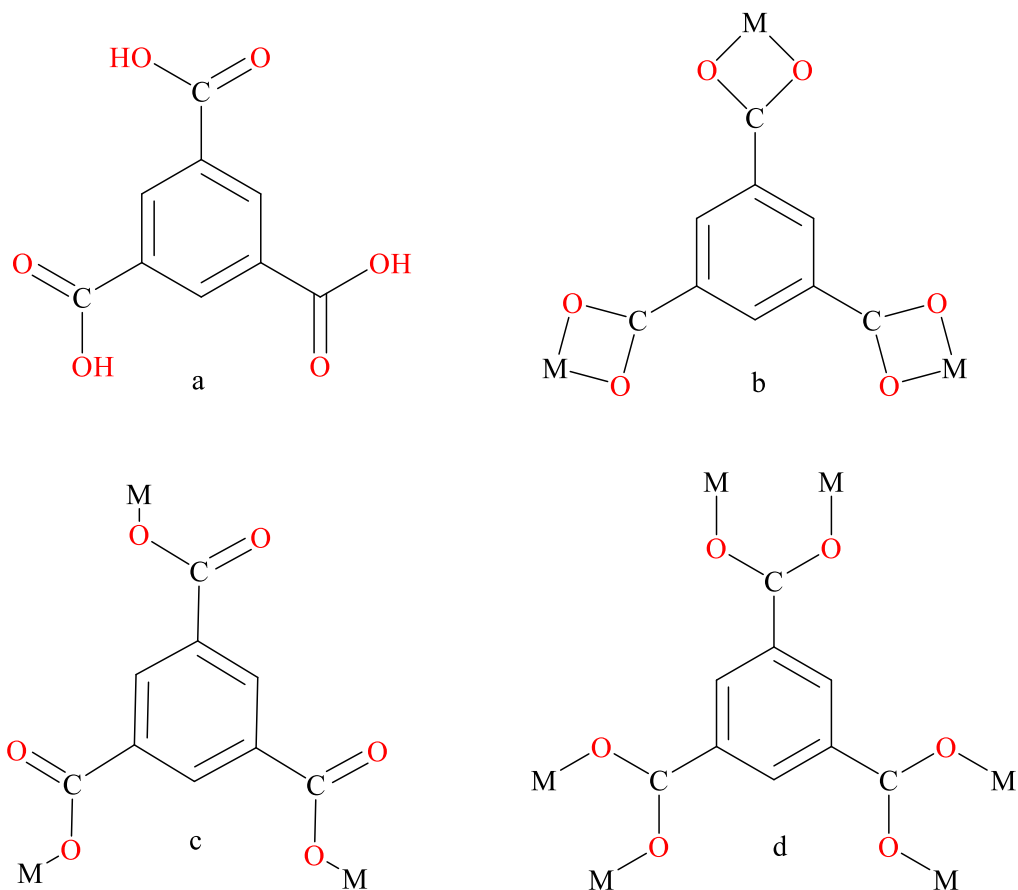
Figure 1.10 a) 1,3,5-benzenetricarboxylic acid and b-d) examples of multidentate coordination modes of 1,3,5-benzenetricarboxylic acid.[37]

1.3.2 Nitrogen-containing ligands

Ligands that contain nitrogen, for example pyridine-based ligands, have been shown to produce very stable MOFs. However, ligands containing primary amines produce much less stable frameworks. This is because primary amines exhibit poorer donor ability towards metal centres occasioned by low electron density on the nitrogen. It is worth mentioning at this juncture that there are also problems associated with the metal-N bond formation with the pyridine-based ligands, as this bond is relatively labile depending on the metal ions involved. Hence there is a possibility of rearrangement of the networks which in turn could give rise to unexpected frameworks leading to supramolecular isomerism.[38]

Most pyridyl ligands, unlike their carboxylate counterparts, are neutral, and once coordinated to a cationic metal centre the resultant network retains its positive charge(s) which must be balanced by counter ions, which occupy the pores of the framework. This can be disadvantageous if such material is to be used for gas adsorption studies.

A significant amount of research has been performed using nitrogen-containing ligands linked to silver(I) centres. Silver(I) ions have soft metal centres which have a high affinity for relatively soft nitrogen ligands. They readily form complexes with varying geometries. Coordination numbers for Ag(I) compounds have been characterised between one and six, showing a variety of geometries.[39] Ag(I) has completely filled 4d orbitals ($4d^{10}$) and usually adopts tetrahedral geometry at the silver centre (see Figure 1.11).
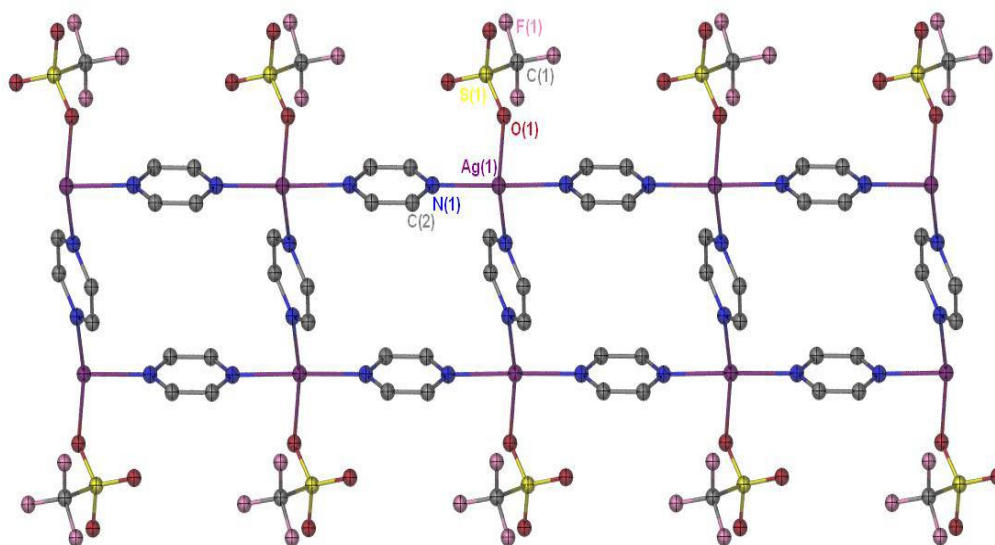
Figure 1.11 Molecular ladder of $\{[Ag_2(pyrz)_3(CF_3SO_3)_2]\}_\infty$ (pyrz = pyrazine).[40]

1.3.3 MOFs containing more than one type of linker

Different terminologies have been used to describe these kinds of MOFs. Yaghi *et al*.[41] called them multivariate MOFs (MTV-MOFs); Baiker and co-workers[42]

termed them MIXMOFs; coordination polymer – a more general term – by Matzger *et al*;[43] and mixed-component MOFs (MC-MOFs) by Burrows and co-workers.[44] This type of MOF makes it possible for further modification of properties of metal-organic frameworks by making use of two different organic linkers in combination with the metal nodes. A strategy known as 'pillaring' has been widely employed by many researchers in the design of MOFs.[46-49] Figure 1.12 shows a schematic representation of pillar-layered MOFs. The linkers acting as linkers can be inserted either in a stepwise manner[50-55] or by using a "one-pot" procedure.[36,56-64]
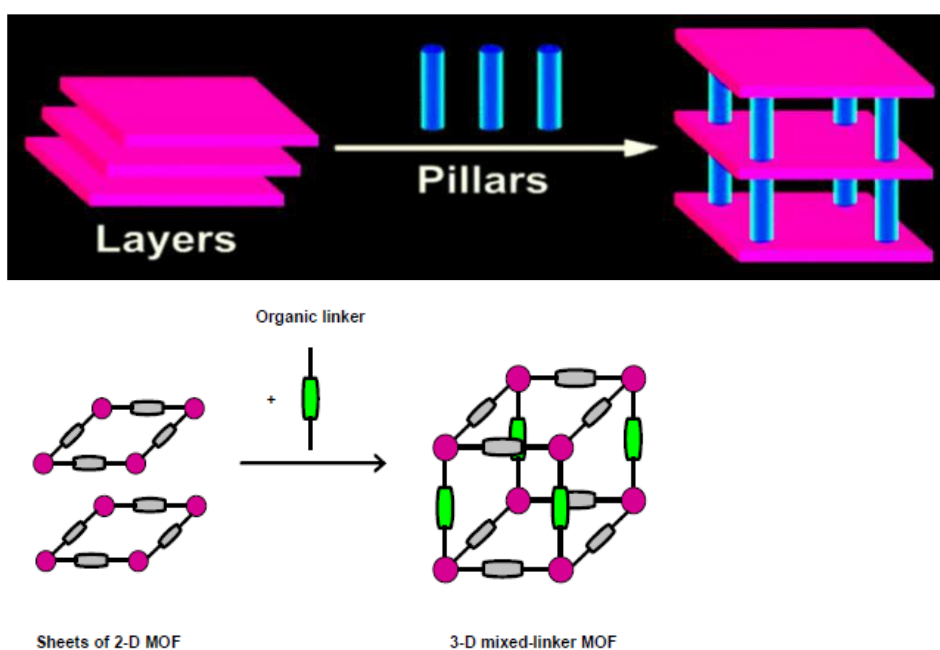
Figure 1.11 Schematic representation of construction of 3-D porous framework by pillar insertion strategy.[49,50]

The bipyridine together with polycarboxylate ligands have been the most reliable and typical organic linkers in constructing mixed-ligand MOFs. The reason for the choice of these connectors could be attributed to the different functionalities they each exhibit; hence each plays a distinct role in the MOFs so formed. The

bipyridine ligands (which are neutral) usually bind to the metal ions as the rod-like bidentate struts whereas the polycarboxylate bridging ligands may take the anionic or protonated form to provide various coordination modes when bound to the metal.

A typical example of MOFs containing two different organic linkers is the Zn-MOF depicted in Figure 1.12. The doubly interpenetrated framework was constructed by Hupp and co-workers[65] using 4,4',4'',4'''-benzene-1,2,4,5-tetrayl-tetrabenzoic acid (L1) and N,N'-di-(4-pyridyl)-1,4,5,8-naphthalenetetracarboxydiimide (L2).
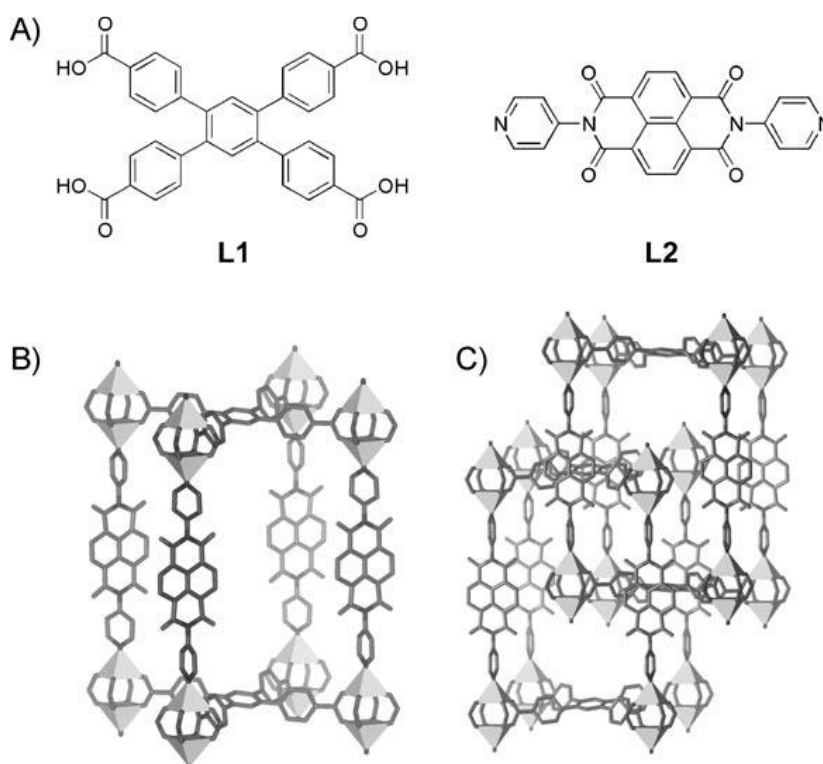
Figure 1.12 A) Chemical structure of L1 and L2. B) Crystal structure of $Zn_2(L1)(L2)$, one level of catenation is omitted to illustrate connectivity. Polyhedra represent zinc ions; Hydrogens omitted for clarity. C) Catenation of $Zn_2(L1)(L2)$. L1 = 4,4',4'',4'''-benzene-1,2,4,5-tetrayl-tetrabenzoic acid and L2 = N,N'-di-(4-pyridyl)-1,4,5,8-naphthalenetetracarboxydiimide.[61]

1.4 Methods of MOFs synthesis

Many methods have been reported for the synthesis of MOFs.[66-68] Prominent among those synthetic routes and worth discussing here are: traditional synthesis (solvothermal and non-solvothermal), microwave-assisted synthesis, electrochemical synthesis, mechanochemical synthesis, sonochemical synthesis and so-called 'green' synthesis. The different synthetic routes and the percentage of MOFs synthesized using the routes are presented in Figure 1.13.

1.4.1 Traditional synthesis

This method of preparing MOFs can be classified into two categories namely solvothermal and non-solvothermal. The term solvothermal is used to depict the use of any kind of solvent and has a much broader coverage than the term hydrothermal which is used when water acts as the solvent for the reaction. While non-solvothermal synthesis takes place below the boiling point of the solvent in open flasks at atmospheric pressure, solvothermal synthesis is performed at the boiling temperature of the solvent or above this boiling point in specially designed enclosed vessels under autogenous pressure. Sophisticated equipment/materials are not required for non-solvothermal synthesis as it can be accomplished both at room temperature and on mild heating. A typical scheme for non-solvothermal preparation of MOFs would involve the choice of the metal salt, organic linker(s) and solvent, as well as pH and temperature adjustment to make for maximal yield of the target MOF. In order to get a precipitate, the reagent concentrations should be selected in such a manner that the conditions for nucleation are achieved. This could be enhanced by increasing temperature so as to bring about solvent evaporation. Additionally, the concentration gradient

can be created by cooling of the solution slowly, solvent layering or slow

diffusion of one of the reactants.[66,69]

(a)

(b)
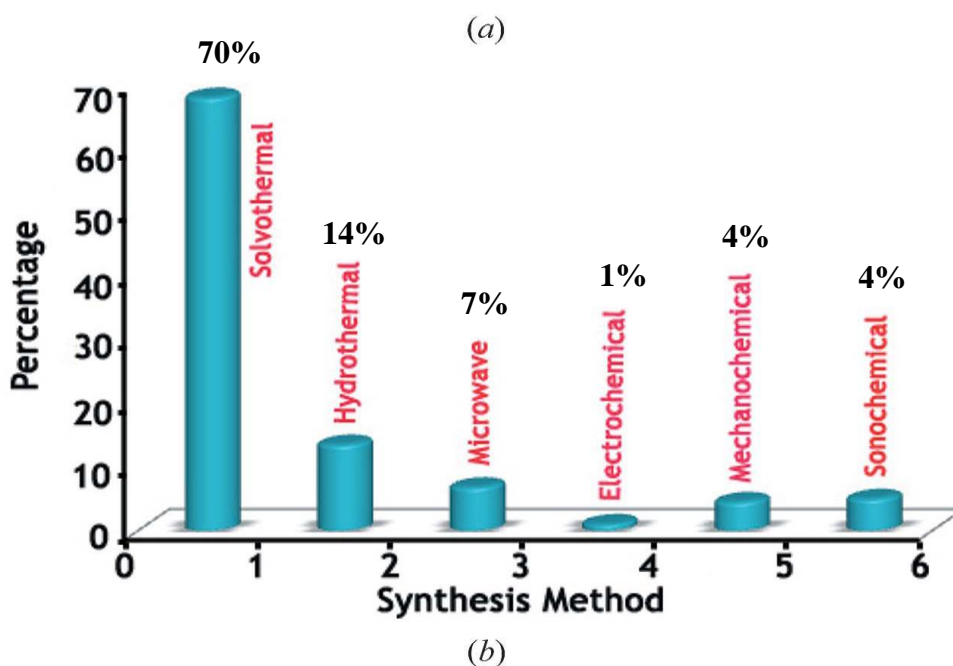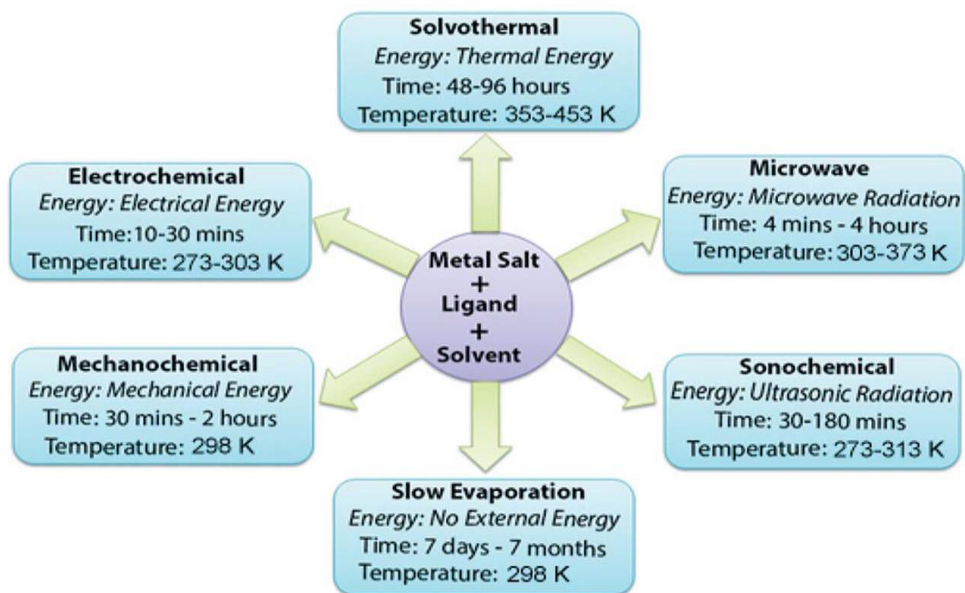
Figure 1.13 (a) Synthesis routes most widely employed for MOFs preparation;
(b) percentage of MOFs synthesized using the various methods. The data shown
was obtained from ref. 67 and valid as of 2013.

In solvothermal synthesis, many starting materials undergo quite unexpected chemical changes, which are usually followed by the formation of nanoscale morphologies which are not obtainable by conventional methods. In vast majority of the syntheses, high-boiling organic solvents such as dimethyl formamide, diethyl formamide, and less commonly, acetonitrile, acetone, ethanol, methanol etc. are utilised. Combination of solvents have also been employed to forestall problems associated with differing solubility for the different starting materials. Solvothermal reactions can be carried out in a wide range of temperature depending on which gives the best result. Generally, glass vials are used for lower temperature reactions. However, at very high temperature (greater than 400 K), the reactions are performed using Teflon-lined autoclaves.[70]

As seen in Figure 1.13, solvothermal method has been the most successful and most widely employed route for the preparation MOFs.

1.4.2 Microwave-assisted synthesis

Microwaves are a form of electromagnetic radiation with frequencies ranging from 300 to 300,000 MHz. They are made up of two components - electrical and magnetic. However, only the former has been found to influence synthesis of compounds.[67] Microwave-assisted synthesis provides a very rapid means for the synthesis of MOFs, and its procedures have been widely used to make nano-sized metal oxides.[71] Microwave-assisted preparation of MOFs involves heating a solution of the starting materials with microwaves for a period of about an hour to produce nanosized crystals. This synthetic method has been termed 'microwave-assisted solvothermal synthesis' for the preparation of MOFs. The

quality of the crystals obtained within a very short period of time by microwave-assisted processes are generally the same as those produced by the regular solvothermal processes.[72-76,130]

1.4.3 Electrochemical synthesis

Electrochemical synthesis is one of the processes being designed to achieve high reproducibility as well as high output of metal-organic framework materials. This is due to the fact that if this method is perfected, it requires no metal salts and offers continuous production of MOF crystals, which is key for production on an industrial scale. There exists the possibility of making MOF crystals under mild conditions by changing solvent and/or pH at room temperature. Here the metal ion is provided by anodic dissolution into the synthesis mixtures that include organic linkers and electrolytes. This enhances the formation of anions during the course of the reaction and helps to initiate a continuous process.[66, 69,77] In order to ensure that metal cations do not get deposited on the cathode, protic solvents are usually employed which can lead to the release of hydrogen during the electrochemical process. Some solvents, such as acrylonitrile, acrylates and maleates could be used in small amount as they get reduced first thereby preventing the above from occurring. This method was used for the first time for the synthesis MOFs (HKUST-1) in 2005 (see Figure 1.14).[78] Copper sheets (5 mm thick) were used as the dissolving anode; they were dipped in a solution of benzene-1,3,5-tricarboxylic acid in methanol together with copper cathodes. Within 150 min after application of voltage, a green-blue precipitate was deposited.

(a)

(b)

20000 : 1   1μm
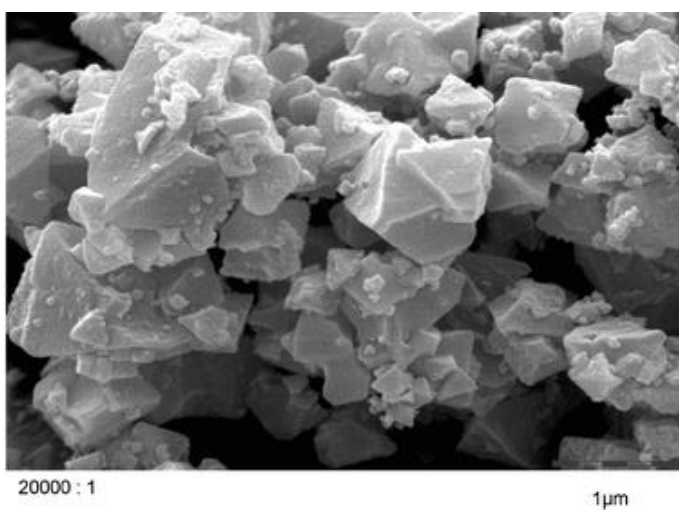
Figure 1.14 (a) Setup for electrochemical synthesis of MOF HKUST-1 and (b) SEM image of the product (magnification, x20 000).[78]

1.4.4 Mechanochemical Synthesis

Mechanochemistry is an area of chemistry which deals with reactions between solids most commonly kick-started only by means of mechanical energy; for instance, by milling in ball mills. This approach has become especially popular as it makes it possible to carry out reactions quickly and in high output with little or no solvent. At present, there is no general theory which explains the physicochemical processes which take place in mechanochemical reactions. The

most common approaches, so far, are the hot-spot model and the magma ± plasma model.[66] Lately, mechanochemical syntheses have been effectively used for the rapid synthesis of MOF materials using a technique known as liquid-assisted grinding (LAG), in which small amount of solvent is added into a solid reaction mixture.[79] Friščić *et al.* have demonstrated that by varying the solvent that is added in a LAG process, one-dimensional, two-dimensional and three-dimensional coordination polymers could be obtained from the same reaction mixture. This strategy has equally been applied for the synthesis of some zeolitic imidazolate frameworks (ZIFs).[80]

1.4.5 Sonochemical synthesis

Sonochemistry is an aspect of chemistry which deals with the study of molecules that undergo chemical change owing to the application of intensive ultrasonic radiation (20 kHz–10 MHz). Ultrasound induces chemical or physical changes as a result of a cavitation process which involves formation, growth and rapid collapse of bubbles in a liquid, creating local hot spots of a short lifetime with high temperature and pressure. These extreme conditions promote chemical reactions by instantaneous formation of a surplus of crystallization nuclei. This method can create homogeneous nucleation centres and considerably reduce the time of crystallization compared with conventional hydrothermal methods.[67] MOF-5 (Figure 1.7) has been successfully synthesised using sonochemical irradiation in 1-methyl-2-pyrrolidinone. The method produced crystals between 5 and 25 µm in 30 min, which is similar to MOF-5 synthesized using either solvothermal or microwave method.[67,81-88]

1.4.6 Green synthesis

This method, in the strictest sense, is not a method per se as it could actually be one or a combination of the methods mentioned earlier performed in such a manner that it 'reduces' or 'eliminates' the use and generation of toxic substances. "Green Chemistry" according to IUPAC[68] can be described as "the invention, design, and application of chemical products and processes to reduce or to eliminate the use and generation of hazardous substances". Relating this definition to MOFs synthesis, green synthesis focuses on making MOFs from reactants, solvents and under conditions (temperature, pressure and reactor) which do not pose any challenge to the environment. These parameters are very critical when green synthesis is to be carried out.

A very good example given by Reinsch in 2016 in a review[68] is that which outlines the different synthetic routes for the preparation of MOF HKUST-1 (HKUST stands for Hong-Kong University of Science and Technology). This copper paddle-wheel MOF is based on the dimeric connection of copper carboxylate units through 1,3,5-benzenetricarboxylate ions as shown in Figure 1.15.
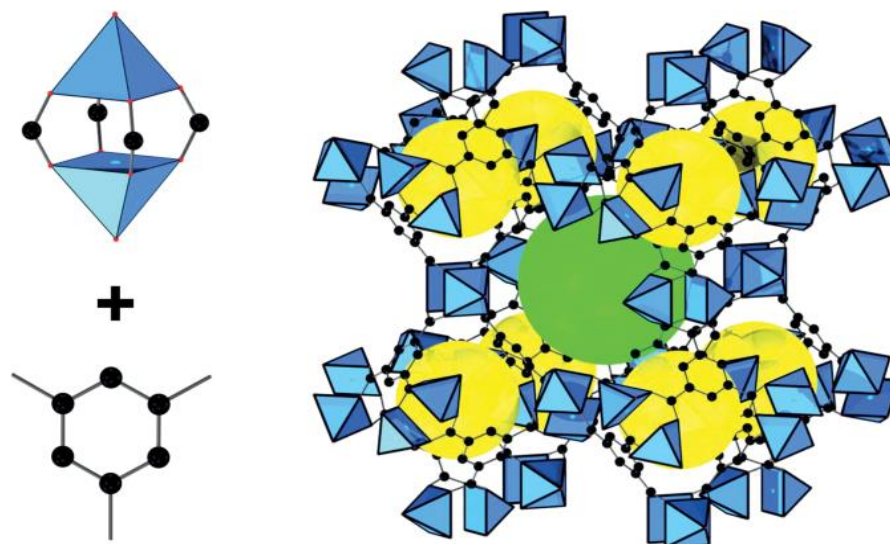
Figure 1.15 The building units of HKUST-1 on the left (copper carboxylate paddlewheel and the core of trimesic acid) and the resulting framework on the right. Two of the three different cavities are displayed as green and yellow spheres, respectively. CuO_5 polyhedra in blue, carbon atoms in black.[89]

The original synthesis route made use of copper nitrate and the solvents were water and ethanol combined at 180 °C for 12 h. These reaction conditions were not only extreme but also led to formation of by-products (copper and cuprous oxide) which are hazardous. Another route involved the use of DMF as solvent at room temperature. A report demonstrated that the by-products formation can be avoided at a lower reaction temperature of 120 °C in ethanol/water mixtures.[90] Mueller and co-workers[91] avoided the use of potentially oxidising nitrate ions by carrying out the synthesis using electrochemical synthesis and were still able to get HKUST-1. One of the most intriguing reports on the synthesis of this MOF is that in which $Cu(OH)_2$ was made use of as inorganic reactant at room temperature. Here water was produced as the only by-product after few hours.[92] This depicts rather optimised synthesis conditions with virtually complete conversion. Of particular interest is the fact that despite using such mild conditions, the apparent specific surface area of the product was approximately 1700 m^2 g^{-1}, thereby surpassing that which was originally reported ($\approx$ 700 m^2 g^{-}

[1]). Another classic example of green MOF synthesis was reported by Stoddart *et al* in 2010 whereby a series of CD-MOFs (CD = cyclodextrin) were made using food grade chemical reagents at room temperature. For instance, CD-MOF-1 was synthesised by the combination of 1.0 equiv of γ-CD (a symmetrical cyclic oligosaccharide that is mass-produced enzymatically from starch) with 8.0 equiv of potassium hydroxide in aqueous solution, followed by vapor diffusion of methanol into the solution during 2–7 days. This reaction yielded colourless, cubic, single crystals, suitable for X-ray crystallography, in approximately 70% yield.[93] The above examples clearly demonstrates that greener synthesis conditions hold the potential for improved material properties.

1.5 MOF characterisation

MOFs have been analysed using various analytical techniques, the choice of which depends on a number of factors such as their periodic structure, sensitivity to high temperature, sensitivity to air and their surface area.[66] The most important attributes of MOFs are actually their high specific surface area and porosity, which are much superior to the analogous properties of silica gels, zeolites and activated carbons.

Brunauer-Emmett-Teller[94] (BET as it is commonly called) method has been extensively used for the determination of the specific surface area of MOFs. This method is done by gas sorption and involves measuring the experimental dependence of adsorption on pressure under isothermal conditions, from which the total surface area of the adsorbent is determined.

MOFs' periodic structure makes it possible for their structure to be determined using X-raydiffraction (XRD), and this has been a very common method in

MOFs analysis. Generally, single crystal X-ray diffraction (SCXRD) is a ubiquitous technique for structural elucidation in chemical sciences as it is able to provide precise location of atoms in 3D space thereby making it possible to relate molecular structure of materials with their reactivity.[95] It is worth mentioning that it is not always possible to grow single crystals of MOFs having the appropriate size and quality for SCXRD, hence powder X-ray diffraction (PXRD) at room temperature is often used. PXRD patterns give a very good insight into the reproducibility of synthesis results and equally make it possible to offer explanation for structural differences between the samples of a given MOF made using different synthetic routes or reaction conditions.[96] Considering large unit cell parameters of MOFs as well as high electron density on metal sites, it can be quite challenging to determine the structure using PXRD. Variable-temperature X-ray diffraction has been used to study the thermal stability of MOFs as well as probing into the effect of guest solvent molecules on their structure.

Thermal stability of MOFs can be more directly investigated using thermogravimetric analysis (TGA). TGA measures the mass of the analysed sample as a function of temperature. In a typical thermogravimetric analysis, the sample is heated to high temperature (usually between 500 and 800 $^{\circ}$C) under inert conditions or atmospheric oxygen. There are series of curves which correspond to the loss of solvent molecules and organic linkers which provide a good insight into the overall stability of the MOF (see Figure 1.16 for a typical TGA plot).
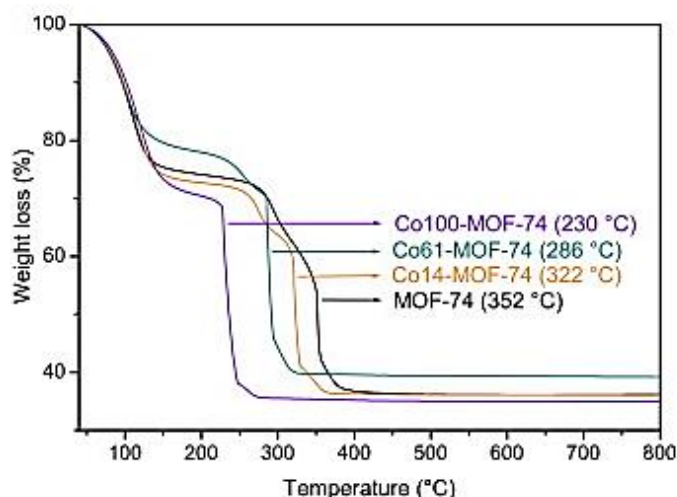
Figure 1.16 TGA plots for MOF-74.[97]

Suffice it to say that no single technique can be used for structural elucidation of MOFs. Other methods used in combination with the aforementioned analyses include elemental analysis (for C, H, N, Metal, etc. quantification), infrared (IR) spectroscopy, nuclear magnetic resonance (NMR) spectroscopy, scanning electron microscopy (SEM), X-ray absorption near-edge structure (XANES), extended X-ray absorption fine-structure (EXAFS), etc.

1.6 Application of MOFs

MOFs have been widely investigated for their applications in gas adsorption/storage, gas separation, catalysis and chemical sensing.[128] Some of the most important applications shall be discussed in this this study. Figure 1.17 shows a schematic representation of some MOFs which are well known for their gas storage capabilities.
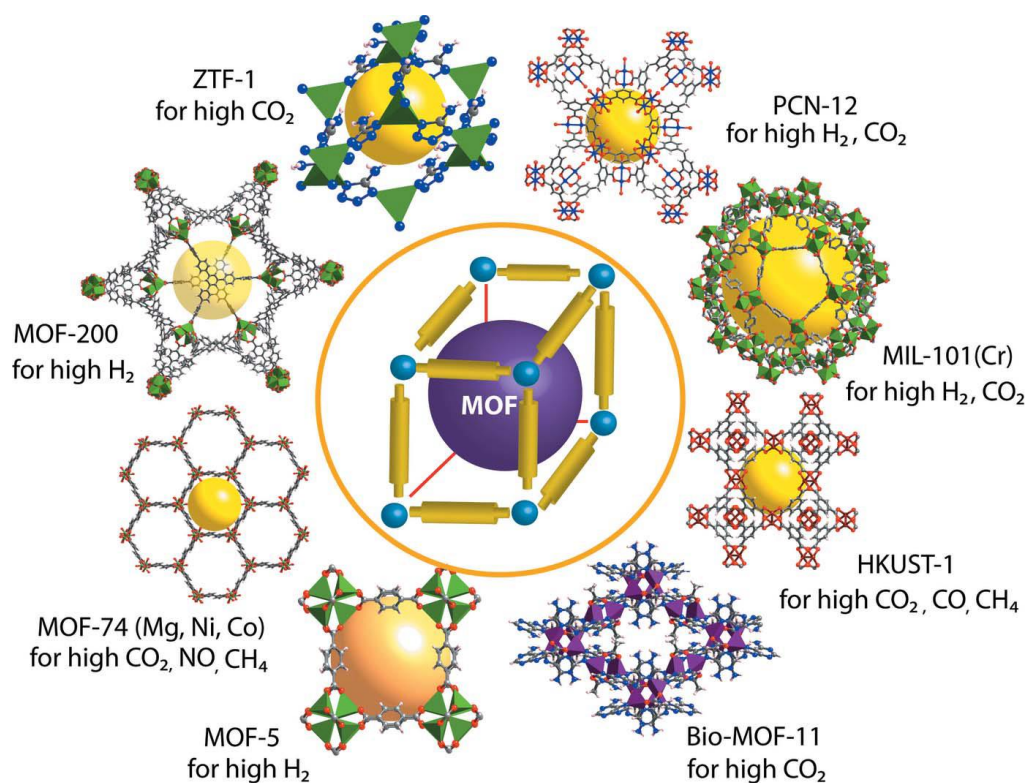
Figure 1.17 Schematic representation of some MOFs which are well known for their gas storage capabilities.[67]

1.6.1 Hydrogen storage

Due to the large gravimetric heat of combustion (120 MJ kg^{-1}) of hydrogen, it has been considered as a promising ideal source of energy. However, because of its low density of 0.08 kg m^{-3} in the gaseous state, storing hydrogen at ambient conditions is difficult. The volumetric storage density of hydrogen is low, and this hinders its use as a fuel, hence effective materials for storage have to be explored. The United States Department of Energy (DOE) set targets of 6 wt%, 45 g L^{-1} and 9 wt%, 81 g L^{-1} respectively for 2010 and 2015 for the gravimetric and volumetric storage for the gas. Porous MOFs have been identified as key to achieving these feats. The storage of this gas using MOFs is influenced by many factors which include but not limited to very high surface area, functionalized polar groups, light weight, open metal centres and specific weak interactions.

Over 300 metal organic framework materials have been tested for hydrogen uptake capacity.[67] MOF-177 is a typical example of MOFs that have shown great potential in H_2 storage.[98] This MOF material has a high BET surface area of about 5000 m^2 g^{-1} and a pore volume of 1.59 cm^3 g^{-1}. It exhibits a gravimetric H_2 uptake of 7.5 wt% at 70 bar and 77 K. Other MOFs which are renowned for their H_2 uptake include MOF-210, MIL-101, HKUST-1, NU-100, PCN-12, NOTT-102 and MOF-205.[99-102]

It goes without saying that MOFs with open metal sites lend high surface area which promotes stronger interaction between the nodes of metal ion and the molecules of H_2. This is what makes the aforementioned MOFs display very high H_2 uptake. Furthermore, from theoretical calculations, doping of MOFs with alkali metals such as Li could have improved H_2 uptake capacity.[67] This is due to the high affinity of these dopants for H_2.

1.6.2 Methane storage

Natural gas is made up 95% methane. Methane is a therefore a potential fuel. It has a very high gravimetric heat of combustion of 50 MJ kg^{-1} compared to gasoline which gravimetric heat of combustion is 44.5 MJ kg^{-1}. Metal organic framework materials have reached the United States Department of Energy target of 180 v/v at ambient temperature and pressure (< 35 bar) for methane. However, active research is still ongoing to further improve the capacity of MOFs for storing the gas.[103] In a review by Li *et al*,[104] four MOFs with excellent methane storage capacities at 270 K and 65 bar were screened. The MOFs are HKUST-1,[105] UTSA-76,[106] NOTT-102,[107] and NU-111[108] (see Figure 1.18). These MOFs were selected because they present very high methane uptake at

298 K. NU-111 possesses an exceptionally high gravimetric uptake of 0.5 g/g at

270 K and 65 bar, attaining the new gravimetric target. NU-111 also exhibits an

unparalleled high working capacity of 239 cm^3 (STP) cm^{-3} at 270 K, which

surpasses the 179 cm^3 (STP) cm^{-3} obtained at 298 K by 34%. The above results

are suggestive of the fact that decrease in the storage temperature could lead to

higher storage capacity for methane in MOFs. A recent study by Li and co-

workers[109] has revealed that incorporation of Lewis basic nitrogen sites into

MOFs could dramatically improve their capacities to store methane.
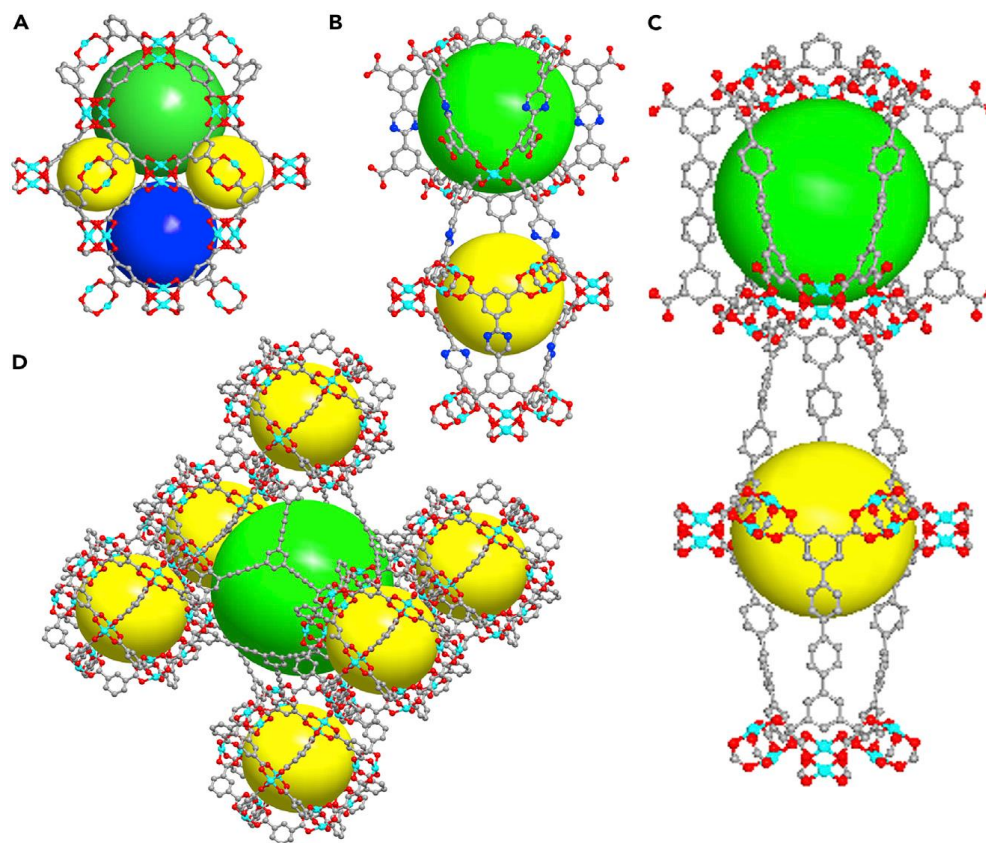
Figure 1.18 X-ray crystal structure of HKUST-1 (A), UTSA-76 (B), NOTT-102 (C), and U-111 (D) indicating their pore cages. The gray, red, cyan, and blue spheres respectively stand for carbon, oxygen, copper, and nitrogen atoms. The bigger yellow, green, and blue spheres denote the pores within the frameworks. The hydrogen atoms are omitted for clarity.[104]

Other notable gases that have been successfully tested for storage in MOF

materials include NO and CO.[110-112]

1.6.3 Magnetic materials

Magnetism in solid materials have found many applications in electromagnetism, devices and sensing. Lately, magnetism has been incorporated into MOFs by using paramagnetic 3d transition metal nodes alongside suitable organic linkers. These kinds of MOFs have been named magnetic metal-organic frameworks (MMOFs).[67] They are based on the first-row transition metals which include V, Cr, Mn, Fe, Co, Ni and Cu, and have contributed immensely to the development of porous molecular magnets.[113, 114] MMOFs can be employed in air separation due to their porosity and magnetic properties.[131] A crucial factor which facilitates magnetism in MOFs is the framework structure itself, which may involve layered geometry with shorter distance of conjugation between the metal clusters. The nature of the organic linkers used for the synthesis of MMOFs has also been considered as key in determining the magnetism in the resulting MOFs.[117] In that case, the radicals present in the organic ligand are responsible for the magnetic properties. Finally, metal-radical combined approaches have been employed to prepare various MMOFs.[115, 116]

1.6.4 MOFs as molecular sensors

Research in the use of MOFs as luminescent materials has attracted a lot of attention due to the potential of MOFs to be applied in small-molecule

sensors,[118-121] pH sensors,[122] concentrators of light for photovoltaic devices, antennae in light-sensitive bioinorganic compounds and high-technology optics. MOFs, in this regard, are quite useful due to their hybrid nature, viz. the inorganic metal ions, the organic linkers as well as the guest molecules. Metal organic frameworks can act as excellent solid-state luminescent materials as a result of their structural predictability and environments which are well defined for the chromophores in crystalline form. Metal ions of the lanthanide series are widely used for the preparation of luminescent MOFs, owing to their electronic transitions from d to f shells, which is accompanied by emission of photon. Europium (Eu) and terbium (Tb) have received the greatest attention due to their attractive lumophores which arise from their narrow emission.[123, 124] Linking the lanthanide metal ions with strongly absorbing ligands greatly enhances MOFs' luminescent properties. Other members of the lanthanide series that have been used as luminescent metal ions include: Dy, Sm, Nd, Gd, Er and Yb. Organic linkers with appreciable conjugation through extended π-systems are responsible for the strong absorption, emission and electronic transition. In the case of organic ligands, π–π^* and n–π^* electronic transitions are usually observed. The luminescent properties of transition-metal MOFs arise only from the linkers.[67] Several types of effect have been reported in the literature.[125-127] They include metal-to-ligand charge transfer (MLCT), ligand-to-metal charge transfer (LMCT), ligand-to-ligand charge transfer (LLCT) and ligand centre luminescence.[132] Naphthalene diimides (NDIs) have found great use as ligands in constructing luminescent MOFs. Anthracene, pyrene, perylene and stilbene types of ligands are also commonly employed.[133]

1.7 Aims and objectives

This research primarily aims at synthesising and characterising novel self-assembled pillared metal-organic frameworks by solvothermal methods using redox-active rylene diimides as organic linkers. The synthesis and characterisation of the rylene diimides used in the project shall also be reported. Host-guest experiments involving the encapsulation of ferrocene shall be investigated and discussed.

1.8 Conclusion

Metal-organic frameworks commonly referred to as MOFs are a class of self-assembled materials constructed from metal-containing nodes and organic linkers. These materials are interesting for their tunability when it comes to rational design, through control of the architecture and functionalization of the pores. These features of MOFs have placed them as potential future materials in gas and energy storage, sensor technology, water harvesting, catalysis, among other interesting applications. The fact that there are different possible combinations of infinite organic linkers with a variety of metal nodes, means this area of research will remain viable over a long period of time.

It is worth concluding this chapter by giving an insight into what are to be expected in the proceeding chapters. While chapter two shall be dedicated to the ligands used in this research, chapters three and four will focus on the MOFs that have been synthesised using the ligands. The encapsulation experiments shall be discussed briefly in chapter five. Materials and the general methods used will be covered in chapter six.

1.9 References

1. H.-C. Zhou and S. Kitagawa, *Chem. Soc. Rev.,* 2014, **43**, 5416-5418.

2. C. R. Pfeiffer, N. Biggins, W. Lewis and N. R. Champness, *CrystEngComm*, 2017, **19**, 5558-5564.

3. H. Furukawa, K. E. Cordova, M. O'Keeffe and O. M. Yaghi, *Science,* 2013, **341**, 1230444.

4. R. Ricco, C. R. Pfeiffer, K. Sumida, C. J. Sumby, P. Falcaro, S. Furukawa, N. R. Champness and C. J. Doonan*, CrystEngComm,* 2016, **18**, 6532–6542.

5. P. Song, B. Liu, Y. Li, J. Yang, Z. Wang and X. Li, *CrystEngComm*, 2012, **14**, 2296

6. D. Peralta, G. Chaplais, A. Simon-Masseron, K. Barthelet, C. Chizallet, A. Quoineaud, and G. Pirngruber, *J. Am. Chem. Soc.*, 2012, **134** 8115–8126.

7. S. Ehrling, E. M. Reynolds, V. Bon, I. Senkovska, T. E. Gorelik, J. D. Evans, M. Rauche, M. Mendt, M. S. Weiss, A. Pöppl, E. Brunner, U. Kaiser, A. L. Goodwin and S. Kaskel. *Nat. Chem.*, 2021, **13,** 568–574.

8. S. Kitagawa, R. Kitaura and S.-i. Noro, *Angew. Chem. Int. Ed.*, 2004, **43**, 2334-2375

9. Z. Wang and S. M. Cohen, *Chem. Soc. Rev.*, 2009, **38**, 1315-1329

10. S. Keskin and S. Kızılel, *Ind. Eng. Chem. Res.*, 2011, **50**, 1799–1812.

11. E. A. Tomic, *J. Appl. Polymer Sci.*, 1965, **9**, 3745–3752.

12. B. F. Hoskins and R. Robson, *J. Am. Chem. Soc.*, 1989, **111**, 5962-5964.

13. T. R. Cook, Y.-R. Zheng and P. J. Stang, *Chem. Rev.*, 2013, **113**, 734-777

14. N. R. Champness, *Dalton Trans.,* 2011, **40**, 10311-10315

15. B. F. Hoskins and R. Robson, *J. Am. Chem. Soc*, 1990, **112**, 1546-1554.

16. R. Robson, B. F. Abrahams, S. R. Batten, R. W. Gable, B. F. Hoskins and J. P. Liu, *ACS Symp. Ser.*, 1992, **499**, 256-273.

17. P. Z. Moghadam, A. Li, X.-W. Liu, R. Bueno-Perez, S.-D. Wang, S. B. Wiggin, P. A. Wood and D. Fairen-Jimenez, *Chem. Sci.*, 2020, **11**, 8373—8387

18. W. Xu and O. M. Yaghi, *ACS Central Science* 2020, **6**, 1348-1354

19. C.-C. Wang, Y.-S. Ho, *Scientometrics,* 2016, **109**, 481-513.

20. O. M. Yaghi, M. O'Keeffe, N. W. Ockwig, H. K. Chae, M. Eddaoudi, J. Kim, *Nature*, 2003, **423**, 705-714

21. G. Férey, C. Mellot-Draznieks, C. Serre, F. Millange, J. Dutour, S. Surble, I. Margiolaki, *Science*, 2005, **309**, 2040-2042.

22. O. I. Lebedev, F. Millange, C. Serre, G. Van Tendeloo, G. Ferey, *Chem. Mater.*, 2005, **17**, 6525-6527.

23. R. Haldar, N. Sikdar and T. K. Maji, *Materials Today*, **18**, 2015, 97-116

24. A. Ferguson, L. Liu, S. J. Tapperwijn, D. Perl, F. Coudert, S. V. Cleuvenbergen, T. Verbiest, M. A. Van der Veen and S. G. Telfer, *Nat. Chem.*, 2016, **8**, 250-257

25. D. Bradshaw, S. El-Hankari and L. Lupica-Spagnolo, *Chem. Soc. Rev.*, 2014, **43**, 5431-5443

26. J. Liu, Y. Hong, Y. Guan, M. Lin, C. Huang and W. Dai, *Dalton Trans.*, 2015, **44**, 653–658

27. O. Shekhah, H. Wang, M. Paradinas, C. Ocal, B. Schupbach, A. Terfort, D. Zacher, R. A. Fischer and C. Woll, *Nat. Mater.*, 2009, **8**, 481-484

28. H. Aggarwal, R. K. Das, P. M. Bhatt and L. J. Barbour, *Chem. Sci.*, 2015, **6**, 4986.

29. G. Verma, S. Butikofer, S. Kumar, and S. Ma, *Top Curr Chem (Z)* **378**, 4.

30. O. K. Farha, J. T. Hupp, *Acc. Chem. Res*. 2010, **43**, 1166−1175.

31. S. Ma, D. Sun, M. Ambrogio, J. A. Fillinger, S. Parkin, H.-C. Zhou, *J. Am. Chem. Soc.* 2007, **129**, 1858−1859.

32. S. R. Batten, *CrystEngComm*, 2001, **3,** 67.

33. M. Eddaoudi, J. Kim, N. Rosi, D. Vodak, J. Wachter, M. O'Keeffe, O. M. Yaghi, *Science*, 2002, **295**, 469-472.

34. J. L. C. Rowsell, O. M. Yaghi, *Microporous Mesoporous Mater.* 2004, **73**, 3-4

35. H. Furukawa, Y. B. Go, N. Ko, Y. K. Park, F. J. Uribe-Romo, J. Kim, M. O'Keeffe, O. M. Yaghi, *Inorg. Chem.*, 2011, **50**, 9147-9152.

36. J. Tao, M. L. Tong, X. M. Chen, *J.Chem. Soc. Dalton Trans.* 2000, 3669-3674.

37. O. M. Yaghi, C. E. Davis, G. Li, H. Li, *J. Am. Chem. Soc*, 1997, **119**, 2861-2868.

38. L. Carlucci, G. Ciani, D. M. Proserpio, F. Porta, *CrystEngComm.,* 2006, **8**, 696-706

39. D. L. Reger, R. F. Semeniuc, C. A. Little, M. D. Smith, *Inorg. Chem.*, 2006, **45**, 7758-7769

40. D. Venkataraman, S. Lee, J. S. Moore, P. Zhang, K. A. Hirsch, G. B. Gardner, A. C. Covey, C. L. Prentice, *Chem. Mater.*, 1996, **8**, 2030-2040.

41. H. Deng, C. J. Doonan, H. Furukawa, R. B. Ferreira, J. Towne, C. B. Knobler, B.Wang, O. M. Yaghi, *Science* 2010, **327**, 846-850.

42. W. Kleist, F. Jutz, M. Maciejewski, A. Baiker, *Eur. J. Inorg. Chem.*, 2009, **2009**, 3552-3561.

43. K. Koh, A. G. Wong-Foy, A. J. Matzger, *Chem. Comm.*, 2009, **0**, 6162-6164.

44. A. D. Burrows, *CrystEngComm*, 2011, **13**, 3623-3642.

45. O. K. Farha, C. D. Malliakas, M. G. Kanatzidis and J. T. Hupp, *J. Am. Chem. Soc*, 2010, **132**, 950-952.

46. H. Chung, P. M. Barron, R. W. Novotny, H.-T. Son, C. Hu and W. Choe, *Cryst. Growth & Design*, 2009, **9**, 3327-3332.

47. B.-Q. Ma, K. L. Mulfort and J. T. Hupp, *Inorg. Chem.*, 2005, **44**, 4912-4914.

48. H. Chun, D. N. Dybtsev, H. Kim and K. Kim, *Chem. Eur. J.*, 2005, **11**, 3521-3529

49. L. Han, L.-P. Xu, L. Qin, W.-N. Zhao, X.-Z. Yan and L. Yu, *Cryst. Growth & Design*, 2013, **13**, 4260-4267.

50. G. Férey, *Chem. Mater.* 2001, **13**, 3084-3098.

51. R. Kitaura, F. Iwahori, R. Matsuda, S. Kitagawa, Y. Kubota, M. Takata, T. C. Kobayashi, *Inorg. Chem.,* 2004, **43**, 6522-6524.

52. Z. Chen, S. Xiang, D. Zhao, B. Chen, *Cryst. Growth & Design*, 2009, **9**, 5293-5296.

53. K. Seki, S. Takamizawa, W. Mori, *Chem. Lett.*, 2001, **30**, 332-333

54. K. Seki, W. Mori, *J. Phys. Chem. B*, 2002, **106**, 1380-1385.

55. H. Chun, H. Jung, G. Koo, H. Jeong, D.-K. Kim, *Inorg. Chem.*, 2008, **47**, 5355-5359.

56. K. Kim, H. Chun, D. N. Dybtsev, H. Kim, *Chem. Eur. J.*, 2005, **11**, 3521-3529.

57. T. K. Maji, M. Ohba, S. Kitagawa, *Inorg. Chem.,* 2005, **44**, 9225-9231.

58. J.-C. Dai, X.-T. Wu, S.-M. Hu, Z.-Y. Fu, J.-J. Zhang, W.-X. Du, H.-H. Zhang, R.-Q. Sun, *Eur. J. Inorg. Chem.*, 2004, **2004**, 2096-2106.

59. B.-Q. Ma, K. L. Mulfort, J. T. Hupp, *Inorg. Chem.*, 2005, **44**, 4912-4914.

60. H. Chun, J. Moon, *Inorg. Chem.*, 2007, **46**, 4371-4373.

61. J. Y. Lee, D. H. Olson, L. Pan, T. J. Emge, J. Li, *Adv. Funct. Mater.,* 2007, **17**, 1255-1262.

62. J. Zhang, L. Wojtas, R. W. Larsen, M. Eddaoudi, M. J. Zaworotko, *J. Am. Chem. Soc,* 2009, **131**, 17040-17041.

63. L.-G. Zhu, H.-P. Xiao, *Z. Anorg. Allg. Chem.,* 2008, **634**, 845-847

64. B. Chen, C. Liang Sr, J. Yang, D. S. Contreras, S. Dai, *Angew. Chem. Int. Ed.,* 2006, **45**, 1390-1393.

65. K. L. Mulfort, O. K. Farha, C. D. Malliakas, M. G. Kanatzidis, and J. T. Hupp, *Chem. Eur. J.* 2010, **16**, 276 – 281.

66. V. V. Butova, M. A. Soldatov, A. A. Guda, K. A. Lomachenko and C. Lamberti, *Russ. Chem. Rev.*, 2016, **85**, 280-307.

67. C. Dey, T. Kundu, B. P. Biswal, A. Mallick and R. Banerjee, *Acta Cryst.*, 2014, **B70**, 3-10.

68. H. Reinsch, *Eur. J. Inorg. Chem.*, 2016, 4290-4299.

69. N. Stock, S. Biswas, *Chem. Rev.*, 2012, **112**, 933-969

70. C. Wang and J. Y. Ying, *Chem. Mater.*,1999, **11**, 3113–3120.

71. A. Lagashetty, V. Havanoor S. Basavaraja, S. D. Balaji and A. Venkataraman, *Sci. Technol. Adv. Mater.*, 2007, **8**, 484–493.

72. H. Bux, F. Liang, Y. Li, J. Cravillon, M. Wiebcke, and J. Caro, *J. Am. Chem. Soc.*, 2009, **131**, 16000–16001.

73. K. Hindelang, S. I. Vagin, C. Anger and B. Rieger, *Chem. Comm.*, 2012, **48**, 2888–2890.

74. W. Liang and D. M. D'Alessandro, *Chem. Comm.*, 2013, **49**, 3706–3708.

75. B. Zornoza, A. Martinez-Joaristi, P. Serra-Crespo, C. Tellez, J. Coronas, J. Gascon, and F. Kapteijn, *Chem. Comm.*, 2011, **47**, 9522-9524.

76. J. Klinowski, F. A. A. Paz, P. Silva and J. Rocha, *Dalton Trans.*, 2011,**40**, 321–330.

77. A. Martinez Joaristi, J. Juan-Alcaniz, P. Serra-Crespo, F. Kapteijn and J. Gascon, *Cryst. Growth Des.*, 2012, **12**, 3489–3498.

78. U. Mueller, M. Schubert, F. Teich, H. Puetter, K. Schierle-Arndt, J. PastreÂ, *J. Mater. Chem.* 2006, **16**, 626-636.

79. P. J. Beldon, L. Fabian, R. S. Stein, A. Thirumurugan, A. K. Cheetham and T. Friscic, *Angew. Chem. Int. Ed.*, 2010, **49**, 9640–9643.

80. T. Friscic, I. Halasz, P. J. Beldon, A. M. Belenguer, F. Adams, S. A. Kimber, V. Honkimaki and R. E. Dinnebier, *Nat. Chem.*, 2013, **5**, 66–73.

81.   N. Arul Dhas, C. P. Raj and A. Gedanken, *Chem. Mater.*, 1998, **10**, 3278–3281.

82.   A. Aslani and A. Morsali, *Inorg. Chim. Acta*, 2009, **362**, 5012–5016.

83.   C. G. Carson, A. J. Brown, D. S. Sholl and S. Nair, *Cryst. Growth Des*. 2011, **11**, 4505–4510.

84.   S. Dharmarathna, C. K. King'ondu, W. Pedrick, L. Pahalagedara and S. L. Suib, *Chem. Mater.*, 2012, **24**, 705–712.

85.   D. W. Jung, D. A. Yang, J. Kim, J. Kim and W. S. Ahn, *Dalton Trans.*, 2010, **39**, 2883–2887.

86.   J. Kim, S. Yang, S. B. Choi, J. Sim, J. Kim and W. Ahn, *J. Mater. Chem.* 2011, **21**, 3070–3076.

87.   P. Mohanty, N. M. Khine Linn and K. Landskron, *Langmuir*, 2009, **26**, 1147–1151.

88.   W.-J. Son, J. Kim, J. Kim and W.-S. Ahn, *Chem. Comm.*, 2008, **0**, 6336-6338.

89.   S. S.-Y. Chui, S. M.-F. Lo, J. P. H. Charmant, A. G. Orpen, I. D. Williams, *Science*, 1999, **283**, 1148–1150.

90.   K. Schlichte, T. Kratzke, S. Kaskel, *Microporous Mesoporous Mater.*, 2004, **73**, 81–88.

91.   U. Mueller, M. Schubert, F. Teich, H. Puetter, K. Schierle-Arndt, J. Pastre, *J. Mater. Chem.*, 2006, **16**, 626–636.

92.   G. Majano, J. Perez-Ramirez, *Adv. Mater.*, 2013, **25**, 1052–1057.

93.   R.A. Smaldone, R. S. Forgan, H.Furukawa, J. J. Gassensmith, A. M. Z. Slawin, O. M. Yaghi, and J. F. Stoddart, *Angew. Chem. Int. Ed*., 2010, **49**, 8630–8634

94.   S. Brunauer, P. H. Emmett, E. Teller, *J. Am. Chem. Soc.*, 1938, **60**, 309-319.

95.   N. R. Champness, C. J. Doonan and W. M. Bloch, *Angew. Chem. Int. Ed.*, 2015, **54**, 12860-12867.

96.   J. Hafizovic, M. Bjorgen, U. Olsbye, P. D. C. Dietzel, S. Bordiga, C. Prestipino, C. Lamberti and K. P. Lillerud, *J. Am. Chem. Soc.*, 2007, **129**, 3612-3620.

97.   J. A. Botas, G. Calleja, M. Sanchez-Sanchez and M. G. Orcajo, *Int. J. Hydrogen Energy*, 2011, **36** 10834-10844.

98.   A. G. Wong-Foy, A. J. Matzger and O. M. Yaghi, *J. Am. Chem. Soc.*, 2006, **128**, 3494–3495.

99. X.-S. Wang, S. Ma, P. M. Forster, D. Yuan, J. Eckert, J. J. Lopez, B. J. Murphy, J. B. Parise and H.-C. Zhou, *Angew. Chem.*, 2008, **120**, 7373–7376.

100. X. Lin, I. Telepeni, A. J. Blake, A. Dailly, C. M. Brown, J. M. Simmons, M. Zoppi, G. S. Walker, K. M. Thomas, T. J. Mays, P. Hubberstey, N. R. Champness, and M. Schroder, *J. Am. Chem. Soc.,* 2009, **131**, 2159–2171.

101. O. K. Farha, A. O. Yazaydin, I. Eryazici, C. D. Malliakas, B. G. Hauser, M. G Kanatzidis, S. T. Nguyen, R. Q. Snurr, and J. T. Hupp, *Nat. Chem.,* 2010, **2**, 944–948.

102. H. Furukawa, N. Ko, Y. B. Go, N. Aratani, S. B. Choi, E. Choi, A. O. Yazaydin, R. Q. Snurr, M. O'Keeffe, J. Kim, and O. M. Yaghi, *Science*, 2010, **329**, 424–428.

103. K. Konstas, T. Osl, Y. Yang, B. Michael, N. Burke, A. J. Hill and M. R. Hill, *J. Mater. Chem.*, 2012, **22**, 16698–16708.

104. B. Li, H. Wen, W. Zhou, J. Q. Xu, and B. Chen, *Chem,* 2016, **1**, 557–580.

105. Y. Peng, V. Krungleviciute, I. Eryazici, J. T. Hupp, O. K. Farha and T. Yildirim, *J. Am. Chem. Soc.*, 2013, **135**, 11887–11894.

106. J. A. Mason, J. Oktawiec, M. K. Taylor, M. R. Hudson, J. Rodriguez, J. E. Bachman, M. I. Gonzalez, A. Cervellino, A. Guagliardi, C. M. Brown, P. L. Llewellyn, N. Masciocchi and J. R. Long, *Nature*, 2015, **527**, 357–361.

107. Y. He, W. Zhou, T. Yildirim and B. Chen, *Energy Environ. Sci*., 2013, **6**, 2735–2744.

108. Y. Peng, G. Srinivas, C. E. Wilmer, I. Eryazici, R. Q. Snurr, J. T. Hupp, T. Yildirim, O. K. and Farha, *Chem. Comm.*, 2013, **49**, 2992–2994

109. B. Li, H. Wen, H. Wang, H. Wu, T. Yildirim, W. Zhou and B. Chen, *Energy Environ. Sci.,* 2015, **8**, 2504–2511.

110. S. Shimomura, M. Higuchi, Y. Matsuda, K. Yoneda, Y. Hijikata, Y. Kubota, Y. Mita, J. Kim, M. Takata, and S. Kitagawa, *Nat. Chem.*, 2010, **2**, 633–637.

111. P. K. Allan, B. Xiao, S. J. Teat, J. W. Knight, and R. E. Morris, *J. Am. Chem. Soc*., 2010, **132**, 3605–3611.

112. A. C. McKinlay, B. Xiao, D. S. Wragg, P. S. Wheatley, I. L. Megson, and R. E. Morris, *J. Am. Chem. Soc*., 2008, **130**, 10440–10444.

113. E. Coronado and G. Minguez Espallargas, *Chem. Soc. Rev*., 2013, **42**, 1525–1539.

114. M. Kurmoo, *Chem. Soc. Rev*., 2009, **38**, 1353–1379.

115. N. Roques, D. Maspoch, I. Imaz, A. Datcu, J.-P. Sutter, C. Rovira and J. Veciana, *Chem. Comm.*, 2008, **27**, 3160–3162.

116. N. Roques, D. Maspoch, F. Luis, A. Camon, K. Wurst, A. Datcu, C. Rovira, D. Ruiz-Molina and J. Veciana, *J. Mater. Chem.*, 2008, **18**, 98–108.

117. M. Arczyński and D. Pinkowicz, *Inorg. Chem.,* 2020, **59**, 13489–13501

118. M. D. Allendorf, C. A. Bauer, R. K. Bhakta and R. J. T. Houk, *Chemical Society Reviews*, 2009, **38**, 1330-1352.

119. Y. Takashima, V. M. Martínez, S. Furukawa, M. Kondo, S. Shimomura, H. Uehara, M. Nakahama, K. Sugimoto and S. Kitagawa, *Nat. Comm.*, 2011, **2**, 168.

120. Z. Z. Lu, R. Zhang, Y. Z. Li, Z. J. Guo and H. G. Zheng, *J. Am. Chem. Soc.*, 2011, **133**, 4172–4174.

121. C. Y. Sun, X. L. Wang, C. Qin, J. L. Jin, Z. M. Su, P. Huang and K. Z. Shao, *Chem. Eur. J.* 2013, **19**, 3639–3645.

122. B. V. Harbuzaru, A. Corma, F. Rey, J. L. Jorda, D. Ananias, L.D. Carlos and J. Rocha, *Angew. Chem. Int. Ed.*, 2009, **48**, 6476–6479.

123. M. L. Reddy and S. Sivakumar, Dalton Trans., 2013, 42, 2663–2678.

124. Y. Cui, H. Xu, Y. Yue, Z. Guo, J. Yu, Z. Chen, J. Gao, Y. Yang, G. Qian and B. Chen, *J. Am. Chem. Soc.*, 2012, **134**, 3979–3982.

125. J. Rocha, L. D. Carlos, F. A. Paz and D. Ananias, *Chem. Soc. Rev.* 2011, **40**, 926–940.

126. D. Zacher, O. Shekhah, C. Woll and R. A. Fischer, *Chem. Soc. Rev.*, 2009, **38**, 1418–1429.

127. S.-Z. Zhan, M. Li, S. W. Ng and D. Li, *Chem. Eur. J.*, 2013, **19**, 10217–10225.

128. S. L. Griffin and N. R. Champness, *Coord. Chem. Rev.*, 2020, **414**, 213295.

129. Y. Chen, X. Bai and Z. Ye, *Nanomaterials*. 2020, **10**, 1481.

130. A. Laybourn, J. Katrib, R. S. Ferrari-John, C. G. Morris, S. Yang, O. Udoudo, T. L. Easun, C. Dodds, N. R. Champness, S. W. Kingman and M. Schröder, *J. Mater. Chem. A*, 2017, **5**, 7333-7338.

131. R. Ricco, L. Malfatti, M. Takahashi, A. J. Hill and P. Falcaro, *J. Mater. Chem. A*, 2013, **1**, 13033-13045.

132. J.-J. Liu, Z.-J. Wang, S.-B. Xia, J. Liu and X. Shen, *Dyes Pigm.*, 2020, **172,** 107856.

133. D. Liu, T.-F. Liu, Y.-P. Chen, L. Zou, D. Feng, K. Wang, Q. Zhang, S. Yuan, C. Zhong and H.-C. Zhou, *J. Am. Chem. Soc.*, 2015, **137**, 7740-7746.

Chapter Two   **Rylene Diimide Linkers in Metal-Organic Synthesis**

2.1 Introduction

Rylenes are a class of polycyclic hydrocarbons constructed by connecting naphthalene units (denoted by 'n' in Figure 2.1) at the so-called peri positions. The first three members of this rylene family are naphthalene, perylene and terrylene with 'n' respectively equals to 1, 2 and 3. Rylene diimides, on the other hand, are organic dyes which have two diimide groups appended at the end positions of rylene[1] as shown in Figure 2.1. Consequently, rylene diimides containing one, two and three naphthalene units are called naphthalene-, perylene- and terrylene diimide respectively.
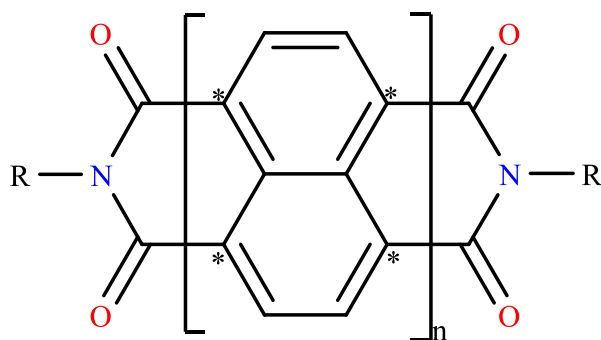
Figure 2.1: General representation of rylene diimides (asterisks indicate the peri positions and 'n' stands for the number of naphthalene units present). R can be any substituent group e.g. alkyl, carboxylic, etc.

The solubility of rylene diimides in common organic solvents such as dichloromethane (DCM), chloroform (CHCl$_3$) and DMF decreases as the number of naphthalene units increases. This is largely due to π-π stacking which becomes very pronounced in the larger members of the family. This stacking can be disrupted by carefully designing the molecule so as to improve their solubility. This is usually done by attaching sterically bulky groups or long alkyl chains at the imide position. It is important to mention that while 'bay' substitution (see Figure 2.2) has a significant effect on the electronic and

optical properties at the molecular level,[34] imide substituents do not affect these properties appreciably.[35] However, as mentioned earlier, imide substituents provide a means of tuning the solubility and aggregation of the molecules.[2]

The most common derivatives of these rylene diimides are the naphthalene-1,4,5,8-tetracarboxydiimide (NDI), perylene-3,4,9,10-tetracarboxy diimide (PDI) and terrylene-3,4,11,12-tetracarboxydiimide (TDI). Figure 2.2 shows the numbering scheme as well as the bay and imide regions in these first three members of the rylene diimide family. NDIs and PDIs are interesting for their predictable redox activity, strong absorbance (hence, high absorption coefficient) and fluorescence (with relatively high quantum yield). These aforementioned properties can easily be modified towards targeted applications. Owing to these interesting characteristics, they have found applications in organic electronics, photovoltaic devices, anion recognition and construction of metal–organic frameworks.[3]

As this research project focuses mainly on the incorporation of these redox-active compounds in MOFs, a quick mention of the most common NDIs and PDIs that have been employed in MOFs shall be presented in this chapter. However, a more detailed review of NDI- and PDI-containing MOFs will be covered in chapter three.
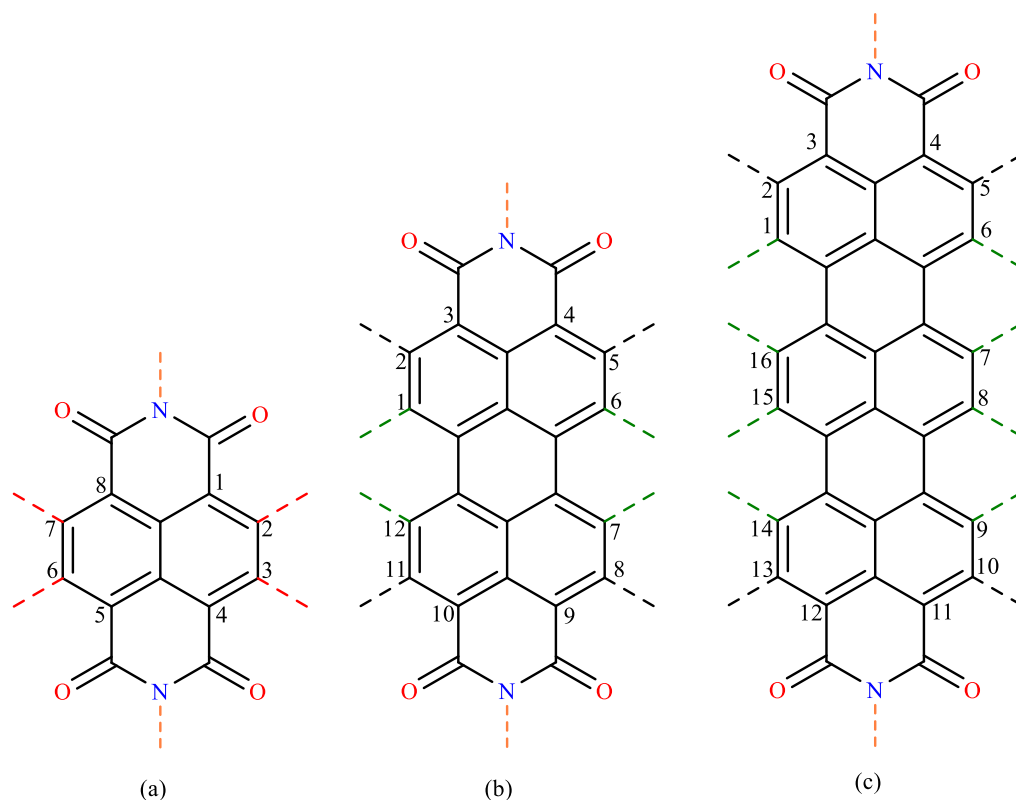
Figure 2.2: General structures for (a) naphthalene diimide (b) perylene diimide and (c)terrylene diimide indicating the numbering schemes. The core, bay, ortho and imide positions are respectively represented using the red, green, black and orange (dashed) lines.

2.2 Rylene diimides in MOF Synthesis.

As mentioned earlier, rylene diimides, particularly naphthalene diimides, have found wide application in the synthesis of metal-organic frameworks. The interest in using this class of materials stems from their interesting properties at the molecular level. Their redox-activity, for instance, is transferred to the highly ordered framework materials that are obtained thereafter. The presence of this rylene diimide ligands in MOFs causes the latter to exhibit unique behaviours such as photochromism,[4,5] and electrochromism.[6] More on this will be presented in chapter three.

2.2.1 NDI Linkers in MOFs

NDIs which are typically used in MOF synthesis are pre-functionalised in order to act as linkers in the MOFs. The most commonly used are the pyridyl- and the carboxylate-based NDIs. The pyridyl and the carboxylic functional groups are usually attached to the NDI core via the imide region. These NDIs are usually symmetric with the same functional groups at both ends. While the pyridyl-based NDIs are usually ditopic, the carboxylic-based counterparts have two or more topicity[7] depending on the number of carboxylic groups present. Other types of NDI ligands used in the construction of framework materials include the azolate or azolide-based NDIs and N-oxydic pyridyl NDI. Some representatives of the different types of NDI linkers are presented in Figure 2.3.
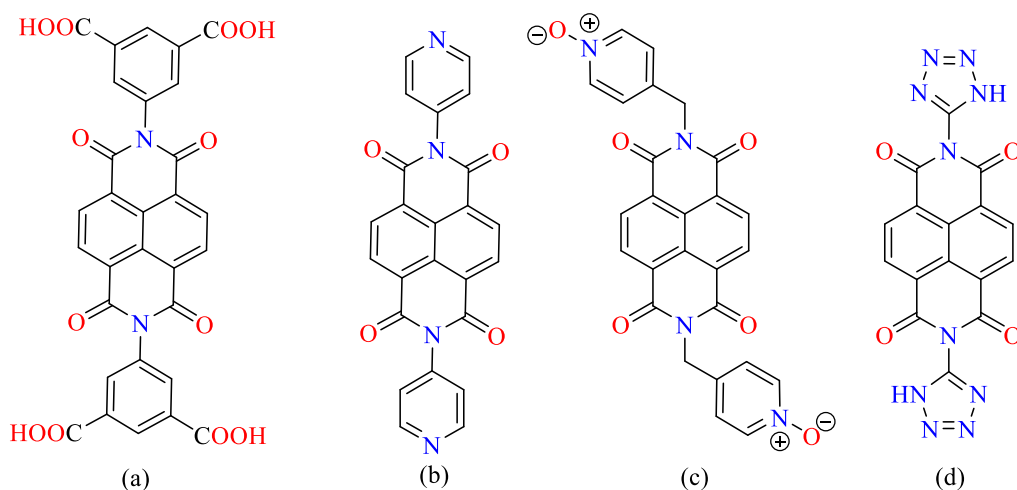
Figure 2.3: Representative NDI linkers utilised in MOFs: (a) carboxylic-based NDI;[8,9] (b)pyridyl-based NDI;[10,11] (c) N-oxydic pyridyl-based NDI[12] and (d) azolate-based NDI.[13]

2.2.2 PDI Linkers in MOFs.

Compared to the NDIs which have been widely used in MOFs construction, PDI-containing MOFs are relatively rare in the literature. The scarcity of this class of MOFs is largely due to the lack of solubility of either the pyridyl or carboxylate-based PDIs as they tend to adopt π-π stacking interactions in common synthetic solvents. This problem can be circumvented by substituting, either at the bay or the imide positions, groups that can disrupt the formation of π-π stacking. Where there is no bulky group present, bases such as triethylamine and sodium hydroxide have been employed to facilitate the solubility of the PDI.[16] To date, only four PDIs, all of which are carboxylic-based, have been successfully used in making MOFs, [14,15,16,17] and the first of them was reported by Turner and co-workers in 2014 (see Figure 2.4).[14] What all these PDIs have in common is that they have some substituents either at the imide or bay region, minimising π-π stacking and facilitating solubility. For instance, four chloro- substituents at the bay position and two benzoic acid substituents, one at each end of the imide positions have been used to achieve the aforementioned desired features (Figure 2.4b).[15] These substituents resulted in a twisted PDI with a dihedral angle of 38.3º and conferred axial chirality on the PDI components of the resulting MOF (details of this will be covered in chapter four).
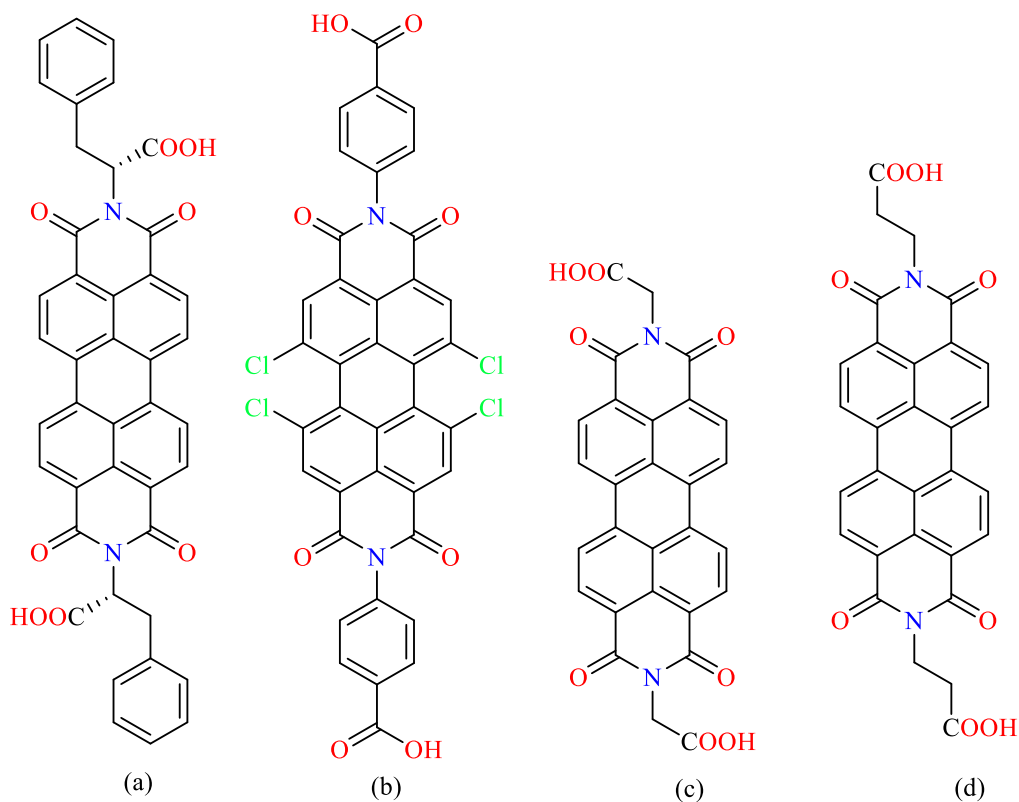
Figure 2.4: Structures of PDIs that have been used in MOFs synthesis.

2.3 Results and Discussion

Three novel ligands comprising two naphthalene diimides and one perylene diimide have been successfully made and incorporated into the construction MOFs (see Figure 2.5). In addition to these, a well-known NDI ligand – N,N'-di-(4-pyridyl)-1,4,5,8-naphthalenetetracarboxydiimide or **DPNDI** (Figure 2.3b) – has also been synthesised and employed in this research. One of the novel rylene diimide linkers is an NDI (named N,N'-bis(2,6-diisopropyl-4-(pyridin-4-yl)phenyl)-1,4,5,8-naphthalenetetracarboxydiimide or **DPPNDI**) while the other is the PDI analogue of the **DPPNDI** named N,N'-bis(2,6-diisopropyl-4-(pyridin-4-yl)phenyl)-3,4,9,10-perylenetetracarboxydiimide or **DPPPDI.** The third linker

is a nicotinic acid-based NDI, N,N'-bis(dinicotinic acid)-1,4,5,8-naphthalenetetracarboxydiimide, **DNNDI**.
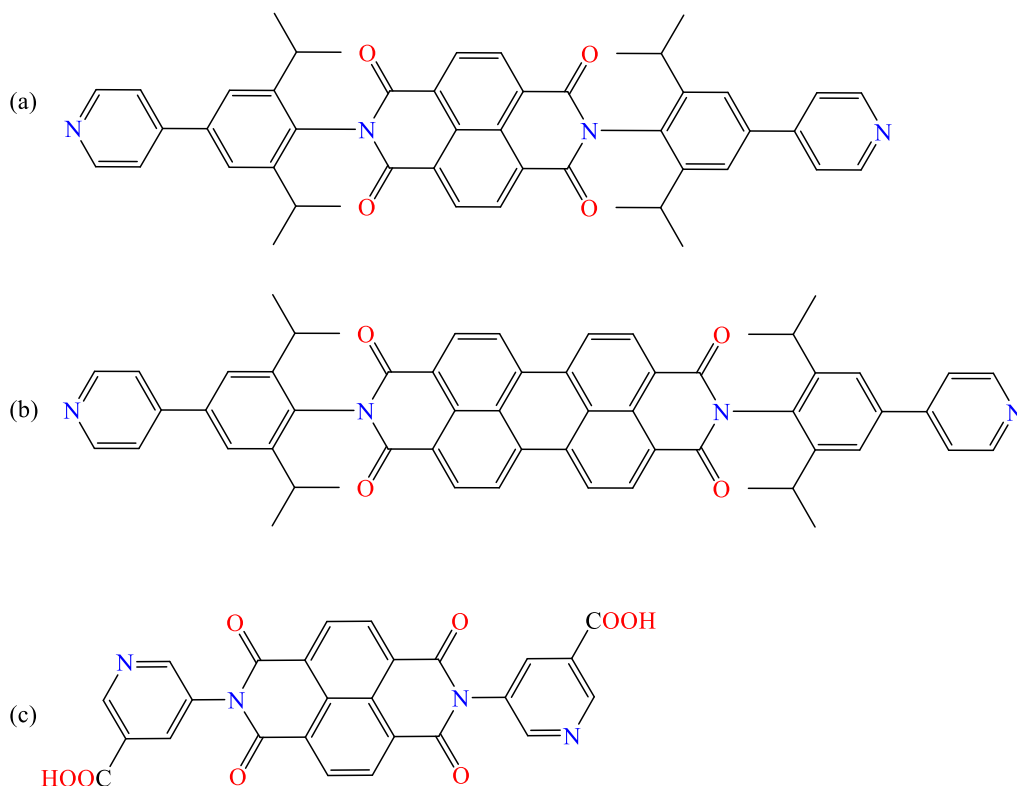
Figure 2.5: Structures of ligands reported in this thesis – (a) **DPPNDI**; (b) **DPPPDI**; (c) **DNNDI**.

2.3.1: Ligand design and synthesis

The design of the **DPPNDI** and **DPPPDI** was made bearing in mind the solution processibility of the rylene diimides. Another factor that was considered in the design was the point of coordination to metal centres. These two requirements were fulfilled through imide substitution of the rylene diimide with a bulky group, 2,6-diisopropyl-4-(pyridin-4-yl)aniline. The synthesis of the aniline was performed following two literature protocols. The first step of the synthesis involves iodination[18] of commercially available 2,6-diisopropylaniline to give 4-iodo-2,6-diisopropyl aniline. This is followed by Suzuki-Miyaura cross-

coupling reaction[19] with pyridine-4-boronic acid pinacol ester to yield 2,6-diisopropyl-4-(pyridine-4-yl)aniline (a novel compound) (see Scheme 2.1 for details) . This compound was characterised using single crystal XRD, NMR, IR, and MS. The IR spectrum is shown in Figure 2.5 and the N-H stretches of the NH_2-group are prominent at 3201 and 3300 cm^{-1}. The crystal structure of the aniline can be found under the crystallography section below in this chapter.
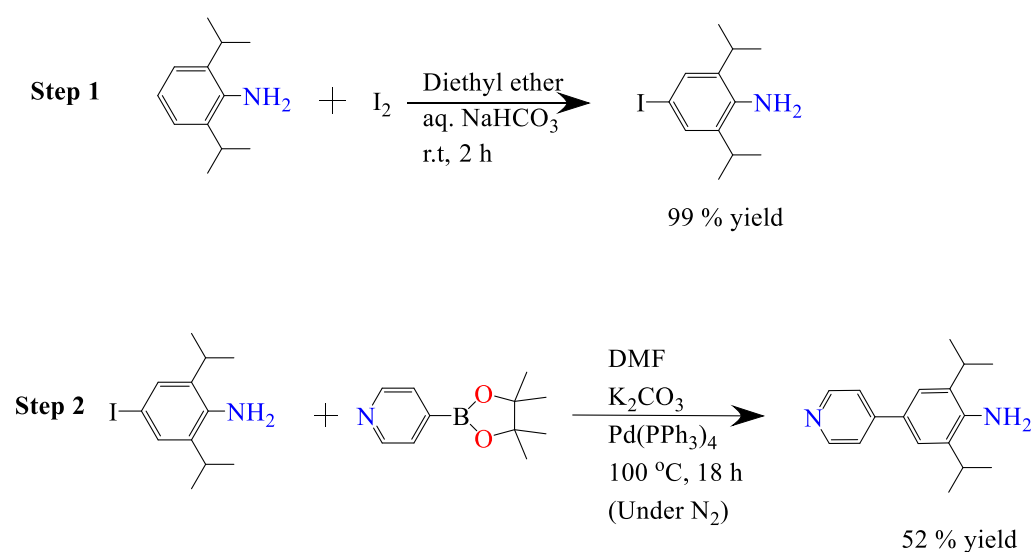
Scheme 2.1: Schematic illustration of the synthesis procedure of 2,6-diisopropyl-4-(pyridin-4-yl)aniline

The preparation of **DPPNDI** and **DPPPDI** was performed using a modified literature procedure.[20] It involves an overnight condensation reaction between 1,4,5,8-naphthalenetetracarboxylic dianhydride, NTCDA, (in the case of the case of **DPPNDI**) and 2,6-diisopropyl-4-(pyridin-4-yl)aniline in DMF under inert (nitrogen) atmosphere at 180 °C (see Scheme 2.2). Following the synthesis the compound was purified by column chromatography using ethyl acetate and DCM (ratio 2:3). For the synthesis of **DPPPDI** on the other hand, the procedure was similar to that for **DPPNDI** except that 3,4,9,10-perylenetetracarboxylic

dianhydride, PTCDA, was used instead of 1,4,5,8-naphthalenetetracarboxylic dianhydride (see scheme 2.2). Both the NTCDA and PTCDA were commercially sourced.

The remaining two ligands, **DNNDI** and **DPNDI**, used in this study were made according to a literature protocol.[21] NTCDA and the corresponding amine (5-aminonicotinic or 4-aminopyridine - both of which were obtained commercially) were condensed in DMF at 120 °C overnight. The resulting solid was purified through vacuum filtration, washed with DMF, acetone and diethyl ether to give an off-white powder in more than 80% yield. As mentioned previously, **DNNDI** is a novel ligand while **DPNDI**, is among the most widely studied NDIs in MOF synthesis. Due to the lack of solubility in common organic solvents like DCM and chloroform of **DNNDI**, extensive characterization of the compound was restricted. Thus, most of the following discussion will be restricted to **DPPNDI** and **DPPPDI**.
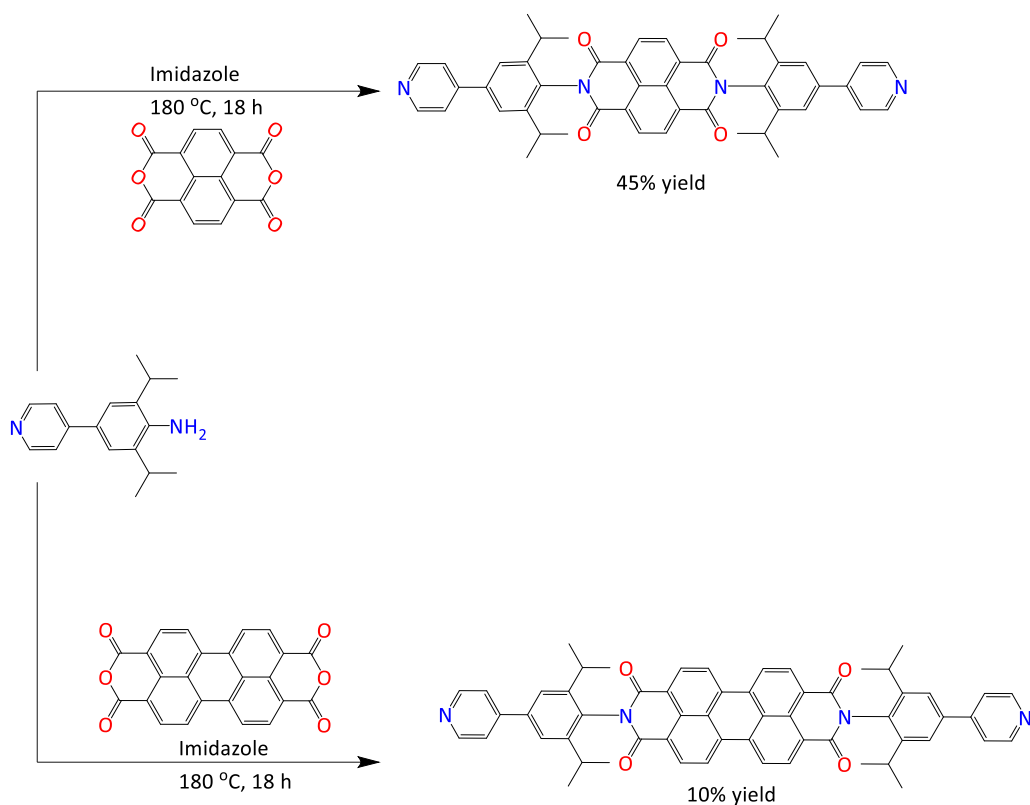
Scheme 2.2: Synthesis of **DPPNDI** (top) and **DPPPDI** (bottom)

2.3.2: X-ray crystallography

Crystals of **DPPNDI**, **DPPPDI** and 2,6-diisopropyl-4-(pyridin-4-yl)aniline suitable for single crystal x-ray diffraction studies were obtained by slow evaporation of DCM solutions of the compounds. The single crystals were selected and mounted on a diffractometer to obtain the crystal structures presented in Figure 2.5. For the **DPPNDI** sample, the crystal was kept at 120(2) K during data collection whereas for the **DPPPDI** sample the data collection was done at 100 K. Using Olex-2,[22] the structure was solved with the SHELXT[23] structure solution program using Intrinsic Phasing and refined with the SHELXL[24] refinement package using Least Squares minimisation.

(a)

(b)

(c)
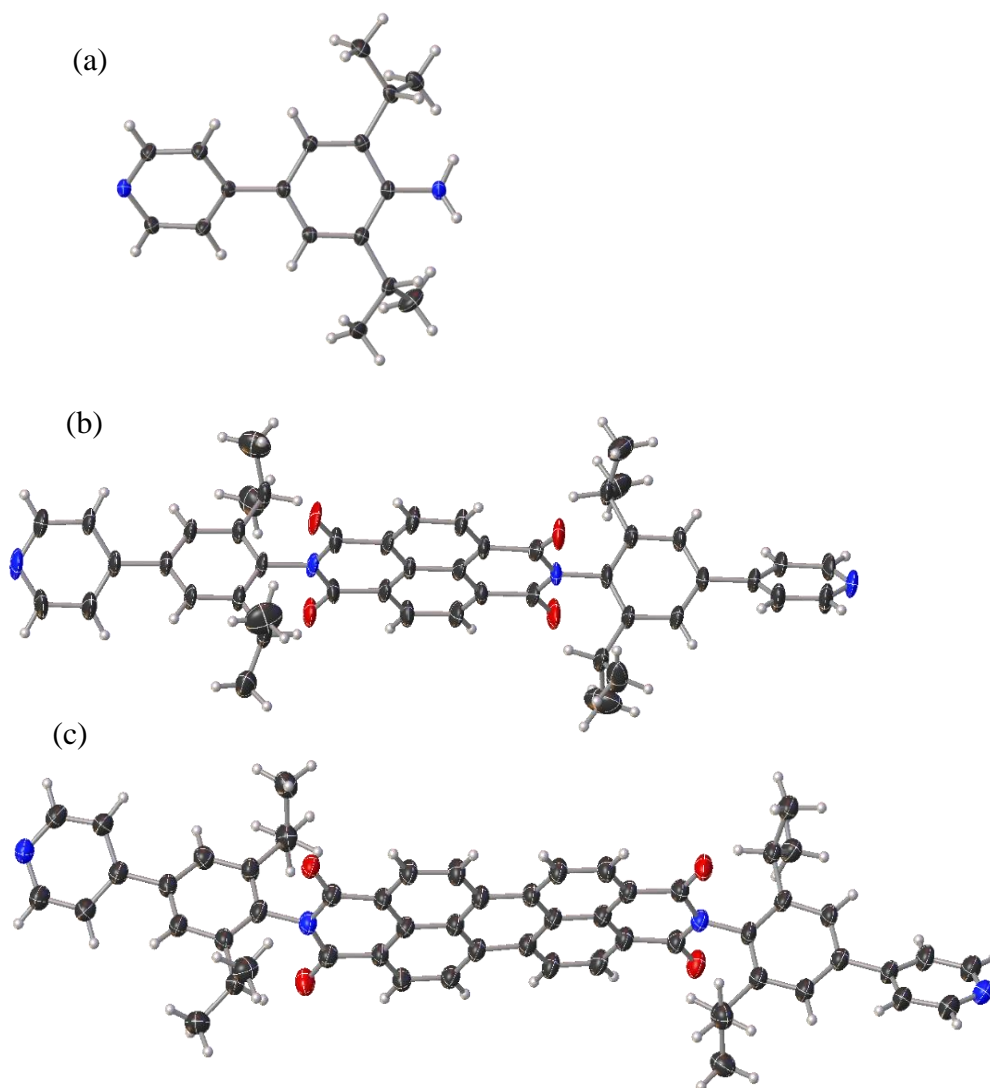
Figure 2.5: ORTEP view of the crystal structure of 2,6-diisopropyl-4-(pyridin-4-yl)aniline (a); **DPPNDI** (b); and **DPPPDI**. (a) and (b) are drawn with 50% displacement ellipsoids; (c) is drawn with 25% displacement ellipsoids. C: black, N: blue O: red and H: light grey

Analysis of the single crystal data reveals that all three compounds crystallised in the monoclinic crystal system with DPPNDI and DPPPDI crystallising in the space group $P2_1/c$ while the aniline crystallised in the *Ia* space group. Summary of the crystal data can be found in Table 2.1.

Table 2.1: Summary of crystal data.

Parameter	Compound		
	2,6-diisopropyl-4-(pyridin-4-yl)aniline	DPPNDI	DPPPDI
Empirical formula	$C_{17}H_{22}N_2$	$C_{48}H_{44}N_4O_4$	$C_{87}H_{73.3}N_6O_6$
Formula weight	254.36	740.87	1298.81
Temperature/K	120(2)	120(2)	100(2)
Crystal system	monoclinic	monoclinic	monoclinic
Space group	*Ia*	*P2₁/c*	*P2₁/c*
a/Å	13.8965(3)	10.8580(5)	10.9703(7)
b/Å	8.5125(2)	16.6435(8)	26.1698(12)
c/Å	12.5715(3)	25.9231(12)	23.2557(19)
α/°	90	90	90
β/°	99.784(2)	98.539(4)	98.084(7)
γ/°	90	90	90
Volume/Å³	1465.50(6)	4632.8(4)	6610.1(8)
Z	4	4	4
ρ_calcg/cm³	1.153	1.062	1.305
μ/mm⁻¹	0.516	0.54	0.077
F(000)	552	1568	2741
Crystal size/mm³	$0.175 \times 0.097 \times 0.071$	$0.319 \times 0.219 \times 0.196$	$0.08 \times 0.05 \times 0.02$
Radiation	Cu Kα (λ = 1.54184)	Cu Kα (λ = 1.54184)	synchrotron (λ = 0.6889)
2θ range for data collection/°	12.242 to 146.864	6.332 to 147.52	3.016 to 72.576
Reflections collected	2940	36421	145817
Independent reflections	1859 [R_{int} = 0.0126, R_{sigma} = 0.0181]	9223 [R_{int} = 0.0475, R_{sigma} = 0.0274]	32427 [R_{int} = 0.2611, R_{sigma} = 0.3877]
Data/restraints/parameters	1859/2/183	9223/0/513	32427/1169/922
Goodness-of-fit on F²	1.08	1.817	0.885
Final R indexes [I>=2σ (I)]	R_1 = 0.0275, wR_2 = 0.0766	R_1 = 0.1477, wR_2 = 0.4601	R_1 = 0.1458, wR_2 = 0.2801
Final R indexes [all data]	R_1 = 0.0277, wR_2 = 0.0769	R_1 = 0.1769, wR_2 = 0.5026	R_1 = 0.5112, wR_2 = 0.4653
Largest diff. peak/hole / e Å⁻³	0.16/-0.14	1.40/-0.34	0.41/-0.22
Flack parameter	-0.4(6)	-	-

The asymmetric unit of **DPPNDI** and the aniline contains one molecule of each compound while that of **DPPPDI** has one and a half molecules of the compound. The pyridyl rings and phenyl rings bearing the isopropyl groups in the three are on different planes with dihedral angles of 33.6º, 43.2º and 34.2º respectively for the aniline precursor (2,6-diisopropyl-4-(pyridin-4-yl)aniline), **DPPNDI** and

DPPPDI. It is, therefore, apparent that **DPPNDI** has the highest torsional angle followed by the **DPPPDI**. Further analysis of the structure shows that the NDI core in **DPPNDI** is planar and almost perpendicular (torsional angle of 84.3^{o}) to the isopropyl-bearing rings. However, the PDI core of the **DPPPDI** is slightly twisted (7.0^{o}), forming a dihedral angle of 87.5^{o} with the phenyl rings carrying the isopropyl groups. The difference in these angles for the PDI and the NDI is most likely due the planarity of the NDI core in **DPPNDI** and the lack of planarity in the PDI core for the **DPPPDI** which most likely arises from the longer PDI core which is more susceptible to distortion. This may also be as a result of the packing arrangements of these compounds in the solid state. Whereas the packed structure of the PDI shows a highly ordered herringbone arrangement as shown in Figure 2.6a, that of the NDI indicates a parallel arrangement among the molecules (Figure 2.6b).
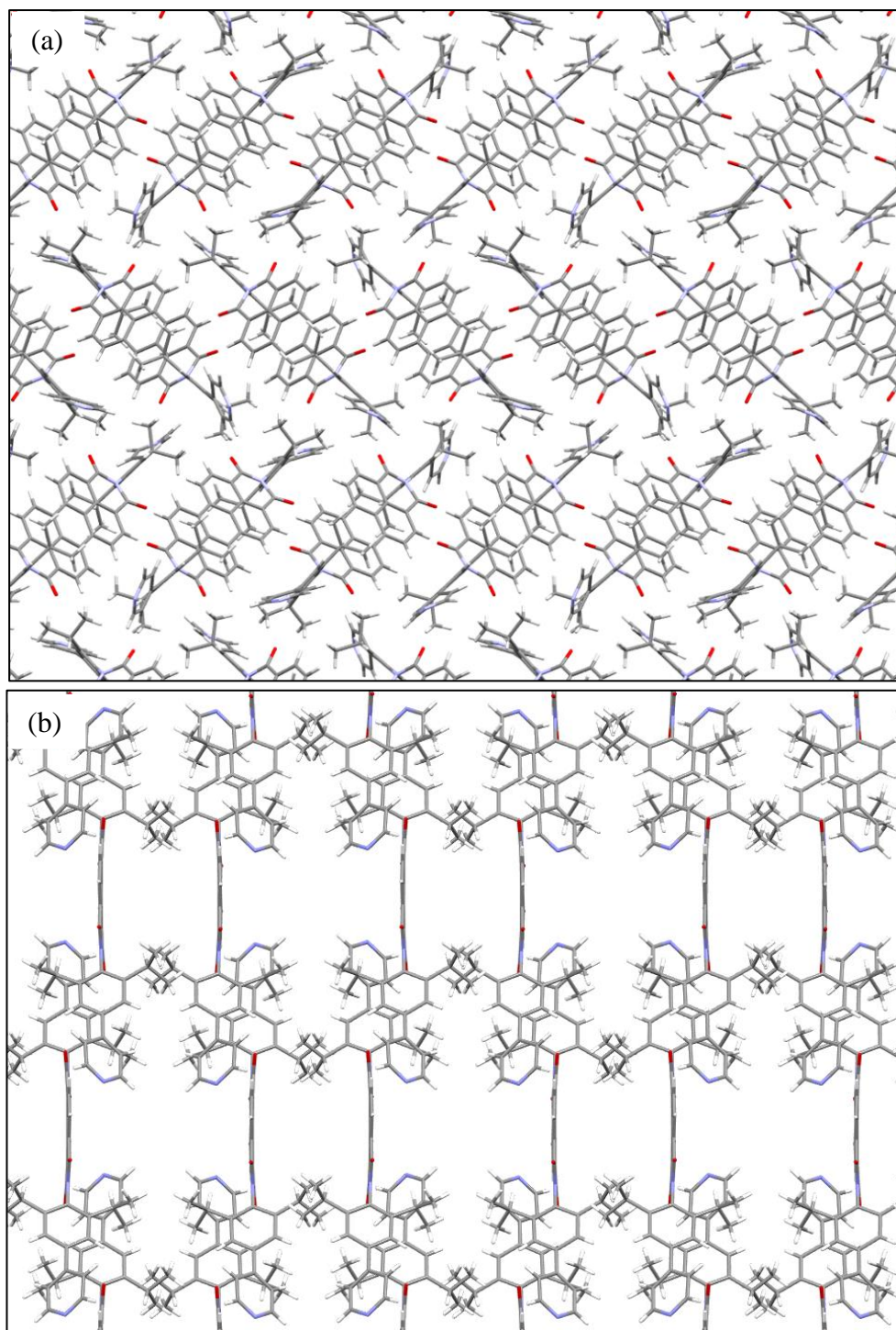
Figure 2.6: (a) The herringbone packing motif in **DPPPDI** and (b) packing motif of **DPPNDI** along the crystallographic *b*-axis. C: grey, N: blue O: red and H: white.

Careful inspection of the packed structures of the **DPPNDI** and **DPPPDI** reveals

that CH/π interactions may be present as shown in Figure 2.7. It is most likely

that the different dihedral angles seen in both compounds are influenced by these interactions between the π electrons of the rylene diimide core and the CH of the isopropyl groups/aromatic CH of the pyridyl. It should be noted that CH/π interaction is the weakest type of intermolecular hydrogen bonding.[25]
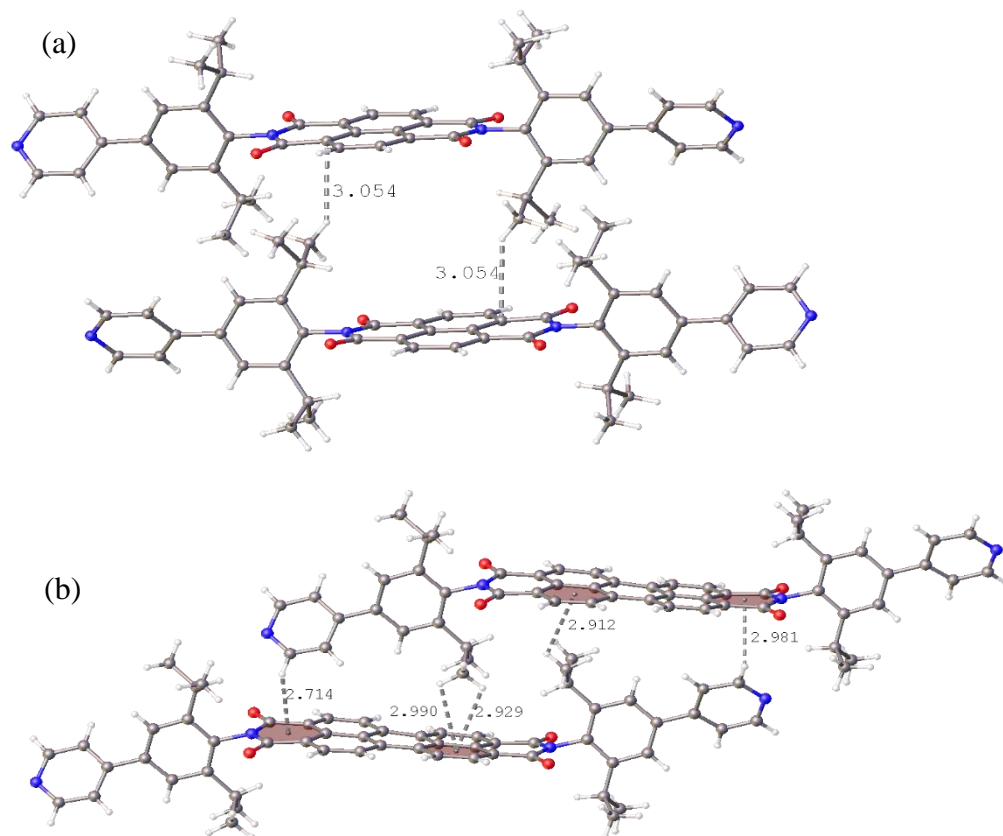
Figure 2.7: CH/π interactions in (a) **DPPNDI** and (b) **DPPPDI**

The experimental and the simulated PXRD patterns for **DPPNDI** and **DPPPDI** are shown in Figure 2.8. For both compounds, their experimental and the powder patterns are dissimilar which could be attributed to the different temperatures in which the experiments were performed. For instance, the single crystal for which the simulation for **DPPPDI** was performed was 100(2) K (and 120(2) for **DPPNDI**) while the actual experimental was conducted at room temperature. At higher temperatures, the thermal motion of the atoms is higher than at lower

temperatures; hence might be the reason for the disagreement in the patterns. However, the purity of the samples was ascertained by NMR spectroscopy as presented at the end of this chapter.
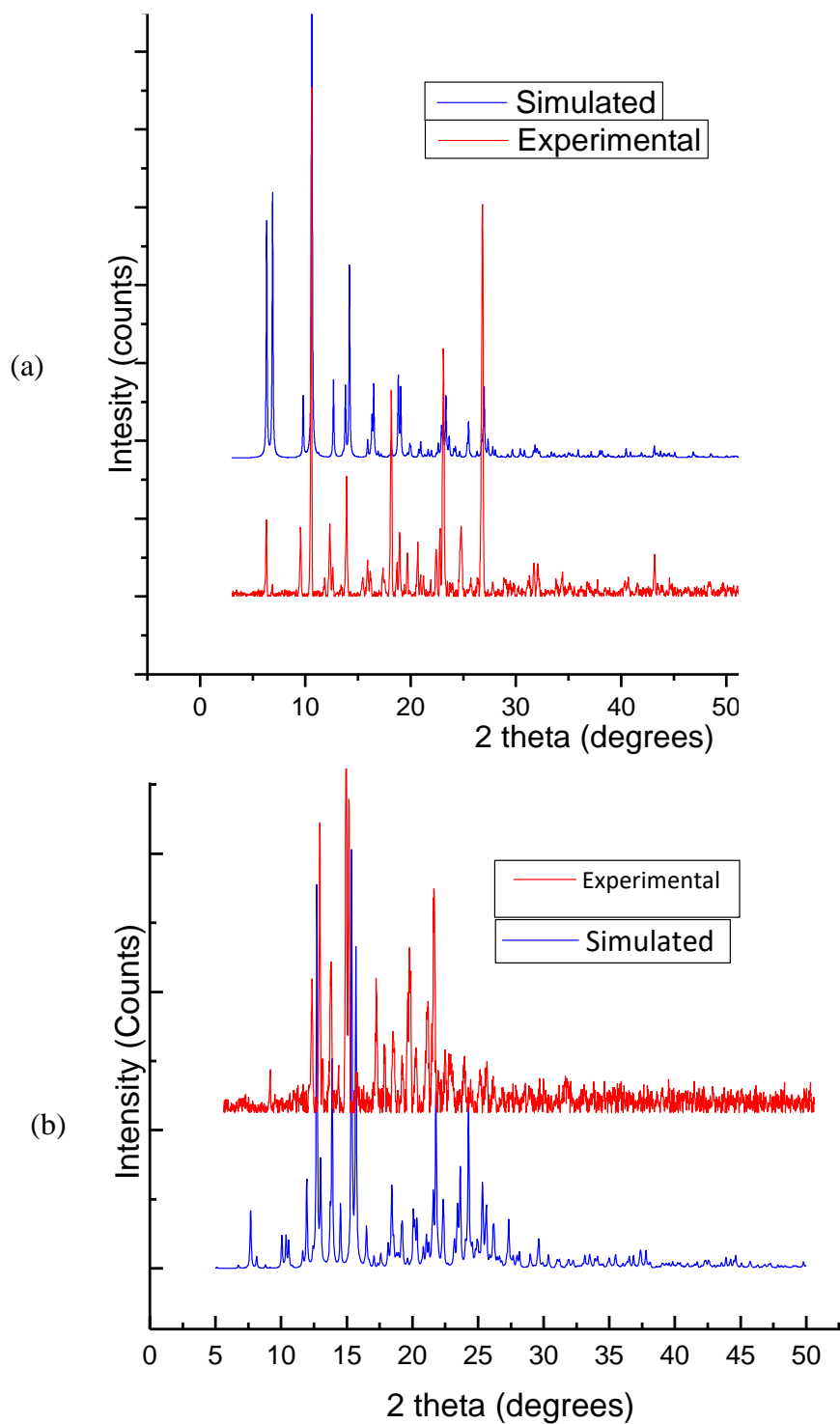
Figure 2.8: Experimental and Simulated powder patterns for (a) **DPPNDI** and (b) **DPPPDI**

2.3.3: Electrochemistry

The electronic behaviours of **DPPNDI** and **DPPPDI** were studied using electrochemistry, involving combination of electroanalytic techniques: cyclic voltammetry (CV), UV-vis spectroelectrochemistry (SEC), electron paramagnetic resonance (EPR) spectroscopy and fluorescence studies. CV was used to investigate the number as well as nature of the redox processes occurring in **DPPNDI** and **DPPPDI.** As these compounds are π-deficient, they tend to undergo reduction at very low voltage. The existence of monoanions and dianions of the reduced species were probed using SEC and EPR. A comparison between the energy associated with the absorption and the emission maxima was made using fluorescence spectroscopy.

2.3.3.1 Cyclic voltammetry

As stated above cyclic voltammetry is commonly used in probing both the number and the nature of redox processes taking place in rylene diimides. Most NDIs and PDIs are known to exhibit two one-electron reversible reductions.[26] The cyclic voltammograms (CVs) for **DPPNDI** and **DPPPDI** indicate that these compounds exhibit this behaviour as shown in Figure 2.9. A conspicuous difference between the two CVs is that the gap between the reduction potentials for **DPPNDI** is about two and a half times that for **DPPPDI**. It can also be seen in Table 2.2 that while that while the first reduction potentials are the same for both compounds, the second reduction is markedly different. This can be rationalised based on the fact that adding a second electron to the small NDI core

causes more repulsion between the incoming electron and the one associated with the first reduction, than would be observed for the larger PDI core.
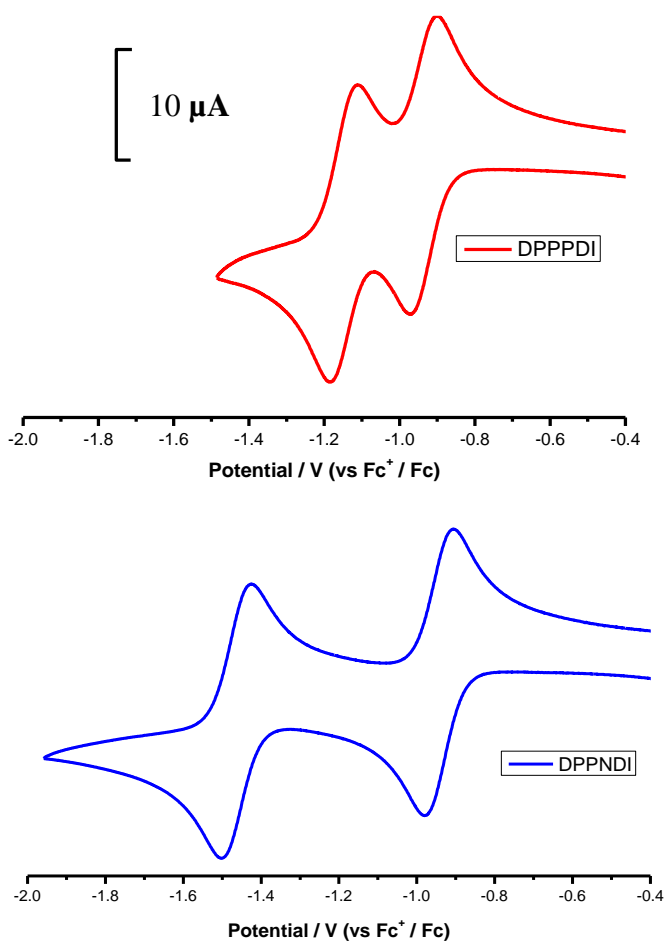
Figure 2.9: Cyclic voltammogram for **DPPPDI** (red) and **DPPNDI** (blue) at 0.1 Vs^{-1}.

This difference between the first and second reduction potentials, $\Delta E_{1/2}$ can be calculated using the equation: $\Delta E_{1/2} = E_{1/2\ (1st\ red)} - E_{1/2\ (2nd\ red)}$. Table 2.2 gives a summary of the CV data for these compounds. A careful look at the table reveals the agreement between the $E_{1/2}$ from CV and square wave (SW). A more detailed analysis of the CV data for **DPPPDI** and **DPPNDI** are respectively shown in Figures 2.10 and 2.11.

Table 2.2: Cyclic voltammetry as a solution in CH_2Cl_2 using $[Bu_4N][BF_4]$ (0.4 M) as supporting electrolyte, at 0.1 Vs^{-1}. Potentials are quoted versus $E_{1/2}$ Fc^+/Fc used as an internal standard. Values in brackets are ΔE $(=E_p^a - E_p^c)$. E_p^a: anodic peak potential and E_p^c: cathodic peak potential.

Compound	1st reduction		2nd reduction		$\Delta E_{1/2}$	ΔE (Fc)
	CV, $E_{1/2}$/V	SW/V	CV, $E_{1/2}$/V	SW/V		
DPPPDI	-0.91 (0.07)	-0.91	-1.13 (0.07)	-1.13	0.22	(0.07)
DPPNDI	-0.92 (0.07)	-0.92	-1.45 (0.08)	-1.44	0.53	(0.07)
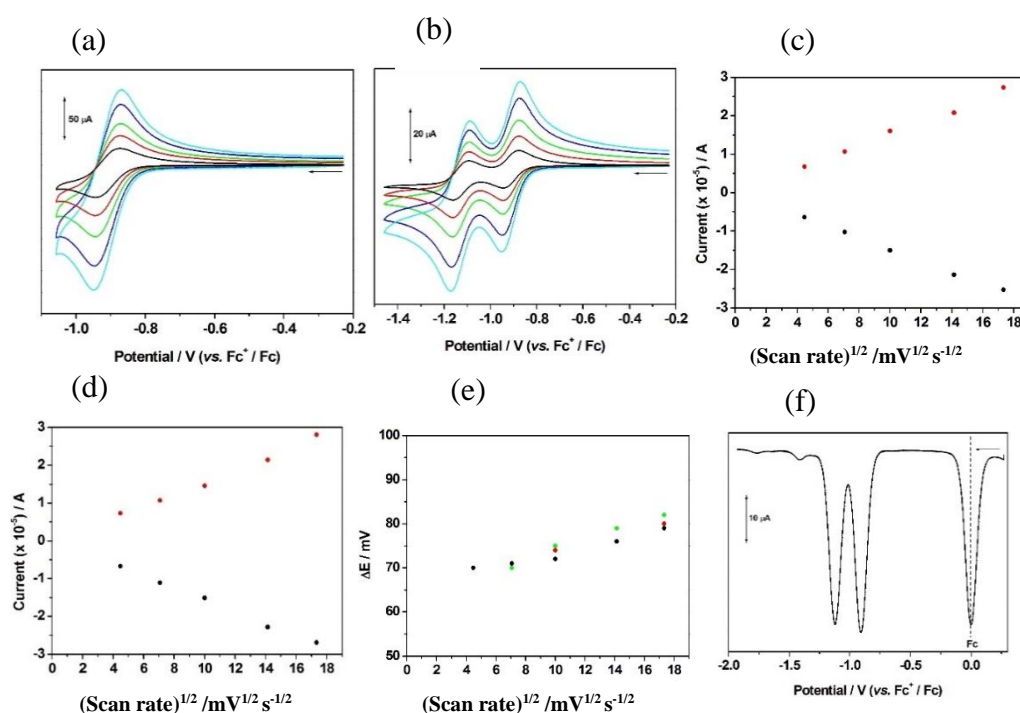
Figure 2.10: Cyclic voltammetry of **DPPPDI** at a glassy carbon electrode in $CH_2Cl_2/[Bu_4N][BF_4]$ (0.4 M) as supporting electrolyte for the first reduction (a) and second reduction (b) at scan rates of 0.02 (black), 0.05 (red), 0.10 (green), 0.20 (blue) and 0.30 (cyan) Vs^{-1}; plots of the peak anodic current (I_p^a) (red dots) and peak cathodic current (I_p^c) (black dots) versus the square root of scan rate for the first reduction (c) and the second reduction (d); (e) plot of the peak separation, ΔE $(=E_p^a - E_p^c)$, for the first reduction (red dots), second reduction (green dots) and ferrocene (in solution) (black dots); (f) square wave voltammetry.

(a)   (b)   (c)

(d)   (e)   (f)

Figure 2.11: Cyclic voltammetry of **DPPNDI** at a glassy carbon electrode in CH_2Cl_2/[Bu_4N][BF_4] (0.4 M) as supporting electrolyte for the first reduction (a) and second reduction (b) at scan rates of 0.02 (black), 0.05 (red), 0.10 (green), 0.20 (blue) and 0.30 (cyan) Vs^{-1}; plots of the peak anodic current (I_p^a) (red dots) and peak cathodic current (I_p^c) (black dots) versus the square root of scan rate for the first reduction (c) and the second reduction (d); (e) plot of the peak separation, ΔE ($=E_p^a - E_p^c$), for the first reduction (red dots), second reduction (green dots) and ferrocene (in solution) (black dots); (f) square wave voltammetry.

2.3.3.2 UV-visible spectroelectrochemistry

UV-visible spectroelectrochemistry (SEC) was used to unequivocally confirm the reduction of **DPPNDI** and **DPPPDI** to their mono- and dianion. Recorded in DCM containing [$^nBu_4N$][BF_4] (0.4 M) as the supporting electrolyte at 273 K, the conversion of the neutral compounds to the charged delocalised radical monoanion (**DPPNDI**$^{•-}$ and **DPPPDI**$^{•-}$) and the interconversion between the mono- and dianion species were successfully probed. The SEC data for the **DPPNDI** are presented in Figure 2.12 and Table 2.3. These data are consistent with those reported in the literature for similar systems.[27] The SEC spectra of the

neutral NDI shows characteristic peaks at 344, 361, and $\lambda_{max} = 382$ nm corresponding to the $0 \rightarrow 0$, $0 \rightarrow 1$ and $0 \rightarrow 2$ vibronic bands respectively. The last two peaks are attributed to the absorbance of the chromophores C=O and C=C and they result from $\pi-\pi^*$ transitions. The smallest of the three peaks appearing at 344 nm is due to n–σ^* transition within the C–N chromophore which agrees with reported spectra of NDIs.[28]

As earlier stated, NDIs are a remarkable class of redox-active compounds, capable of undergoing two single one-electron electron reductions either chemically or electrochemically. Herein, the neutral **DPPNDI** undergoes electrochemical reduction to generate the radical monoanion, **DPPNDI•−**. The conversion of the neutral NDI to the radical monoanion causes the emergence of a bathochromically shifted new set of intense and unique (to NDIs in general) visible and near-infrared (NIR) absorption bands at 479 nm (λ_{max}), 617 nm, 617 nm and 778 nm.
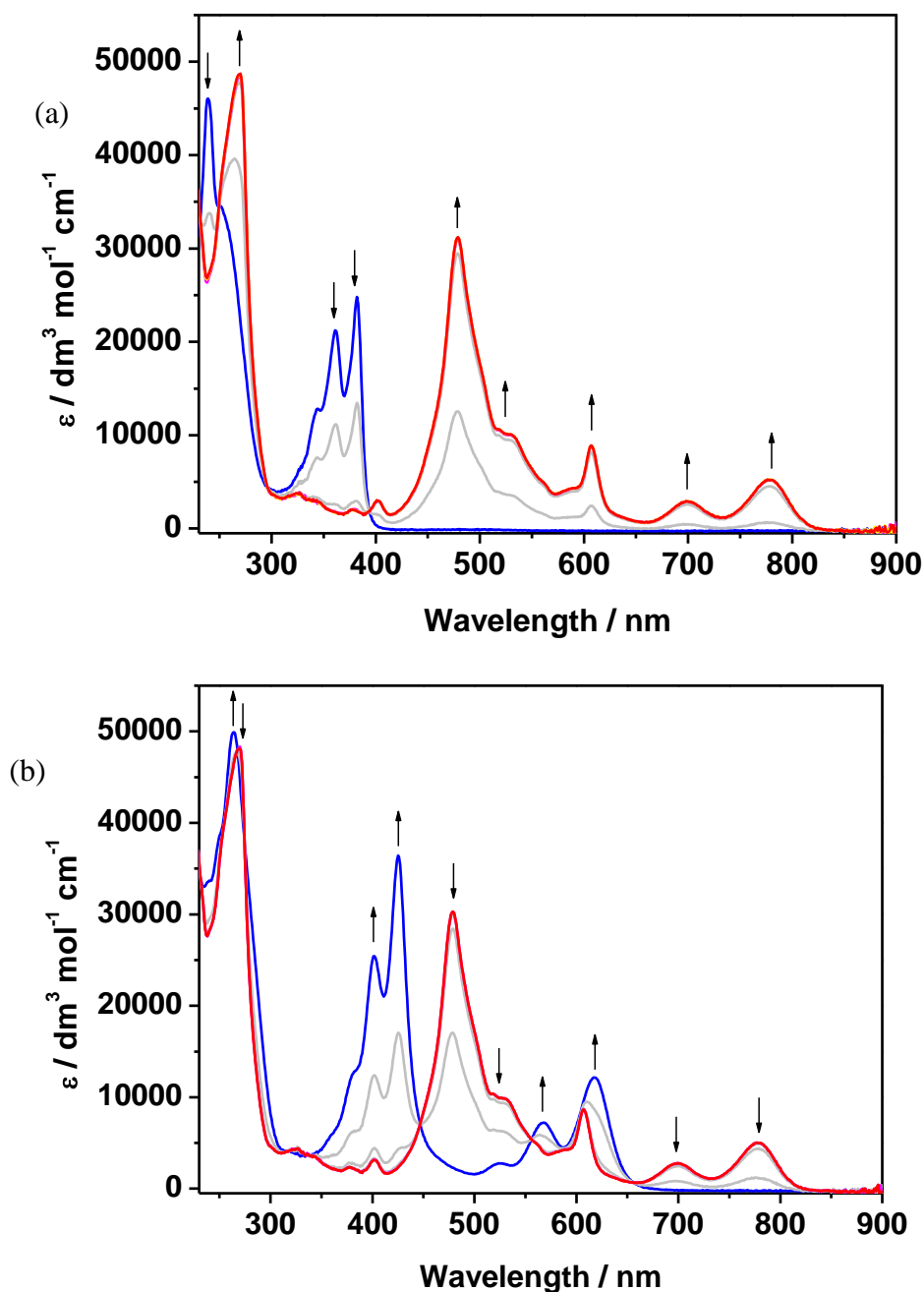
Figure 2.12: UV-vis absorption spectra of **DPPNDI** showing: a) the inter-conversion of redox states between **DPPNDI** (blue) and **DPPNDI**$^{\cdot-}$ (red); b) the inter-conversion of redox states between **DPPNDI**$^{\cdot-}$ (red) and **DPPNDI**$^{2-}$ (blue). Spectra were recorded in CH_2Cl_2 containing $[^nBu_4N][BF_4]$ (0.4 M) as the supporting electrolyte at 273 K. Arrows indicate the progress of the stated inter-conversion.

Peaks for the second reduction were observed as the mono-reduced species are converted to the dianion species with characteristic peaks appearing between the major peaks of the first and the neutral species as seen in Figure 2.12. **DPPPDI**

also undergoes similar reduction profile - as the NDI - with the first reduced species, **DPPPDI$^{\bullet-}$**, exhibiting intense absorbance peaks at longer wavelengths. The overall profile for the interconversion between the monoanion and dianion also agrees well with those that have been reported previously in the literature.[29] More details are provided in Table 2.3 and Figure 2.13. When the peaks for **DPPPDI** (as well as those for the reduced states) are compared to the corresponding peaks for **DPPNDI** (as well as those for the reduced states), those for the latter appear at lower energy.

Table 2.3: UV/vis spectroelectrochemistry[a]

	Neutral	1st reduction	2nd reduction
	λ_{abs}/nm ($\varepsilon \times 10^{-4}$ /mol^{-1}dm^{3}cm^{-1})	λ_{abs}/nm ($\varepsilon \times 10^{-4}$ /mol^{-1}dm^{3}cm^{-1})	λ_{abs}/nm ($\varepsilon \times 10^{-4}$ /mol^{-1}dm^{3}cm^{-1})
DPPPDI	251 (8.5), 260 (8.6), 355 (0.4), 371 (0.5), 436 (0.6), 462 (2.1), 494 (5.8), 531 (9.9)	266 (7.8), 280 (7.2), 681 (4.9), 703 (8.1), 715 (8.5), 766 (2.4), 797 (5.6)	**272 (7.7), 284 (9.8), 296 (8.9), 394 (0.4), 534 (5.0), 573 (10.0), 597 (4.3), 649 (2.2), 736 (0.5), 810 (0.1)**
DPPNDI	**238 (4.6), 250 (3.5), 344 (1.3), 361 (2.1), 382 (2.5)**	**270 (4.9), 323 (0.4), 376 (0.2), 401 (0.3), 479 (3.1), 607 (0.9), 698 (0.3), 776 (0.5)**	**264 (5.0), 401 (2.5), 425 (3.6), 524 (0.3), 617 (1.2),**

[a] In CH$_2$Cl$_2$ containing [^{n}Bu$_4$N][BF$_4$] (0.4 M) as supporting electrolyte, at 273 K. All processes are chemically reversible under these conditions
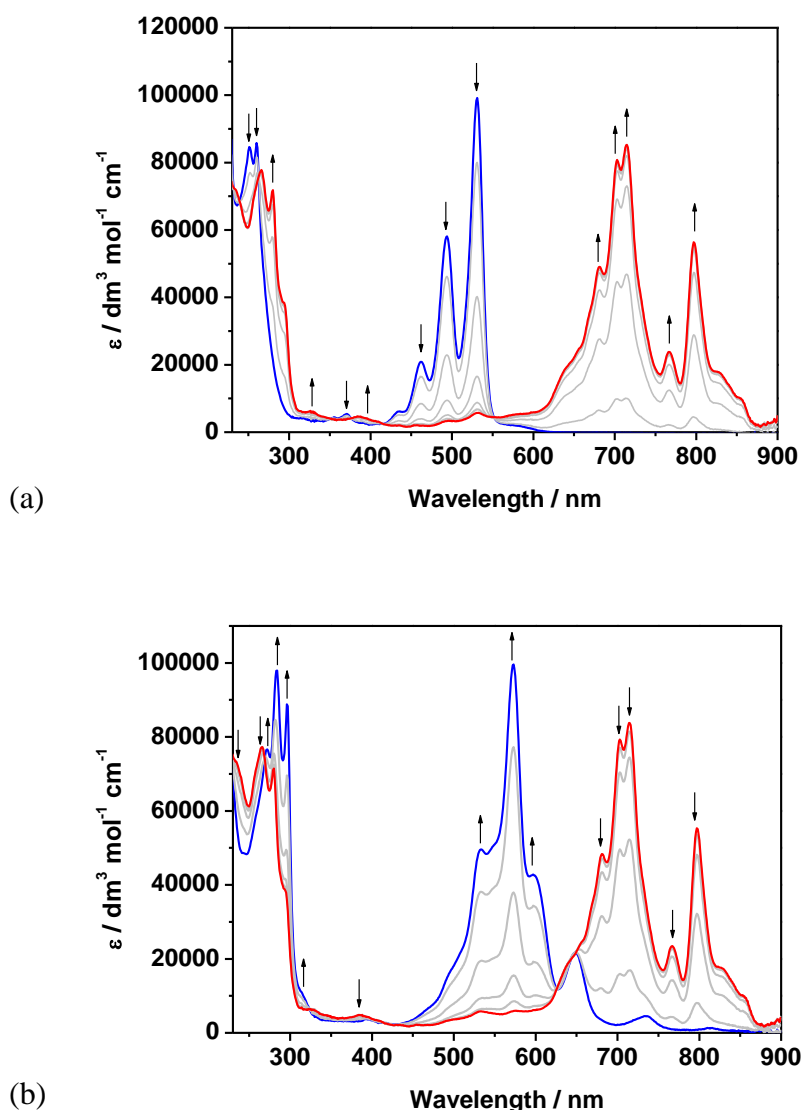
Figure 2.13 UV-vis absorption spectra of **DPPPDI** showing: a) the inter-conversion of redox states between **DPPPDI** and **DPPPDI$^{\bullet-}$**; b) the inter-conversion of redox states between **DPPPDI$^{\bullet-}$** and **DPPPDI^{2-}**. Spectra were recorded in CH_2Cl_2 containing [^{n}Bu$_4$N][BF$_4$] (0.4 M) as the supporting electrolyte at 273 K. Arrows indicate the progress of the stated inter-conversion.

2.3.3.3 Electron paramagnetic resonance (EPR) studies

To further support evidence for the existence of radical anions as probed by the

CV and SEC measurements, EPR studies were employed. NDIs and PDIs are

known to function as good electron acceptors. Therefore, any addition of electron to form radical anions would go into the lowest unoccupied molecular orbital (LUMO). **DPPNDI**$^{\bullet-}$ produces a 13-line EPR spectrum (Figure 2.14b) centred at g_{iso} = 2.0038 with a line width of 0.07 G while that of **DPPPDI** is more complex with a 23-line spectrum centred at g_{iso} = 2.0035 and a line with of 0.10 G. The simulated spectra were generated using the parameters listed in Table 2.4 and matches nicely with the experimentally obtained spectra. These data are also in good agreement with those reported in the literature for systems similar to **DPPNDI**[30] and **DPPPDI**.[31]

(a)   **(b)**
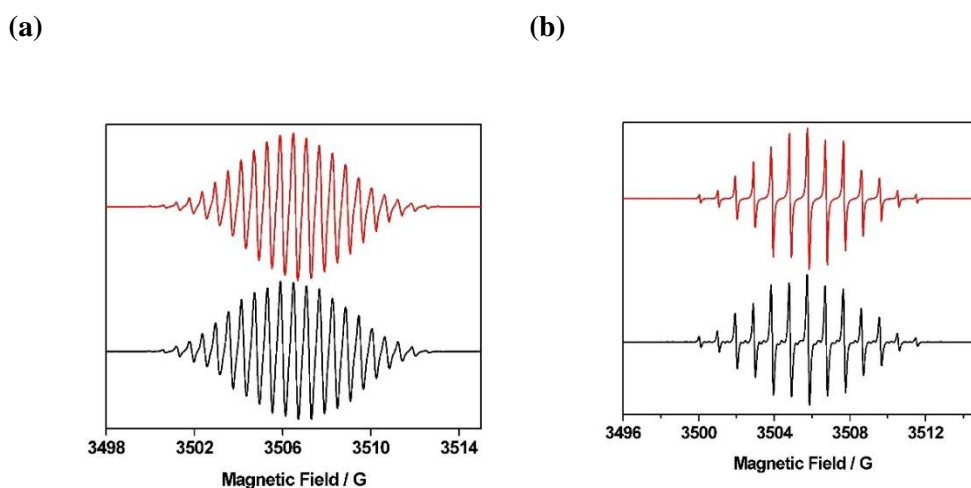
Figure 2.14: Experimental (black) and simulated (red) X-band EPR spectra of: (a) **DPPPDI**$^{\bullet-}$ and (b) **DPPNDI**$^{\bullet-}$. Samples of the anions were electrogenerated by reduction of the parent molecules at 273 K as CH_2Cl_2 containing [$^{n}Bu_4N$][BF_4] (0.4 M) as the supporting electrolyte. Spectra were recorded at ambient temperature.

Table 2.4: Parameters used in the simulation of EPR spectroscopic data[a]

Compound	g_{iso}	a_{iso} / x 10^{-4} cm^{-1}	Linewidth / G	Lineshape
DPPPDI	2.0035	1.633 (4H), 0.547 (8H), 0.607 (2N)	0.10	Lorentzian
DPPNDI	2.0038	1.771 (4H), 0.911 (2N)	0.07	Lorentzian

[a] In CH_2Cl_2 containing [NBu_4][BF_4] (0.4 M) as supporting electrolyte, at ambient temperature.

2.3.3.4 Fluorescence studies

NDIs and PDI are notable for their fluorescence properties. In addition to the above discussed electroanalytic techniques, fluorescence studies were conducted for **DPPNDI** and **DPPPDI**. While the fluorescence spectrum of the **DPPPDI** has all the expected features, it is notable that the emission spectrum for **DPPNDI** is not a reflection of the absorption spectrum (Figure 2.15). In addition to the asymmetry of the emission spectrum for **DPPNDI**, the Stokes shift is much larger than expected for a typical NDI system reported in the literature.[32] The lack of expected features and the large Stokes shift in the emission spectrum of **DPPNDI** could be attributed to the presence of a small amount of impurity in the sample. The precise explanation for the unusual emission spectrum observed for **DPPNDI** is unclear.

(a)   (b)
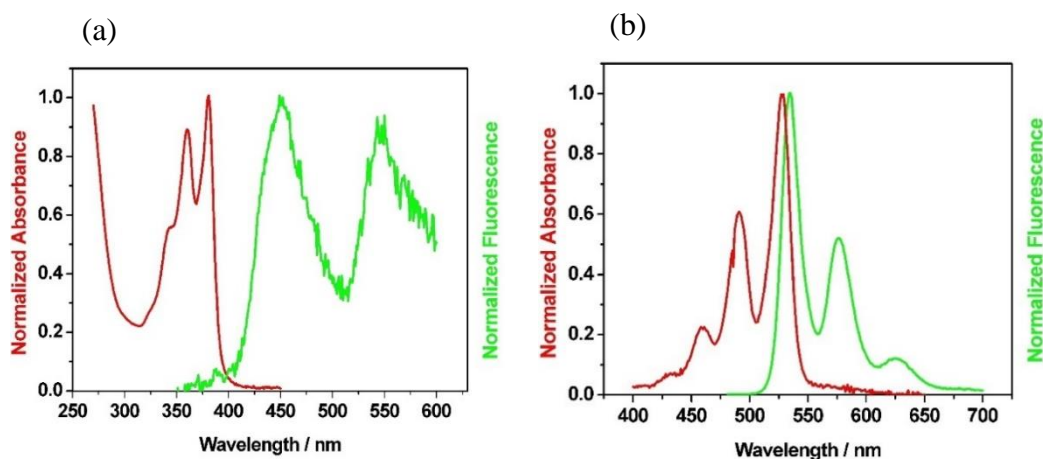
Figure 2.15: Fluorescence spectra of (a) **DPPNDI**[a] and (b) **DPPPDI**[b]. [a] **DPPNDI** in chloroform, quinine sulfate in 0.5 M sulfuric acid was used as the standard. [b] **DPPPDI** in chloroform, perylene orange in chloroform as standard.

This discussion will therefore focus on **DPPPDI** absorption and emission spectra. For the measurement, perylene orange in chloroform was used as a standard. It should be noted that perylene orange in chloroform has a quantum

yield (QY) of 0.99. Using the same solvent negates the need for solvent correction (via refractive indices); therefore, a plot of integrated intensity (from fluorescence data) with absorbance (from UV/vis data) gives a gradient for the standard for **DPPPDI**. The data show straight lines, with good correlation (Figure 2.16). The quantum yield of 0.89 was obtained by calculating the ratio of these gradients multiplied by the QY (0.99) of the standard.

(a)
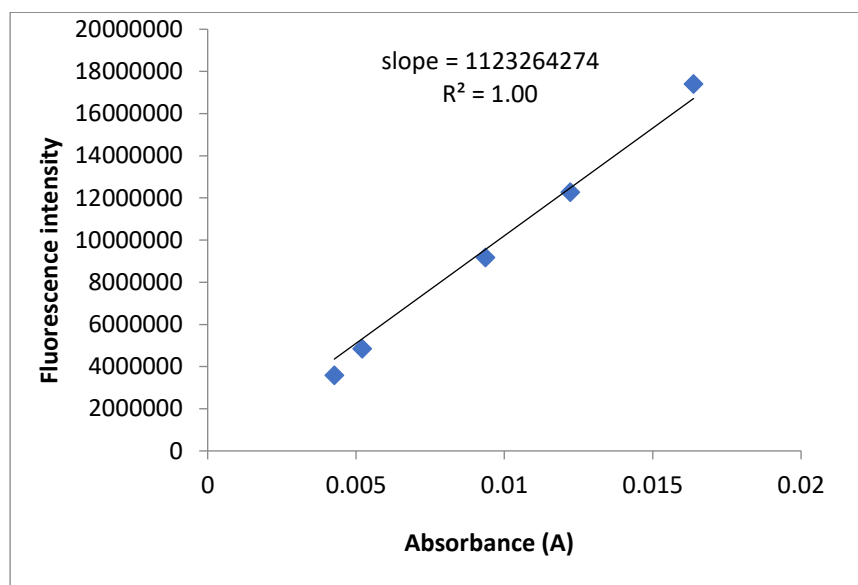
(b)
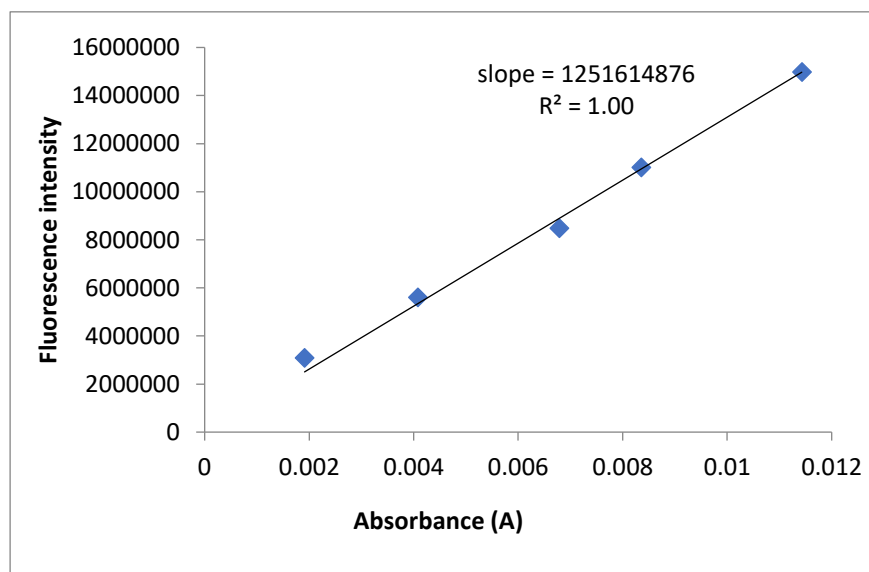
Figure 2.16: Plots of fluorescence intensity vs absorbance for (a) **DPPPDI** and (b) the standard (perylene orange)

Aside the QY for **DPPPDI**, the Stokes shift was also calculated. Stokes shift is the difference between the energies (cm^{-1}) corresponding to the bands of absorption ($\lambda_{\text{max absorption}}$) and emission ($\lambda_{\text{max emission}}$) maxima. The value obtained

for the Stokes shift of **DPPPDI** is 247 cm^{-1} or 30.63 meV and is consistent with those found in the literature for imide substituted PDI systems.[33]

2.4 Conclusion

Three novel rylene diimide ligands suitable for metal-organic synthesis have been successfully prepared and characterised. Two of the compounds – one an NDI and the other a PDI – contain the bulky isopropyl groups which are responsible for disrupting π-π interaction and enhance their solubility in common organic solvents such as chloroform, dichloromethane, DMF, etc. The electronic behaviours of these compounds were studied using a range of electroanalytic techniques viz; cyclic voltammetry, UV-vis spectroelectrochemistry, electron paramagnetic resonance and fluorescence studies. The data from all these techniques support the observation that the compounds, **DPPNDI** and **DPPPDI**, are able to undergo two one-electron reduction processes. The CVs for both compounds indicate that the compounds have the same half wave potential ($E_{1/2}$) with numerical value of around -0.92 V vs Fc/Fc^{+} for the first reduction. However, these values are significantly for the second reduction process with $E_{1/2}$ values of -1.13 and -1.45 V vs Fc/Fc^{+} respectively for **DPPPDI** and **DPPNDI**. These data are consistent with those reported in the literature for similar systems.

The SEC for both **DPPPDI** and **DPPNDI** confirms the formation of the respective radical anions and second reduced species. Furthermore, the formation of radical anions was further supported by the EPR results with **DPPNDI** producing a 13-line EPR spectrum centred at g_{iso} = 2.0038 and **DPPPDI** showing a 23-line spectrum centred at g_{iso} = 2.0035.

Finally, fluorescence studies of these compounds showed a rather inconclusive result for the NDI, **DPPNDI**, due to the absence of mirror image of the absorption spectrum in the emission spectrum. However, the fluorescence data for the PDI agrees with literature. **DPPPDI** has a QY of 0.89 which corresponds to 247 cm^{-1} or 30.63 meV. These compounds will be employed in the next three chapters for the synthesis of MOFs.

2.5 Materials and methods

2.5.1 Synthesis of 4-iodo-2,6-diisopropylaniline

The iodination of 2,6-diisopropylaniline to give 4-iodo-2,6-diisopropylaniline was carried out following a literature report[18]. To make the 4-iodo-2,6-diisopropyl aniline, 9.04 g (53.02 mmol) of 2,6-diisopropylaniline in 50 mL diethylether and 14.80 g (58.31 mmol) of iodine dissolved in 150 mL saturated solution of NaHCO$_3$ were reacted together in a 500-mL round-bottom flask under constant stirring. The reaction was stopped after 2 h followed by addition of 6.5 g (26.19 mmol) of Na$_2$S$_2$O$_3$. The crude product was extracted with Et$_2$O (2 x 25 mL) and the solvent removed in vacuo to yield 15.91 g (52.49 mmol, 99% yield) of the dark-blue oily product. ^{1}H NMR (400 MHz; CDCl$_3$) δ 7.30 (s, 2H), 3.76 (br. s., 2H), 2.87 (spt, J = 6.8 Hz, 2H), 1.26 (d, J = 6.8 Hz, 12H). *m/z* calculated for [C$_{12}$H$_{18}$NI]$^+$ 304.18, found 304.19.

2.5.2 Synthesis of 2,6-diisopropyl-4-(pyridin-4-yl)aniline

Using Suzuki-Miyaura cross-coupling reaction,[19] 2,6-diisopropyl-4-(pyridin-4-yl)aniline was synthesised. Pyridine-4-boronic acid pinacol ester (0.865 g, 4.2 mmol), 4-iodo-2,6-diisopropyl aniline (1.212 g, 4 mmol), K_2CO_3 (1.104 g, 8 mmol) and $Pd(PPh_3)_4$ (0.092 g, 0.08 mmol) were added to flask and dissolved in dry DMF. The solution was heated (under N_2 and constant stirring) at 100 °C for 18 h, filtered through celite, extracted using DCM and the solvent removed in vacuo. The resulting crude product was purified by column chromatography involving DCM, ethylacetate (ratio of 3:2) and silica to give 0.53 g (2.08 mmol, 52% yield) of the yellow product. ^1H NMR (400 MHz, CDCl$_3$) δ = 8.61 (d, J = 1.0 Hz, 2 H), 7.50 (d, J = 1.0 Hz, 2 H), 7.37 (s, 2 H), 3.97 (br. s., 2 H), 3.00 (spt, J = 6.8 Hz, 2 H), 1.36 (d, J = 6.8 Hz, 12 H). ^{13}C NMR (101MHz, CDCl$_3$) δ = 150.0, 149.2, 141.7, 132.8, 121.6, 120.9, 28.1, 22.4. FTIR was obtained using ATR: 3469, 3299, 3197 cm^{-1} aromatic ν(N-H), 2959, 2846 cm^{-1} aromatic ν(C-H). m/z calculated for $[C_{17}H_{22}N_2]^+$ 254.18, found 254.19.

2.5.3 Synthesis of N,N'-bis(2,6-diisopropyl-4-(pyridin-4-yl)phenyl)-1,4,5,8-naphthalenetetra-carboxydiimide (DPPNDI)

DPPNDI was made using an adaptation of a method reported in the literature.[20] Carried out on a Schlenk line under an inert atmosphere (N_2), a mixture of H-imidazole (2.00 g), 1,4,5,8-napthalenetetracarboxylic dianhydride (79 mg, 0.295 mmol) and 2,6-diisopropyl-4-(pyridin-4-yl)aniline (225 mg, 0.885 mmol) was heated to 180 °C for 18 h. The reaction mixture was cooled to room temperature and extracted into chloroform (2 x 30 mL) then washed with HCl (2 M, 3 x 60 mL), Na_2CO_3 (2 M, 60 mL) and brine (60 mL). The organic extract was dried

with MgSO$_4$, filtered and the solvent removed in vacuo. This product was purified by column chromatography (silica, [DCM:EtOAc] [3:2]) to yield 99 mg of the orange product (0.134 mmol, 45% yield). ^{1}H NMR (400 MHz, CDCl$_3$) δ = 8.94 (s, 4H), 8.73 (d, *J* = 6.15 Hz, 4H), 7.56 - 7.63 (m, 8H), 2.79 (spt, *J* = 6.90 Hz, 4H), 1.24 (d, *J* = 6.90 Hz, 24H) ^{13}C NMR (101 MHz, CDCl$_3$) δ = 162.9, 150.3, 148.5, 146.6, 140.0, 131.8, 127.7, 126.9, 123.3, 122.0, 29.5, 24.0. FTIR was carried out using ATR: 2957-2844 cm^{-1} aromatic ν(C-H), 1702 cm^{-1} ν(C=O). *m/z* calculated for [C$_{48}$H$_{44}$N$_4$O$_4$]$^+$ 740.34, found [M+H]$^+$ 741.34.

2.5.4 Synthesis of N,N'-bis(2,6-diisopropyl-4-(pyridin-4-yl)phenyl)-3,4,9,10-perylenetetra-carboxydiimide (DPPPDI)

DPPPDI was made using an adaptation of a method reported in the literature.[20] Performed on a Schlenk line under an inert atmosphere (N$_2$), a mixture of H-imidazole (10.00 g), 3,4,9,10-perylenetetracarboxylic dianhydride (0.918 g, 2.34 mmol) and 2,6-diisopropyl-4-(pyridin-4-yl)aniline (1.785g, 7.00 mmol) was heated to 180 °C for 18 h. The reaction solution was cooled to room temperature and extracted into chloroform (2 x 30 mL) then washed with HCl (2 M, 3 x 60 mL), Na$_2$CO$_3$ (2 M, 60 mL) and brine (60 mL). The organic extract was then dried with MgSO$_4$, filtered and the solvent removed in vacuo. The product was purified by column chromatography (silica, [DCM:Methanol] [50:1]) to yield 202.42 mg of the dark red product (2.34 mmol, 10% yield). ^{1}H NMR (400 MHz, CDCl$_3$) ^{1}H NMR (400MHz, CDCl$_3$) δ = 8.86 - 8.75 (m, 8 H), 8.72 (d, *J* = 6.0 Hz, 4 H), 7.63 - 7.56 (m, 8 H), 2.84 (spt, *J* = 6.9 Hz, 4 H), 1.25 (d, *J* = 6.9 Hz, 24 H) ^{13}C NMR (101MHz, CDCl$_3$) δ = 163.1, 149.9, 148.3, 146.4, 139.3, 134.9, 131.9, 131.2, 129.9, 126.6, 123.1, 123.0, 122.8, 121.7, 29.1, 23.7. FTIR was

done using ATR: 2966-2867 cm^{-1} aromatic ν(C-H), 1702 cm^{-1} ν (C=O). *m/z* calculated for [C$_{58}$H$_{48}$N$_4$O$_4$]$^+$ 864.37, found [M+H]$^+$ 865.37.

2.5.6 N,N'-bis(4-pyridyl)-1,4,5,8-naphthalenetetracarboxydiimide (DPNDI)

DPNDI was synthesized following the procedures reported in the literature.[21] A mixture of 0.8 g (3 mmol) of 1,4,5,8-naphthalenetetracarboxylic dianhydride (NTCDA) and 0.56 g (6 mmol) of 4-aminopyridine in 20 mL of N,N-dimethylformamide (DMF) was heated at 120 $^\circ$C for 8 h . The solution was cooled to room temperature yielding a crystalline solid. The crude product was collected by vacuum filtration and purified by recrystallizing from hot DMF to obtain DPNDI as an off-white/golden crystalline solid (0.95 g, 2.26 mmol, 75.59% yield). ^{1}H NMR (400 MHz; CDCl$_3$) δ = 9.20 (d, *J* = 6.8 Hz, 4H), 9.11 (s, 4H), 8.45 (d, J = 6.8 Hz, 4H). ^{13}C NMR (101 MHz; CDCl$_3$) δ = 162.51, 162.07, 161.64, 161.20, 118.44, 112.81, 110.00. MS (OA-TOF): *m/z* calculated for [C$_{24}$H$_{12}$N$_4$O$_4$]$^-$ 420.09, found 420.00.

2.5.7 N,N'-bis(dinicotinic acid)-1,4,5,8-naphthalenetetracarboxydiimide, DNNDI

DNNDI was synthesized following a modified literature procedure.[21] To a 50-mL two-neck flask containing 20 mL of DMF was dissolved 915 mg (7.50 mmol) of 5-aminonicotinic acid. The solution was heated under stirring at 100 $^\circ$C for 15 minutes forming a white cloudy suspension. 800 mg of 1,4,5,8-naphthalenetetracarboxylic dianhydride (NTCDA) was added giving rise to a brown solution. After 18 h the reaction was cooled to room temperature. The

solid component was filtered under vacuum, washed with DMF, acetone and diethyl ether to obtain an off-white powder with a yield of 95% (1.45 g, 2.85 mmol. ^{1}H NMR (400 MHz; CDCl$_3$) δ = 13.71 (s, 2H), 9.19 (d, J = 1.8, 2H), 8.92 (d, J = 2.3, 2H) 8.78 (s, 4H), 8.52 (m, 2H), 7.96 (s, 2H). FT-IR (neat, cm^{-1}) 3079 (ν O-H carboxylic acid), 1715, (ν C=O).

2.6 References

1.   X. Zhao, Y. Xiong, J. Ma and Z. Yuan, *J. Phys. Chem. A,* 2016, **120**, 7554-7560.
2.   C. Huang, S. Barlow and S. R. Marder, *J. Org. Chem.,* 2011, **76**, 2386-2407.
3.   N. Pearce, E. S. Davies, R. Horvath, C. R. Pfeiffer, X.-Z. Sun, W. Lewis, J. McMaster, M. W. George and N. R. Champness, *Phys. Chem. Chem. Phys.* 2018, **20**, 752– 764.
4.   J.-J. Liu, Z.-J. Wang, S.-B. Xia, J. Liu and X. Shen, *Dyes Pigm.*, 2020, **172**, 107856.
5.   B. Garai, A. Mallick, R. Banerjee, *Chem. Sci.* 2016, **7**, 2195–2200.
6.   K. AlKaabi, C. R. Wade and M. Dincă, *Chem*, 2016, **1**, 264-272.
7.   B. S. Pilgrim and N. R. Champness, *ChemPlusChem,* 2020, **85**, 1842– 1856
8.   M.-H. You, M.-H. Li, H.-H. Li, Y. Chen and M.-J. Lin, *Dalton Trans.*, 2019, **48**, 17381–17387.
9.   B. Garai, A. Mallickab and R. Banerjee, *Chem. Sci.,* 2016, **7**, 2195–2200.
10.   Y. Takashima, V. M. Martínez, S. Furukawa, M. Kondo, S. Shimomura, H. Uehara, M. Nakahama, K. Sugimoto and S. Kitagawa, *Nat Commun*, 2011, **2,** 168.
11.   C. F. Leong, B. Chan, T. B. Faust and D. M. D'Alessandro, *Chem. Sci.,* 2014, **5**, 4724–4728.
12.   Z. Xiang, Y.-B. Shan, T. Li, C.-C. Huang, X.-H. Huang and M.-J. Lin, *Acta Cryst.,* 2019, C**75**, 38–45.
13.   T.-T. Li, Y.-M. Liu, T. Wang, S.-R. Zheng, *Inorg. Chem. Commun.*, 2017, **84**, 5–9.
14.   S. A. Boer, Y. Nolvachai, C. Kulsing, L. J. McCormick, C. S. Hawes, P. J. Marriott and D. R. Turner, *Chem.-A Eur. J.,* 2014, **20**, 11308-11312
15.   B. Lü, Y. Chen, P. Li, B. Wang, K. Müllen and M. Yin, *Nat. Commun.,* 2019, **10**, 767
16.   Z. Zhong, R. Li, W. Lin, X. Xu, X. Tian, X. Li, X. Chen, L. Kang, *Appl. Cat. B*: *Envir.,* 2020, **260**, 118135.
17.   L. Zeng, T. Liu, C. He, D. Shi, F. Zhang and C. Duan, *J. Am. Chem. Soc.,* 2016, **138**, 3958−3961

18. A. Hospital, C. Gibard, C. Gaulier, L. Nauton, V. Thery, M. El-Ghozi, D. Avignant, F. Cisnetti and A. Gautier, *Dalton Trans.,* 2012, **41**, 6803-6812.

19. F. Wang, R. Tanaka, Z. Cai, Y. Nakayama and T. Shiono, *Appl. Organometal. Chem.,* 2015, **29**, 771-776.

20. A. D. Hendsbee, S. M. McAfee, J.-P. Sun, T. M. McCormick, I. G. Hill and G. C. Welch, *J. Mater. Chem. C*, 2015, **3**, 8904

21. S. Jensen, K. Tan, W. P. Lustig, D. S. Kilin, J. Li, Y. J. Chabal, and T. Thonhauser, *Chem. Mater.*, 2019, **31**, 7933-7940.

22. O.V.Dolomanov, L. J. Bourhis, R. J. Gildea, J. A. K. Howard and H. Puschmann, 2009, *J. Appl. Cryst.* **42**, 339-341.

23. G. M. Sheldrick, *Acta Cryst.* A, 2015, **71**, 3-8.

24. G. M. Sheldrick, *Acta Cryst.* C, 2015, **71**, 3-8.

25. S. Tsuzuki and A. Fujii, *Phys. Chem. Chem. Phys.*, 2008, **10**, 2584

26. L. Yang, P. Langer, E. S. Davies, M. Baldon, K. Wickham, N. A. Besley, E. Besley, N. R. Champness, *Chem. Sci.* 2019, **10**, 3723–3732.

27. A. L. D. Yonkeu, M. M. Ndipingwi, C. Ikpo, K. Nwambaekwe , S. Yussuf, H. Tesfay and E. Iwuoha, *Polymers*, 2020, **12**, 2894.

28. Sheshanath V. Bhosalea, Chintan H. Janiab and Steven J. Langford, *Chem. Soc. Rev*. 2008, **37**, 331–342.

29. H.-X. Gong, Z. Cao, M.-H. Li, S.-H. Liao and M.-J. Lin, *Org. Chem. Front.*, 2018, **5**, 2296–2302.

30. G. Andric, J. F. Boas, A. M. Bond, G. D. Fallon, K. P. Ghiggino, C. F. Hogan, J. A. Hutchison, M. A. P. Lee, S. J. Langford, J. R. Pilbrow, G. J. Troup and C. P. Woodward, *Aust. J. Chem.*, 2004, **57**, 1011 —1019.

31. M. Supura and S. Fukuzumi, *ECS J Solid State Sci Technol*, 2013, **2**, M3051-M3062.

32. M. A. Kobaisi, S. V. Bhosale, K. Latham, A. M. Raynor and S. V. Bhosale, *Chem. Rev.* 2016, **116**, 11685−11796.

33. A. Sanguineti, M. Sassi, R. Turrisi, R. Ruffo, G. Vaccaro, F. Meinardi and L. Beverina, *Chem. Commun.*, 2013, **49**, 1618 —1620.

34. X. Zhan, A. Facchetti, S. Barlow, T. J. Marks, M. A. Ratner, M. R. Wasielewski and S. R. Marder, *Adv. Mater.*, 2011, **23**, 268–284.

35. F. Kong, M. Lin and T. Qiu, *Lumin.,* 2018, **33**, 1209–1216.

Chapter three   Rylene Diimide Metal-organic Frameworks

3.1 Introduction

Chapter one covered the general, albeit not exhaustive, aspects of metal-organic frameworks (MOFs). In this chapter, however, the discussion will revolve around the rylene diimide-containing metal-organic frameworks (RDMOFs). RDMOFs are a subclass of redox-active MOFs constructed by incorporating either NDIs or PDIs as linkers (details on NDIs and PDIs can be found in chapter two). Redox-active MOFs, as the name implies, are a class of MOFs that have the ability to undergo some electron transfer processes, i.e. loss and gain of electrons. Understanding and taking advantage of the principles of engendering redox-activity in MOFs have led to the emergence of materials with huge potential applications in fuel cells,[1] thermoelectrics,[2-4] electrical switches,[5] gas storage and separation,[6] electrocatalysis,[7] microporous conductors,[8] sensing,[9] electrochromic devices,[10] supercapacitors,[11] amongst others. Redox activity is bequeathed on MOFs by carefully selecting metal ions and/or organic linker that are redox-active themselves.

Interests in RDMOFs have continued to surge after a 2005 study[11] by Hupp *et al*. As chapter one has covered the synthetic methods and most of the techniques used in characterizing MOFs, this chapter will briefly review the literature with particular emphasis on the techniques that are almost exclusively used in characterizing redox-active MOFs. Also, to be covered in the review will be the applications of RDMOFs. After the review section, the results and discussion based on the current study will be presented. It is important to bear in mind that this chapter and the next two are interrelated in that while this chapter will be dedicated to the pyridyl NDI/PDI-based MOFs, chapter four will focus on a series of nicotinic acid NDI-based MOFs; and chapter five will look at the host-guest chemistry of some of the MOFs. As stated earlier, the proceeding sections

will survey the literature landscape, within the last 10 years, of RDMOFs classifying them into the pyridyl-, carboxylate- and azolate-based RDMOFs.

3.2 Brief review of the recent developments in rylene diimide metal-organic frameworks (RDMOFs)

3.2.1 Carboxylate-based RDMOFs

In chapter two, it was pointed out that rylene diimides that are used for MOF synthesis are pre-functionalised in order to act as linkers. Generally speaking, carboxylate based-MOFs are among the most common types of MOFs reported in the literature and this is largely due to how easy it is for the carboxylates to coordinate to the metal centres. Taking advantage of the ease of bay-functionalising rylene diimide, chemists in the field have been able to synthesise a moderate number of NDI- and far fewer PDI-based carboxylic acids for use in the preparation of RDMOFs. Some of these ligands have been presented in chapter one but more examples are shown in Figure 3.1.
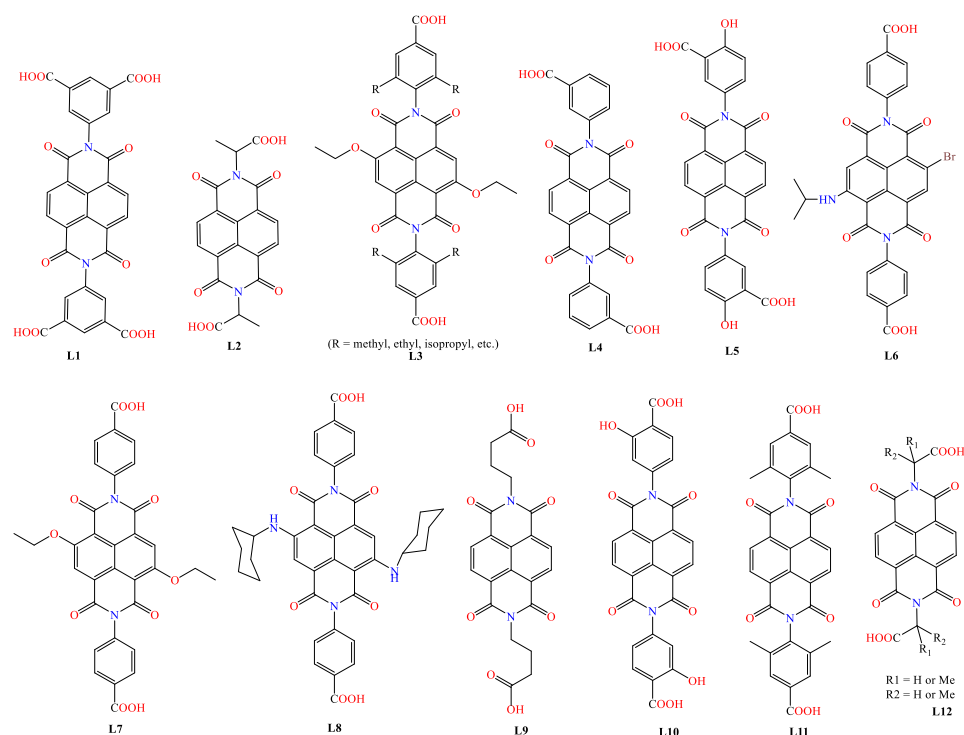
Figure 3.1: Structures of some carboxylic rylene diimides in MOFs; **L1**,[12,13,21-23,31] **L2**,[14-16] **L3**,[17] **L4**,[18-20] **L5**,[24,25] **L6**,[27] **L7**,[27] **L8**,[27] **L9**,[28,29] **L10**,[30] **L11**,[32] **L12**.[33,34]

3.2.1.1 Carboxylate-based NDI-MOFs

Carboxylate-based NDI-MOFs have been widely reported for their photochromism, electrochromism, sensing, catalysis and ability to store gases, amongst other applications. Two framework materials (Figure 3.2) were constructed by Lin and coworkers[12] from the reaction of $Ca(NO_3)_2$ or $SrCl_2$, **L1** and DMF in a Teflon-lined autoclave which was heated at 100 °C for 36 h. The materials are isostructural donor-acceptor (D-A) hybrid heterostructures with infinite 1-D carbon-doped alkaline-earth metal oxide clusters and X-aggregated NDI dimers as electron donors and acceptors, respectively. They were found to possess diametrically opposite photochromic sensitivities and photocatalytic activities which were attributed to the different cations in the inorganic clusters. Another closely related Mg based MOF also constructed with **L1** has been reported to demonstrate reversible photochromism through radical formation on

exposure to sunlight.[13] It was equally applied in solid-state sensing/detection of electron-rich organic amines thanks to the electron-deficient NDI ligands.
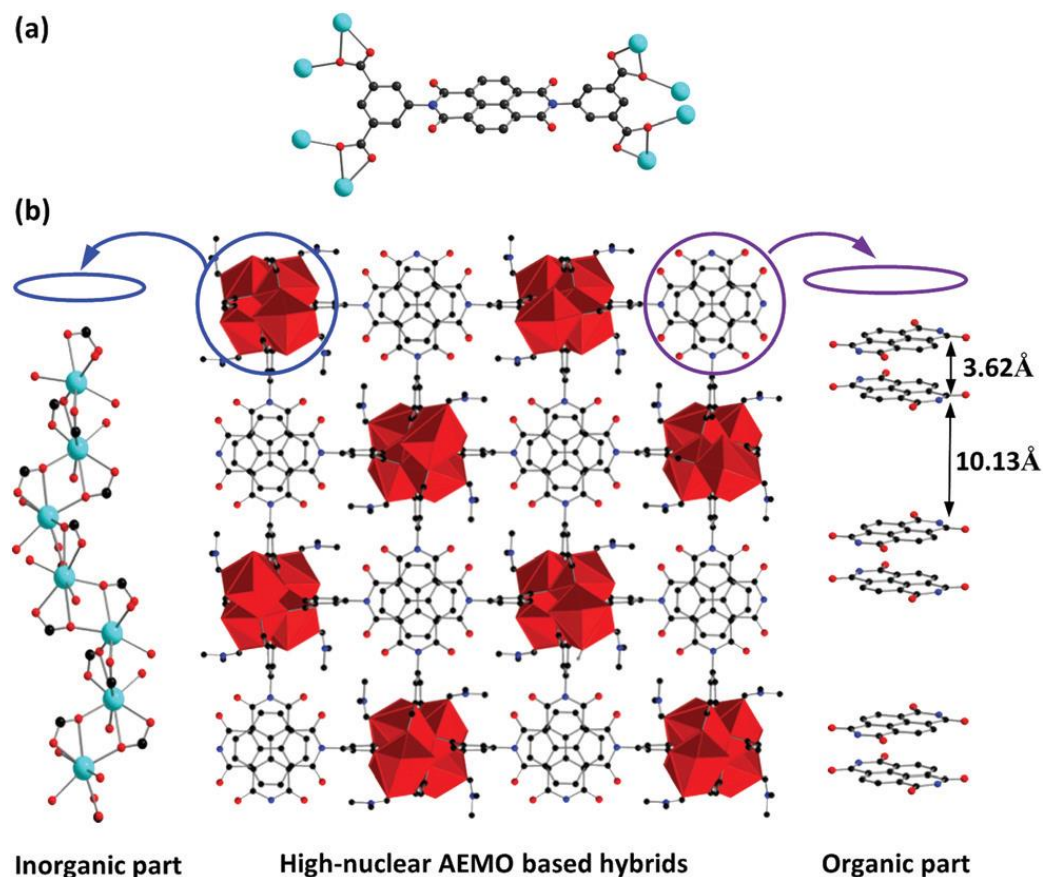
Figure 3.2: X-ray crystal structure of a Ca-**L1** hybrid showing the structure and binding scheme of organic tectons (a), and the infinite 1-D alkaline-earth metal oxide clusters and X-aggregated NDI dimers (b). H atoms and solvent molecules are omitted for clarity.[12]

The solvothermal synthesis of a homochiral and heterochiral MOF, Cd-**L2,** has been reported by Oh *et al*.[14] The morphologies of these materials were controlled by using the chirality in **L2** as a parameter to tune the synthesis (Figure 3.3). It is worth noting that the micro/nano crystals of the materials exhibit both photochromic and photodetecting properties. The results demonstrate a simple, yet powerful strategy for the application of coordination networks containing redox-active ligands in micro-/nano-optoelectronics. A very closely related work

by the same group of researchers led by Oh made use of **L2** and Zn^{2+} and further underscores the versatility of these chiral self-sorted multifunctional supramolecular biocoordination polymers (SBCPs) as chiral, chemiresistive and photoactive sensors.[15] Some nine homochiral coordination polymers constructed using Cd^{2+}, Mn^{2+} and Zn^{2+} in conjunction with **L2** were found to form both catenane and rotaxane motifs.[16]
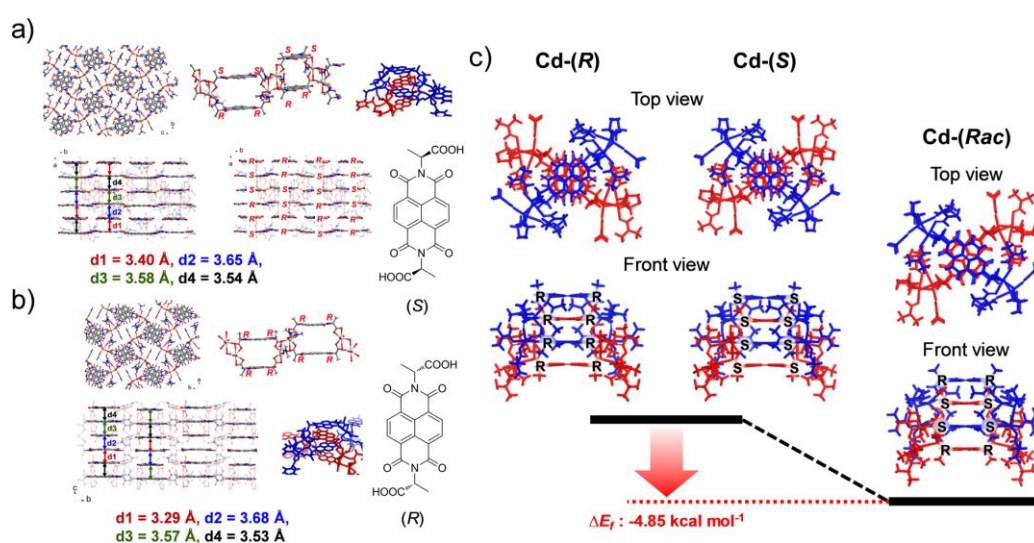
Figure 3.3: (a, b) Crystal structures of Cd-**L2** (a) (Rac)-**L2**-Cd; top left shows *a*-axis projection, top middle shows unit description containing two L2 units in 1D chain with description of chirality, top right shows polycatenation of 1D chains, bottom left shows π−π stacking scheme with centroid-centroid distances, and bottom right shows chiral configuration in this SCN and (b) (R)-**L2**-Cd; top left shows *c*-axis projection, top right shows unit description containing two L2 units in 1D chain with description of chirality, bottom left shows π−π stacking scheme with centroid-centroid distances, bottom right shows chiral configuration in this **L2**-Cd, and bottom right shows polycatenation of 1D chains. Scheme on the right demonstrate the chemical structure of two enantiomeric **L2** ligands, which have coordination with cadmium in SCN. (c) Formation energy (ΔE_f) calculation results for chiral discrimination of **L2**-Cd cluster models. Blue- and red-coloured clusters represent each unit of catenane motif, which is composed of two **L2** ligands connected by a Cd centre. For clear view of cluster models, top and front views are presented, and the arrangements of chiral centres are shown by small letters in the front view.[14]

In order to demonstrate the potential of MOF-based crystal engineering approaches that can be universally applied to control the photophysical

properties of organic semiconductor materials, Wöll and co-workers[17] developed a strategy that prevents photoluminescence (PL) quenching in crystalline dye molecules by tuning the packing of the chromophore. By incorporating photoactive NDIs into MOFs and tailoring the molecular alignment, they were able to determine, using computational analysis, the optimal alignment of the core-substituted NDIs producing high yield of emissive J-aggregates. A rigorous photophysical characterization showed the formation of J-aggregates with bright green emission and PL quantum yields of up to 2.3% which is a record value for crystalline NDI-based materials. This study combined **L3** and Zn for the synthesis of the MOFs.

A microporous MOF, $[Cu_2(\textbf{L4})(H_2O)_2]\cdot 5DMF\cdot dioxane\cdot 3H_2O$ (namely **FJU-101** and its activated form **FJU-101a**), constructed from the reaction of **L4** and $Cu(NO_3)_2$, which was able to display high methane storage of up to 212 (or 181) $cm^3(STP)\ cm^{-3}$ at room temperature and 65 (35) bars has been reported.[18,19] This high performance for methane uptake was ascribed to the polar carbonyl sites inherent in **L4** which facilitate strong electrostatic interactions with methane. This material is also interesting for its high C_2H_4 and CO_2 uptake of 142 $cm^3(STP)$ per g and 219.1 $cm^3(STP)$ per g. Figure 3.4 shows the crystal structure of **FJU-101** and CH_4 adsorption isotherm while the C_2H_4 sorption isotherms are presented in Figure 3.5. A one-dimensional coordination polymer, $Mg(\textbf{L4})_2(DMF)_2$, has been reported to exhibit reversible photochromic behaviour upon irradiation.[20] $Mg(\textbf{L4})_2(DMF)_2$ crystallised in the triclinic P-1 space group from the reaction between $Mg(NO_3)_2.6H_2O$ and **L4** in $DMF/ethanol/H_2O$.
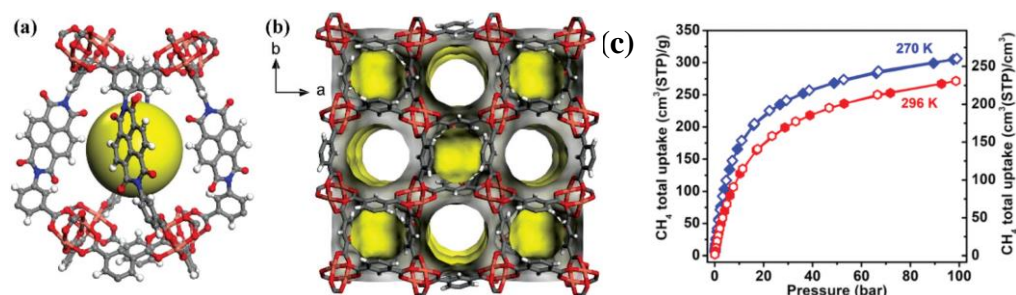
Figure 3.4: Single crystal structure of FJU-101: (a) a spherical-like $[Cu_{16}(L4)_4]$ nano-sized cage; (b) the 3D framework structure with a 1D cylindrical channel viewed along the crystallographic *c*-axis (Orange: Cu, gray: C, red: O, blue: N and white: H); (c) High-pressure methane adsorption isotherms of FJU-101a at 270 K and 296 K (Solid symbols: adsorption; open symbols: desorption).[18]
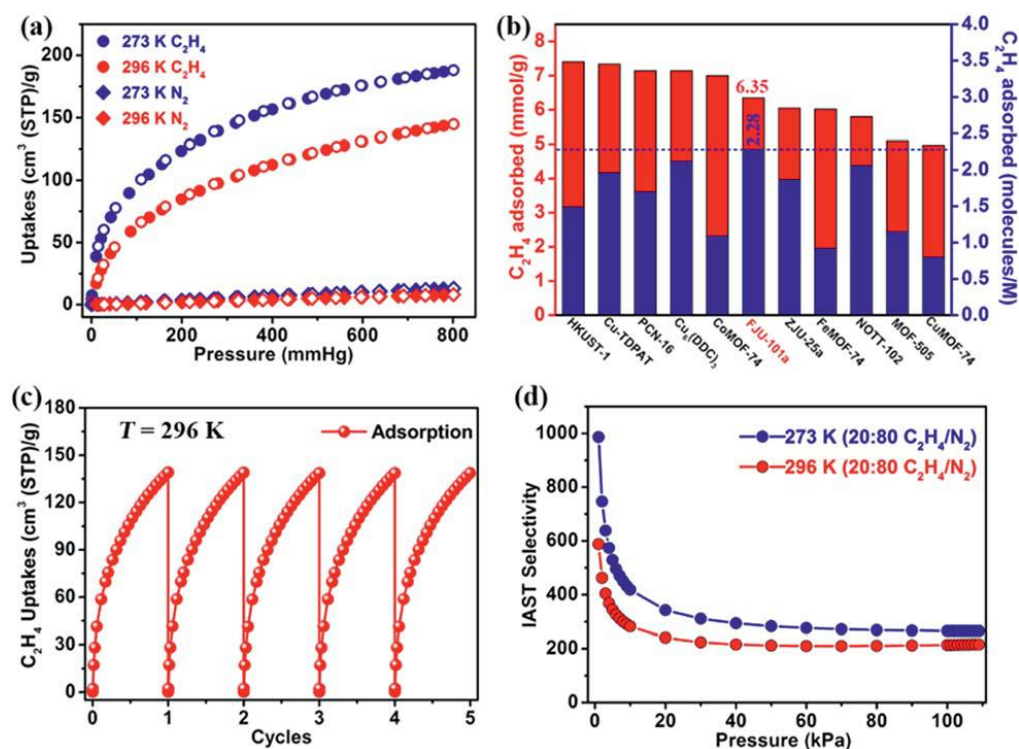
Figure 3.5: (a) FJU-101a single-component gas sorption isotherms for C_2H_4 and N_2 at 273 K and 296 K under 1 bar. (b) Comparison of the C_2H_4 uptake capacity of FJU-101a with that of best performing MOFs at ambient conditions. (c) Five cycles of ethylene adsorption for FJU-101a at 296 K. (d) IAST (ideal adsorbed solution theory) adsorption selectivities of FJU-101a for C_2H_4/N_2 (20/80) gas mixture at 273 K and 296 K.[19]

Xiang *et al.* reported a MOF formulated as ([Zn(**L1**)$_{0.5}$(bpy)(H$_2$O)]·3.5H$_2$O, **FJU-34**) which was obtained as light yellow block crystals after 2 days from the reaction of **L1**, 4,4'-bipyridine and Zn(NO$_3$)$_2$·6H$_2$O.[21] This MOF has a unique double interpenetration and a rare ***mog*** topological net (Figure 3.6c-d). The framework also displays excellent stability at different temperatures and pH conditions (Figure 3.6e-f). It was found to exhibit reversible photochromism varying from yellow to brown.
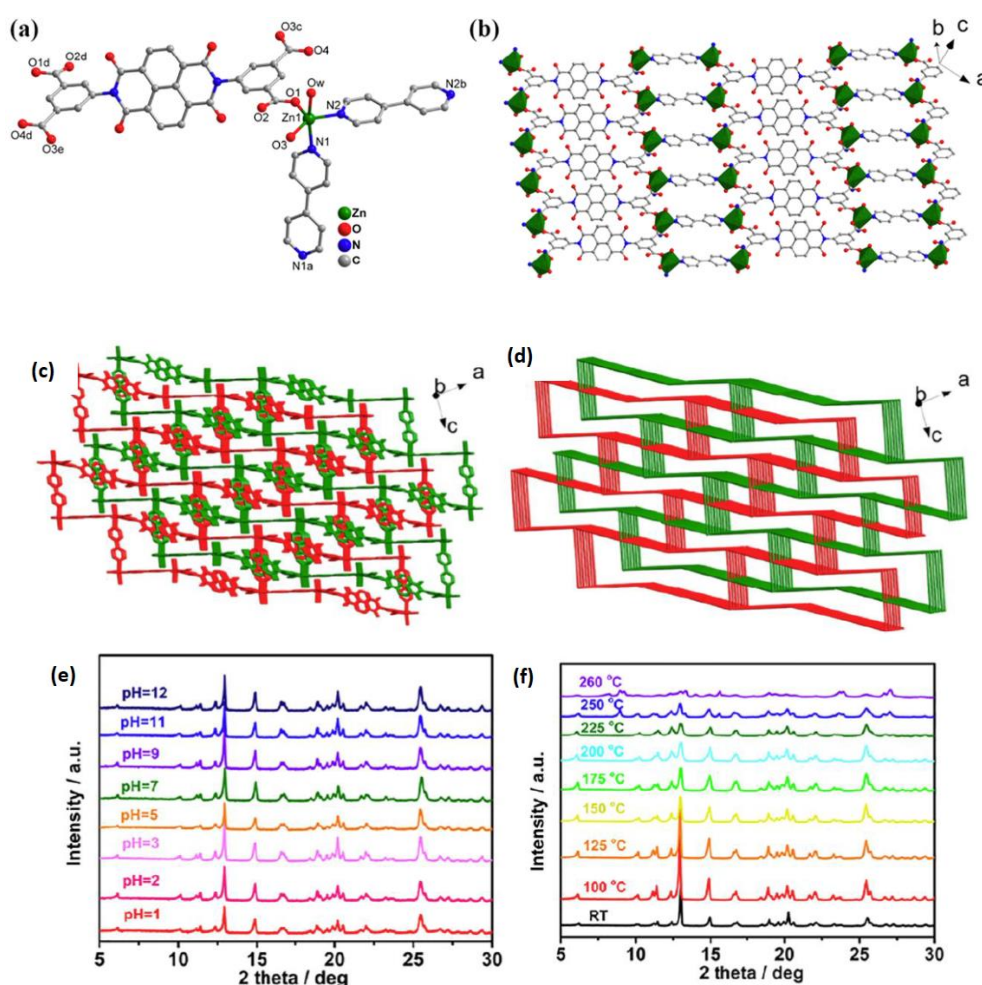
Figure. 3.6: (a) Structure of FJU-34 coordination environments of the Zn atoms, (b) The infinite 1D chain units [Zn$_2$L1] are connected by bipy ligands to form 2D layer. (c) View of the doubly interpenetrated 3D framework (d) Schematic view of the *mog* topology network (H atoms and guest molecules are omitted for clarity). (e) PXRD patterns of FJU-34 under different pH conditions. (f) PXRD patterns of FJU-34 at varying temperatures.[21]

A calcium MOF, [Ca$_2$**L1**(DMF)$_4$].2DMF, with photochromic properties has been reported.[22] It was made by the solvothermal reaction of **L1** and Ca(NO$_3$)$_2$.4H$_2$O in DMF at 100 °C for 72 h. The yellow crystals obtained exhibit a unique doubly interpenetrated 7-connected net with a total point symbol of {3^6.4^9.5^6}. The MOF features a reversible photochromism. Four other MOFs, made with **L1,** based on Cd^{2+}, Zn^{2+}, Ca^{2+} and Ba^{2+} were studied by Xiao and colleagues and were all found to exhibit reversible colour change on exposure to light as shown in Figure 3.7.[23]
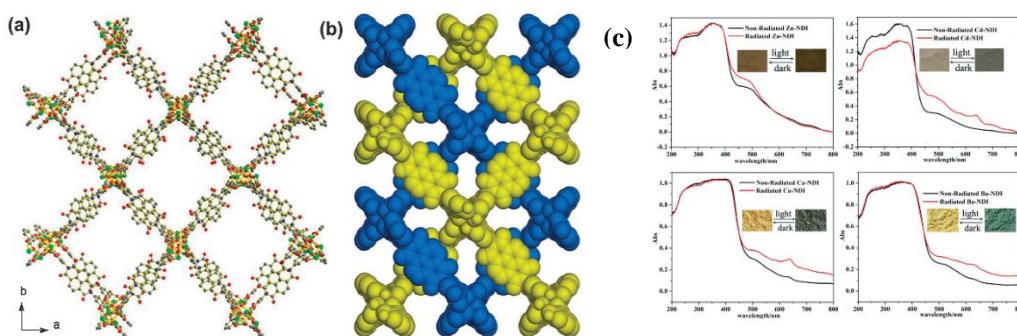
Figure 3.7: (a) View of the single 3D network of [Ca$_2$L1(DMF)$_4$].2DMF with channels. (b) Space-filling representation of the doubly interpenetrated network showing strong π…π interactions.[7] (c) UV-vis diffuse-reflectance spectra of Zn- (top left), Cd- (top right), Ca- (bottom left) and Ba-L1 MOF (bottom right) before and after irradiation; the inset shows the photochromic effect of the MOFs powder from photographic images.[23]

Powder samples of two MOFs synthesised using Ni^{2+}and Mg^{2+} with **L5** have been shown to display excellent electrochromic behaviour.[24] It is notable that these MOFs have the MOF-74 topology[25] and the redox-active and electrochromic properties (Figure 3.8) reported stemmed from **L5** that was incorporated during their construction. Electrochromic materials are materials that undergo colour change or light absorption when current is applied across them and this makes them quite useful for potential application in devices such

as smart windows. The application of these MOFs in fluoride detection has been investigated and they have proven to have high potential in being developed into solid-state sensor device for fluoride and as such offer advantage over solution-phase methods.[26]
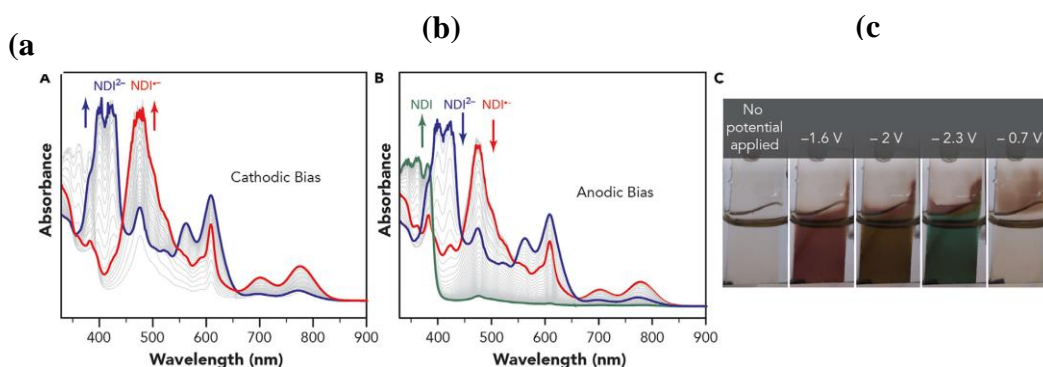
Figure 3.8: Spectroelectrochemical data of Ni_2**L5** collected by transmission UV-Vis spectroscopy show the reversible formation of $[NDI]^{\bullet-}$ and $[NDI]^{2-}$ when (a) reducing and (b) oxidizing step potentials of -0.5 to -2 and -2 to -0.5 respectively were applied (versus Fc/Fc^+). (c) Images of reversible colour switching of Ni_2**L5** films at several reducing potentials (–1.6, –2, and -2.3 V versus Fc/Fc+). Complete reversibility to the neutral transparent state was achieved by applying a reverse anodic bias (-0.7 V versus Fc/Fc^+).[24]

Three Zn MOFs were constructed using core substituted NDIs (**L6, L7** and **L8**).[27] As a result of the different substituent groups on the parent NDI, the colours of the thin films were markedly different ((Zn(**L6**)$_2$ - pink), Zn(**L7**)$_2$ - (yellow) and Zn(**L8**)$_2$ - (blue) grown on quartz). This study demonstrates how the electronic properties of NDI-based MOFs can be controlled by simply installing substituents of desirable characteristics on the parent NDI ligand.

A series of coordination polymers made from **L9** and some alkali metals (Li^+, Na^+ and K^+), alkaline earth metals (Ca^{2+}, Mg^{2+}), transition metals (Cd^{2+}, Mn^{2+}, Ni^{2+}, Co^{2+}, Zn^{2+}) and lanthanides (La^{3+}, Eu^{3+}, Tb^{3+}, Sm^{3+} and Gd^{3+}) have been reported by Li and co-workers.[28,29] Time-resolved photoluminescence studies

were carried out on the polymers and the results indicated the solid-state photoluminescence of the polymers is a superposition of two emissive states with higher energy state centred around 460 nm (lifetime τ = ca. 0.1 ns) which was attributed to the locally excited state. The red-shifted emission band was assigned to the delocalized state (τ = ca. 1 ns). This work demonstrates the effectiveness of coordination chemistry as a tool for modulating interchromophoric couplings. It also shows that the degree of π-stacking can be quantified by simple photoluminescence analysis.

Saha and colleagues constructed a honeycomb-shaped electroactive MOF from Zn and **L10** in DMF/EtOH/H$_2$O and showed that by incorporating electron-rich planar tetrathiafulvalene (TTF) as guests, the electronic band-gap could be reduced by ca. 1 eV.[30] This led to an improvement in electron delocalization occasioned by the guest-mediated π-donor/acceptor stacks (Figure 8) which the authors concluded did give rise to a higher electrical conductivity.
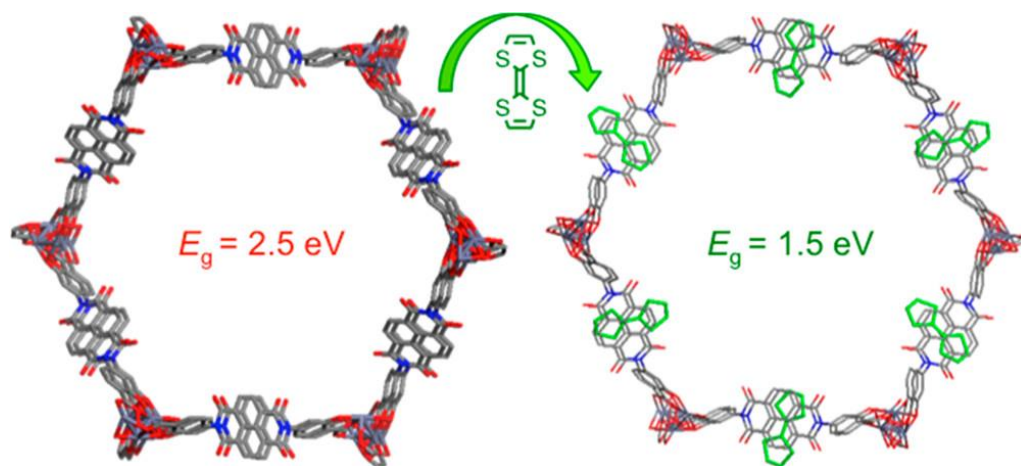
Figure 3.9: Structures of activated Zn$_2$(**L10**)(H$_2$O)$_5$(DMF)$_{1.5}$ before (left) and after TTF doping.[30]

Three MOFs with unprecedented topologies were made by the reaction of **L1** with Nd^{3+} (MOF-590), Eu^{3+} (MOF-591) and Tb^{3+} (MOF-592).[31] All three MOFs

were solved in the triclinic P-1 space group. They were employed, in the one-pot synthesis of styrene carbonate, as catalysts in the oxidative carboxylation of styrene and CO_2 under mild conditions (1 atm CO_2, 80 °C, solvent-free). Table 3.1 shows the optimized reaction conditions for the one-pot synthesis process.

Table 3.1 Optimization of reaction conditions for one-pot oxidative carboxylation of styrene and CO_2 catalyzed by MOF-590, -591, and -592[a]
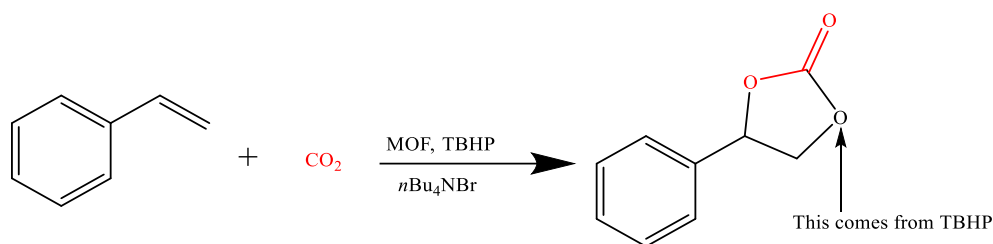
no.	MOF	con. (%)[c]	sel. (%)[c]	Yield (%)[c]	
				SC	SO
1	MOF-590	93	94	87	3
2[b]	MOF-590	97	87	84	8
3	MOF-591	95	85	81	3
4	MOF-590	98	82	80	5

[a] Reaction conditions: styrene (3.9 mmol), MOF (0.18 mol %, based on molecular weight), anhydrous tert-butyl hydroperoxide (TBHP) in decane (7.4 mmol), nBu$_4$NBr (8 mol %), CO_2 (balloon pressure), 80 °C, 10 h. [b]TBHP in H_2O. [c]The catalytic conversion (con.) of styrene, selectivity (sel.) of styrene carbonate, and yield of products were determined by GC-FID analysis using biphenyl as the internal standard. SC = styrene carbonate; SO = styrene oxide.[31]

Wasielewski and co-workers reported a Zr(IV)-based UiO-**L11** MOF constructed with ZrCl$_4$ and **L11** in DMF/AcOH solution.[32] The presence of wide spacing between the NDI molecules in addition to the weak electronic coupling through space or the Zr$_6$ nodes prevents the deactivation of the excited state, hence, helps to maintain the monomer-like photochemical reactivity in the

material. The reductive photodegradation of CH_2Cl_2 (Scheme 1) shows that UiO-**L11**$^{\bullet-}$ has a strong photoreducing power. Ott and co-workers also carried out studies which include potentiometric titrations of this MOF and they showed that the proton-responsive behaviour through the hydroxy groups on **L12** and the bridging Zr-μ3-OH of the secondary building units gave values of 6.10 and 3.45 respectively for their pK_a.[33] They went further to grow the MOF on fluorine-doped tin oxide (FTO) substrate and the material so grown exhibits reversible electrochromism due to step-wise one-electron reduction of the NDI. Charge propagation via the thin film occurred through NDI-to-NDI hopping mechanism which charges were balanced by electrolyte transport, resulting in cyclic voltammograms (see Figure 3.10) of the thin films that were typical of a diffusion-controlled process.

$$\text{UiO-NDI}^{\bullet-} \xrightarrow{h\nu} \text{UiO-}^{*}\text{NDI}^{\bullet-} \qquad (1)$$

$$CH_2Cl_2 \xrightarrow{\text{UiO-}^{*}\text{NDI}^{\bullet-}} \left| CH_2Cl_2 \right|^{\bullet-} \longrightarrow \left| CH_2Cl \right|^{\bullet} + Cl^{-} \qquad (2)$$

$$\qquad (3)$$
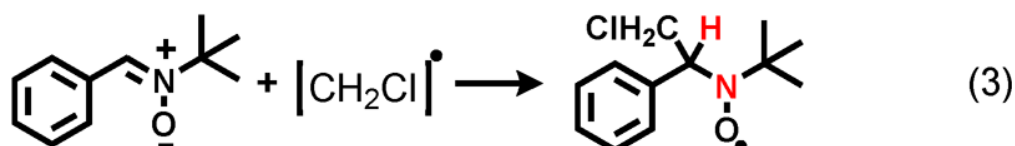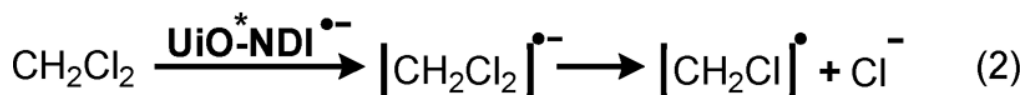
Scheme 3.1: Mechanism of CH_2Cl_2 reduction by photoexcited UiO-NDI$^{\bullet-}$ radical anions and n-tert-butyl-α-phenylnitrone (pbn)-spin adduct formation[a].[32]
[a] Hyperfine-contributing nuclei of primary interest are highlighted in red.
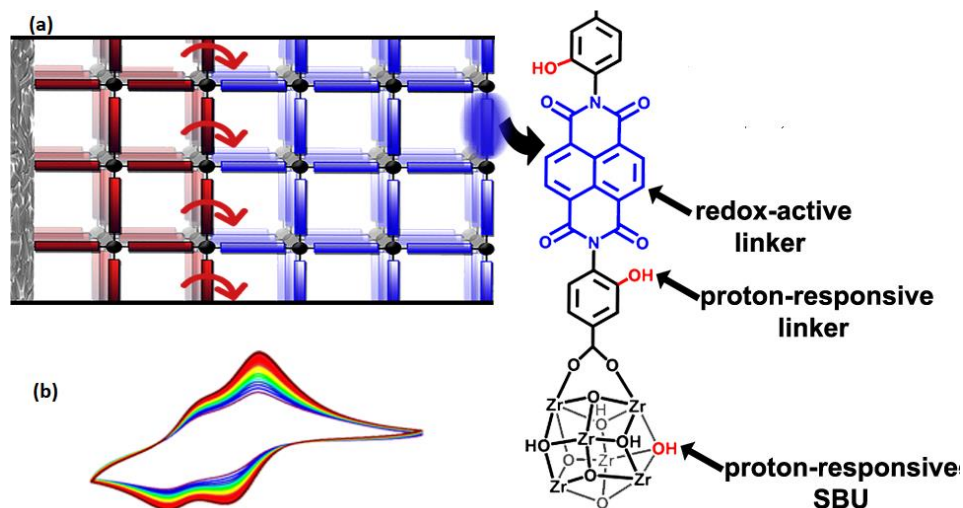
Fig. 3.10 (a) A 3D schematic showing the mechanism of charge propagation in UiO-L12; and (b) The cyclic voltammogram showing multiple scans at 100 mV s^{-1} with increasing current density on progressive scans.[33]

A series of coordination polymers based on Co^{2+}, Cu^{2+} and Zn^{2+}, solvothermally prepared using **L12**, were studied to understand how the structures of the polymers change with respect to small alterations in the steric bulk in the organic linker.[34] Switching between H and/or CH_3, it was discovered that seven (with $R_1=CH_3$ and $R_2=H$ or R_1 and $R_2=H$) out of the ten reported materials show preference for the ligands to be closely packed in a parallel manner whereas the remaining three coordination polymers (with R_1 and $R_2=CH_3$) show interactions occurring between the NDI cores in a more perpendicular fashion.

3.2.1.2 Carboxylate-based PDI-MOFs

As discussed in chapter two, only a few PDI-MOFs have been reported to date, and this is largely due to solubility challenges associated PDIs. Here a brief review of these MOFs will be presented highlighting interesting properties and applications. The PDIs that have been successfully used in MOF synthesis are shown in Figure 3.[11]
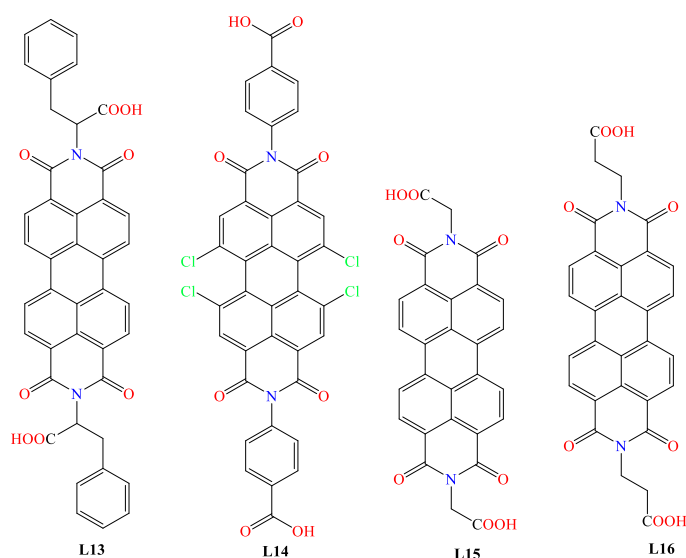
Figure 3.11: Structures of PDIs used in MOFs construction

To the best of our knowledge, only five PDI-based MOFs – all of which contain carboxylate-functionalised PDIs – have been reported to date.[35-39] The first PDI-based coordination polymer formulated as [Mn-**L13**(DMF)$_2$] was reported by Turner and co-workers.[35] The 2D coordination polymer transforms into a 3D framework material through interpenetration. It was employed as a stationary liquid chromatographic phase and was demonstrated to resolve selected racemic mixtures of 1-phenylethanol, pantolactone, and limonene with enantiomeric and chemical selectivity. The NDI analogue of this linker, has been used for the construction of seven coordination polymers based on either Mn^{2+} or Cd^{2+}.[40]

A Zr-PDI MOF recently reported by Yin and colleagues was constructed by reacting ZrCl$_4$ and **L14** in DMF/AcOH mixture.[36] The PDI ligand had substituents both at the bay and the imide positions (see Figure 2.4b) which led to a twist of the PDI. This twist, occasioned by the substituents, is responsible for the solubility of the ligand for incorporation into MOF synthesis. Analysis of the single crystal structure of Zr-**L14** revealed it to be a 3D framework

99

crystallizing in the tetragonal space group $I4_1/a$ with a $Zr_6(\mu_3\text{-}O)_4(\mu_3\text{-}OH)_4$ octahedral cluster in which the six vertices of the octahedron are occupied by Zr^{4+} centres and the eight triangular faces are capped in alternate fashion by four μ_3-OH and four μ_3-O groups, as shown in Figure 3.12. The full structure shows the full coordination of the $Zr_6(\mu_3\text{-}O)_4(\mu_3\text{-}OH)_4$ by 12 carboxylate units of **L14**. Amine adsorption studies carried out on this MOF led to in-situ generation of radical anions via photo-induced electron transfer. The radical anions were found to be stable for at least 30 days and exhibit high near-infrared photothermal conversion efficiency. This study sheds light on the potential application of PDI-based metal organic frameworks in photothermal therapy.
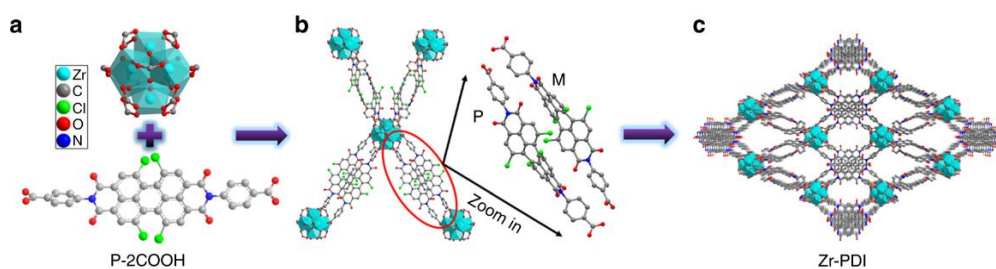
Figure 3.12: (a)Synthesis of 3D porous Zr-**L14** showing the structures of Zr-cluster and **L14** (b) Connection mode of Zr-cluster (the Zr-cluster is fully coordinated by 12 carboxylate units) and molecular arrangement of chiral **L14** (c) Crystal structure of Zr-**L14** viewed along the crystallographic a-axis.[36]

Duan and co-workers reported a two-dimensional Zn-**L15** coordination polymer which was used in the photocatalytic reduction of aryl halides and oxidation of alcohols and amines driven by visible-light.[37] Another study involving **L15** has been conducted where one-dimensional nanorods of Co^{2+}-**L15** was implicated in the in-situ production of iron oxy-hydroxide (α-FeOOH) for the oxidation of water.[38] The catalyst has the ability to split water – even under acidic conditions – by using visible light, giving a maximum release of O_2 of more than

$25 \ \text{mmol} \ \text{g}^{-1} \ \text{h}^{-1}$. The activity and stability of the catalyst remains unaffected after at least three cycles. The mechanism of the catalytic process in shown in Figure 3.13a. The nanorods were synthesised under ambient conditions by addition of aqueous solution of $Co(NO_3)_2$ to **L15** in DMF/water/triethylamine as shown in Figure 3.13b. The last of the known PDI-based metal-organic frameworks to be mentioned here is a MOF constructed through a layer-by-layer approach using Zn^{2+} and **L16** on a template monolayers of graphene oxide.[39] It is interesting to state that no significant π-π stacking was observed in the structure.
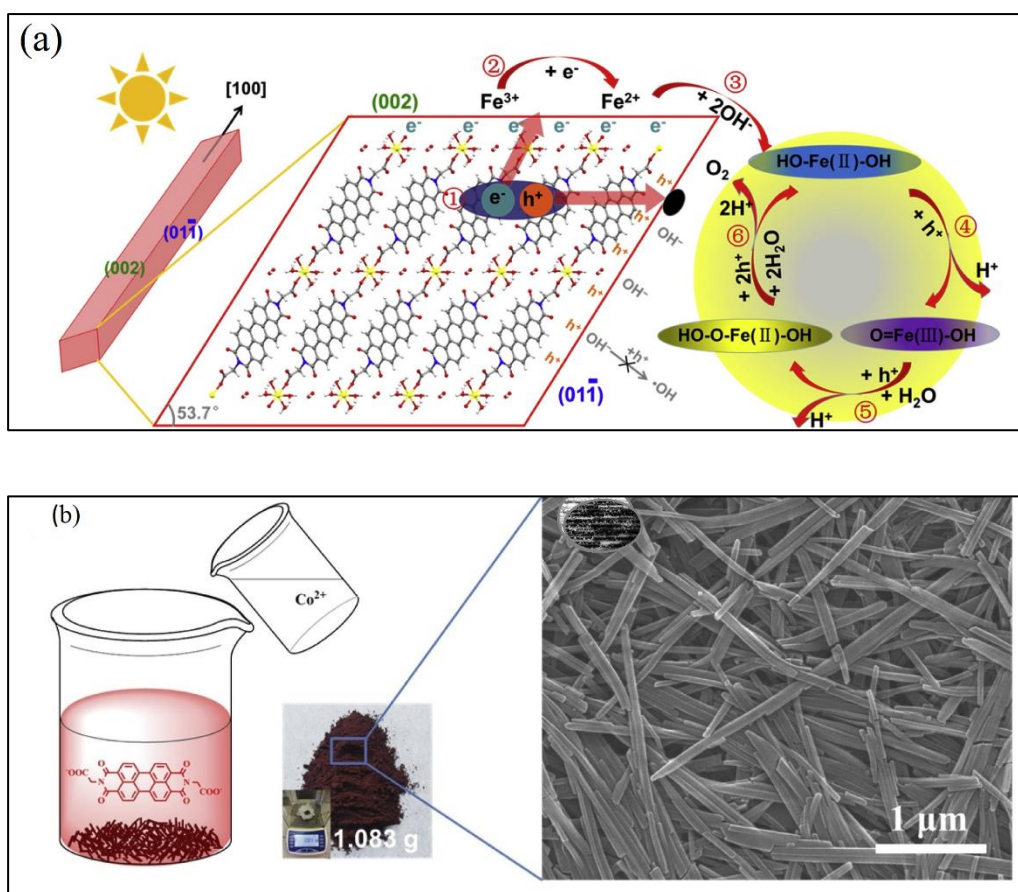
Figure 3.13: (a) Mechanism for the photocatalytic water splitting using Co^{2+}-**L15**; (b) synthesis (left) and TEM of the nanorods (right). The nanorods were synthesised under ambient conditions by addition of aqueous solution of $Co(NO_3)_2$ to **L15** in DMF/water/triethylamine.[38]

3.2.2 **Pyridyl-based NDI Metal-organic Frameworks**

The majority of the reported RDMOFs contain pyridyl-based NDI linkers – the most common of which is N,N'-bis(4-pyridyl)-1,4,5,8-naphthalenetetracarboxydiimide or DPNDI/DPNI as it is commonly referred to among researchers. The ubiquity of this subclass of RDMOFs stems from the fact the lone pairs on the pyridyl nitrogen can easily be used to coordinate a metal cation. The structures of some of the pyridyl-based NDIs employed in MOFs preparation are shown in Figure 3.14
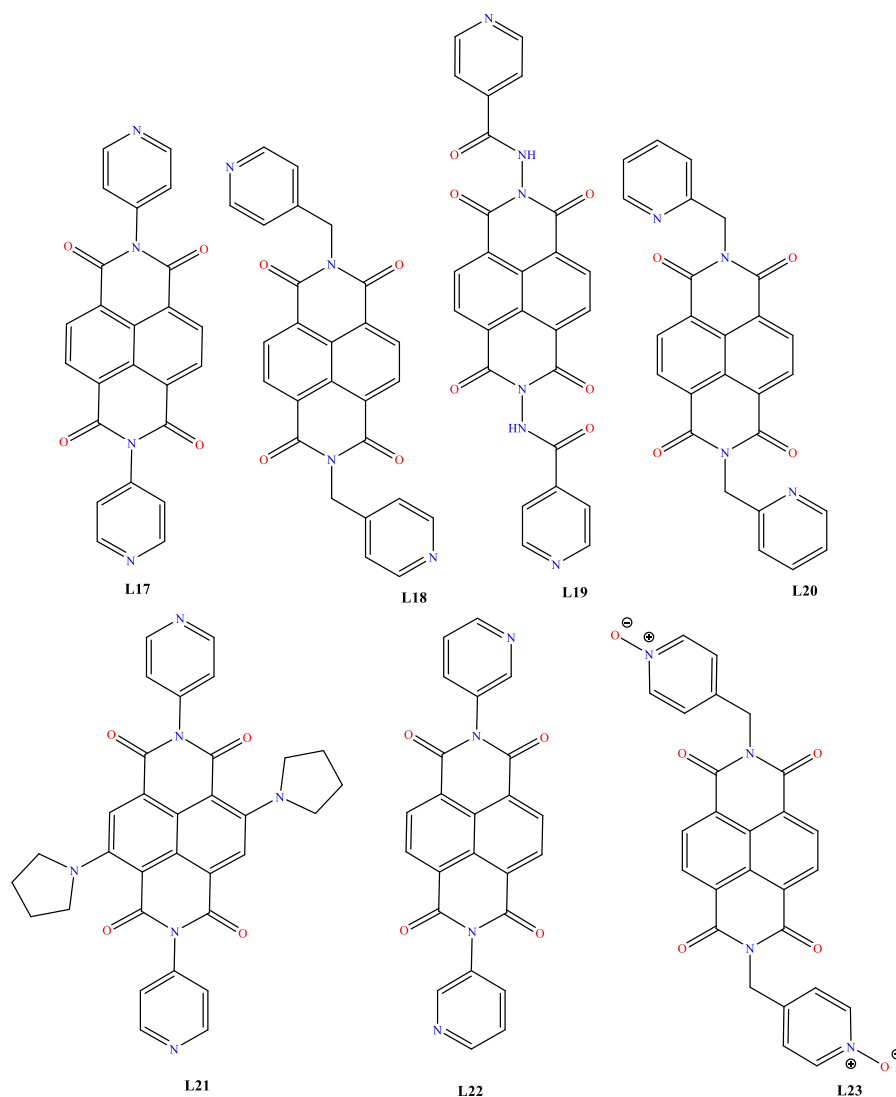
Figure 3.14: Structures of pyridyl-based NDIs in MOFs synthesis

A coordination polymer formulated as [Cu$_2$(**L18**)$_2$(o-BDC)$_2$] (o-BDC = 1,2-benzenedicarboxylate) with open Cu^{2+} sites has been reported by Yang *et al.*[41] This material selectively separates ethanol over acetonitrile at room temperature – this is noteworthy because these solvents have similar physicochemical properties and form azeotropes at a specific concentration because of the similar boiling points (acetonitrile, 81.1 °C; ethanol, 78.4 °C). A combination of vapour adsorption and NMR studies reveal that [Cu$_2$(**L18**)$_2$(o-BDC)$_2$] could significantly separate hydroxylic from non-hydroxylic guests. [Cu$_2$(**L18**)$_2$(o-BDC)$_2$] was made from the reaction of **L18**, Cu(NO$_3$)$_2$·6H$_2$O, and disodium 1,2-benzenedicarboxylate in H$_2$O/CH$_3$OH/CHCl$_3$ (1:3:10). The mixture was stirred and then sealed in a 20 mL Teflon-lined autoclave and heated in an oven at 70 °C for 7 days. The single crystal structure and the adsorption isotherms for this MOF are shown in Figure 3.15.
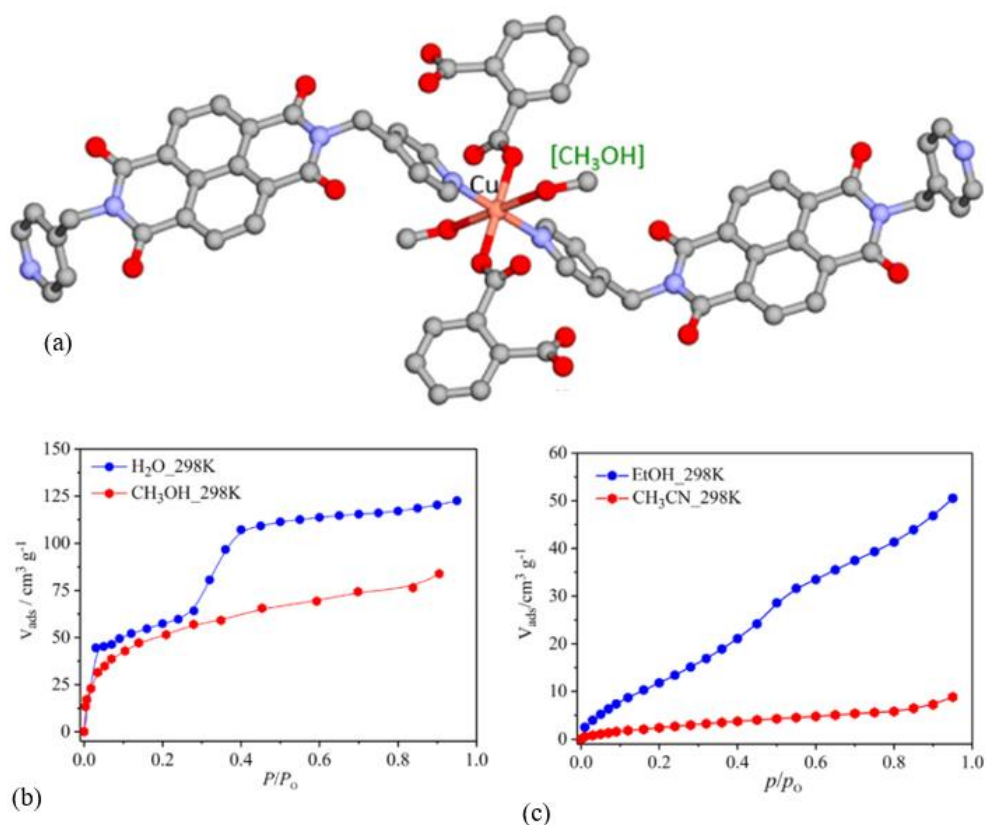
Figure 3.15: (a) Single crystal structure of [Cu$_2$(**L18**)$_2$(o-BDC)$_2$]. MeOH showing the coordination environments around Cu (II) ion. (b) Adsorption isotherms with different vapours.[41]

Niu and co-workers have developed two polyoxometalate-incorporated metal-organic frameworks (POMOFs) and have successfully applied them as photocatalysts.[42,43] Both MOFs crystallised in the monoclinic space group $P2_1$ and were made by carefully assembling pyrrolidine-2-yl-imidazole, **L18** and $K_5[BW_{12}O_{40}] \cdot 5H_2O$ (a polyoxometalate or POM) into one single framework. One MOF was based on Zn^{2+} (See Figure 3.16) and the other on Co^{2+}. Another POMOF which has been used as a photocatalyst has been reported.[44] This MOF produced two kinds of long-lived charge-separated states for reduction reactions upon irradiation. The authors concluded that these photogenerated stable charge-separated states have potential for applications in photocatalytic reactions of substrates containing several functional groups.
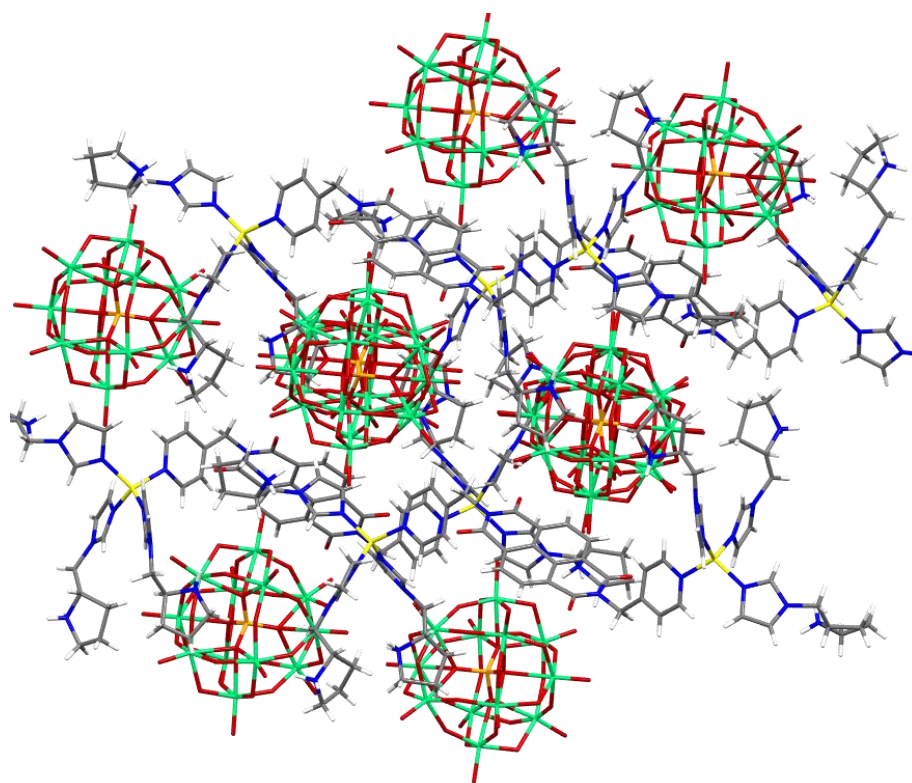
Figure 3.16: Packed single crystal structure of Zn^{2+} POMOF viewed along the crystallographic *b*-axis (redrawn from the CIF). (C=grey, N=blue, O=red, Zn=yellow, W=green, B=orange and H=white).[42]

It is important to mention that POMs are used as catalysts for epoxidation of olefins due to their stability against oxidative degradation while pyrrolidine-2-yl-imidazole on the other hand is capable of acting as an electron donor thereby enhancing photoinduced electron transfer in the presence of a photosensitizer such as NDI. The thoughtful combination of these constituents led to frameworks which are superb in terms of their catalytic ability as well as their selectivity. Whereas the Zn-based POMOF was employed in the photocatalytic oxidation of amines and olefins,[42] the Co-based POMOF was used as a photocatalyst in the photoreduction of aryl halides and cycloaddition of epoxides with CO_2.[43]

The effect of secondary building linker geometry on the photochromic properties of **L19**-based MOFs have been investigated.[45] Zhang and colleagues constructed three Cd-**L19** MOFs by varying only the carboxylic acids. The carboxylic acids used in the synthesis include isophthalic acid (*m*-H_2BDC), terephthalic acid (*p*-H_2BDC) and naphthalene-2,6-dicarboxylic acid (2,6-H_2NDC); and the resulting MOFs were formulated as [Cd(**L19**)(*m*-BDC)(DMF)], [Cd$_2$(**L19**)$_2$(*p*-BDC)$_{0.5}$(MAC)$_2$] (MAC = methanoic acid) and [Cd(**L19**)(2,6-NDC)(H_2O)$_2$] respectively. While [Cd$_2$(**L19**)$_2$(*p*-BDC)$_{0.5}$(MAC)$_2$] crystallises in the monoclinic space group *C*2/*c*, [Cd(**L19**)(*m*-BDC)(DMF)] and [Cd$_2$(**L19**)$_2$(*p*-BDC)$_{0.5}$(MAC)$_2$] prefer the triclinic space group *P*-1. The MOFs exhibit photochromic behaviour and different kinds of interactions as shown in Figure 3.17. The stability and the dimensionality of all the MOFs were ascribed to the N–H···O interaction while the photoinduced electron transfers were attributed to the face-to-face π–π stacking and lone pair–π interactions inherent in the structures. A Zn(II) MOF based on **L19,** isostructural to [Cd(**L19**)(2,6-

NDC)(H_2O)$_2$], has equally been shown to exhibit π–π stacking and N–H···O interaction in addition to possessing photochromic and photo-controlled fluorescence quenching behaviours when irradiated with 300 W xenon lamp.[46] Other studies utilising **L17** and **L18** that also investigated how cooperative lone pair-π and coordinative interactions dictates metal-ion-directed self-assembly of NDI ligands in coordination have been reported.[47,48]
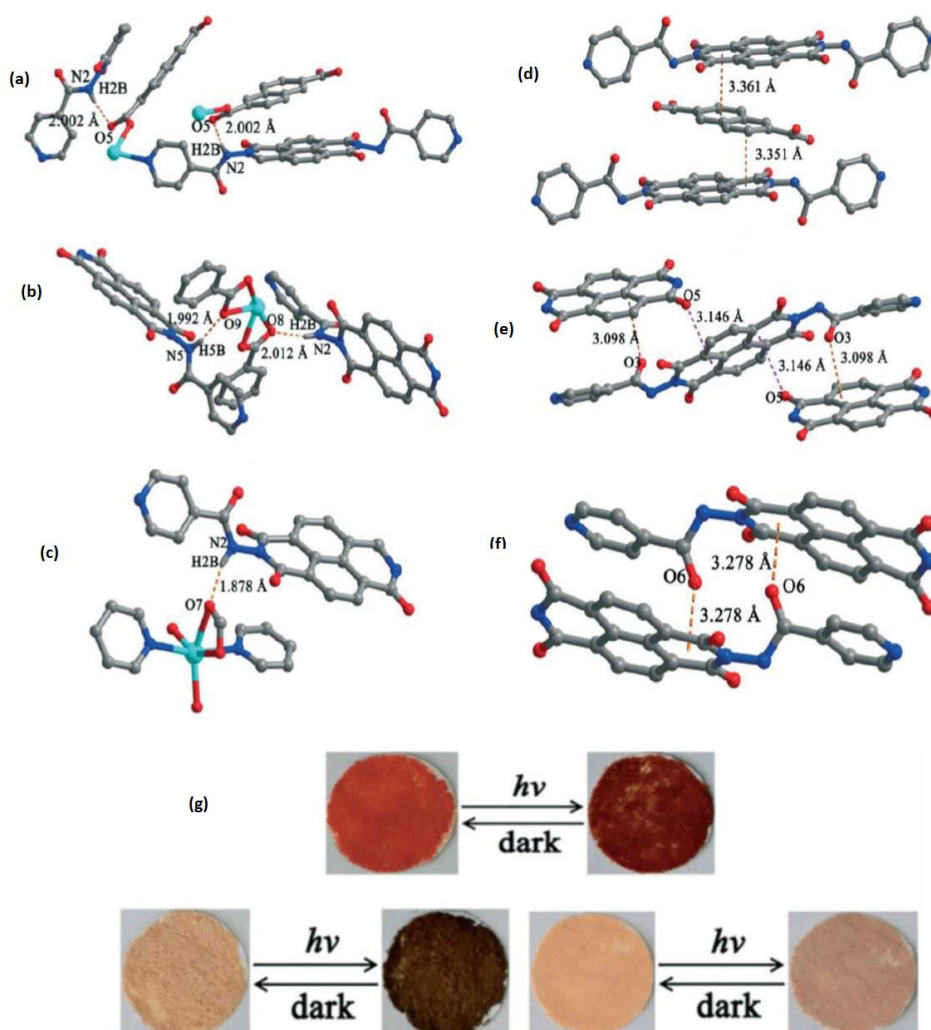
Figure 3.17: (a-c) N–H···O hydrogen bonds between **L19** ligands and neighbouring dicarboxyl groups in [Cd(**L19**)(2,6-NDC)(H_2O)$_2$], [Cd(**L19**)(*m*-BDC)(DMF)] and [Cd$_2$(**L19**)$_2$(*p*-BDC)$_{0.5}$(MAC)$_2$] respectively. (d-f) Face-to-face π–π stacking interactions in [Cd(**L19**)(2,6-NDC)(H_2O)$_2$] (d), and lone pair–π interactions in [Cd(**L19**)(*m*-BDC)(DMF)] (e) and [Cd$_2$(**L19**)$_2$(*p*-BDC)$_{0.5}$(MAC)$_2$] (f) between adjacent NDI ligands. (g) Photographs of [Cd(**L19**)(2,6-NDC)(H_2O)$_2$] (top), [Cd(**L19**)(*m*-BDC)(DMF)] (bottom left) and [Cd$_2$(**L19**)$_2$(*p*-BDC)$_{0.5}$(MAC)$_2$] (bottom right) before and after irradiation using a xenon lamp (300 W).[45]

Kitagawa and co-workers have carried out extensive research on an entangled MOF, $Zn_2(BDC)_2$(**L17**), constructed from **L17**, Zn^{2+} and benzene-1,4-dicarboxylic acid.[49,50] They reported that the MOF can act as a decoding host capable of accommodating a class of organic compounds – namely benzene, toluene, xylene, anisole and iodobenzene - and able to discriminate between them producing a matching readout.[50] It was observed that there was intense turn-on emission when the aromatic guests were incorporated and the luminescent colour that resulted was due to the substituent of the guest molecule. Further study of this MOF involved a detailed photophysical investigation and it was found that there was a linear correlation between the fluorescence lifetime values of the exciplexes and the dipole moments on the one hand; and the charge transfer complexes and the ionization potentials of the different substituted organic guests on the other hand.[49] Tuning light emission toward white light has also been investigated in $Zn_2(BDC)_2$(**L17**).[51]

Two semiconductive coordination polymers formulated as [Cu_2I_2(**L17**)] and [PbI_2(**L17**)] have been constructed by respectively layering methanol solution of CuI and PbI_2 with DMF solution of **L17** using a crystallization tube.[52] While [Cu_2I_2(**L17**)] crystallizes in the monoclinic space group $P2_1/c$, [PbI_2(**L17**)] adopts the monoclinic space group $C2/c$. Despite having similar 2D heterostructures, they are dissimilar in terms of photon-induced electron transfer properties. This difference lies in the fact that the HOMO energy level of [$PbI_2]_n$ cluster is lower than that of the [Cu_2I_2] chain (see Figure 3.18) and this makes it easy for [Cu_2I_2(**L17**)] to undergo intermolecular electron transfer to generate

a long-lived separated state which can in turn be harnessed in artificial photosynthesis.
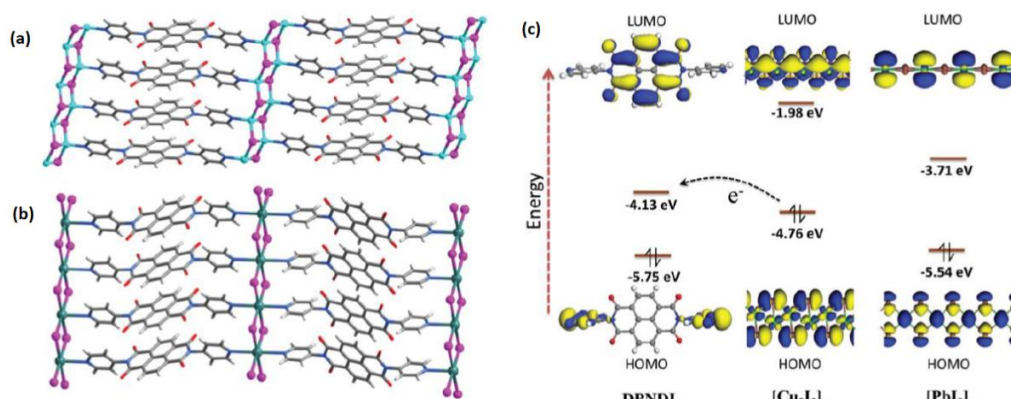
Figure 3.18: (a-b) 2D structures of (a) [Cu$_2$I$_2$(**L17**)] and (b) [PbI$_2$(**L17**)]; aqua Cu, green Pb, gray C, blue N, pink I, white H. (c) HOMO and LUMO energy levels of **L17**, and the inorganic units [Cu$_2$I$_2$]$_n$ and [PbI$_2$]$_n$.[52]

A cobalt-based MOF, [Co$_2$(DPNDI)(2,6-NDC)$_2$]·7(DMF), made from the reaction of Co(NO$_3$)$_2$·6H$_2$O, **L17** and H$_2$NDC, in mixed solvents, DMF/CH$_3$OH, (3:1 v/v) at 80 °C for 5 days has been reported.[53] The resulting crystals - which were dark green blocks - were found, using single crystal X-ray diffraction (SCXRD), to have crystallized in the triclinic space group *P*-1. This framework structure is doubly interpenetrated with the **pcu** topological net. The crystal structure of [Co$_2$(**L17**)(2,6-NDC)$_2$]·7(DMF) reveals a paddle-wheel {Co$_2$} clusters linked by two **L17** ligands and four deprotonated 2,6-NDC ligands as shown in Figure 3.19. Studies of the solvatochromic behaviour uncovers the high sensitivity of this MOF toward water making it a potential candidate for use in humidity sensing and moisture detection.
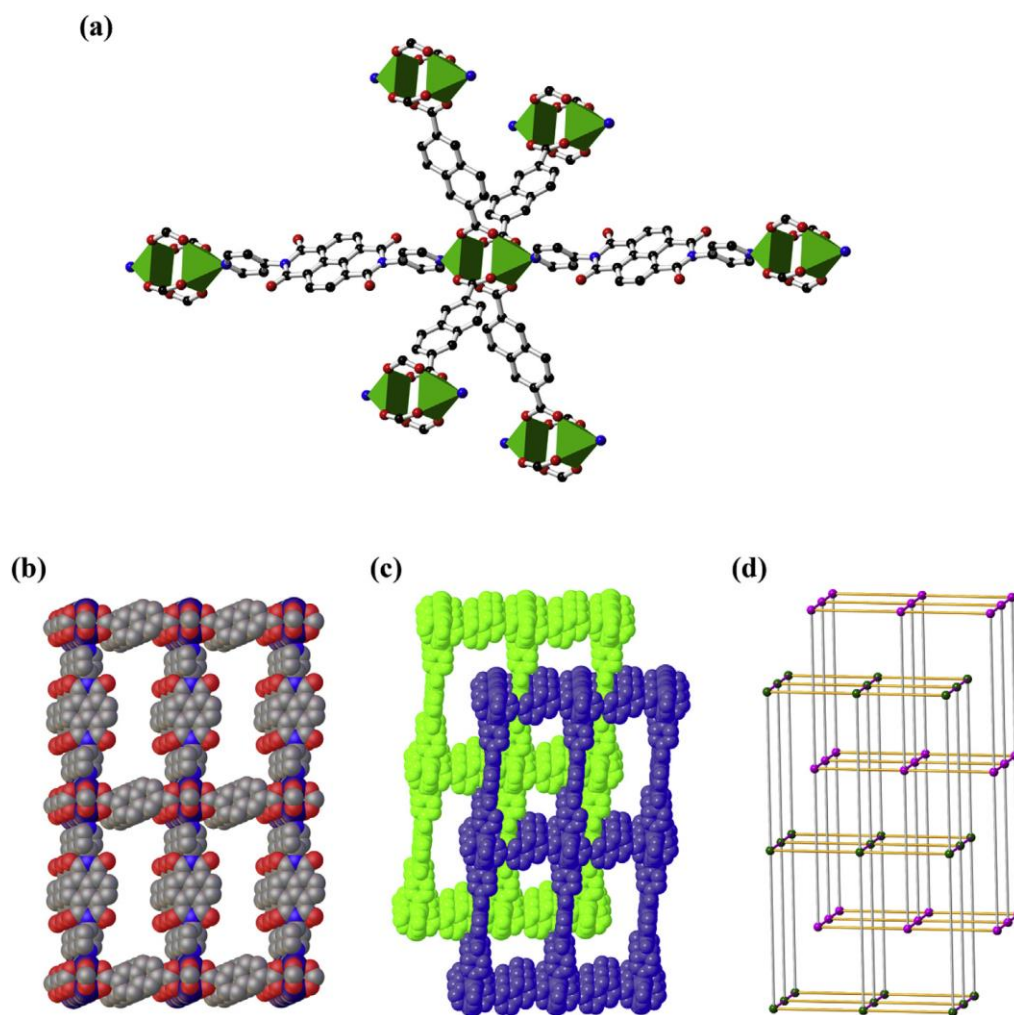
Figure 3.19: Structure of $[Co_2(\textbf{L17})(2,6\text{-NDC})_2]\cdot 7(DMF)$ showing the (a) coordination environments between paddle-wheel $\{Co_2\}$ clusters and Ligands; (b) space filled 3D structure; (c) 2-fold interpenetrated 3D structure; and (d) simplified pcu 3D topological network.[53]

Three zinc-based one-dimensional coordination polymers, $[Zn(\textbf{L18})Cl_2]\cdot H_2O$, $[Zn(\textbf{L18})(CH_3CN)_4]\cdot(ClO_4)_2\cdot 2H_2O$, and $[Zn(\textbf{L18})(H_2O)_4]\cdot(CF_3SO_3)_2\cdot 3H_2O$ were prepared by respectively reacting $ZnCl_2$, $Zn(ClO_4)_2$, or $Zn(CF_3SO_3)_2$ with $\textbf{L18}$.[54] While $[Zn(\textbf{L18})(H_2O)_4]\cdot(CF_3SO_3)_2\cdot 3H_2O$ crystallizes in the triclinic space group $P\text{-}1$, $[Zn(\textbf{L18})Cl_2]\cdot H_2O$ and $[Zn(\textbf{L18})(CH_3CN)_4]\cdot(ClO_4)_2\cdot 2H_2O$ crystallize in the monoclinic space groups $C2/c$ and $P2_1/n$ respectively. These compounds exhibit structural diversity owing to varying coordination abilities, sizes and geometries of counter anions. Anion exchange experiments were performed on

[Zn($\textbf{L18}$)(H$_2$O)$_4$].(CF$_3$SO$_3$)$_2$.3H$_2$O in which CF$_3$SO$_3^-$ was completely replaced by NO$_3^-$, ClO$_4^-$ or SCN$^-$ and the results show that this compound has a potential for anion recognition because of the structural changes that could be facilitated by the coordination ability of the anions. A closely related work making use of $\textbf{L17}$ has been reported.[55] The study involves three cadmium-based coordination polymers, [Cd(NO$_3$)$_2$($\textbf{L17}$)(CH$_3$OH)].CH$_3$OH, [Cd(SCN)$_2$($\textbf{L17}$)], and Cd($\textbf{L17}$)$_2$(DMF)$_2$.2ClO$_4$, which were synthesised from $\textbf{L17}$ and Cd(NO$_3$)$_2$, Cd(SCN)$_2$, and Cd(ClO$_4$)$_2$, respectively. These compounds all display structural diversity attributable to the different coordination ability as well as the geometries of the counterions. Whereas [Cd(NO$_3$)$_2$($\textbf{L17}$)(CH$_3$OH)].CH$_3$OH and Cd($\textbf{L17}$)$_2$(DMF)$_2$.2ClO$_4$ exhibit photochromic behaviour, [Cd(SCN)$_2$($\textbf{L17}$)] does not. The photochromism, electron spin resonance (ESR) spectra and photoluminescence are shown in Figure 3.20. The role of counter anion interactions in NDI-containing frameworks has been shown using a series of coordination compounds based on Zn(II), Ag(I) and $\textbf{L20}$ which have been successfully synthesised and crystallographically characterised.[56]
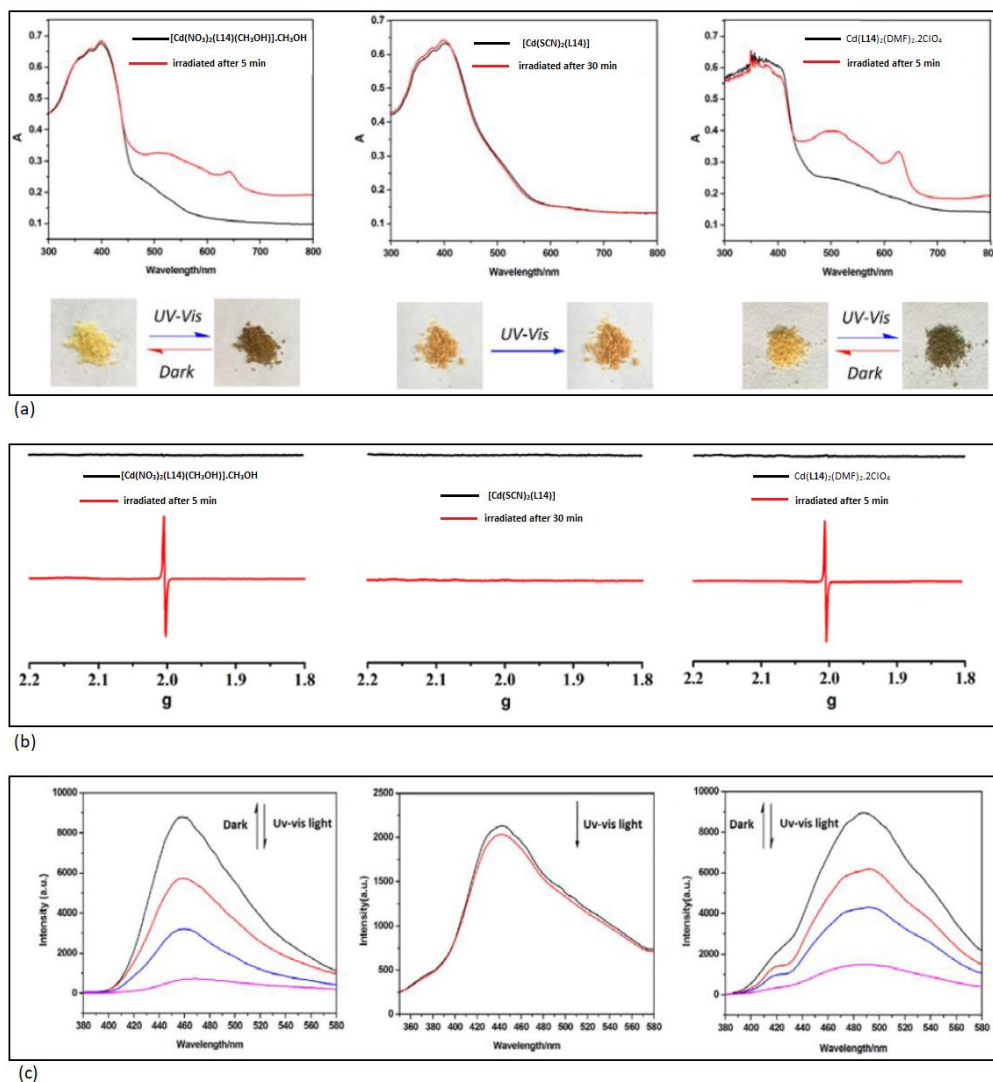
Figure 3.20: (a) UV−Vis diffuse reflectance spectra (with images of colour change); (b) ESR data; and the photocontrolled tunable luminescence performance spectra; for [Cd(NO$_3$)$_2$(**L17**)(CH$_3$OH)].CH$_3$OH (left), [Cd(SCN)$_2$(**L17**) (middle) and Cd(**L17**)$_2$(DMF)$_2$.2ClO$_4$ (right).[55]

Dincă and colleagues investigated and assigned an unexpected transition previously reported by Hupp and co-workers[11] for a Zn(II)-based MOF, Zn$_2$(2,6-NDC)$_2$(**L17**).[57] Combining photophysical measurements with constrained density functional theory, they were able to conclude that indeed the transition was an interligand charge transfer (CT) originating from π-stacked **L17**/2,6-NDC dimers instead of the alternative orthogonal pairs within the framework. This study underscores the need for incorporating synthetic strategies and

theoretical studies for better understanding of the nature of transitions occurring within this kind of framework materials. Further characterisation of this MOF using *in situ* solid state UV-Vis-NIR spectroelectrochemical techniques has been performed by D'Alessandro *et al*.[58] and the results provide evidence for the reduction of the neutral **L17** to the mono-anion radical which could in turn be reduced to the dianion species.

A similar DFT study on a Zn(II), 2,6-H_2NDC and **L18**-based coordination polymer, [(Zn(DMF)NO$_3$)$_2$(NDC)(**L18**)] has been carried out in which the compound was found to exhibit two accessible states as a result of the successive reduction of the core of **L18**.[59]

A MOF, [(Zn(DMF))$_2$(TTFTC)(DPNI)], reported by D'Alessandro and co-workers[60] was prepared by the solvothermal reaction of Zn(NO$_3$)$_2$.6H_2O, H_4TTFTC (tetrathiafulvalenetetracarboxylic acid) and **L17** in DMF. The MOF crystallizes in the monoclinic space group *P*2$_1$/*c* and the asymmetric unit comprises a Zn^{2+} ion tetrahedrally coordinated to half a TTFTC and **L17** ligand in addition to one DMF molecule. The packed structure of this framework reveals a diamondoid topology and some level of $\pi - \pi$ interaction between **L17** and TTFTC ligands (Figure 3.21). The incorporation of H_4TTFTC and **L17**, which are electron donor and acceptor respectively, in this framework facilitates a charge transfer within the crystalline structure. This charge transfer was investigated using various solid-state techniques such as UV-Vis-NIR, EPR, electrochemistry, Raman spectroscopy, in addition to Vis-NIR SEC and EPR SEC. Density functional theory (DFT) computational calculations were also performed to corroborate the results of the experimental studies. This MOF has been further investigated using *in situ* Raman spectroscopy techniques for

clearer understanding of the electronic behaviours.[61] This study can be extended to other redox-active MOFs for the elucidation of their electronic structures.
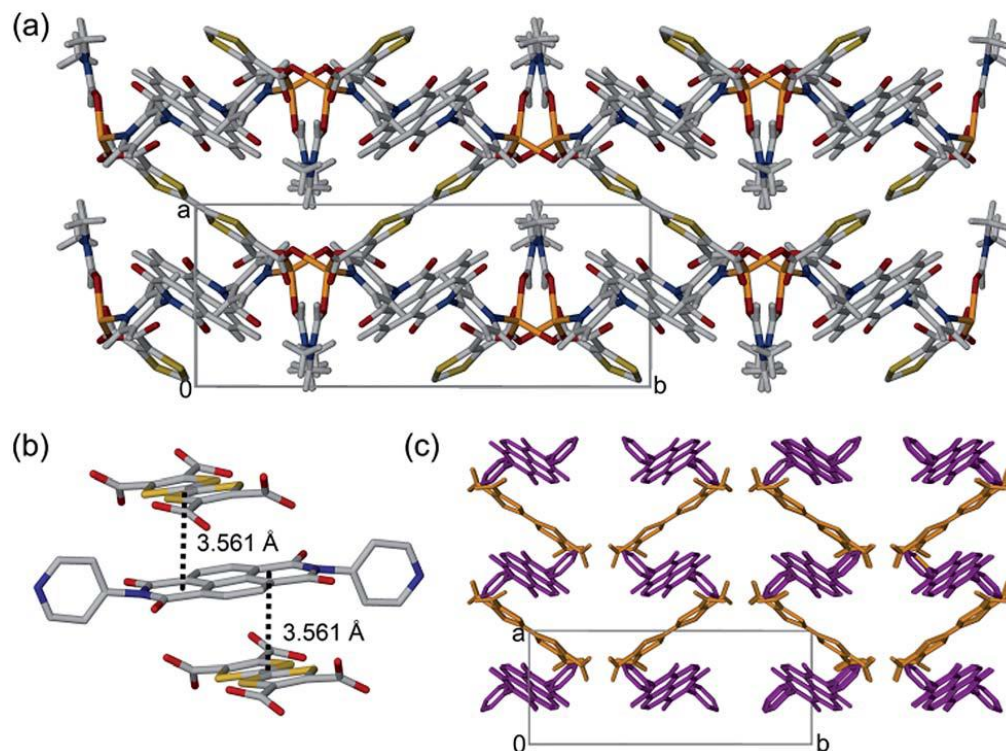
Figure 3.21: (a) Crystal structure of [(Zn(DMF))$_2$(TTFTC)(**L17**)] viewed down the crystallographic *c*-axis. (b) Stacking of the TTFTC and **L17** ligands C = grey; O = red; N = blue; S = yellow; Zn = orange. (c) Stacking of TTFTC (orange) and **L17** (purple) in a herringbone fashion. Hydrogen atoms and solvent have been excluded for clarity.[60]

A one-dimensional zigzag coordination polymer made from the reaction of 1:1 mixture of Pd(dppe)(TfO)$_2$ [dppe = ¼ 1,2-bis(diphenylphosphino)ethane] and **L17** (scheme 2) has been shown to exhibit high selectivity for F$^-$ ions in aqueous medium in the presence of other ions including Cl$^-$, Br$^-$, I$^-$, NO$_2^-$, NO$_3^-$, AcO$^-$, H$_2$PO$_4^-$ and PF$_6^-$.[62] Electrochemical studies involving UV-Vis spectroscopy and cyclic voltammetry show the suppression of the π-acidity of **L17** due to **L17**/TfO$^-$ interactions while Pd(II)-coordination of **L17** boosts its π-acidity.

Scheme 3.2: Synthesis of a Pd(II) and **L17**-based coordination polymer. The electrostatic potential (ESP) map of **L17** ligand shows electron rich (red) and deficient (blue) domains.[42]
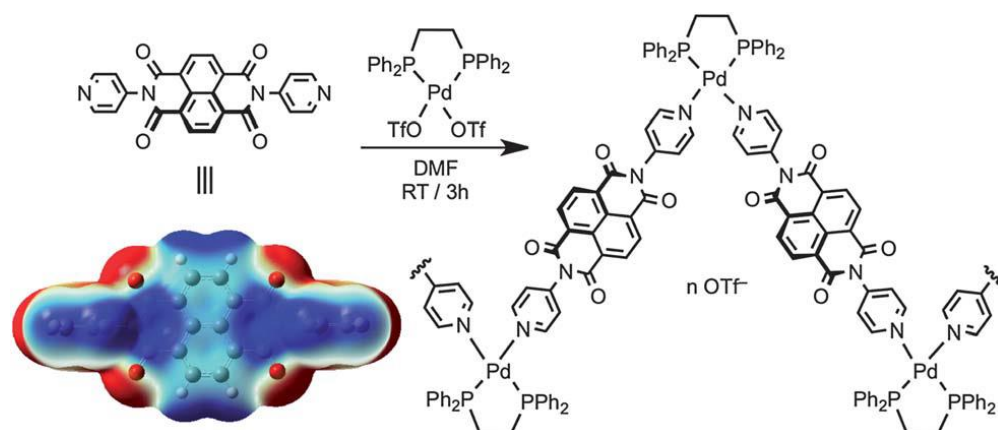
Two isomeric coordination polymers - [Cd(**L18**)(m-BDC)]$_n$ and [Cd(**L18**)(p-BDC)]$_n$ - based on Cd(II), m-H$_2$BDC (or p-H$_2$BDC) and **L18** have been structurally and spectroelectrochemically characterised.[63] Each of the isomeric forms exhibits different photochromic behaviour to that of the other. They both exhibit similar 2D structures which extend into 3D structures owing to the presence of several interactions such as CH–π, π–π and lone pair–π interactions. The UV-Vis spectra and the interactions in [Cd(**L18**)(m-BDC)]$_n$ and [Cd(**L18**)(p-BDC)]$_n$ are shown in Figure 3.22.
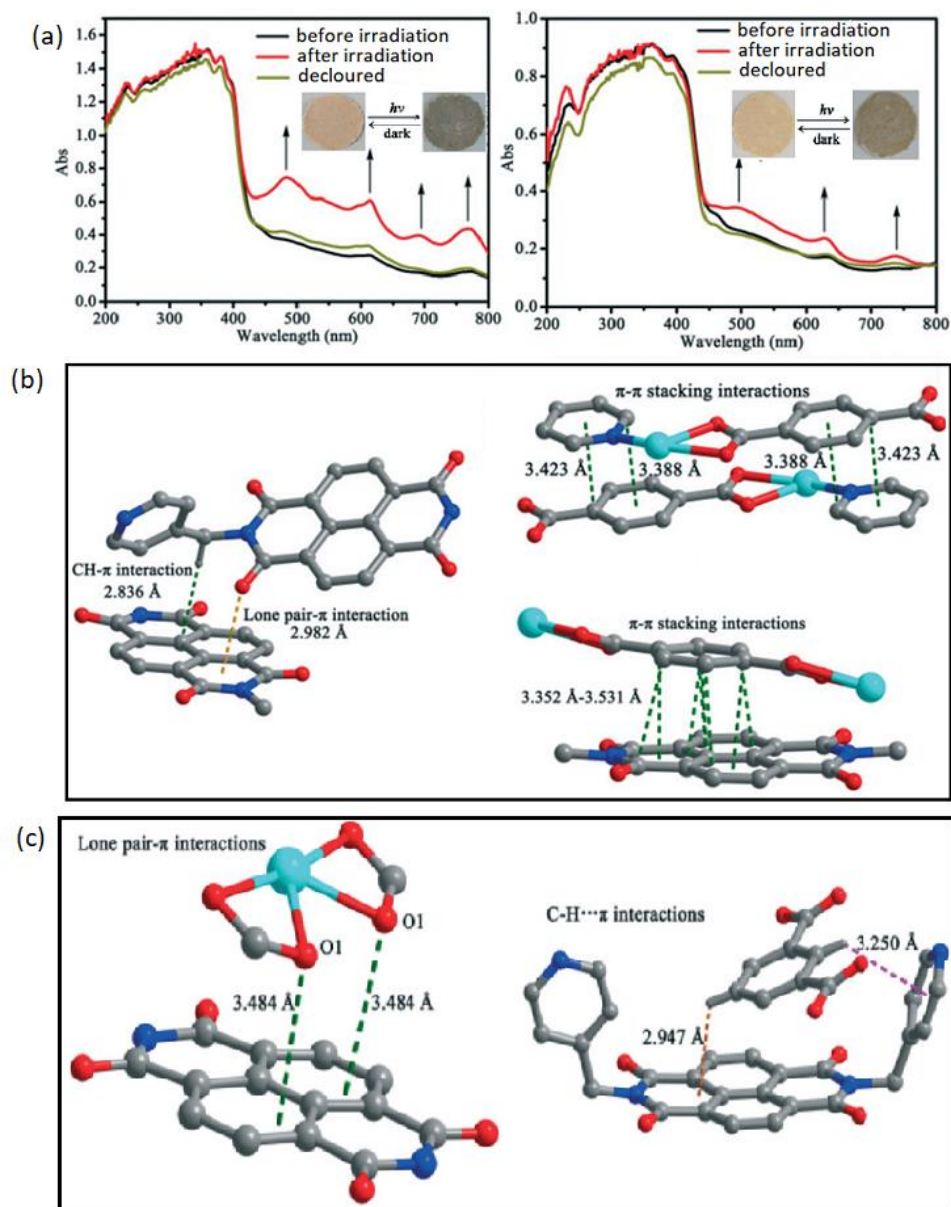
Figure 3.22 (a) UV-vis spectra and photographs showing photochromic behaviours of [Cd(**L18**)(*m*-BDC)]$_n$ (top left) and [Cd(**L18**)(*p*-BDC)]$_n$ (top right) with photographic images showing colour change upon irradiation. (b) Different interactions in [Cd(**L18**)(*p*-BDC)]$_n$ (c) Different interactions in [Cd(**L18**)(*m*-BDC)]$_n$.[63]

Demets and co-workers have successfully shown that a MOF (Fig. 18a) constructed by solvothermally reacting Co(NO$_3$)$_2$·6H$_2$O, **L17** and H$_2$BDC could act as a light-modulated electrical semiconductor.[64] This material is highly crystalline, electrochemically active, electrically semiconducting and photoactive. An electronic device was also fabricated to study the

electrical/photoelectrical conductivity in this MOF (Figure 3.23). Using this four-point device, the semiconductivity of the MOF was measured by direct voltage bias and the observed anisotropic electrical semiconduction showcases a photoresistive–photoresponsive dual behaviour producing an exceptionally high responsivity of $2.5 \times 10^5 \, \text{A W}^{-1}$. This work unarguably opens a new front in MOF devices development. Another study by Saha and co-workers has demonstrated that by encapsulating complementary π-systems such as π-acid methyl viologen guests in a redox-active MOF based on Zn(II), TCPB (TCPB = 1,2,4,5-tetrakis-(4-carboxyphenyl)benzene) and **L21**, the electrical conductivity can be substantially enhanced due to the formation of extended π-stacks with the redox-active ligands.[65]
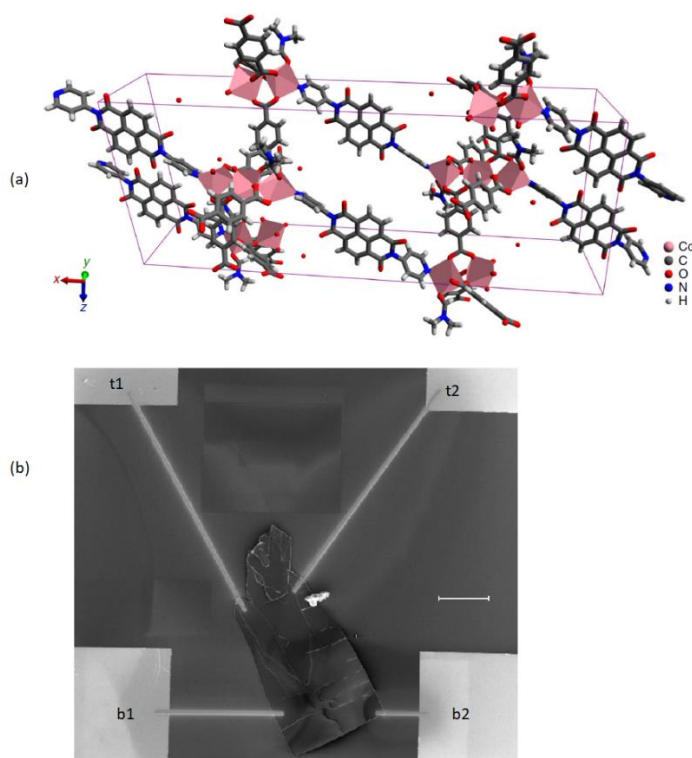
Figure 3.23 (a) Crystal structure of Co-**L17**.BDC MOF showing the unit cell. The unit cell belongs to the monoclinic space group C2/c, water was modelled at 1/4 occupancy and its hydrogens are omitted for clarity. (b) SEM image of the device used in all electrical and photoelectrical characterisations. It consists of a *p*-Si/SiO$_2$ wafer onto which the MOF single crystal is connected to Au pads, labelled t1, b1, t2 and b2, by deposited Pt electrodes. Scale bar = 100 μm.[64]

A MOF constructed by slow diffusion of an ethanol solution of $ZnSiF_6 \cdot 6H_2O$ into an NMP (N-methylpyrrolidin-2-one) solution of **L17** have been reported to be interpenetration-free.[66] The absence of interpenetration was attributed to the deliberate imposition of lone pair-π interactions using molecules that possess lone-pairs such as NMP on the one hand and iodine as guest molecules on the other hand. The crystal structure of the material confirms that it is, indeed, a non-interpenetrated cuboid three-dimensional framework crystallising in the tetragonal space group *P*4*/mmm* as shown in Figure 3.24a. Further work on this MOF was performed by Dai and colleagues[67] in which naphthalene was incorporated as a guest molecule, transforming the crystals from being weakly emissive to orange-emissive (Figure 3.24b). The resulting host-guest system was employed as sensor for various organic amines including triethyl amine, diethyl amine, aniline and hydrazine.
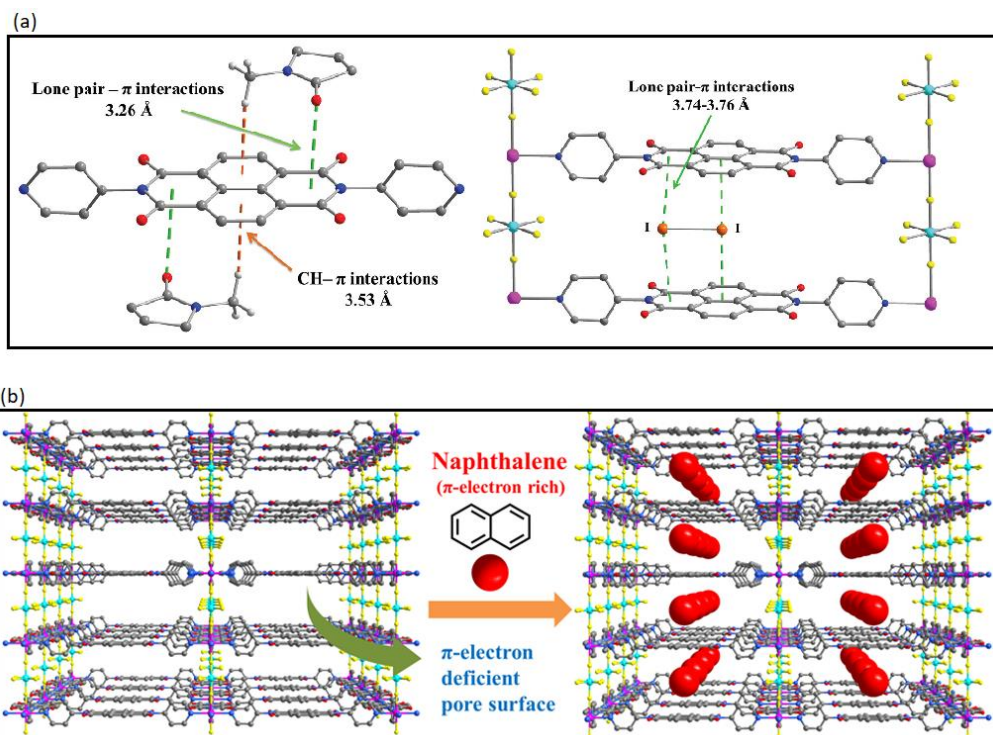
Figure 2.24: (a) Lone pair-π interactions in Zn-**L19** that prevented the potential interpenetration.[66] (b) The encapsulation of naphthalene into Zn-**L19** that converted the otherwise weakly emissive material into a highly (orange) emissive material.[67]

Three coordination polymers based on Ni(II) and **L17** have been synthesized and crystallographically characterised.[68] While the direct solvothermal reaction of Ni(NO$_3$)$_2$.6H$_2$O with **L17** in DMF resulted in a one-dimensional coordination polymer ([Ni(**L17**)$_2$.4DMF]$_n$), carrying out the same reaction with the addition of H$_2$BDC or 2,6-H$_2$NDC produced 2D framework materials, ([Ni$_2$(NO$_3$)$_2$(BDC)$_2$(**L17**)$_2$]$_n$) or ([Ni$_2$(NO$_3$)$_2$(2,6-NDC)$_2$(**L17**)$_2$]$_n$). Whereas [Ni(**L17**)$_2$.4DMF]$_n$ crystallizes in the tetragonal space group *I*-42*d*, the other two prefer the triclinic space group *P*-1. Further examination of the crystal structures revealed some degree of lone pair-π and π-π interactions in all of the compounds.

A set of nine coordination polymers, three of which were made from the reaction of **L18** with Mn(II), Co(II) or Cd(II), have been structurally elucidated.[69] The results revealed that the structure as well as the topology of complexes are

dictated by the conformation and coordination mode of organic linkers and the coordination geometry of metal centres. The photoluminescence properties of the materials were also investigated.

The flexibility of **L18** in coordination compounds has been studied in five coordination polymers formulated as $\{[Cu(\mathbf{L18})_2(NO_3)_2].2CHCl_3\}_n$, $\{[Cu(\mathbf{L18})_2(NO_3)_2].3C_7H_8\}_n$, $[Cu(\mathbf{L18})_2(CF_3SO_3)(H_2O)].CF_3SO_3.H_2O.CH_3OH\}_n$, $[Cd(\mathbf{L18})_2]_n.n\mathrm{SiF}_6.x(CH_3OH).y(CHCl_3)]_n$ and $[Zn(\mathbf{L18})_2(CF_3SO_3)_2]_n.x(\text{solvent}).$[70] By varying the metal centres, anions and solvents, **L18** can take on either *Z* or *U*-mode conformations to assemble 4-connecting metal nodes stretching either in a plane or in three dimensions, giving rise to 2D bat-like or dumbbell-like (4,4)-sql topological or 3D dia- type building units (see Figure 3.25).
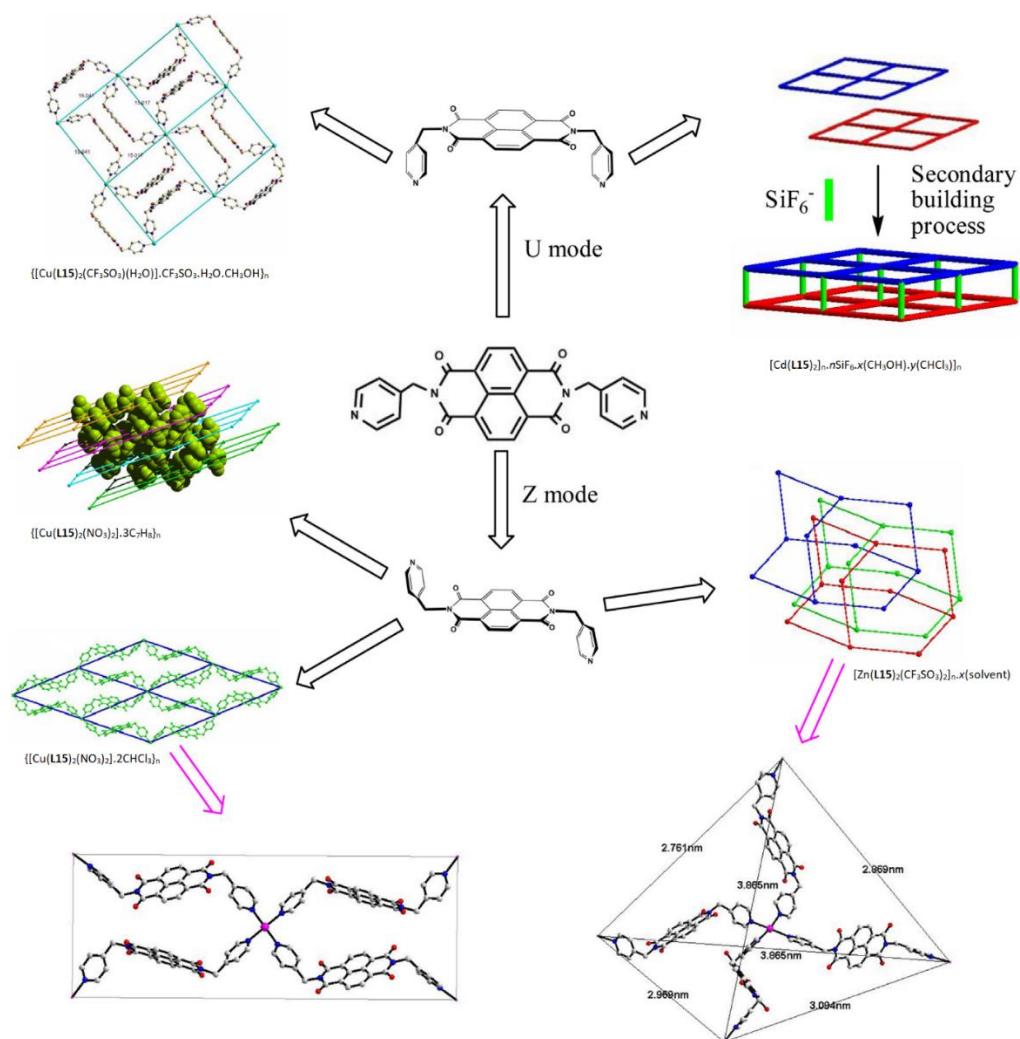
Figure 3.25: Structural flexibility of **L18** in MOFs.[70]

Two photochromic coordination polymers namely [Zn$_2$(**L22**)(TPDC)$_2$] and [Cd$_6$(**L20**)(TPDC)$_6$(DMF)$_6$] have been solvothermally prepared by the reaction of a mixture of TPDC (thiophene-2,5-dicarboxylic acid), **L22** and the corresponding metal salt (Zn(NO$_3$)$_2$.6H$_2$O or Cd(NO$_3$)$_2$.4H$_2$O).[71] Crystallising in the monoclinic space group *C*2/*c*, the asymmetric unit of the Zn-based material comprises one Zn^{2+} ion, one deprotonated TPDC^{2-} linker and a half **L22** ligand with each TPDC^{2-} ligand acting as a μ$_4$-linker, connecting two paddle wheel [Zn$_2$(COO)$_4$] units. Two nitrogen atoms from the pyridine ends of two **L22** ligands are situated at the apical positions of the [Zn$_2$(COO)$_4$] units. The

Cd-based structure on the other hand chooses to crystallise in the monoclinic space group $P2_1/c$ with three independent Cd^{2+} environments. The coordination around the metal centres and the packed structures for both materials are shown in figure 21. EPR measurements reveals that these materials generate the **L22**$^{\bullet-}$ radicals upon irradiation.
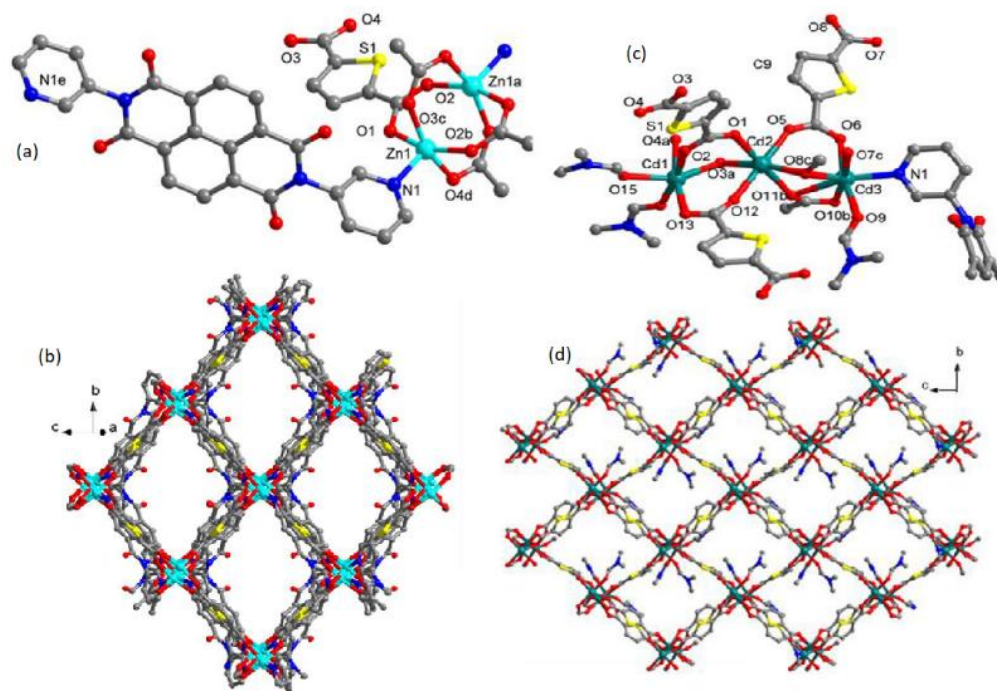
Figure 3.26: (a-b) Crystal structure of [Zn$_2$(**L22**)(TPDC)$_2$] showing coordination environment of Zn^{2+} ion and the 3D structure. (c-d) Crystal structure of [Cd$_6$(**L22**)(TPDC)$_6$(DMF)$_6$] indicating the coordination environment of Cd^{2+} ions and the 2D layer viewed along the *bc*-axis.[71]

Three isostructural one-dimensional coordination polymers, [ZnX$_2$(**L17**)] (X = Cl, Br or I) have been reported to exhibit different photochromic properties owing to different lone pair–π interactions between the capped halogen atoms and **L17** moieties.[72] This study was able to show the link between the strength of lone pair- π and the resultant photochromic behaviour of coordination polymers; thereby serving as a reference work for design of photochromic materials.

3.2.3 Azolate-based NDI Metal-organic Frameworks

A few MOFs containing azolate-based NDIs have been reported in the literature. The points of coordination to the metals are usually the nitrogen atoms of the azolate groups attached as imide substituents to the NDI. Two of these subclass of NDI linkers are shown in Figure 3.26.

(X = H, SEt, NHEt)

L24

L25
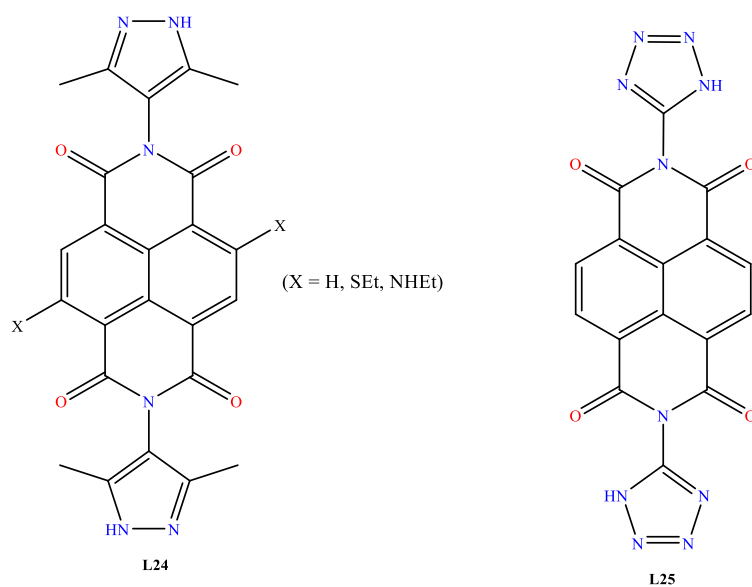
Figure 3.25: Structures of two azolate-bearing NDIs used in MOFs synthesis

Three pyrazolate-based NDI linkers (**L24**: X=H, NHEt or SEt**)** have been used in conjunction with Zn to form the corresponding MOFs which were obtained as microcrystalline powders. Analysis of the powder patterns revealed that the MOFs are isostructural 2D materials composed of infinite chains of tetrahedral Zn^{2+} ions bridged by pyrazolate groups.[73,74] The first report on these MOFs features an investigation into the hydrophilicity of these framework structures before and after post-synthetic oxidation and the results show a shift from being hydrophobic (as-synthesised) to being hydrophilic upon post-synthetic oxidation (Figure 3.26). The thin films of these MOFs on FTO were later employed in the spectroelectrochemical characterization.[73] The cyclic voltammograms and the UV-Vis spectra are shown in Figure 3.26b and 3.26c respectively.
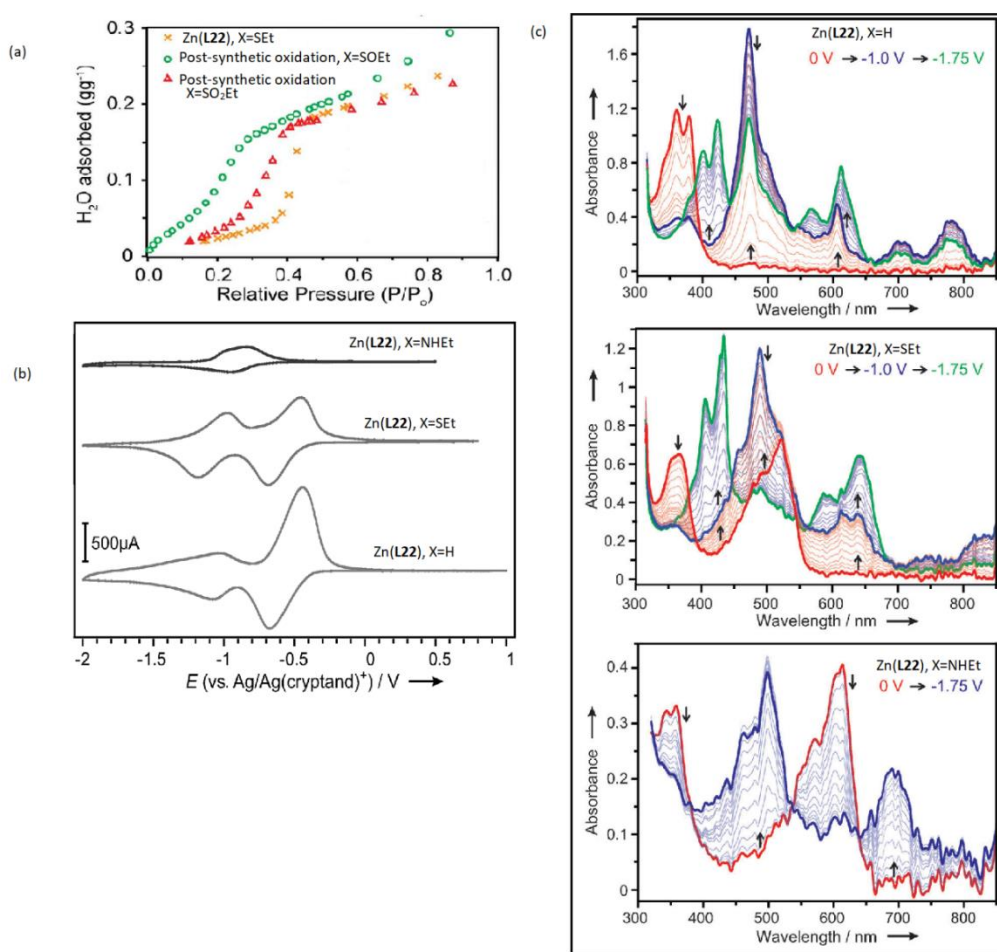
Figure 3.26: (a) H₂O adsorption isotherms for Zn(**L24**), X=Set before after post-synthetic oxidation measured at 77 K and 293 K (b) Cyclic voltamogramms of Zn(**L24**), X=H, SEt or NHEt. (c) Transmission UV/Vis spectra for Zn(**L24**), [X=H, SEt or NHEt] films on FTO substrates in DMF solution containing 0.1m [(nBu)₄N]PF₆. UV/Vis absorption spectra were collected at 6 s intervals during the cathodic scan (10 mVs_1) of a CV measurement. All potentials are measured versus a Ag/Ag(cryptand)+ reference electrode.[73,74]

Three 3D pyrazolate-based MOFs, prepared by the solvothermal reactions of **L24** (X=H), Cd²⁺ ion and the respective carboxylic acid, namely terephthalic acid (H₂BDC), 2-aminoterephthalic acid (NH₂-H₂BDC), or 2,6-naphthalenedicarboxylic acid (2,6-H₂NDC), were found to exhibit to different degrees of interpenetration attributable to the shape and size/length of the second carboxylic linker.[75] The frameworks containing H₂BDC (Figure 3.27) and NH₂-H₂BDC have 5-fold interpenetration while that made with 2,6-H₂NDC is a 4-

fold (2+2) interpenetrated network. Two of the MOFs were reported to possess reversible photochromism upon light irradiation. Four other tetrazolate (**L25**)-based coordination compounds – one based on Zn(II)[76] and three based on Cd(II)[77] - have been structurally characterized; the framework based on Zn(II) exhibits both photochromic and electrochromic behaviours upon irradiation.
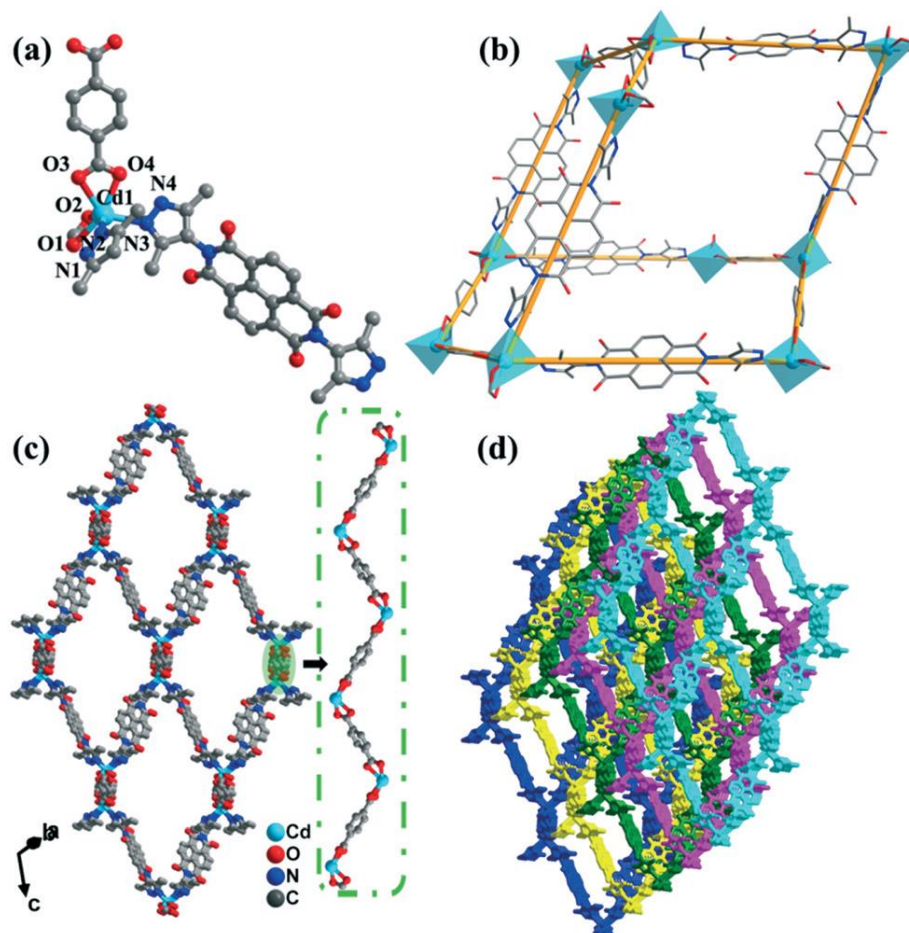
Figure 3.27 Structure of [Cd(**L24**; X=H)$_2$(BDC)$_2$]$_n$ showing (a) Local coordination environment of Cd(II) atoms; (b) perspective view of a single *dia* unit cage; (c) 3D single *dia* framework with 1D zigzag {Cd(COO)}$_n$ chain showing the 1D channels; (d) representation of 5-fold interpenetrating (five different 3D nets are shown in five different colors). H atoms have been omitted for clarity.[75]

3.2.4 N-oxydic Pyridyl Naphthalenediimide containing Coordination Polymers

Four lanthanide (Ln = Eu, Gd, Dy, Er) coordination polymers based on **L23**, formulated as $\{[Ln(\mathbf{L23})_{1.5}.(NO_3)_3].MeOH\}_n$ have been hydrothermally synthesised and crystallographically characterized.[78] It was revealed, on analysis of the single crystal structure, that all the compounds are isomorphic and that each metal centre is surrounded by nine O atoms in a distorted tricapped trigonal–prismatic geometry (Figure 3.28a). In each of the network structures, two metal centres are bridged by two *cis* **L23** to form a ring, which is further bridged by *trans* **L23** to generate 1D chains. π-π stacking is observed between pyridine rings of neighbouring chains (Figure 3.28b) and π-π interactions between naphthalene rings of **L23** (Figure 3.28c) resulting in a 2D and the final 3D supramolecular network respectively.
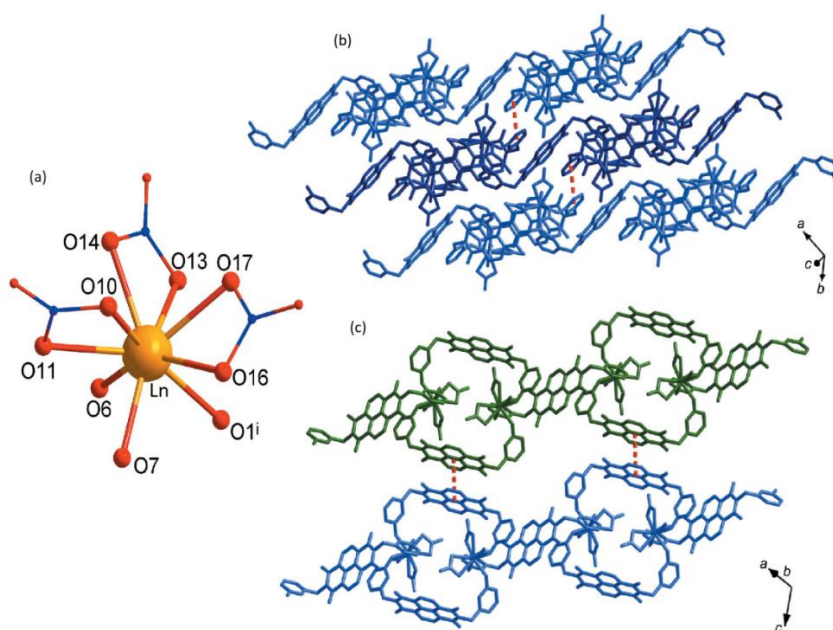
Figure 3.28 (a) Coordination environment of Ln^{3+} (Ln = Er, Dy, Gd, Eu) in $\{[Ln(\mathbf{L23})_{1.5}.(NO_3)_3].MeOH\}_n$ (b) The π-π interactions (red dashed lines) between pyridine rings. (c) The π-π interactions between L23 units. H atoms have been omitted for clarity.[78]

3.3 Results and Discussion

As explained earlier, the MOFs that shall be discussed in this chapter are those constructed from **DPNDI**, **DPPNDI** or **DPPPDI** while those prepared using **DNNDI** shall be reported in the next chapter. Most NDI ligands are insoluble in common organic solvents. For instance, **DPNDI** – one of the most widely used in MOF synthesis – is highly insoluble in common organic solvents such as DCM, chloroform, acetone, diethyl ether, etc. This insolubility is related to the strong π-π interactions between neighbouring NDI moieties. However, they are able to dissolve in electron-rich, aprotic solvents such as dimethylformamide (DMF), dimethylacetamide (DMA), diethylformamide (DEF) and 1-Methyl-2-pyrrolidone (NMP). The good solubility in these solvents may be attributed to their high polarity and could be related to the formation of lone pair–π interactions between the solvents and the NDI π-acceptors during dissolution.[47] It is worth mentioning that **DPPNDI** and **DPPPDI** are readily soluble in common organic solvents like DCM, chloroform, acetone, etc; thereby making them useful for other applications aside from MOF preparation. Each of the MOFs, as will be seen shortly, were synthesised by using either $Ni(NO_3)_2.6H_2O$ or $Co(NO_3)_2.6H_2O$ in conjunction with two ligands (an NDI or PDI and a carboxylic acid) under solvothermal conditions at $100\,^{\circ}C$ using DMF or DEF as solvent. In each of the MOFs, the carboxylic acid in combination with the metal ions, produces a two-dimensional sheet which is transformed into a three-dimensional framework structure by the PDI or NDI acting as a pillar; hence these MOFs can be described as pillared-layer MOFs. Many combinations of the metal salts above with the named ligands were tried and the feasibility or otherwise in making the intended MOFs have been shown for future reference

(see Table 3.2). Several attempts (including varying reaction conditions such as solvent, mole ratios of reactants, temperature and reaction time) made to prepare the Ni(II) MOFs using DPPNDI and NDC^{2-} did not yield any positive results. The reason that the Ni^{2+} analogues did not form MOFs is not yet understood. This section will start with the NDI-containing MOFs and will be wrapped up with the PDI analogues. A total of seven MOFs will be presented in this section. All the MOFs have been crystallographically and their electronic properties characterised and the results of these studies are presented herein.

Table 3.2 Summary of results of DPPNDI/DPPPDI MOF syntheses

Metal ion/Ligand combination	Co(II)	Ni(II)
DPNDI + NDC^{2-}	✓	Reported[68]
DPPNDI + $BPDC^{2-}$	✓	✓
DPPNDI + NDC^{2-}	✓	✗
DPPPDI + $BPDC^{2-}$	✓	✗
DPPPDI + NDC^{2-}	✓	✗

3.3.1 NDI MOFs

3.3.1.1 Synthesis and crystal structure of [Co(NDC)(DPNDI)(NO₃)]. 2.5DMF (1)

Crystals of **1** suitable for a single crystal X-ray diffraction experiment were grown via the solvothermal reaction of $Co(NO_3)_2.6H_2O$ with DPNDI and H_2NDC in a 20-ml scintillation vial using DMF as the solvent. The reaction lasted for 24 h in an oven which temperature was set at 100 °C. The crystal was kept at 120 K during data collection on a single crystal diffractometer. Using

Olex-2,[79] the structure was solved with the SHELXT[80] structure solution program using Intrinsic Phasing and refined with the SHELXL[81] refinement package using Least Squares minimisation. The crystal data and refinement parameters for **1** are given in Table 3.3.

Table 3.3 Summary of crystal data and structure refinement of **1**.

Empirical formula	$[C_{30}H_{15}CoN_5O_9].$ 2.5 DMF
Formula weight	648.4
Temperature/K	120(2)
Crystal system	triclinic
Space group	P-1
a/Å	11.0912(10)
b/Å	11.4480(11)
c/Å	16.0382(9)
α/°	86.464(6)
β/°	88.819(6)
γ/°	66.924(9)
Volume/Å^3	1869.9(3)
Z	2
ρ_{calc}g/cm^3	1.152
μ/mm^{-1}	4.033
F(000)	658
Crystal size/mm^3	$0.32 \times 0.136 \times 0.094$
Radiation	Cu Kα (λ = 1.54184)
2θ range for data collection/°	8.41 to 150.47
Index ranges	$-9 \leq h \leq 13, -12 \leq k \leq 14, -19 \leq l \leq 19$
Reflections collected	13688
Independent reflections	7433 [R_{int} = 0.0528, R_{sigma} = 0.0623]
Data/restraints/parameters	7433/487/424
Goodness-of-fit on F^2	1.112
Final R indexes [I>=2σ (I)]	R_1 = 0.1131, wR_2 = 0.2797
Final R indexes [all data]	R_1 = 0.1230, wR_2 = 0.2955
Largest diff. peak/hole / e Å^{-3}	2.54/-0.95

The asymmetric unit of **1** shown in Figure 2.4 consists of an atom of Co, a nitrate ion, a DPNDI molecule, a half of an NDC unit, 2.5 DMF molecules and a molecule of water. A solvent mask was calculated using PLATON SQUEEZE[82] and 194 electrons were found in a volume of 747 Å^3 in 1 void per unit cell. This is consistent with the presence of 2.5 molecules of DMF per asymmetric unit which account for 200 electrons per unit cell. Four of the carbon atoms of the naphthalene core for the NDC are disordered over two positions with 60:40 occupancy.
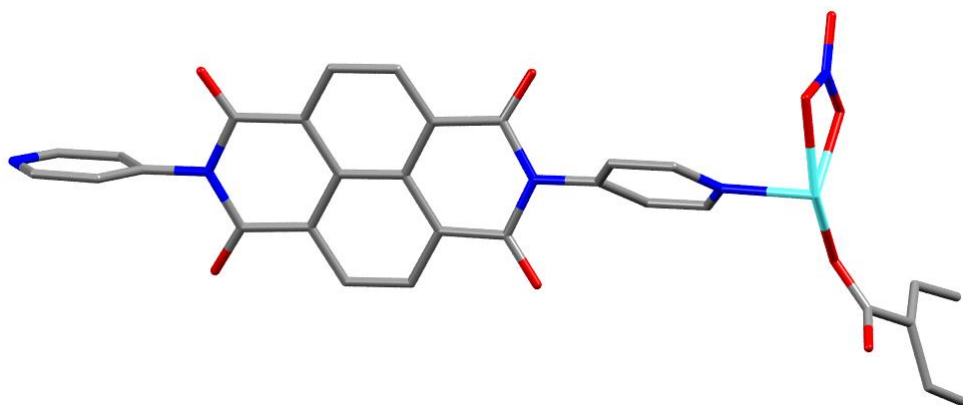
Figure 3.29: The asymmetric unit of **1**. (grey = C, turquoise = Co, red = O and blue = N). For clarity, uncoordinated solvent molecules, disordered carbon atoms of the NDC at 40% occupancy and H atoms have been omitted.

Mercury software[83] was used to further analyse the structure of **1.** The extended structure of **1** (Figure 3.30a) reveals two Co^{2+} centres, each of which is coordinated to a full NDC^{2-} and two molecules of **DPNDI**. Compound **1** is a novel, porous, non-interpenetrated two-dimensional framework having, as determined by ToposPro,[84] the **sql** topological net with the point symbol $\{6^4.4^2\}$ as shown in Figure 3.30b. It is worth mentioning that although **1** is not a paddlewheel MOF, this net is quite common among two-dimensional paddlewheel MOFs constructed from metals such as Ni, Co, Zn, Cu, Fe, etc. and can be described as the assembly of squares – essentially made up of 4-c

vertices.[85] Compound **1** crystallises in the triclinic space group P-1. The Co(II) centre is six-coordinate and adopts a distorted octahedral geometry, which is expected given the chelating nature of the bound nitrate group (Figure 3.30a). The nitrate groups also prevent the growth of **1** along the terminal k^2-nitrate direction, thereby stopping it from becoming a three-dimensional framework. It is important to mention that nickel analogue of **1** has been reported previously by our research group.[68] Each cobalt ion is bound to a single nitrate group that occupies two coordination sites, nitrogen atoms from two separate **DPNDI** ligands are positioned at opposite sides of the distorted octahedron and to single oxygen atoms from two separate naphthalene dicarboxylates, such that each assumes a μ_2 bridging mode, connecting two Co(II) centres to give rise to a paddlewheel-like SBU, $\{[M(k^2\text{-}O_2NO)]_2(\mu^2\text{-}O_2CR)_2\}$ (Figure 3.30a).
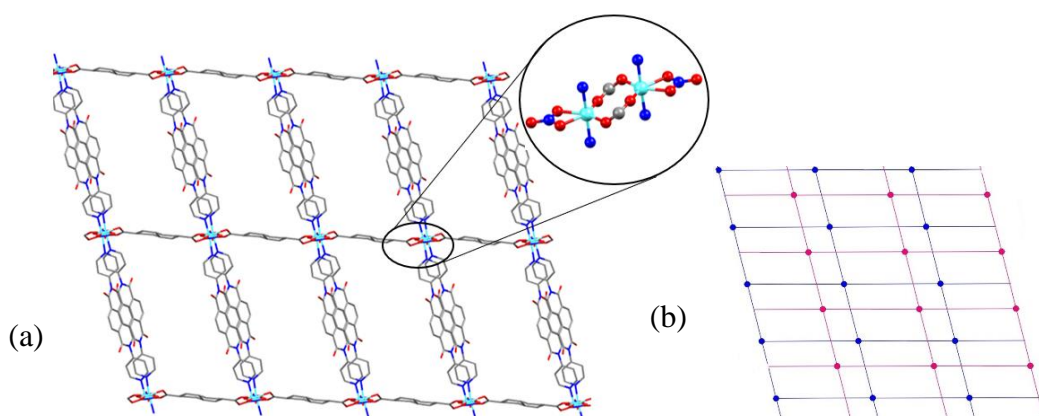
Figure 3.30 (a) packed structure of **1** showing the rectangular channels and the coordination environment around the metal centre; (grey = C, turquoise = Co, red = O and blue = N). Hydrogen atoms and disordered solvent molecules have been excluded for clarity. (b) the *sql* net showing two neighbouring two-dimensional lattices (in blue and red) of **1**.

The rigidity of the inorganic building unit in **1** ensures that two adjacent **DPNDI** units stack directly facing one another, giving rise to a bi-pillared layered framework that has rectangular channels (12.43 Å x 19.69 Å). The **DPNDI** is the longer side while the NDC^{2-} is the shorter of the rectangular channels. The

Co-N bond lengths of 2.148(4) Å and 2.137(4) Å are in consonance with those reported for similar framework materials in the literature.[68] Similarly, the Co-O bond lengths are self-consistent ranging from 1.997(3) Å to 2.198(4) Å. The bond angles made by O and N with either Co1 or Co2 are around 90° ranging from 87.49° to 97.30°. (see the appendix section for the full list of bond lengths and angles). The dihedral angles between the pyridyl rings and the naphthalene core of the **DPNDI** linker are 52.75° and 78.72°. Some interactions that are inherent in **1** include π-π interactions between adjacent **DPNDI** moieties and lone pair-π interactions as shown in Figure 3.31. The π-π and the lone pair distances of 3.523 Å and 3.208 Å respectively are in agreement with those for **DPNDI** containing MOFs in the literature.[47,86] While the π-π interaction is intramolecular, the lone pair- π interaction, however, is intermolecular and has a wider implication of transforming the entire structure of **1** into a three-dimensional network.
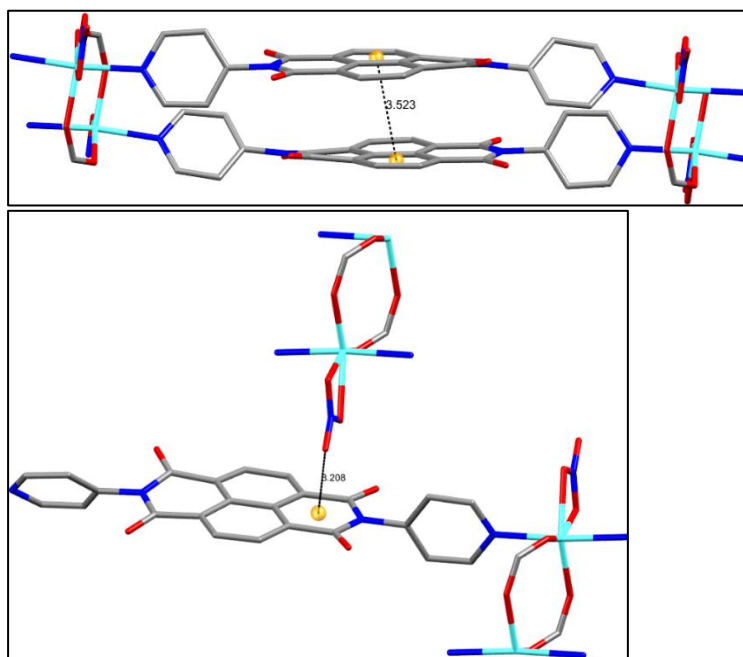
Figure 3.31: π-π interaction (top) and lone pair-π interaction (bottom) in **1**. The centroids are shown in orange spheres and the distances in dashed lines. (grey = C, turquoise = Co, red = O and blue = N). Hydrogen atoms and disordered solvent molecules have been excluded for clarity.

3.3.1.2 Synthesis and crystal structure of [Co$_2$(NDC)$_2$(DPNDI)$_2$].7DMF (2)

The framework of **2** was made using a similar method and reagents to that for **1** except that the mole ratios of the starting materials were different. Compound **2** was serendipitously made during an attempt to obtain a pure phase of **1**. During the synthesis of **1**, it was observed that, in addition to the pink needle-like crystals of **1**, there were also a trace amount of dark green crystals. By varying the mole ratios of the starting materials, a pure phase of **2** was obtained. It is equally worth mentioning that a year after the successful synthesis in our lab, **2** was reported by Han *et al*.[53] However, the synthetic approaches are different. For the literature report of **2** for instance, 0.04 mmol of Co(NO$_3$)$_2$·6H$_2$O, 0.2 mmol of **DPNDI** and 0.2 mmol H$_2$NDC were mixed together and dissolved in a mixed solvent system consisting of 12 mL DMF and 4 mL CH$_3$OH. The resulting solution was stirred at room temperature for 10 min, transferred into a Teflon-lined reactor and sealed in a 23-mL stainless steel autoclave, and heated at 80 °C for 5 d in an oven. For the current study, on the other hand, a mixture of Co(NO$_3$)$_2$·6H$_2$O (23 mg, 0.08 mmol), DPNDI (44 mg, 0.104 mmol) and H$_2$NDC (44 mg, 0.204 mmol) were dissolved in 4 mL DMF in a 20-mL scintillation vial. The solution was stirred for about 5 min, the vial was tightly capped and heated in an oven at 100 °C for 24 h to yield dark green crystals of **2**. Another key difference is that the reported structure of **2** crystallizes in the triclinic space group P-1, but the version presented in the current study crystallizes in the chiral monoclinic space group P2$_1$ with higher crystallographic data quality as shown in Table 3.4.

Table 3.4 Comparison of crystal data of 2.

Parameters	Current study	Reported reference 53
Empirical formula	$[Co_2(NDC)_2(DPNDI)_2].7DMF$	$\{[Co_2(DPNDI)(2,6\text{-}NDC)_2]\cdot 7(DMF)\}_n$
Temperature/K	120.00(10) K	298 K
Crystal system	monoclinic	Triclinic
Space group	$P2_1$	P -1
a/Å	13.0219(5)	13.1010(12)
b/Å	22.0970(7)	13.1601(13)
c/Å	13.1042(6)	22.320(2)
α/°	90	85.9070(10)
β/°	103.039(4)	89.455(2)
γ/°	90	78.485(2)
Volume/Å³	3673.5(2)	3761.1(6)
Z	2	2
ρ_{calc}g/cm³	1.334	0.853
μ/mm⁻¹	0.528	0.482
F(000)	1534	980
Crystal size/mm³	$0.149 \times 0.132 \times 0.085$	-
Radiation	Mo Kα (λ = 0.71073)	Mo Kα (λ = 0.71073)
2θ range for data collection/°	6.222 to 57.376	4.86 to 50.04
Index ranges	$-15 \leq h \leq 17, -29 \leq k \leq 27, -17 \leq l \leq 16$	-
Reflections collected	64075	12934
completeness	99.80%	97.40%
Independent reflections	16406 [R_{int} = 0.0610, R_{sigma} = 0.0638]	-
Data/restraints/parameters	16406/553/924	12938/1/688
Goodness-of-fit on F^2	1.073	1.005
Final R indexes [I>=2σ (I)]	R_1 = 0.0518, wR_2 = 0.1137	0.1219, 0.2733
Final R indexes [all data]	R_1 = 0.0745, wR_2 = 0.1259	0.2038, 0.2997
Largest diff. peak/hole / e Å⁻³	0.70/-0.43	0.72, -1.13
Flack parameter	0.442(16)	-

The asymmetric unit of **2**, as shown in Figure 3.32a, comprises two crystallographically independent Zn^{2+} centres, two NDC^{2-} units, a **DPNDI** molecule and seven molecules of DMF trapped in the pore.
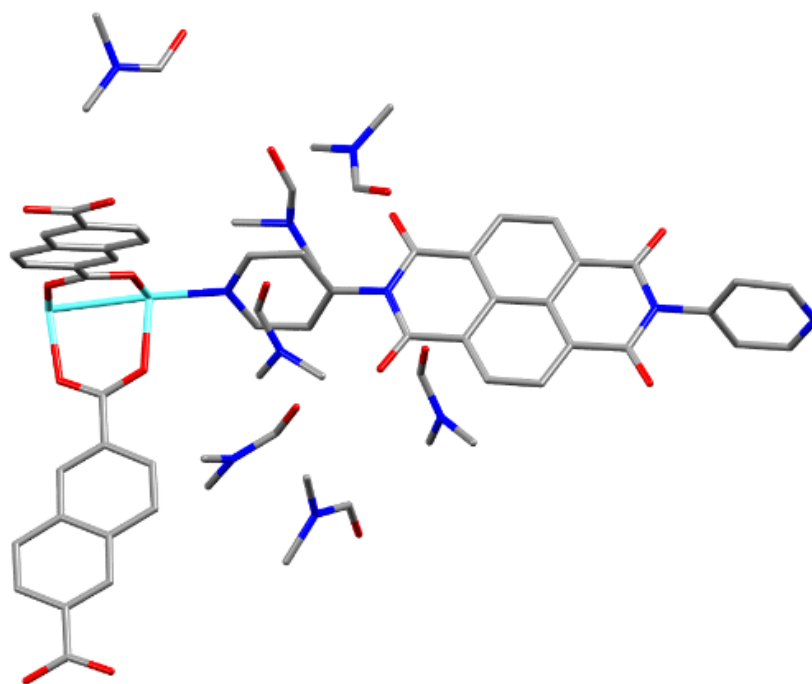
Figure 3.32: Structure of **2** showing the symmetric unit. (grey = C, turquoise = Co, red = O and blue = N). Hydrogen atoms molecules have been excluded for clarity.

The grown structure indicates that **2** possesses the $M_2(\mu_2\text{-}O_2CR)_4$ paddlewheel SBU in which four different carboxylate units of NDC building blocks are bonded to two cobalt atoms in a bis-bidentate fashion resulting in two-dimensional sheets. These dinuclear SBUs are coordinated by two **DPNDI** linkers, forming a three-dimensional paddlewheel pillared MOF. This arrangement of the ligands around the cobalt cations are illustrated in Figure 3.33.
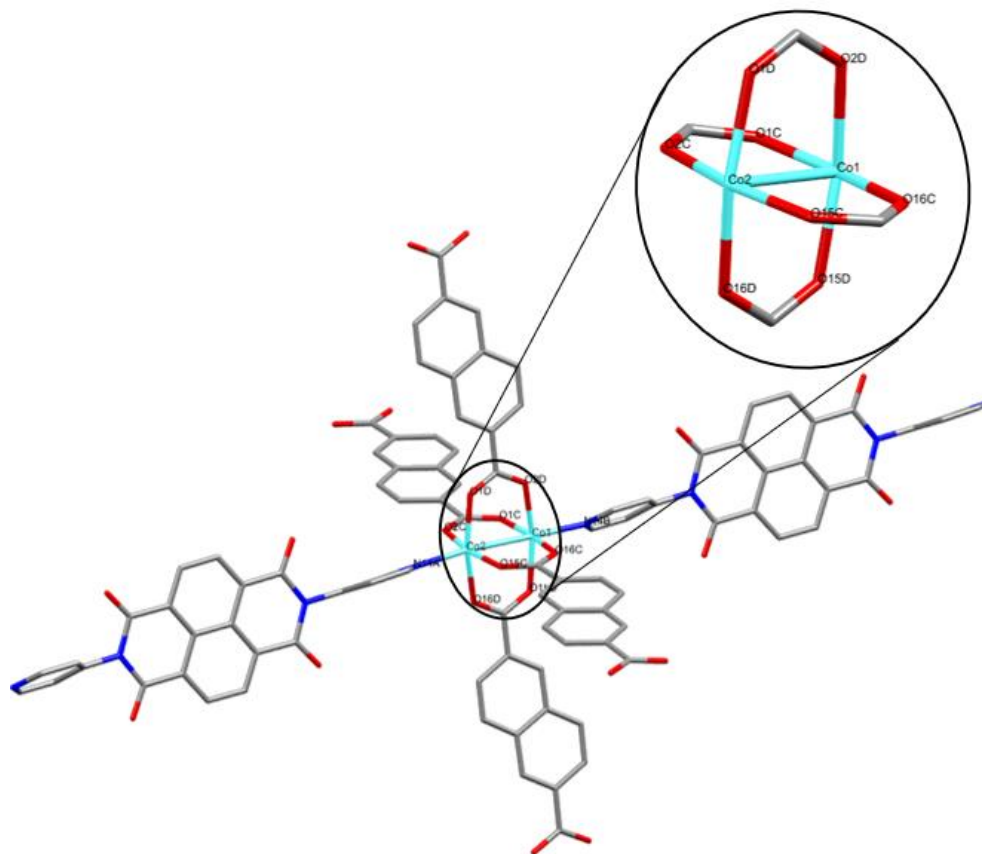
Figure 3.33: Coordination environment around the metal centres. The insert shows the $M_2(\mu_2\text{-}O_2CR)_4$ paddlewheel SBU. (grey = C, turquoise = Co, red = O and blue = N). Hydrogen atoms and solvent molecules have been excluded for clarity.

Classifying the underlying net using the so-called cluster representation in Topos,[85] it was revealed that **2** is a three-dimensional, doubly interpenetrated framework with the **pcu** topology and point symbol of $\{4^4.6^2\}$. However, if the standard simplification method is used in which case individual metal centre is considered as a node, the resulting underlying net has the **sqc493** topology with the point symbol $\{3^2.6^2.7^2\}\{3^4.4^6.6^4.7\}$. Both the **pcu** and **sqc493** are among the most common topological types in three periodic coordination polymers.[87] The packed structure of **2** and the underlying net are presented in Figure 3.34. Further analysis of the structure of **2**, the rectangular channel of one of the lattices, has a dimension of 13.02 Å x 19.47 Å measured with reference to the metal centres as

the corners of the rectangle. This void is, however, not completely accessible to guests due to the interpenetration which partitions it into four smaller channels two of which are much larger than the other two.

(a)

(b)
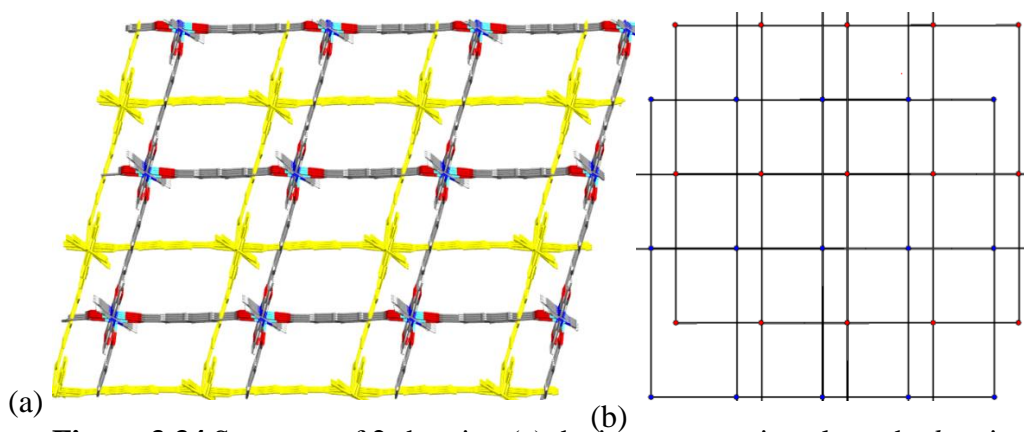
Figure 3.34 Structure of **2** showing (a) the interpenetration along the *b*-axis; and (b)the underlying **pcu** nets the two lattices shown in blue and red spheres. (grey = C, turquoise = Co, red = O and blue = N). Hydrogen atoms and solvent molecules have been excluded for clarity. The second lattice for the packed structure is in yellow.

The Co1-Co2 distance of 2.6671(7) Å does not represent an actual bond, but an indication of M-M interaction.[88] The Co-N14A and Co-N14B are respectively 2.01 Å and 2.047 Å while the Co-O bond lengths range between 2.033 and 2.000 Å. The bond angles made by O and N with either Co1 or Co2 are around 90°, ranging from 85.65° to 99.60°. These values are consistent with those expected of an octahedral complex and similar to those obtained for **1**. The dihedral angles between the pyridyl rings and the naphthalene core of the **DPNDI** ligands are 65.73° and 76.41°. Full lists of bond angles and lengths can be found in the appendix section.

There is an important π-π interaction that is observed between the two lattices of **2**. The naphthalene ring belonging to the NDC of one lattice π-stacks with NDI

core of the second lattice at a centroid-centroid distance of 3.499 Å as demonstrated in Figure 3.35
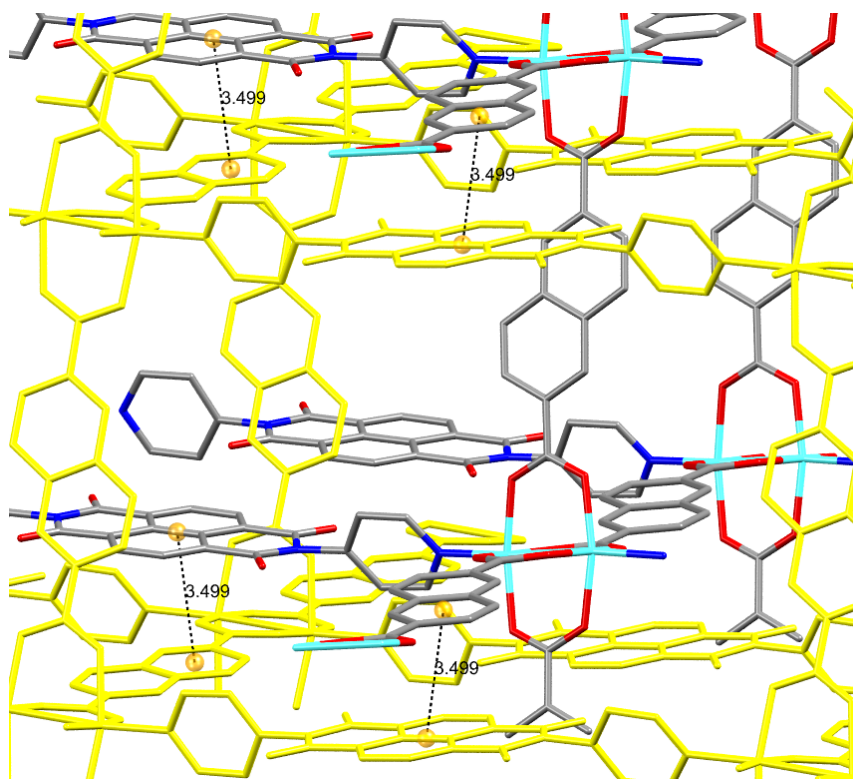
Figure 3.35 π- π stacking in **2**. (The second lattice is shown in yellow; the centroids are shown in orange spheres; grey = C, turquoise = Co, red = O and blue = N). Hydrogen atoms and occluded solvents are removed for clarity.

3.3.1.3 Synthesis and crystal structure of [Co₂(NDC)₂(DPPNDI)].6DMF (3)

Single crystals of compound **3** were grown under solvothermal conditions by reacting a mixture of $Co(NO_3)_2 \cdot 6H_2O$, H_2NDC and DPPNDI in DMF. Compound **3** is a novel framework material that crystallises in the triclinic P-1 space group. A summary of the crystal structure data and the refinement is given in Table 3.5.

Table 3.6 Summary of crystal data and structure refinements of 3.

Empirical formula	$C_{72}H_{56}Co_2N_4O_{12}$
Temperature/K	120.15
Crystal system	triclinic
Space group	P-1
a/Å	12.9691(2)
b/Å	13.09940(10)
c/Å	28.3251(3)
α/°	84.9090(10)
β/°	87.2540(10)
γ/°	85.5280(10)
Volume/Å^3	4774.43(10)
Z	2
ρ_{calc}g/cm^3	0.895
μ/mm^{-1}	3.085
F(000)	1332.0
Crystal size/mm^3	$0.187 \times 0.146 \times 0.072$
Radiation	Cu Kα ($\lambda = 1.54184$)
2θ range for data collection/°	6.842 to 158.402
Index ranges	$-15 \leq h \leq 16$, $-16 \leq k \leq 16$, $-35 \leq l \leq 35$
Reflections collected	117307
Independent reflections	19792 [$R_{int} = 0.0563$, $R_{sigma} = 0.0292$]
Data/restraints/parameters	19792/1503/819
Goodness-of-fit on F^2	1.091
Final R indexes [I>=2σ (I)]	$R_1 = 0.0753$, $wR_2 = 0.2394$
Final R indexes [all data]	$R_1 = 0.0833$, $wR_2 = 0.2467$
Largest diff. peak/hole / e Å^{-3}	0.60/-1.00

The asymmetric unit of the single crystal X-ray structure is similar to that of **2** as presented in Figure 3.36. In fact, **2** and **3** are isoreticular, differing only in the NDI linker. While **2** contains **DPNDI**, **3** has **DPPNDI** acting as a pillar. Suffice it to say that **DPPNDI** (23.923 Å) is much longer than **DPNDI** (15.371 Å) in their respective MOFs. However, compared to the free ligand in which the length is 24.063 Å, **DPPNDI** contained in the MOF is slightly shorter. This is likely due to the restriction imposed on the ligand, and its conformation, in the framework.
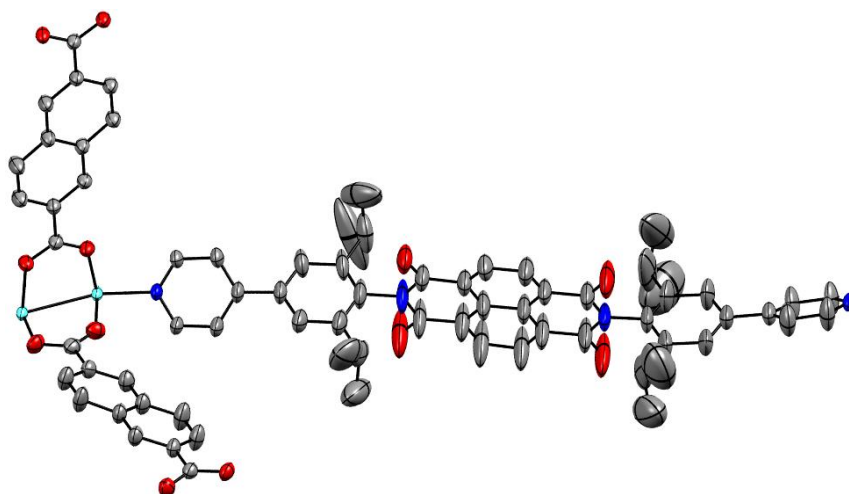
Figure 3.36 Asymmetric unit of **3** (atoms are drawn at 50% ellipsoid; grey = C, turquoise = Co, red = O and blue = N; hydrogen atoms have been removed for clarity).

Like **2**, the extended structure of **3** reveals a doubly interpenetrated three-dimensional framework structure, the **pcu** or the **sqc493** topology (depending on the classification method used as discussed earlier for **2**). The bond lengths and angles around the metal atoms are all similar to those in **2**. Again, a full list of these can be found in the appendix.

Owing to the presence of the sterically bulky isopropyl groups in **DPPNDI**, no π-π stacking involving the NDI core is observed in **3**. Nevertheless, other weak interactions viz; hydrogen bonding, CH/π and π-π interactions are dominant throughout the entire framework as illustrated in Figure 3.37. All these interactions exist between the lattices that make up **3**. The rectangular channels in **3,** without considering the interpenetrated lattice has a dimension of 25.56 Å x 13.10 Å when viewed along the crystallographic *a*-axis. The dihedral angles found between the pyridyl ring and the isopropyl-bearing phenyl rings are 37.20º and 31.57º for the two ends of the **DPPNDI** ligand; and 76.86º and 89.24º between the NDI core and the isopropyl-bearing phenyl ring. Compared to the

83° for free ligand, the torsional angle between the NDI core and the isopropyl-bearing phenyl ring in **3** is higher with the two entities being nearly perpendicular to each other.
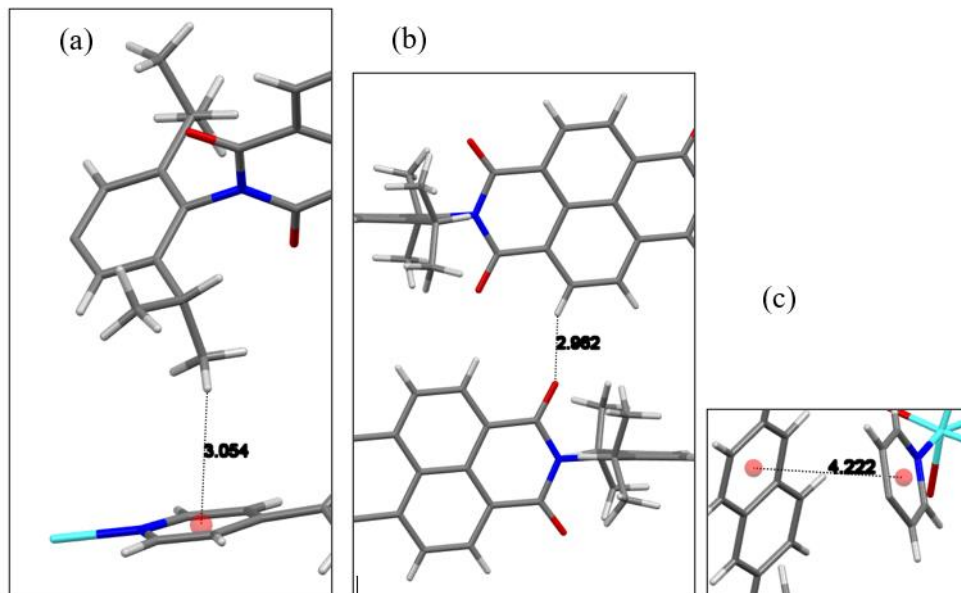
Figure 3.37 Possible intermolecular interactions in **3**; (a) CH/π interaction (b) hydrogen bonding; and (c) π-π interaction. (grey = C, turquoise = Co, red = O, blue = N and white = hydrogen).

3.3.1.4 Synthesis and crystal structure of [Co$_2$(BPDC)$_2$(DPPNDI)]. 3DMF.H$_2$O (4) and [Ni$_2$(BPDC)$_2$(DPPNDI)].13.5DMF.3H$_2$O (5)

These two MOFs, **4** and **5**, are analogues of each other, crystallizing in the triclinic space group P-1. They were synthesised solvothermally by adding the corresponding metal salt – Co(NO$_3$)$_2$.6H$_2$O or Ni(NO$_3$)$_2$.6H$_2$O – to a mixture of H$_2$BPDC and **DPPNDI** in DMF. The mixture, in a tightly capped 20 mL scintillation vial, was stirred at room temperature and heated in an oven at 100 °C for 24 h to yield the desired crystals (dark brown for the cobalt- and green for the nickel-MOF). Table 3.7 contains the crystallographic and refinement data for **4** and **5**.

Table 3.7 Summary of crystal data and structure refinement of **4** and **5.**

Parameters	4	5
Empirical formula	$C_{89.75}H_{88.58}Co_2N_{8.59}O_{16.59}$	$C_{108}N_{14.5}Ni_2O_{24.5}$
Formula weight	1670.68	2009.65
Temperature/K	120(2)	120(2)
Crystal system	triclinic	triclinic
Space group	P-1	P-1
a/Å	15.19480(10)	15.0983(8)
b/Å	15.2068(3)	15.1738(6)
c/Å	28.4154(2)	28.3231(8)
α/°	92.7500(10)	92.867(3)
β/°	97.0670(10)	97.323(3)
γ/°	95.0750(10)	95.039(4)
Volume/Å^3	6478.84(14)	6398.7(5)
Z	2	2
ρ_{calc}g/cm^3	0.856	1.043
μ/mm^{-1}	2.391	0.912
F(000)	1748	2003
Crystal size/mm^3	$0.233 \times 0.179 \times 0.141$	$0.186 \times 0.136 \times 0.081$
Radiation	Cu Kα ($\lambda = 1.54184$)	Cu Kα ($\lambda = 1.54184$)
2θ range for data collection/°	7.02 to 156.55	5.858 to 146.268
Index ranges	$-15 \le h \le 19$, $-18 \le k \le 19$, $-36 \le l \le 30$	$-18 \le h \le 16$, $-18 \le k \le 12$, $-34 \le l \le 35$
Reflections collected	86829	50777
Independent reflections	26595 [$R_{int} = 0.0603$, $R_{sigma} = 0.0407$]	24978 [$R_{int} = 0.0718$, $R_{sigma} = 0.0850$]
Data/restraints/parameters	26595/1298/1182	24978/2150/1360
Goodness-of-fit on F^2	1.279	2.147
Final R indexes [I>=2σ (I)]	$R_1 = 0.0998$, $wR_2 = 0.3005$	$R_1 = 0.2103$, $wR_2 = 0.5243$
Final R indexes [all data]	$R_1 = 0.1082$, $wR_2 = 0.3102$	$R_1 = 0.2307$, $wR_2 = 0.5400$
Largest diff. peak/hole / e Å^{-3}	1.20/-0.80	2.57/-1.11

In terms of connectivity of the underlying nets, **4 and 5** have the **pcu** topology, as discussed earlier for **2** and **3**. Their asymmetric unit is shown in Figure 3.38 are similar to those of **2** and **3** and the bond angles and lengths are very closely related to those of **3**.
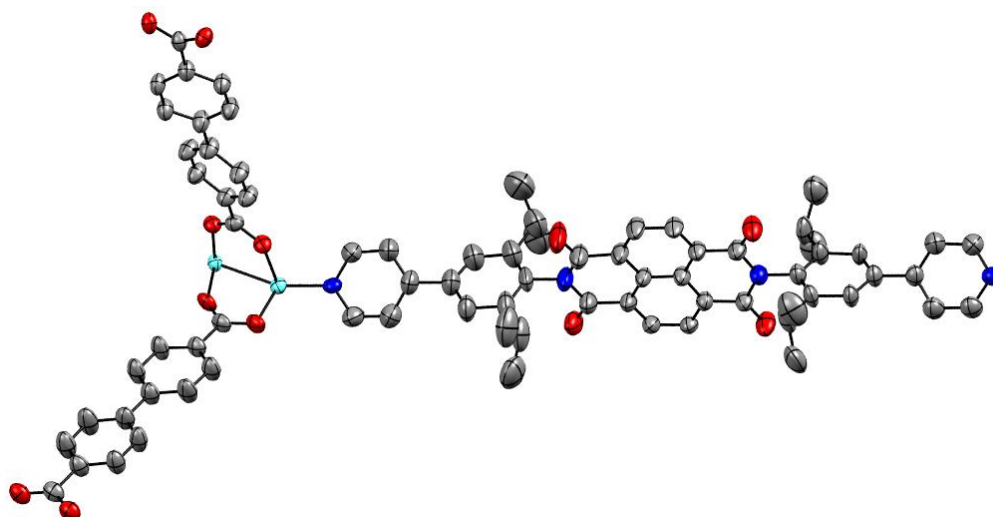
Figure 3.38: ORTEP representation of the asymmetric unit of **4** or **5**. (The ellipsoid is drawn at 50%; grey = C, turquoise = Co or Ni, red = O, blue = N; hydrogen and pore solvents have been removed for clarity).

An interesting feature worth discussing in **4** and **5** is the planarity of the biphenyl rings of the BPDC in the structure. Of the two independent BPDC units in the asymmetric unit, one is planar while the other is twisted with a torsional angle of 28.27°. This large dihedral angle shown in the twisted rings is a consequence of the π-π stacking (with a centroid-centroid distance of 3.579 Å) between one of the rings of the affected BPDC unit and the NDI core (Figure 3.39a). Meanwhile, the BPDC unit which maintains its planarity is sandwiched between two NDI units in which the edges of the NDI core point towards the face of the planar BPDC rings (Figure 3.39b). As the distances between the edges and faces are wide apart, no CH/π interactions were observed.
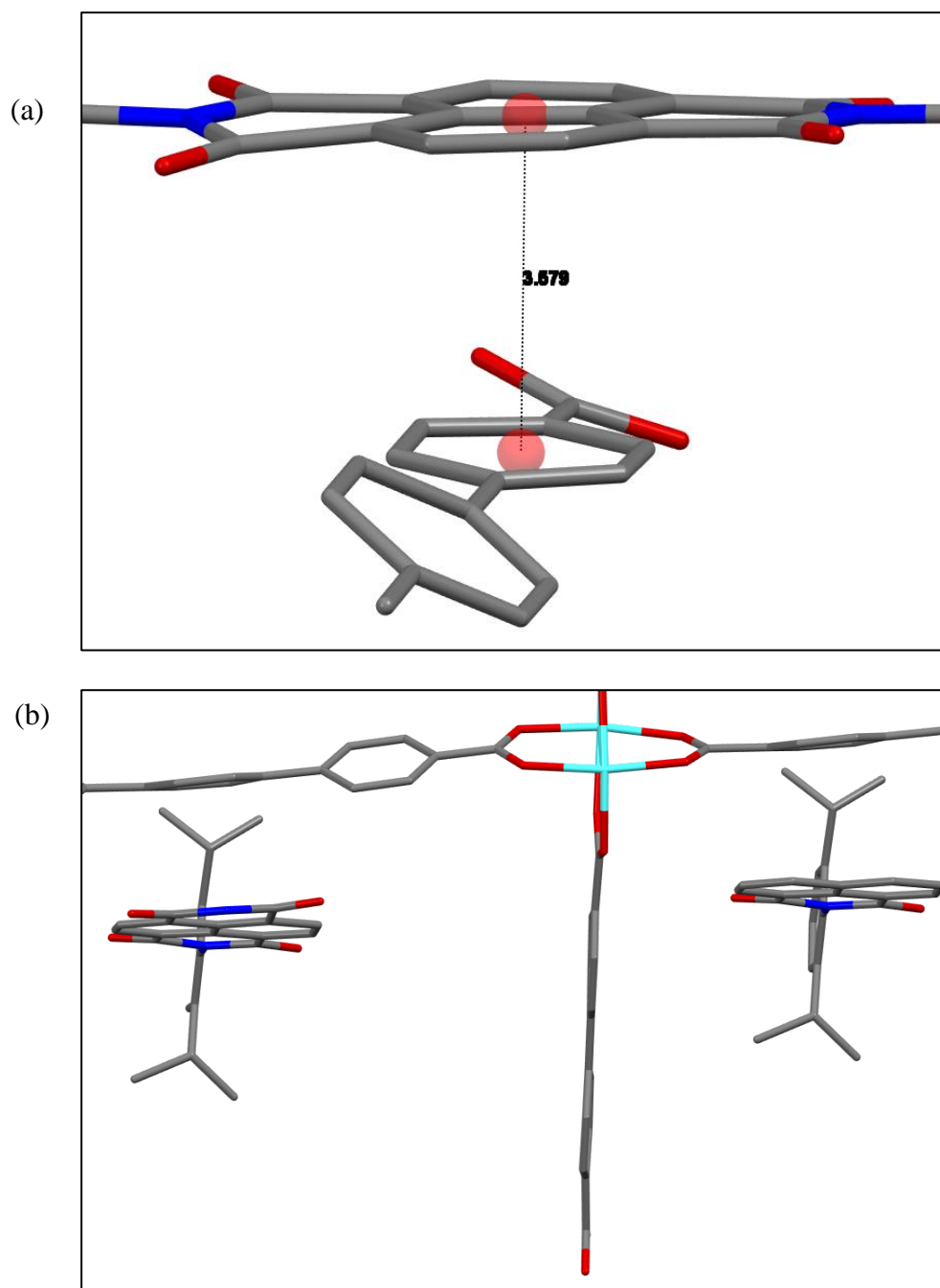
Figure 3.39: Interactions in **4** and **5** showing (a) π-π stacking between the BPDC^{2-} and the **DPPNDI** ligand. (b) the arrangements of the **DPPNDI** units adjacent to the planar BPDC^{2-}. (grey = C, turquoise = Co or Ni, red = O, blue = N; hydrogen have been removed for clarity)

3.3.2 PDI MOFs

3.3.2.1 Synthesis and crystal structure of [Co$_2$(BPDC)$_2$(DPPPDI)].xDMF.yH$_2$O (6)

Single crystals of compound **6** of the right quality for SCXRD were grown under solvothermal conditions by reacting Co(NO$_3$)$_2 \cdot$6H$_2$O, biphenyl-4,4'-dicarboxylic acid and **DPPPDI** in DMF. Compound **6** crystallises in the monoclinic P2$_1$/c space group. The crystals are very weakly diffracting and so the data was collected at the Diamond Light Source facility on I19. Before going into details to discuss the structure of **6**, it should be noted that multiple data sets were collected to ascertain the actual structure. All the data sets turned out to produce the same structure following analysis. Some key crystal data and refinement parameters for **6** are shown in Table 3.8. Due to the poor quality of the diffraction, the diffraction limit set to 1.3 Å, R$_{int}$ of 9.8% *(after truncation of data to 1.3 Å)*, I/sigma of 9.8, R$_1$ (after SQUEEZE) of 16.1% and data to parameter ratio 11.1.

Table 3.8: Summary of crystal data and structure refinement of **6**.

Empirical formula	$C_{185.5}H_{136}Co_{4.33}N_8O_{27}$
Formula weight	3164.33
Temperature/K	100(2)
Crystal system	monoclinic
Space group	$P2_1/c$
a/Å	38.9603(10)
b/Å	15.2249(3)
c/Å	41.3988(16)
α/°	90
β/°	117.769(2)
γ/°	90
Volume/Å³	21554.2(12)
Z	4
ρ_{calc}g/cm³	0.967
μ/mm⁻¹	0.351
F(000)	6552
Crystal size/mm³	$0.07 \times 0.03 \times 0.025$
Radiation	Synchrotron radiation ($\lambda = 0.6889$)
2θ range for data collection/°	1.912 to 30.728
Index ranges	$-29 \leq h \leq 29, -11 \leq k \leq 11, -31 \leq l \leq 31$
Reflections collected	78006
Independent reflections	10339 [$R_{int} = 0.0889, R_{sigma} = 0.1015$]
Data/restraints/parameters	10339/3315/931
Goodness-of-fit on F²	1.268
Final R indexes [I>=2σ (I)]	$R_1 = 0.1610, wR_2 = 0.4076$
Final R indexes [all data]	$R_1 = 0.2322, wR_2 = 0.4433$
Largest diff. peak/hole / e Å⁻³	2.27/-0.73

The asymmetric unit contains four cobalt atoms (two paddle wheel units), two **DPPPDI** ligands and five biphenyl-4,4'-dicarboxylate (BPDC) ligands. In addition to these full occupancy residues, the asymmetric unit also contains electron density refined as two partial occupancy cobalt atoms indicative of a cobalt paddle wheel unit which is incongruous with the other residues (Figure 3.40a). Although the partial occupancy cobalt atoms are surrounded by electron density peaks compatible with the coordination sphere of a paddle wheel unit, a sensible model for these peaks could not be developed.

The weak low-resolution data does not support refinement with anisotropic displacement parameters, other than for the full occupancy cobalt atoms. Two of the anisotropic cobalt cations are restrained to have more isotropic displacement parameters; electron density peaks adjacent to these two cobalt cations indicated a minor disorder component in the paddle wheel conformation for which a model could not be developed. The packing view of **6** illustrating how bent the **DPPPDI** ligands are in MOF is shown in Figure 3.40b.
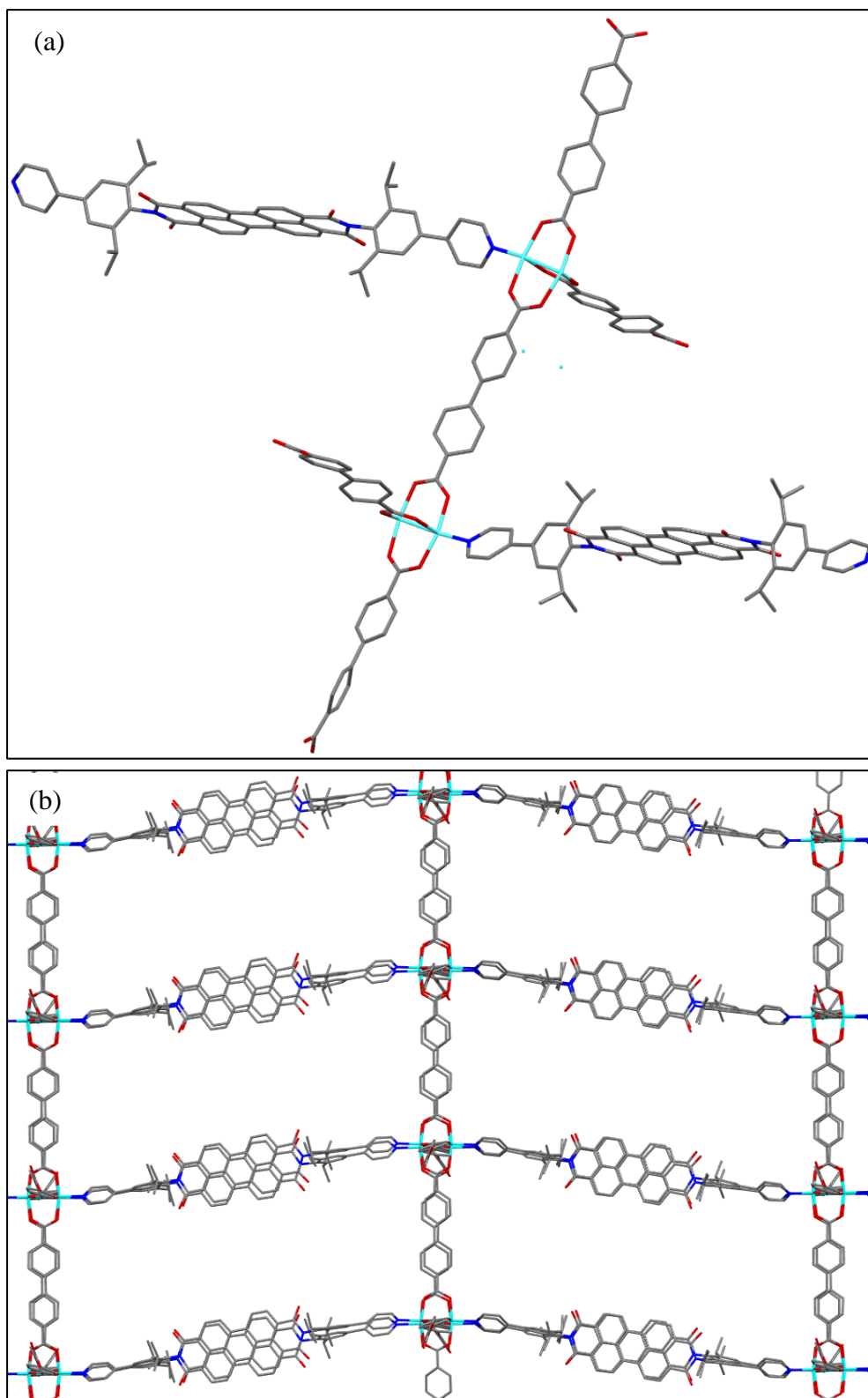
Figure 3.40: (a)Asymmetric unit of **6** and (b) extended structure of one of the latices of **6** along the *c*-axis. (grey = C, turquoise = Co, red = O, blue = N; hydrogen atoms have been removed for clarity)

Both of the PDI ligands are coordinated to the axial sites of paddle wheel units via both of their pyridyl groups. Three of the biphenyl ligands are coordinated to paddle wheels at both ends. Two of the biphenyl ligands are coordinated to a paddle wheel at one end and are uncoordinated at the other end – the carboxylate moiety of one of these two ligands is modelled at half-occupancy. A general trend in the displacement parameters along the two unbound ligands indicates the presence of conformational disorder which could not be modelled. The unbound carboxylate groups overlap with the region where the postulated partial occupancy cobalt paddle wheel residues reside, but in a manner incompatible with their mutual coordination.

As refined, the crystal structure possesses two-fold interpenetrated two-dimensional-sheets with the unbound carboxylate groups projecting above and below the plane of these sheets (see Figure 3.41c). If the nature of the disorder in the region of the unbound carboxylate groups and partial occupancy cobalt atoms could be resolved, then the framework would have three-dimensional connectivity as seen in **4** and **5**. As the resolution is very low, the bond lengths and angles cannot be relied upon for discussion. However, it is worthy of note the values based on this resolution are not far from those expected around the metal centres. For instance, the bond angles range from 88.95^{o} to 92.25^{o} around the Co1-Co2 paddle wheel, and 86.14^{o} to 90.67^{o}. The Co-O/N bond lengths are also sensible between 1.991 Å and 2.085 Å. All these values for the bond angles and bond lengths are consistent with those found for **3**, **4** and **5**.

A careful analysis of the structure reveals that **6** exhibits some π-π stacking between one of the phenyl rings of BPDC and the perylene core of the PDI within a distance of 3.422 Å (Figure 3.41a). This interaction is similar to that seen in **4**

and **5** (centroid-centroid distance of 3.579 Å). Another subtle but possible interactions in **6** is the CH/π interaction occurring between the aromatic CH of the BPDC and the isopropyl-bearing phenyl ring of the **DPPPDI** ligand. This CH/π communication can also be observed between the CH of the isopropyl group of the **DPPPDI** moiety and the isopropyl-bearing phenyl ring of the adjacent **DPPPDI** ligand as illustrated in Figure 3.41b.
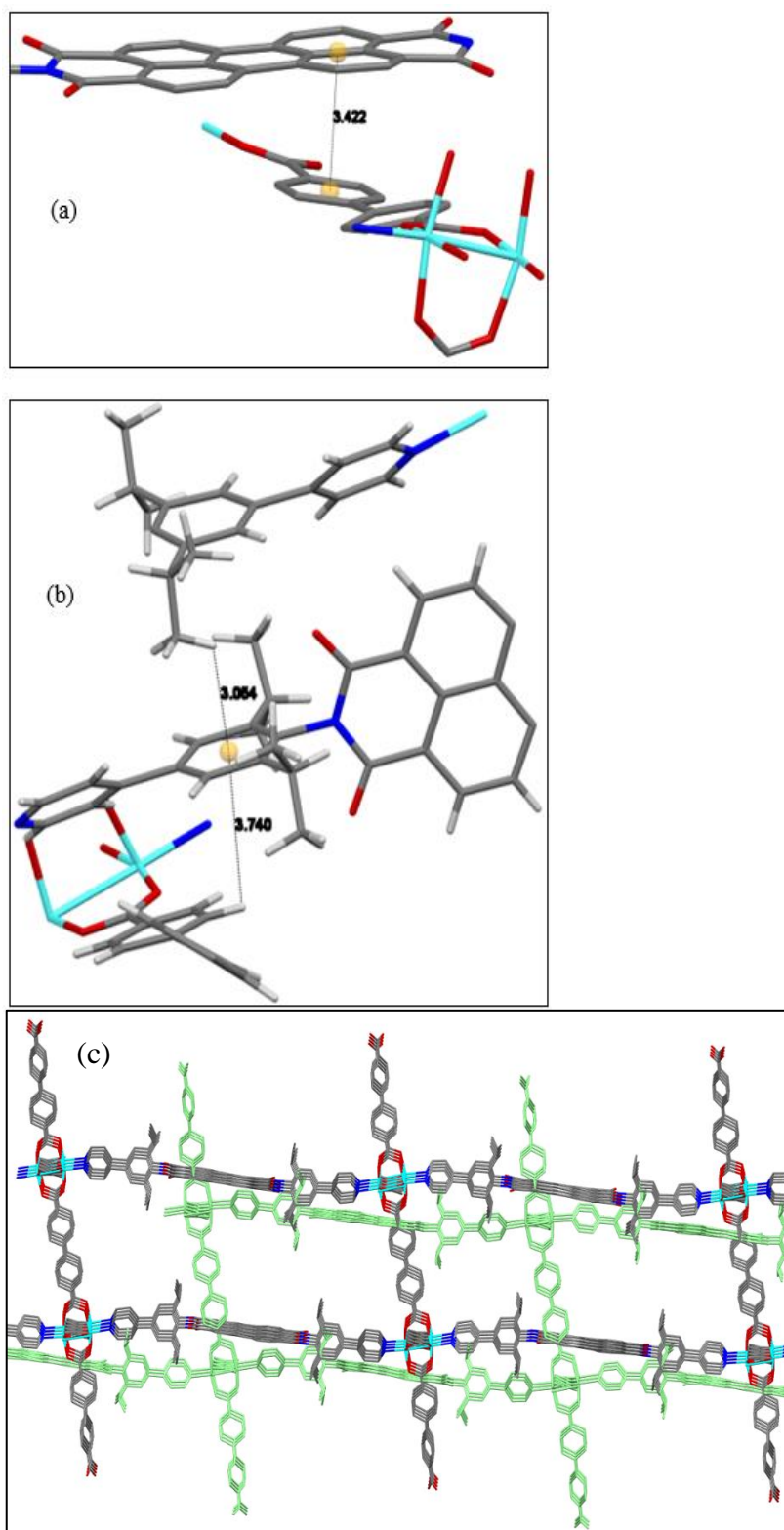
Figure 3.41: (a) π-π interaction (b) CH/π interactions in **6**. (c) doubly interpenetrated network of **6** showing the uncoordinated carboxylates pointing above and below the plane of the 2D sheets. (grey = C, turquoise = Co, red = O, blue = N, white = hydrogen (in b); hydrogen atoms (in a and c) have been removed for clarity).

3.3.2.2 Synthesis and crystal structure of [Co$_2$(NDC)$_2$(DPPPDI)]$.x$DMF$.y$H$_2$O (7)

Compound **7** was synthesised using the same method as for the other six MOFs described above. The crystal data and refinement details are contained in Table 3.9. The asymmetric unit for **7** (Figure 3.42a) shows that the framework is isoreticular to that observed for **3**, simply replacing the **DPPNDI** ligand in **3** with **DPPPDI** in **7**. Inspection of the asymmetric unit reveals that the perylene core of the PDI ligand is considerably bent, making an angle of 167.94^o with the centroid as indicated in Figure 3.42a. However, the perylene core in **6** appear largely planar. Both **7** and **3** are doubly interpenetrated, crystallising in the triclinic space group P-1 with similar connectivity around the metal centres. The longer **DPPPDI** linker means the rectangular channel in **7** is much longer than that observed in **3**. The dimensions of the channel, excluding any interpenetration, is 32.00 Å by 13.20 Å. The framework structure of **7** is shown in Figure 3.42b and details of bond angles and bond lengths of **7** can be found in the appendix.

Table 3.9: Summary of crystal data and structure refinement of **7.**

Empirical formula	$C_{186.5}H_{176.5}Co_4N_{15.5}O_{31.5}$
Formula weight	3374.64
Temperature/K	100(2)
Crystal system	triclinic
Space group	P-1
a/Å	12.677(4)
b/Å	13.196(5)
c/Å	31.941(8)
α/°	85.58(3)
β/°	88.50(2)
γ/°	89.20(4)
Volume/Å^3	5325(3)
Z	1
ρ_{calc}g/cm^3	1.052
μ/mm^{-1}	0.341
F(000)	1764
Crystal size/mm^3	-
Radiation	synchrotron ($\lambda = 0.6889$)
2θ range for data collection/°	1.24 to 36.494
Index ranges	$-11 \leq h \leq 11, -11 \leq k \leq 11, -29 \leq l \leq 29$
Reflections collected	28185
Independent reflections	8270 [$R_{int} = 0.1006$, $R_{sigma} = 0.0726$]
Data/restraints/parameters	8270/1682/909
Goodness-of-fit on F^2	1.758
Final R indexes [I>=2σ (I)]	$R_1 = 0.1681$, $wR_2 = 0.4288$
Final R indexes [all data]	$R_1 = 0.1848$, $wR_2 = 0.4479$
Largest diff. peak/hole / e Å^{-3}	2.36/-0.83
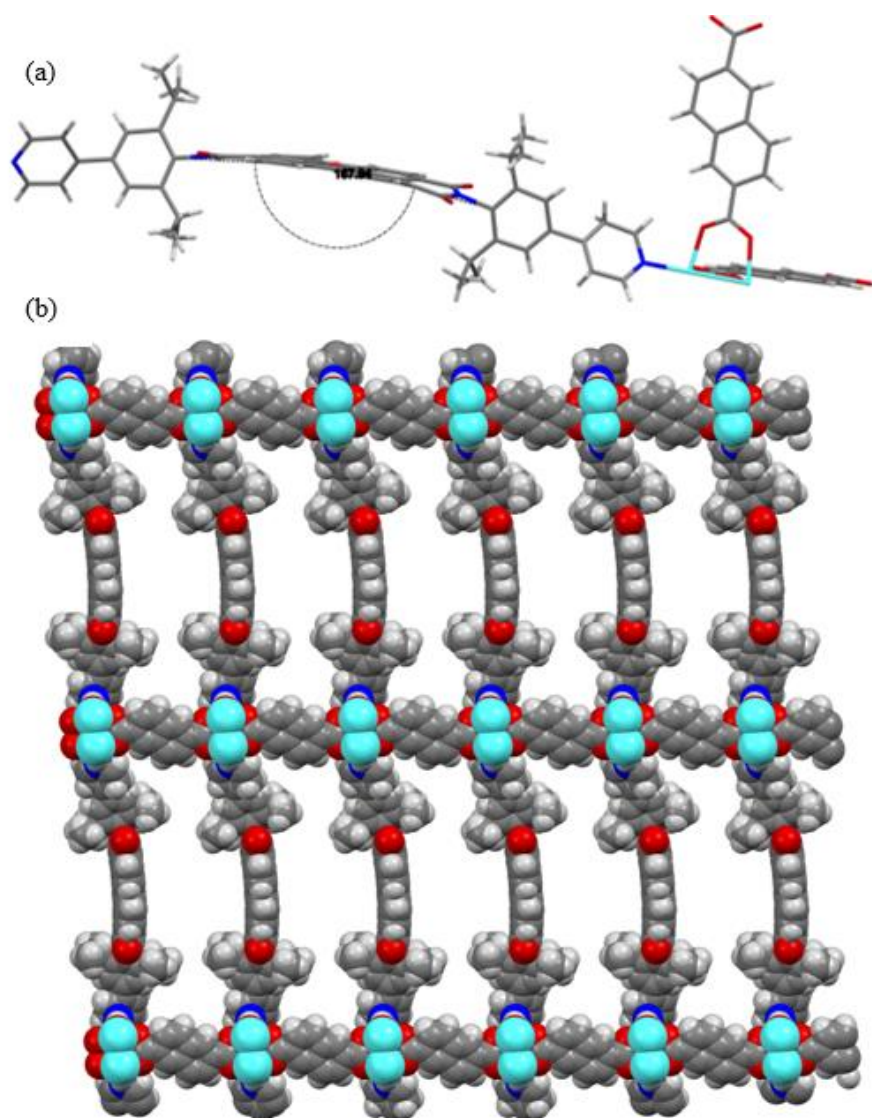
Figure 3.42: (a) Asymmetric unit (the included angle is 167.94°); and (b) space-filling representation of the packed structure of **7** along the crystallographic *a*-axis. (grey = C, turquoise = Co, red = O, blue = N, H = light grey; Only one lattice of the doubly interpenetrated network is shown in (b).

Considering the proximity of the naphthalene ring of the NDC linker to the perylene, it reasonable to suggest that some π-π interactions exist between the two interpenetrating networks that make up the structure of **7**. This, of course, is similar to the π-π stacking interaction present in **3**, **4** and **5** (see Figure 3.43).
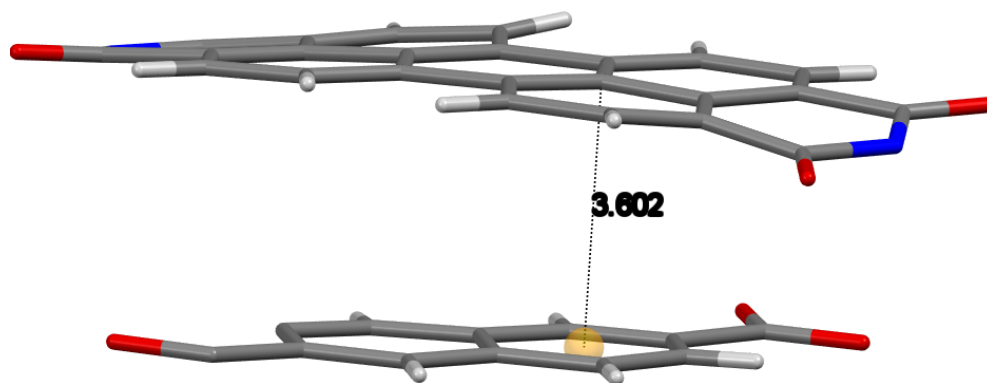
Figure 3.43: π-π stacking interaction in **7**; (grey = C, red = O, blue = N, light grey = H).

Table 3.10 presents key crystallographic data for all the MOFs (**1**-**7**) discussed so far. This will provide a quick snapshot of all the data therein making comparison easier. The solvent accessible void volume was calculated using PLATON SQUEEZE.[83]

Table 3.10: Some crystallographic information for **1-7.**

Parameter	Compound						
	1	**2**	**3**	**4**	**5**	**6**	**7**
Metal system	Co(II)	Co(II)	Co(II)	Co(II)	Ni	Co(II)	Co(II)
Rylene diimide	**DPNDI**	**DPNDI**	**DPPNDI**	**DPPNDI**	**DPPNDI**	**DPPPDI**	**DPPPDI**
Crystal system	Triclinic	monoclinic	Triclinic	Triclinic	Triclinic	monoclinic	Triclinic
Space group	P-1	$P2_1$	P-1	P-1	P-1	$P2_1/c$	P-1
SBU	$\{[M(k^2\text{-}O_2NO)]_2(\mu^2\text{-}O_2CR)_2\}$	$M_2(\mu_2\text{-}O_2CR)_4$	$M_2(\mu_2\text{-}O_2CR)_4$	$M_2(\mu_2\text{-}O_2CR)_5$	$M_2(\mu_2\text{-}O_2CR)_6$	$M_2(\mu_2\text{-}O_2CR)_7$	$M_2(\mu_2\text{-}O_2CR)_8$
Interaction	π-π and lone pair-π	π-π	π-π, CH/π and lone pair-π	π-π	π-π	π-π and CH/π	π-π
Dimensionality	2-D	3-D	3-D	3-D	3-D	2-D	3-D
Topology type	**sql**	**pcu or sqc493**	**pcu or sqc493**	**pcu or sqc493**	**pcu or sqc493**	**-**	**pcu or sqc493**
Interpenetration	2-fold	2-fold	2-fold	2-fold	2-fold	2-fold	2-fold
Void dimension (Å)	19.69 x 12.43	19.47 x 13.10	28.01 x 12.97	28.06 x 15.21	27.95 x 15.10	32.25 x 15.23	32.00 x 13.20
Solvent accessible volume per unit cell (%)	37	54	47	34	57	39	49

3.3.3 Powder X-ray diffraction (PXRD)

To complement the information obtained from SCXRD studies, PXRD is often employed by MOF chemists to ascertain the phase purity of materials. The method is valuable for determining the structure of unknown MOFs, where single crystals are not suitable for SCXRD, although some expertise is required to refine the data so obtained.[24,89] There is no gainsaying that SCXRD remains one of the most powerful techniques for the elucidation of the structure of three-dimensional materials down to the atomic level, providing unambiguous information on the structure-function properties of such materials.

The PXRD patterns of **1-7** were recorded and compared to those simulated from the crystallographic information files (CIFs) using Mercury software.[84] This comparison is invaluable because only one crystal is used in obtaining the structure of material via SCXRD; hence not necessarily a representation of the bulk of the sample. Figure 3.44a-g shows the PXRD patterns of **1-7** with the

simulated and the actual patterns stacked for comparison. It is observed that the peaks in most cases largely agree and any difference could be attributed the loss of crystallinity due to solvent loss from MOF pores. In all instances, additional peaks are observed, suggesting a small degree of contamination most likely from the starting materials.

(g)
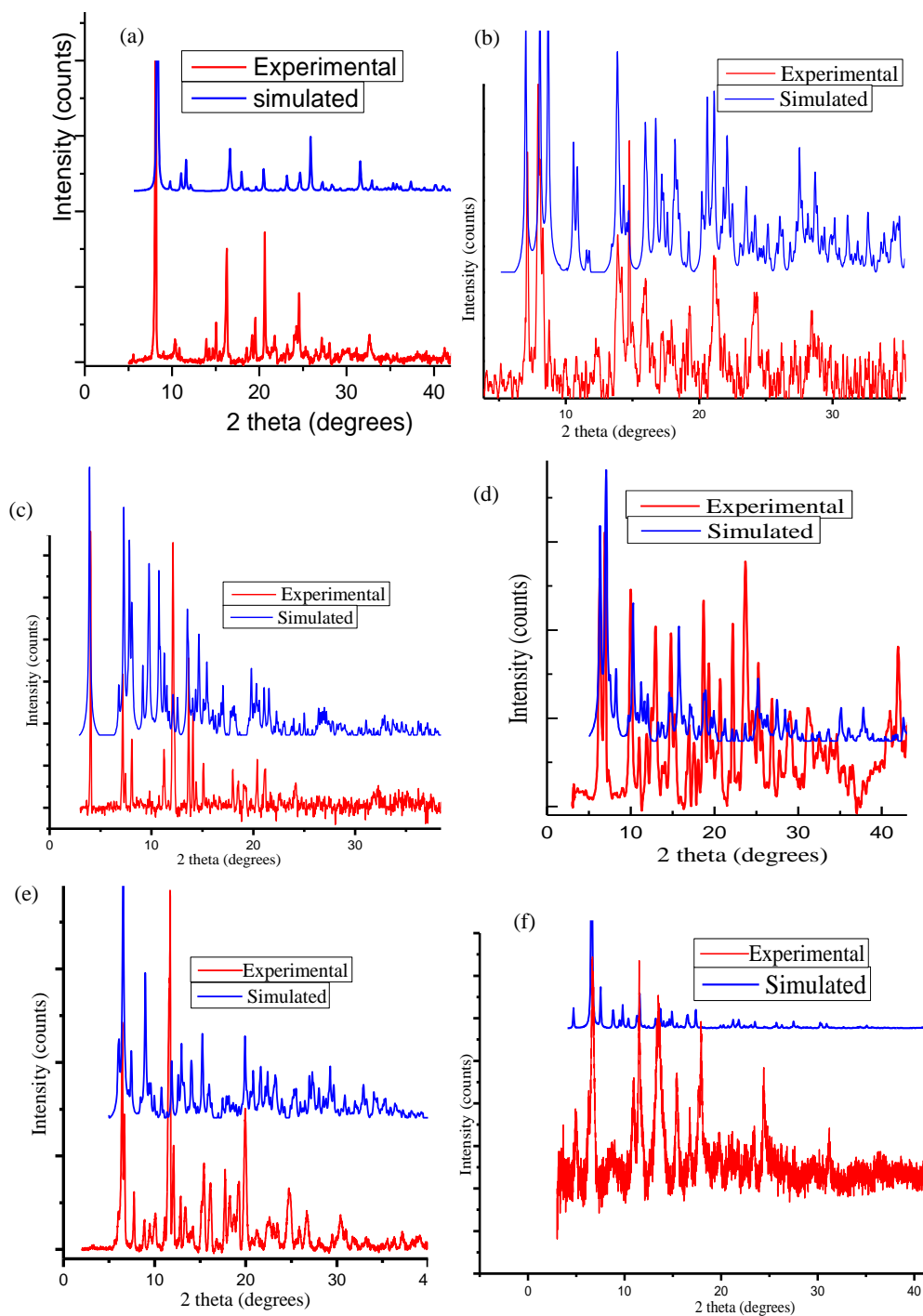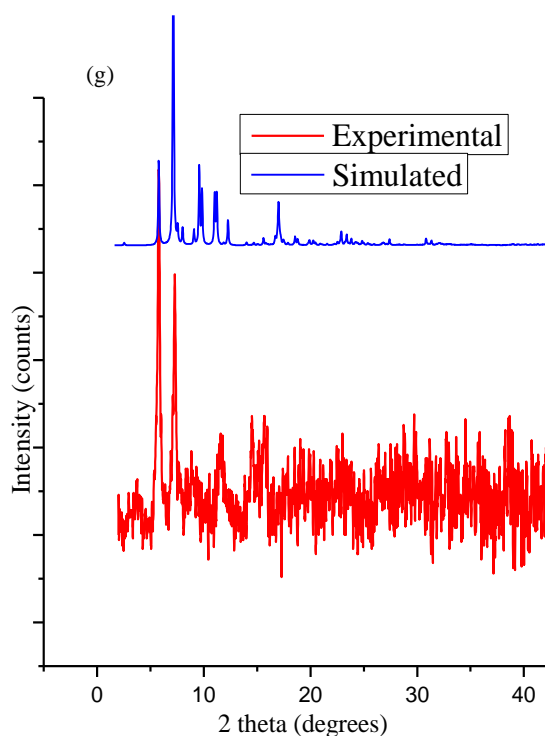
Figure 3.44: Experimental (red) and simulated (blue) PXRD patterns of (a) **1**; (b) **2**; (c) **3**; (d) **4**; (e) **5**; (f) **6**; (g) **7**.

3.3.4 Scanning Electron Microscopy (SEM)/ Energy Dispersive X-Ray Analysis EDX

As mentioned in chapter one, SEM is one of the most commonly used techniques for the analysis of surface morphology of MOFs. It can also provide insight into the purity of the materials potentially providing evidence of particles with distinct morphology. When performed in conjunction with EDX, not only are the scanning electron micrographs produced, a knowledge of the elemental composition can be obtained as shown in Figure 3.45 for compounds **1**-**7**. The crystals of **1** are seen to have needle morphologies while those of **2**, **3**, **4** and **5** are blocks of more than 50 µm in size. The crystals of **6** are observed as disks with the surface showing the existence of some layering with the different strata somewhat interwoven. Finally, the micrographs for **7** reveals that the crystals are

a cluster of plates which exhibit curved character. Micrographs of different magnifications for each of these MOFs can be found at the end of this chapter.
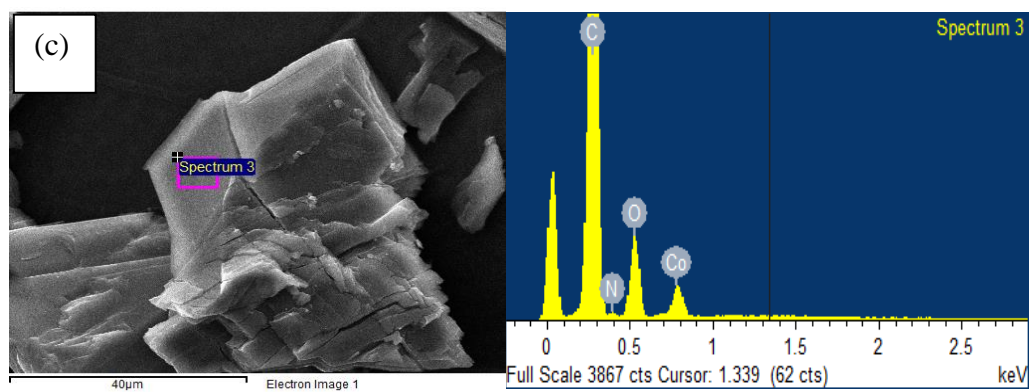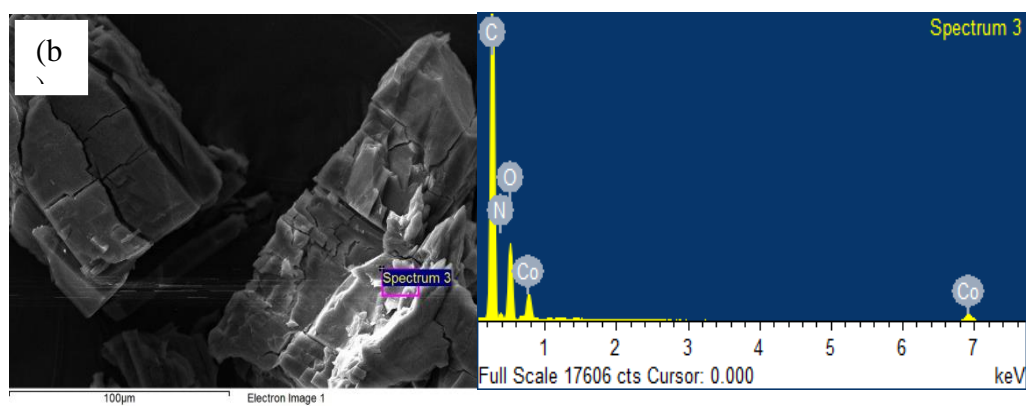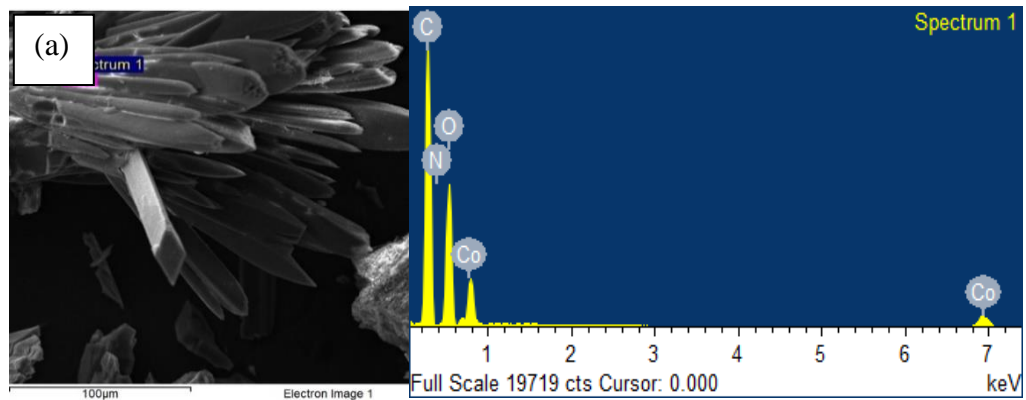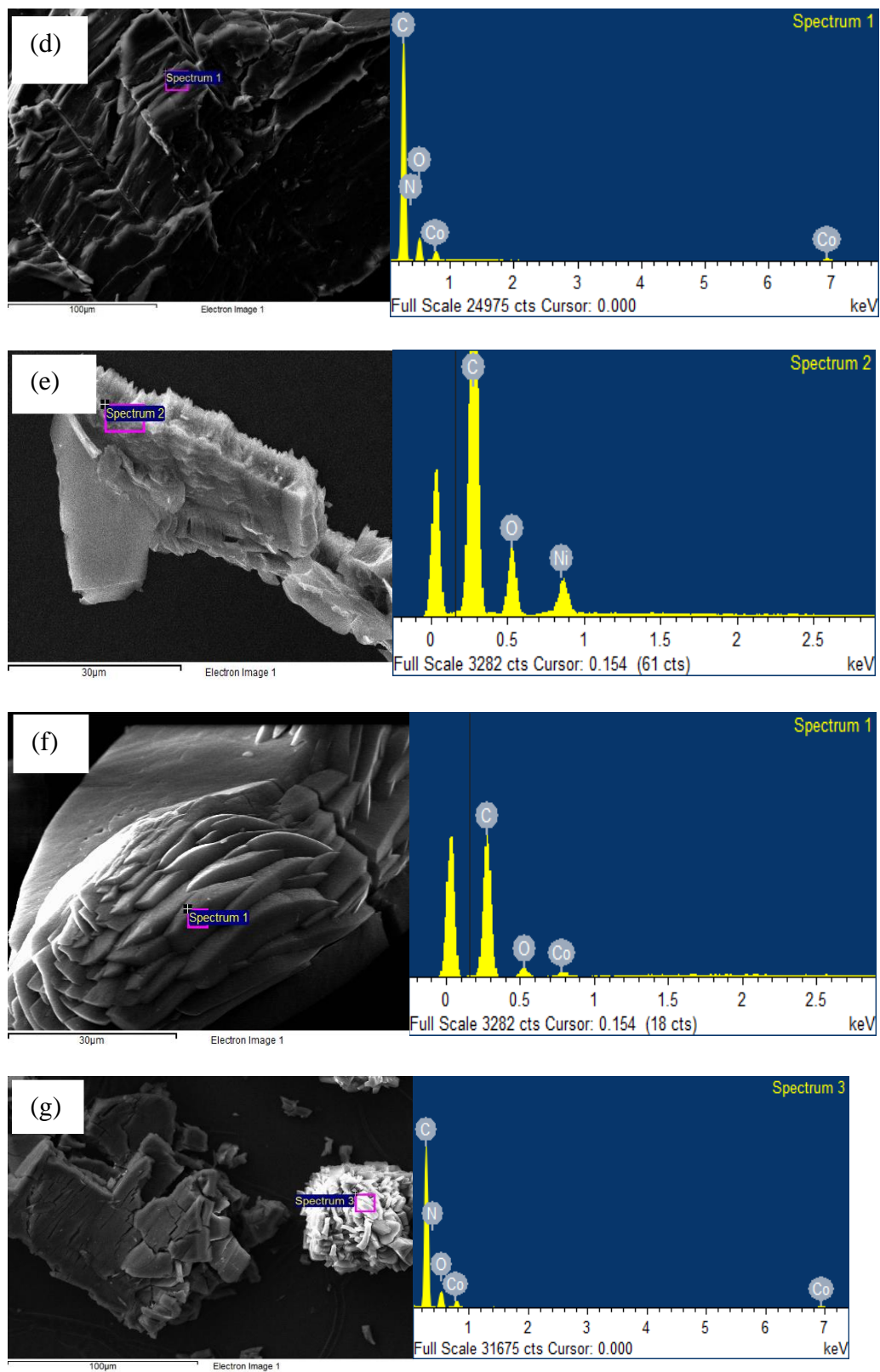
Figure 3.45: SEM/EDX of (a) **1**; (b) **2**; (c) **3**; (d) **4**; (e) **5**; (f) **6**; (g) **7**

3.3.5 Thermogravimetric analysis (TGA)

Thermogravimetric analysis (TGA) is another widely employed technique for the characterisation of MOFs. This is vital as it provides information on the thermal stability of the MOFs which in turn can be indispensable for certain applications of the materials. TGA curves for **1-7** are presented in Figure 3.46. Due to zero-tolerance to DMF-containing materials in the lab where these measurements were performed, all the analysis were performed on samples in which solvent exchange with acetone had been carried out. Prior to the TGA measurements, the as-synthesised samples were filtered, washed with acetone to remove any unreacted starting materials and soaked in acetone for three days to ensure complete solvent exchange.

The TGA curves for all the materials reveal that they are stable up to between 350 ^{o}C and 450 ^{o}C. The weight loss up to about 550 ^{o}C indicates the loss of the ligands at which point the framework decomposed completely. It could be inferred from the curve for **2** that despite soaking the solvent for up to three days, the weight loss from 85-114 ^{o}C can be ascribed to the loss of water molecules or perhaps, the trapped acetone molecules in the pore.
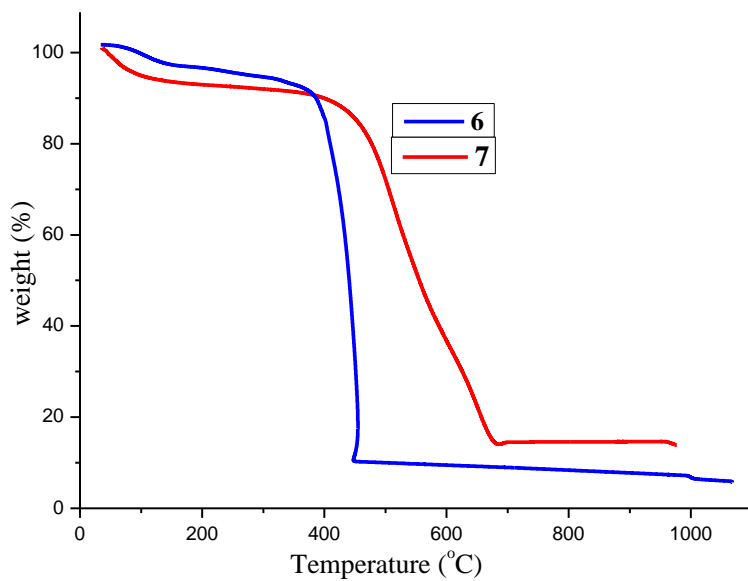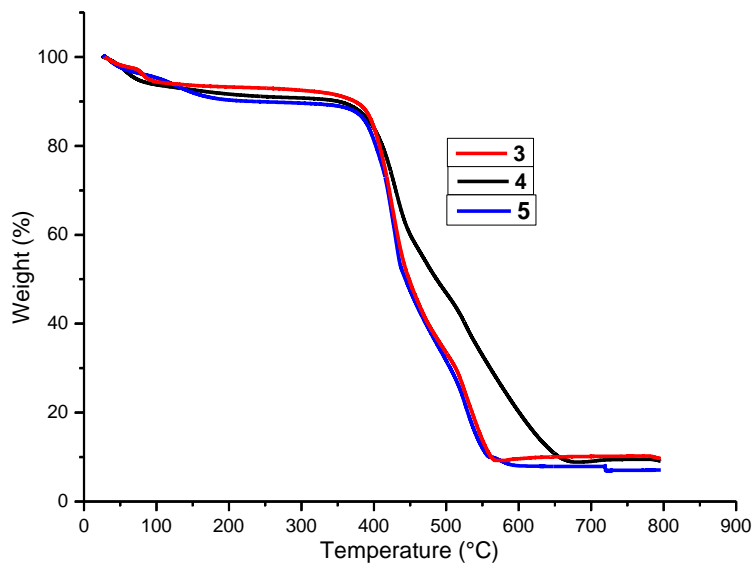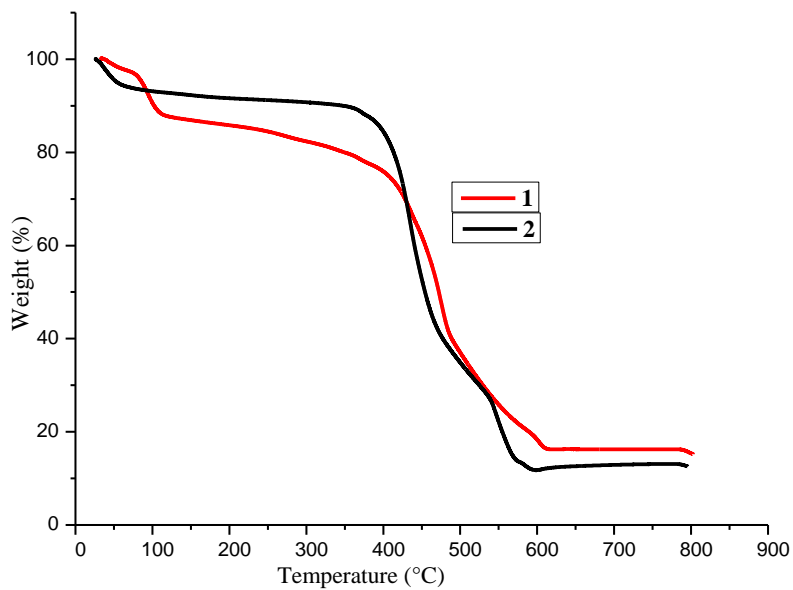
Figure 3.46: TGA curves of 1-7.

3.3.6 Electrochemistry

The electronic behaviour of **1-7** was investigated using electrochemical methods, including the combination solid-state cyclic voltammetry (CV) and UV-vis spectroelectrochemistry which was recorded in transmittance mode. As mentioned previously in chapter two, CV can be used to investigate both the number and the nature of the redox processes occurring any redox-active material. Recall that the CVs and SEC for the ligands were performed in solution. However, as MOFs are not soluble in virtually all the organic solvents, used for such measurements, and if they do dissolve this is accompanied by disassembly of the framework, some modification must be made to instrumental configuration, as well as the samples, in order to perform the aforementioned experiments. One of the major achievements of this research was the fabrication, in conjunction with an electrochemist, of a suitable and reliable method for probing the solid state electrochemistry of MOFs in particular and, indeed, any insoluble solid materials in general.

2.3.3.1 Solid state cyclic voltammetry (CV)

Solid state CV was performed on **1** - **7**, encapsulated on the surface of a glassy carbon electrode by a $LiClO_4$ intercalated polyvinylchloride (PVC) matrix.[58,90] Consistent with the electrochemistry of diimides in general, each of the NDI, or PDI, containing MOFs exhibit two reductions to form mono- and di-anionic species (see Table 3.11 and Figure 3.47). The first reduction occurs at similar potentials whether NDI- or PDI-based whilst the separation is greater between the first and second reduction for NDIs (ca. 0.50 V) than for their PDI counterparts (0.26 V) as a result of greater coulombic repulsion between

electrons added into a smaller molecular framework (Table 3.11). When the results are compared, it can be seen in the table that **1** and **2** which contain **DPNDI** ligand show a second reduction occurring at approximately $E_{1/2}$ = -1.30 V with a corresponding $\Delta E_{1/2}$ of 0.43 V. However, for **3-5** which were contain **DPPNDI** the same second reduction is observed at ca. -1.43, giving an $\Delta E_{1/2}$ of 0.56 V. The MOFs made from **DPPPDI**, **6** and **7** have the least $\Delta E_{1/2}$ due to the ease with which electrons can be added to **DPPPDI** compared to either **DPNDI** or **DPPNDI,** as discussed above. The increase (negative) in the second redox potential from ca. -1.30 V in **DPNDI** based MOFs to ca. -1.43 V for **DPPNDI** implies that the imide substituents affect the redox activity of the MOFs. The potentials obtained for **1**-**2** are consistent with those reported for other NDI containing MOFs.[59] Examples of PDI containing MOFs are rarer[36] and the results presented in this work on **6** and **7** represent the first reporting of PDI-based MOF electrochemistry.

Table 3.11: Solid state cyclic voltammetry on a glassy carbon electrode using LiClO$_4$ intercalated PVC as supporting matrix, in DMF/[Bu$_4$N][BF$_4$] (0.2 M) at 0.1 Vs^{-1}. Potentials are quoted versus $E_{1/2}$ Fc$^+$/Fc used as an internal standard. Values in brackets are ΔE (=$E_p{}^a$ – $E_p{}^c$).

Compound	Linker	1st reduction		2nd reduction		$\Delta E_{1/2}$	$\Delta E(Fc)$
		CV, $E_{1/2}$/V	SW/V	CV, $E_{1/2}$/V	SW/V		
1	DPNDI	-0.88(0.08)	-0.89	-0.28(0.10)	-1.32	0.4	0.07
2	DPNDI	-0.87(0.13)	-0.89	-1.32	-1.34	0.45	0.07
3	DPPNDI	-0.88(0.10)	-0.88	-1.41(0.11)	-1.44	0.56	0.07
4	DPPNDI	-0.88(0.08)	-0.88	-1.44(0.09)	-1.44	0.56	0.08
5	DPPNDI	-0.88(0.08)	-0.88	1.43(0.09)	-1.44	0.55	0.08
6	DPPPDI	-0.86(0.10)	-0.86	-1.12(0.12)	-1.14	0.26	0.09
7	DPPPDI	-0.85(0.08)	-0.86	-1.11(0.11)	-1.13	0.26	0.08

A change in redox state of a compound occurs when current flows (as a result of electron transfer) between the compound and the electrode. For cyclic

voltammetry in solution, heterogeneous electron transfer follows mass transport of the compound along an induced concentration gradient to give a current response proportional to the square root of scan rate, and with $\Delta E \neq 0$ V, that is diffusion dependent, but not necessarily diffusion limited. This differs from the response expected if the MOF were to interact strongly with the electrode surface (chemical modification) whereby the current would be proportional to scan rate and ΔE (= $E_p{}^a - E_p{}^c$) = 0 V (a pseudo capacitive response). Since the latter is not observed then it can be concluded that the electrochemical response has a diffusive component, as can be seen from the plots of $I_p{}^c$ or $I_p{}^a$ versus the square root of scan rate (Figure 3.47c-d and Figure 3.48c-d) and that $\Delta E > 0$ V. However, unlike a standard solution response, this is not a result of the movement of the compound down a concentration gradient, since the MOFs are insoluble, therefore what is being observed is a 'diffusion-like' response that may result from either exchange-like electron hopping, as observed in high porosity MOFs featuring large apertures, or counter-ion motion.[91] The solid state cyclic voltammograms of **3** and **6** respectively representing the NDI- and PDI-based MOFs are shown in Figures 4.47 and 4.48.

In all cases we observe reasonable symmetry about a central point therefore $E_{1/2}$ values are quoted for each couple. By comparison with the response for the Fc^+/Fc couple, in solution, under these conditions, we note that ΔE (= $E_p{}^a - E_p{}^c$) for the MOFs is larger, and increases with increasing scan rate suggesting that the couples all have a component of kinetic control (Figures 3.47c-e and 3.48c-e) .[92] It is likely that the electrochemical response results from electron transfers between NDIs (or PDIs) located close to the surface, in close proximity to the electrode. The current response to reduction and re-oxidation appears to

correlate with the square root of scan rate and this may result from slow electron hopping between NDIs (or PDIs) separated by insulating 'metal' layers;[93] although the slow diffusion of electrolyte through the pores of the MOFs, as a result of ionic interactions, blocked pores or extended pathways, may also contribute to this response.[58,59,94] The inclusion of Figure 3.47f and 3.48f intended to demonstrate the initial profile and the final profile of the voltammograms. It is apparent that a change occurs between the initial and final experiments. We assign this change to the material not having stabilised on the substrate at the onset of the experiment but stability is achieved after a few cycles to produce what would be expected of NDI- and PDI-based MOFs' CVs as seen in Figure 3.47a,b and 3.48a,b.
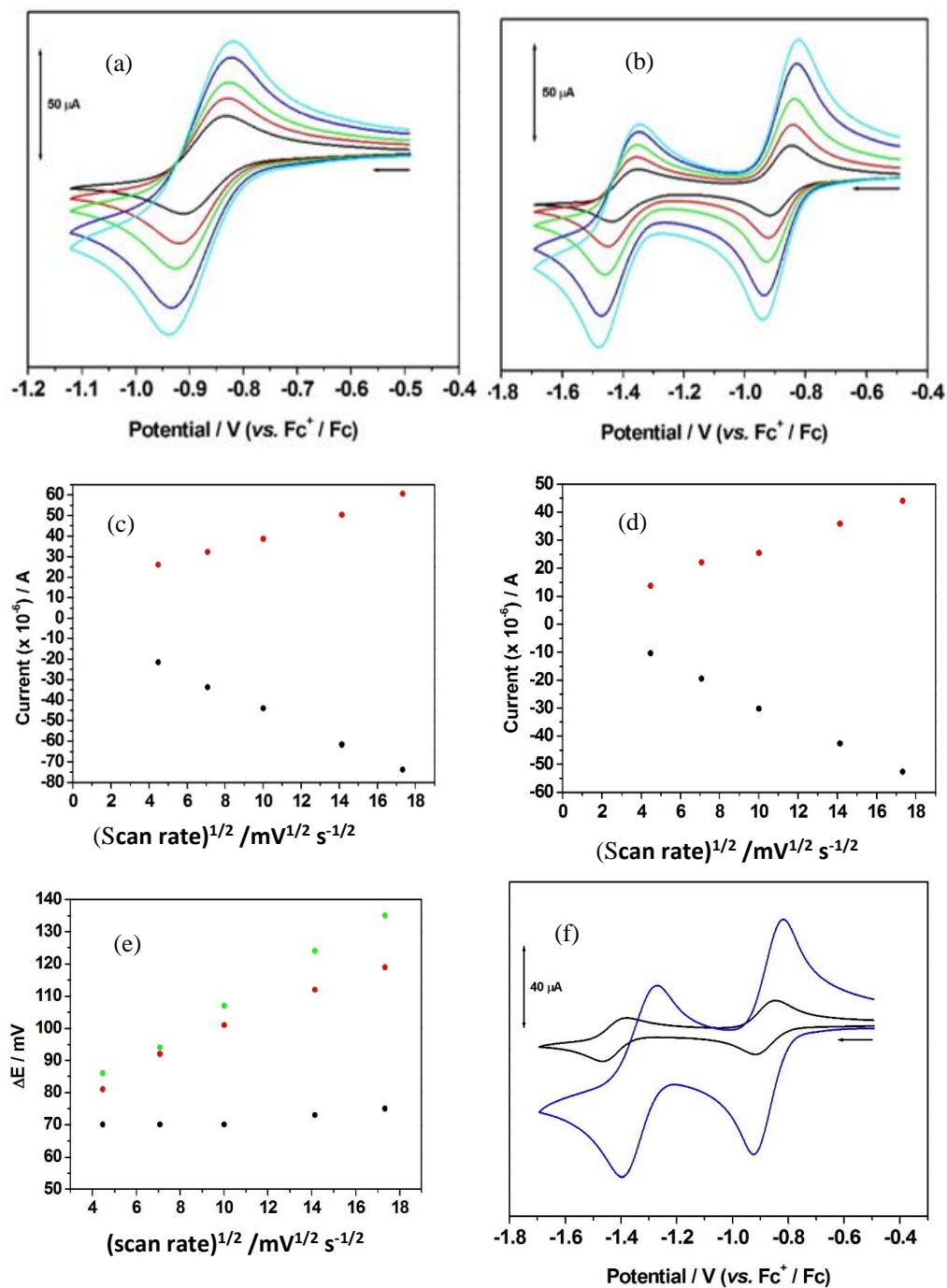
Figure 3.47 Solid state cyclic voltammetry of **3** on a glassy carbon electrode using LiClO$_4$ intercalated PVC as supporting matrix in DMF/[Bu$_4$N][BF$_4$] (0.2 M) for the first reduction (a) and second reduction (b) at scan rates of 0.02 (black), 0.05 (red), 0.10 (green), 0.20 (blue) and 0.30 (cyan) Vs^{-1}; plots of the peak anodic current (I$_p^a$) (red dots) and peak cathodic current (I$_p^c$) (black dots) versus the square root of scan rate for the first reduction (c) and the second reduction (d); (e) plot of the peak separation, ΔE (=E$_p^a$ – E$_p^c$), for the first reduction (red dots), second reduction (green dots) and ferrocene (in solution) (black dots); (f) initial profile (blue) and stabilised profile (black), at 0.1 Vs^{-1}.

Figure 4.48 Solid state cyclic voltammetry of **6** on a glassy carbon electrode using LiClO$_4$ intercalated PVC as supporting matrix in DMF/[Bu$_4$N][BF$_4$] (0.2 M) for the first reduction (a) and second reduction (b) at scan rates of 0.02 (black), 0.05 (red), 0.10 (green), 0.20 (blue) and 0.30 (cyan) Vs^{-1}; plots of the peak anodic current (I$_p^a$) (red dots) and peak cathodic current (I$_p^c$) (black dots) versus the square root of scan rate for the first reduction (c) and the second reduction (d); (e) plot of the peak separation, ΔE ($=E_p^a - E_p^c$), for the first reduction (red dots), second reduction (green dots) and ferrocene (in solution) (black dots); (f) initial profile (blue) and stabilised profile (black), at 0.1 Vs^{-1}.

2.3.3.2 UV-Vis Spectroelectrochemistry (SEC)

Samples for SEC were grown on fluorine-doped tin oxide glass slides as thin films using similar conditions to those for the respective MOFs. In a typical synthesis, the FTO glass slide was washed with alconox and water, then rinsed with acetone followed by ethanol. A self-assembled monolayer (SAM)[95] was prepared prior to the MOF reaction using 1 mmol of the carboxylic acid linker in DMF and heating in the oven at 100 $^{\circ}$C overnight. The glass slide was then removed from the solution, rinsed briefly with DMF and transferred into a 20-mL vial containing a stirred reaction mixture for MOF synthesis (using the same strategy as used for bulk MOF crystallisation). The vial was tightly capped and heated in the oven for 24 h. On completion of the reaction, the vial was removed from the oven and cooled to room temperature. The resulting FTO glass slide was washed with DMF to remove any unreacted starting materials and crystals that do not adhere strongly to the surface.

The SEC experiments were carried out by installing a conducting fluorine-doped tin oxide (FTO) glass slide, onto which a thin film of the MOF had been grown as explained above, into our home-fabricated cell containing DMF. The working electrode was the conductive FTO MOF film, the secondary electrode a Pt wire and the reference electrode a saturated calomel electrode (SCE), bridged to the cell. The cell was installed in the spectrometer and a potential applied at room temperature.

It should be noted that the key to a successful measurement of the SEC is formation of a uniform thin film. This however, was challenging for most of the MOFs. While only **3** and **6** were able to produce thin films suitable for this

experiment, the rest of the MOFs crystallised too quickly (forming clusters of crystals) to produce any uniform film on the FTO substrate. Fortunately, the SEC of **3** (Figure 3.49) is a **DPPNDI** based MOF and as such provides insight into the electrochemistry of its analogues, **4** and **5**. Similarly, the SEC of **6** (Figure 3.50) made from **DPPPDI** could be used to infer the behaviour of **7**. For the SEC of both **3** and **6**, the profiles closely match those of the free ligands, **DPPNDI** and **DPPPDI** respectively as seen in Chapter Two.

The SEC UV-vis spectra of **3** is shown in Figure 3.49. It should be noted that the use of FTO glass limits the wavelength, which is not transparent across the full UV-visible range, that can be observed during the SEC experiment and thus only the formation of the first reduced state was studied in detail. Thus, we observed only the peaks between 480 and 780 nm ($\lambda_{max} \sim$ 480 nm) corresponding to the first reduced species.[73,74] This is, however, not a problem for **6** in which the spectra of all three species – neutral, mono-anion and dianion- fall within the wavelength range for FTO glass (ca. 400 – 800 nm).[96]
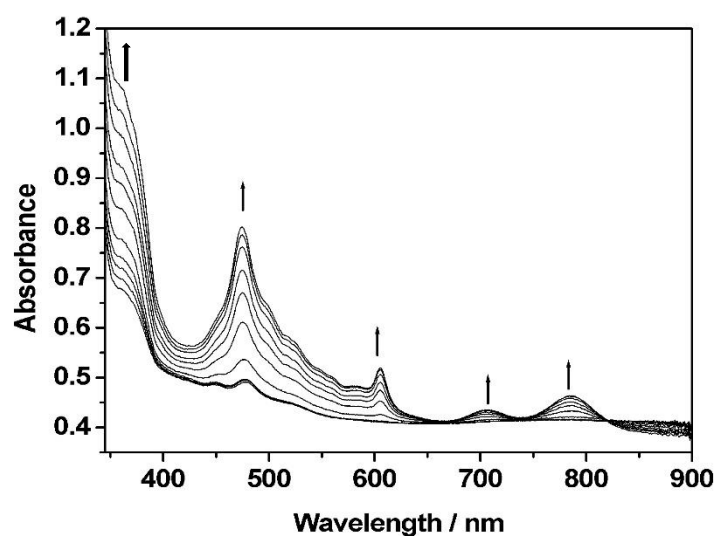
Figure 3.49: UV-vis absorption spectra of **3** showing the formation of **3**$^{\bullet-}$; Arrows indicate the progress of the stated inter-conversion.

In Figure 3.50a three peaks from about 450 – 550 nm corresponding to the neutral species of **6** can be observed and assignable to $\pi-\pi^*$ transitions. The reduction in intensity of these peaks coincides with the emergence of a new set of peaks at longer wavelengths between 570 nm and 800 nm with λ_{max} around 700 nm. As the experiment progressed, these peaks associated with the first reduced species **6**$^{\bullet-}$ decreased steadily with a concomitant appearance of the absorption bands which λ_{max} of approximately 670 nm, attributable to the second redox state **6**$^{2-}$.

The solid state spectra for both **3** and **6** clearly demonstrate the retention of the electrochemical behaviour of the parent rylene diimide linkers (measured in solution) in the resulting framework structures. Spectroelectrochemical studies reported for NDI-based MOFs using transmission mode, as performed in this study, or reflectance mode support this observation.[58,73,74]
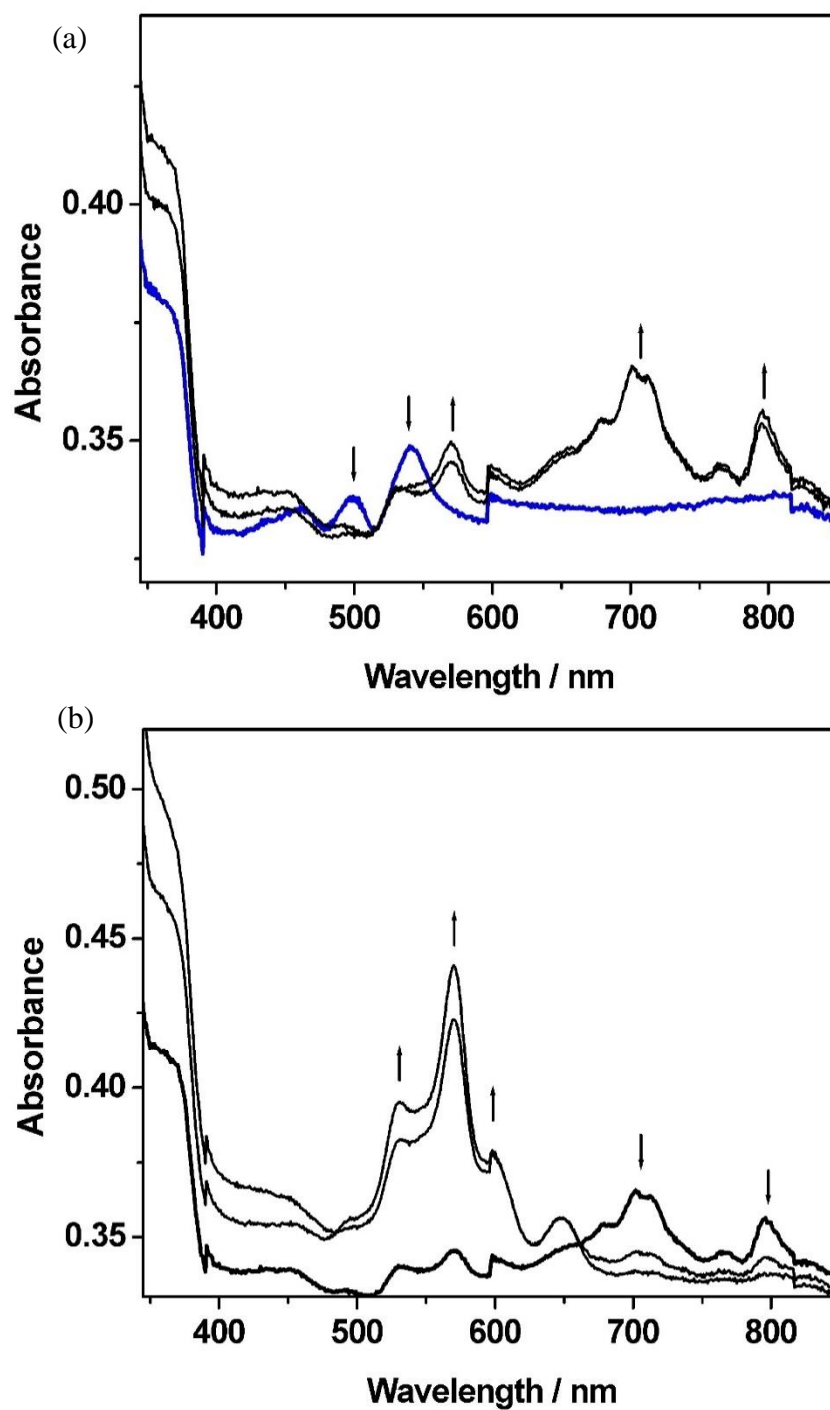
Figure 3.50: UV-vis absorption spectra of **6** showing: a) the inter-conversion of redox states between **6** (in blue) and **6**$^{\bullet-}$ (black); b) the inter-conversion of redox states between **6**$^{\bullet-}$ and **6**$^{2-}$. Arrows indicate the progress of the stated inter-conversion.

3.4 Conclusion

Seven novel rylene diimide based MOFs have been successfully synthesised using Co(II) in the case of **1**, **2**, **3**, **4**, **6**, **7** and Ni(II) for **5**. The metals adopt distorted octahedral geometry in all the reported MOFs. The frameworks were characterised using crystallographic and electroanalytic techniques. The synthesis of **1** (2-D) and **2** (3-D) shows the possibility to make MOFs of different dimensionality by merely changing the molar ratios of the starting materials. All the MOFs exhibit 2-fold interpenetration and the **pcu** topological net apart from **1** which has the **sql** net. The framework structures **1**-**7** are thermally stable up to about 450 ^{o}C, beyond which they lose integrity.

The solid state CV and the SEC measured for **3** and **6** demonstrate that the electrochemistry of these MOFs is dictated chiefly by the rylene diimide linkers, with both CV and SEC experiments producing peaks that mimic those of the free ligands in solution. It is important to reiterate that MOFs containing PDIs are not common in the literature, and this study has succeeded in adding **6** and **7** to the list, bringing the total number of coordination polymer containing PDI moieties so far discovered to seven. Also, to be noted is the fact that this work presents the first report on pyridyl-based PDI MOFs and provides the first insight into the spectroelectrochemistry of PDI-MOFs in general.

3.5 Materials and methods

3.5.1 Synthesis of [Co(NDC)(DPNDI)(NO₃)]. 2.5DMF (1)

A mixture of $Co(NO_3)_2 \cdot 6H_2O$ (30 mg, 0.103 mmol), 2,6-naphthalenedicarboxylic acid (11 mg, 0.051 mmol) and DPNDI (11 mg, 0.026 mmol) was added to DMF (2 mL) in a 20-mL scintillation vial. The vial was tightly capped and heated in an oven at 100 °C for 24 h to yield pale pink crystals of **1**. The product was found to be insoluble in common organic solvents including DMF, acetone, chloroform and DCM. Scanning electron micrographs of **1** are shown in Figure 3.51
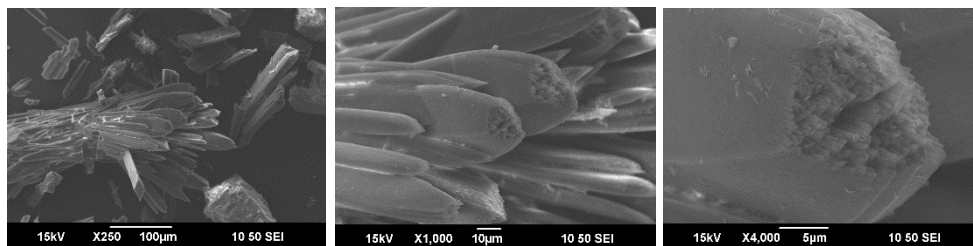
Figure 3.51: SEM images of **1** at different magnification

3.5.2 Synthesis of [Co₂(NDC)₂(DPNDI)₂].7DMF (2)

A combination of $Co(NO_3)_2 \cdot 6H_2O$ (23 mg, 0.08 mmol), DPNDI (44 mg, 0.104 mmol) and 2,6-naphthalenedicarboxylic acid (44   mg, 0.204 mmol) was dissolved in 4 mL DMF in a 20-mL scintillation vial. The solution was stirred for about 5 min, the vial was tightly capped and heated in an oven at 100 °C for 24 h to yield dark green crystals of **2**. The product was found to be insoluble in common organic solvents such as DMF, acetone, chloroform and DCM. SEM images of **2** are presented in Figure 3.52.
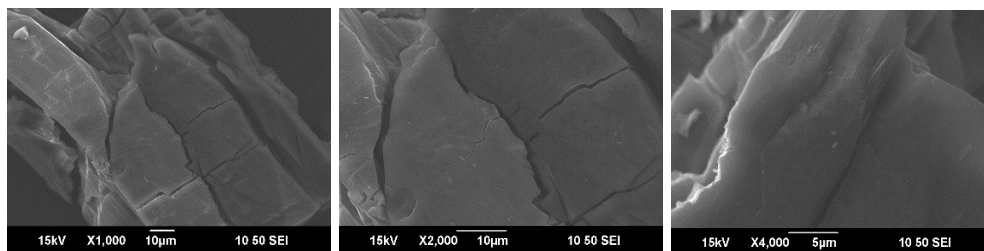
Figure 3.52: SEM images of **2** at different magnification

3.5.3 Synthesis of [Co₂(NDC)₂(DPPNDI)].6DMF (3)

Co(NO$_3$)$_2$·6H$_2$O (30 mg, 0.103 mmol), 2,6-naphthalenedicarboxylic acid (11 mg, 0.051 mmol) and DPPNDI (19 mg, 0.026 mmol) were dissolved in DMF (2 mL) in a 20-mL scintillation vial. The vial was tightly capped and heated in an oven at 100 °C for 24 h to yield purple crystals of **3**. The product was found to be insoluble in common organic solvents such as DMF, acetone, chloroform and DCM. SEM images of **3** are presented in Figure 3.53.
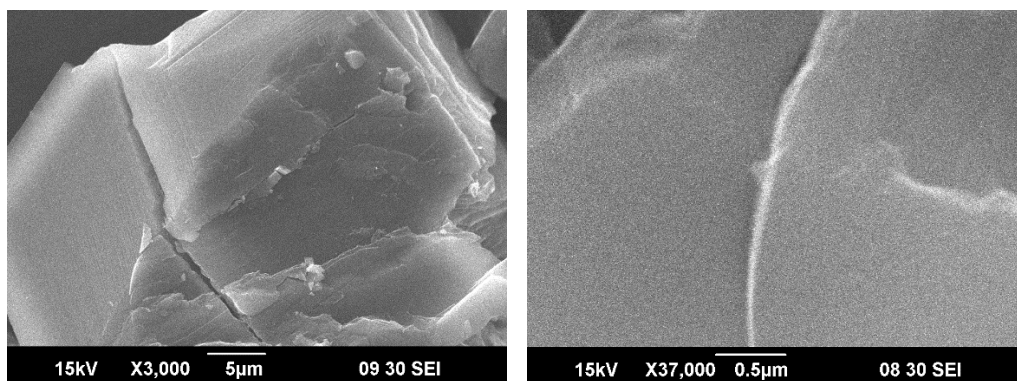
Figure 3.53: SEM images of **3** at different magnification.

3.5.4 Synthesis of [Co₂(BPDC)₂(DPPNDI)]. 3DMF.H₂O (4)

The reaction of Co(NO$_3$)$_2$·6H$_2$O (30 mg, 0.103 mmol), biphenyl-4,4'-dicarboxylic acid (11 mg, 0.051 mmol) and DPPNDI (95 mg, 0.026 mmol) in DMF (2 mL) in a 20-mL scintillation vial heated in an oven at 100 °C for 24 h produced dark brown crystals of **4**. The crystals were found to be insoluble in

174

common organic solvents like DMF, acetone, chloroform and DCM. SEM images of **4** are presented in Figure 3.54.
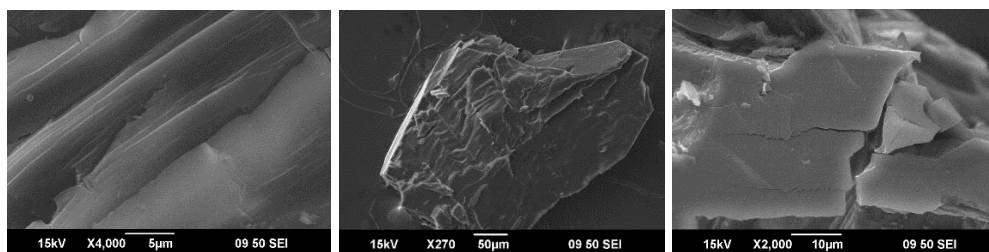
Figure 3.54: SEM images of **4** at different magnification.

3.5.5 Synthesis of [Ni$_2$(BPDC)$_2$(DPPNDI)].13.5DMF.3H$_2$O

Crystals of **5** were prepared from a reaction involving Ni(NO$_3$)$_2$·6H$_2$O (30 mg, 0.103 mmol), biphenyl-4,4'-dicarboxylic acid (11 mg, 0.051 mmol) and DPPNDI (19 mg, 0.026 mmol) in DMF (10 mL) contained in a 20-mL scintillation vial and heated in an oven at 100 °C for 24 h. The green crystals obtained were found to be insoluble in common organic solvents like DMF, acetone, chloroform and DCM. SEM images of **5** are presented in Figure 3.55.
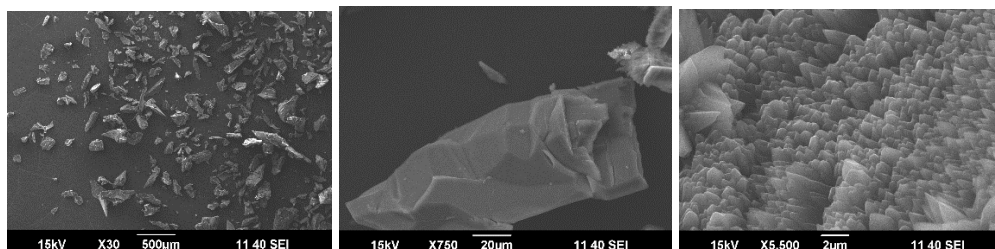
Figure 3.55: SEM images of **5** at different magnification.

3.5.6 Synthesis of [Co$_2$(BPDC)$_2$(DPPPDI)].xDMF.yH$_2$O (6)

Crystals of **6** were prepared from a reaction involving Co(NO$_3$)$_2$·6H$_2$O (15 mg, 0.052 mmol), biphenyl-4,4'-dicarboxylic acid (6 mg, 0.026 mmol) and DPPPDI (9 mg, 0.010 mmol) in DMF (1 mL) contained in a 20-mL scintillation vial and heated in an oven at 100 °C for 24 h. The resulting brownish-red crystals were

found to be insoluble in common organic solvents like DMF, acetone, chloroform and DCM. SEM images of **6** are presented in Figure 3.56.
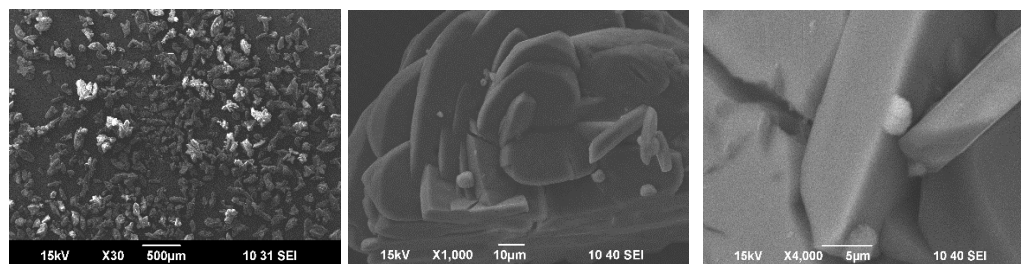
Figure 3.56: SEM images of 6 at different magnification.

3.5.7 Synthesis of [Co$_2$(NDC)$_2$(DPPPDI)].xDMF.yH$_2$O (7)

A mixture of Co(NO$_3$)$_2$·6H$_2$O (15 mg, 0.052 mmol), 2,6-naphthalenedicarboxylic acid (6 mg, 0.026 mmol) and DPPPDI (9 mg, 0.010 mmol) was added to DMF (1 mL) in a 20-mL scintillation vial. The vial was tightly capped and heated in an oven at 100 °C for 24 h to yield brownish-red crystals of **7**. The product was found to be insoluble in common organic solvents including DMF, acetone, chloroform and DCM. Scanning electron micrographs of **7** are shown in Figure 3.57.
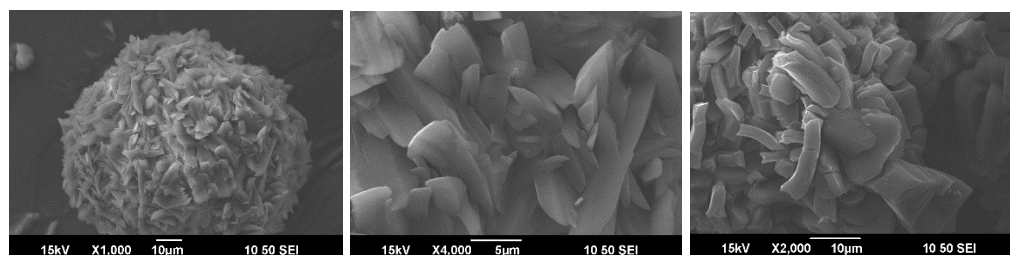
Figure 3.57: SEM images of **7** at different magnification.

3.6 References

1. Y. Ren, G. H. Chia and Z. Gao, *Nano Today*, 2013, **8**, 577– 597
2. A. A. Talin, R. E. Jones and P. E. Hopkins, *MRS Bull.*, 2016, **41**, 877–882.
3. K. J. Erickson, F. L´eonard, V. Stavila, M. E. Foster, C. D. Spataru, R. E. Jones, B. M. Foley, P. E. Hopkins, M. D. Allendorf and A. A. Talin, *Adv. Mater.*, 2015, **27**, 3453–3459.
4. Y. Fan, Z. Liu and G. Chen, *Small*, **2021**, 2100505.

5.   J. Calbo, M. J. Golomb and A. Walsh, *J. Mater. Chem. A*, 2019, **7**, 16571–16597.

6.   K. L. Mulfort and J. T. Hupp, *J. Am. Chem. Soc.*, 2007, **129**, 9604–9605.

7.   L. Sun, M.G. Campbell and M. Dincă, *Angew. Chem. Int. Ed.*, 2016, **55**, 3566-3579

8.   D. M. D'Alessandro, *Chem. Commun.,* 2016, **52**, 8957—8971.

9.   Y. Zhou and L. Han, *Coord. Chem. Rev.*, 2021, **430**, 213665.

10. G. Xu, P. Nie, H. Dou, B. Ding, L. Li and X. Zhang, *Mater. Today*, 2017, **20**, 191–209.

11. B.-Q. Ma, K. L. Mulfort and J. T. Hupp, *Inorg. Chem.*, 2005, **44**, 4912-4914.

12. M.H. You, M.H. Li, H.H. Li, Y. Chen and M.J. Lin, *Dalton Trans*, 2019, **48**, 17381-17387.

13. A. Mallick, B. Garai, M. A. Addicoat, P. St. Petkov, T. Heine and R. Banerjee, *Chem. Sci.,* 2015, **6**, 1420–1425.

14. X. Shang, I. Song, J.H. Lee, W. Cho, H. Ohtsu, G.Y. Jung, J. Ahn, M. Han, J.Y. Koo, M. Kawano, S. K. Kwak and J. H. Oh, *ACS Appl. Mater. Interfaces*, 2019, **11**, 20174-20182.

15. X. Shang, I. Song, G.Y. Jung, W. Choi, H. Ohtsu, J.H. Lee, J.Y. Koo, B. Liu, J. Ahn, M. Kawano, S. K. Kwak and J. H. Oh, *Nat. Commun.*, 2018, **9**, 3933.

16. S. A. Boer and D. R. Turner, *CrystEngComm*, 2017, **19**, 2402–2412.

17. R. Haldar, A. Mazel, M. Krstić, Q. Zhang, M. Jakoby, I. A. Howard, B. S. Richards, N. Jung, D. Jacquemin, S. Diring, W. Wenzel, F. Odobel and C. Wöll, *Nat. Commun.,* 2019, **10,** 2048.

18. Y. Ye, R.-B. Lin, H. Cui, A. Alsalme, W. Zhou, T. Yildirim, Z. Zhang, X. Xiang and B. Chen, *Dalton Trans.*, 2020, **49**, 3658 —3661.

19.   Y. Ye, Z. Ma, L. Chen, H. Lin, Q. Lin, L. Liu, Z. Li, S. Chen, Z. Zhang and S. Xiang, *J. Mater. Chem. A*, 2018, **6**, 20822 —20828.

20. J.-J. Liu, T. Liua and C.-C. Huang, *Acta Cryst*. C, 2017, **73**, 437–441.

21. F. Wei, Y. Ye, W. Huang, Q. Lin, Z. Li, L. Liu, S. Chen, Z. Zhang, and S. Xiang, *Inorg. Chem. Commun.,* 2018, **93,** 105–109.

22. L. Han, L. Qin, L. Xu, Y. Zhou, J. Sunb and Xiaodong Zou, *Chem. Commun.,* 2013, **49**, 406-408

23. J. Li, Y.-C. Xu, H.-J. Qiu and D.-R. Xiao, *CrystEngComm*, 2018, **20**, 2430–2439.

24. K. AlKaabi, C. R. Wade and M. Dincă, *Chem,* 2016, **1**, 264–272

25. N. L. Rosi, J. Kim, M. Eddaoudi, B. Chen, M. O'Keeffe and O. M. Yaghi, *J. Am. Chem. Soc.* 2005, **127**, 1504– 1518.

26. H. C. Wentz and M. G. Campbell, *Polyhedron,* 2018, **154**, 309-313.

27. R. Haldar, A. Mazel, R. Joseph, M. Adams, I. A. Howard, B. S. Richards, M. Tsotsalas, E. Redel, S. Diring, F. Odobel, and C. Wöll, *Chem. - Eur. J.,* 2017, **23**, 14316 – 14322.

28. C. Chen, Y. Wu and H. Li, *Eur. J. Org. Chem.,* **2019**, 1778–1783.

29. C. Chen and H. Li*, Z. Anorg. Allg. Chem.* 2019, **645**, 888–892.

30. Z. Guo, D. K. Panda, M. A. Gordillo, A. Khatun, H. Wu, W. Zhou and S. Saha, *ACS Appl. Mater. Interfaces,* 2017, **9**, 32413−32417.

31. H. T. D. Nguyen, Y. B. N. Tran, H. N. Nguyen, T. C. Nguyen, F. Gándara and P. T. K. Nguyen, *Inorg. Chem.,* 2018, **57**, 13772-13782.

32. S. Goswami, J. N. Nelson, T. Islamoglu, Y.-L. Wu, O. K. Farha and M. R. Wasielewski, *Chem. Mater.,* 2018, **30**, 2488−2492.

33. B. A. Johnson, A. Bhunia, H. Fei, S. M. Cohen and S. Ott, *J. Am. Chem. Soc.* 2018, **140**, 2985−2994.

34. N. Kyratzis, W. Cao, E. I. Izgorodina and D. R. Turner, *CrystEngComm*, 2018, **20**, 4115–4126.

35. S. A. Boer, Y. Nolvachai, C. Kulsing, L. J. McCormick, C. S. Hawes, P. J. Marriott and D. R. Turner, *Chem.-A Eur. J.,* 2014, **20**, 11308-11312.

36. B. Lü, Y. Chen, P. Li, B. Wang, K. Müllen and M. Yin, *Nat. Commun.,* 2019, **10**, 767

37. L. Zeng, T. Liu, C. He, D. Shi, F. Zhang and C. Duan, *J. Am. Chem. Soc.,* 2016, **138**, 3958−3961.

38. Z. Zhong, R. Li, W. Lin, X. Xu, X. Tian, X. Li, X. Chen, L. Kang, *Appl. Catal., B,* 2020, **260**, 118135.

39. A. K. Reshetnikovaa, A. I. Zvyaginaa, Yu. Yu. Enakievaa, V. V. Arslanova and M. A. Kalinina, *Colloid J.*, 2018, **80**, 684–690.

40. S. A. Boer and D. R. Turner, *Cryst. Growth Des.*, 2016, **16**, 6294−6303.

41. G.-B. Li, B.-Q. Song, S.-Q. Wang, L.-M. Pei, S.-G. Liu, J.-L. Song and Q.-Y. Yang, *ACS Omega,* 2019, **4**, 1995−2000.

42. J. He, Q. Han, J. Li, Z. Shi, X. Shi and J. Niu, *J. Catal.*, 2019, **376**, 161–167.

43. J. He, J. Li, Q. Han, C. Si, G. Niu, M. Li, J. Wang and J. Niu, *ACS Appl. Mater. Interfaces*, 2020, **12**, 2199−2206.

44. J.-J. Liu, Y. Wang, M.-J. Lin, C.-C. Huang and W.-X. Dai, *Dalton Trans.*, 2015, **44**, 484–487.

45. C. Fu, H.-Y. Wang, G.-S. Zhang, L. Li, Y.-N. Sun, J.-W. Fu and H. Zhang, *CrystEngComm*, 2018, **20**, 4849–4856.

46. M-L. Wang, C. Fu, L. Li and H. Zhang, *Inorg. Chem. Commun.,* 2018, **94**, 142–145.

47. X. Fang, X. Yuan, Y.-B. Song, J.-D. Wang and M.-J. Lin, *CrystEngComm*, 2014, **16**, 9090–9095.

48. J.-J. Liua, Z.-J. Wanga, S.-B. Xiaa, J. Liub, X. Shen, *Dyes Pigm.*, 2020, **172**, 107856.

49. V. Martínez Martínez, S. Furukawa, Y. Takashima, I. López-Arbeloa and S. Kitagawa, *J. Phys. Chem. C*, 2012, **116**, 26084−26090.

50. Y. Takashima, V. Martínez-Martínez, S. Furukawa, M. Kondo, S. Shimomura, H. Uehara, M. Nakahama, K. Sugimoto and S. Kitagawa, *Nat. Commun.,* 2011, **2,** 168.

51. R. Sola-Llano, V. Martínez-Martínez, S. Furukawa, Y. Takashima and I. López-Arbeloa, *Polymers,* 2018, **10**, 188.

52. J.-J. Liu, Y. Chen, M.-J. Lin, C.-C. Huang and W.-X. Dai, *Dalton Trans.,* 2016, **45**, 6339–6342.

53. L. Qin, S. Zhou, Y. Zhou, L. Han, *J. Solid State Chem.*, 2019, **277**, 658-664.

54.	G.-B. Li, J.-R. He, J.-M. Liu and C.-Y. Su, *CrystEngComm*, 2012, **14**, 2152–2158.

55.	J.-J. Liu, S.-B. Xia, Y.-L. Duan, T. Liu, F.-X. Cheng and C.-K. Sun, *Polymers,* 2018, **10**, 165.

56.	J. I. Lovitt, Chris S. Hawes and T. Gunnlaugsson, *CrystEngComm*, 2019, **21**, 207–217.

57.	B. D. McCarthy, E. R. Hontz, S. R. Yost, T. V. Voorhis and M Dinca, *J. Phys. Chem. Lett.* 2013, **4**, 453−458.

58.	P. M. Usov, C. Fabian and D. M. D'Alessandro, *Chem. Commun*. 2012, **48,** 3945-3947.

59.	C. F. Leong, B. Chan, T. B. Faust, P. Turner and D. M. D'Alessandro, *Inorg. Chem.* 2013, **52**, 14246−14252.

60.	C. F. Leong, B. Chan, T. B. Faust and D. M. D'Alessandro, *Chem. Sci.,* 2014, **5**, 4724–4728.

61.	P. M. Usov, C. F. Leong, B. Chan, M. Hayashi, H. Kitagawa, J. J. Sutton, K. C. Gordon, I. Hod, O. K. Farha, J. T. Hupp, M. Addicoat, A. B. Kuc, T. Heine and D. M. D'Alessandro, *Phys. Chem. Chem. Phys*., 2018, **20**, 25772-25779.

62.	S. Guha, F. S. Goodson, R. J. Clark and S. Saha, *CrystEngComm*, 2012, **14,** 1213–1215.

63.	C. Fu, G.-S. Zhang, H.-Y. Wang, L. Li, J.-W. Fu, Y.-N. Sun and H. Zhang, *CrystEngComm*, 2018, **20**, 6821–6827.

64.	E. Castaldelli, K. D. G. I. Jayawardena, D. C. Cox, G. J. Clarkson, R. I. Walton, L. Le-Quang, J. Chauvin, S. R. P. Silva and G. J.-F. Demets, *Nat. Commun.,* 2017, **8,** 2139.

65.	Z. Guo, D. K. Panda, K. Maity, D. Lindsey, T. G. Parker, T. E. Albrecht-Schmitt, J. L. Barreda-Esparza, P. Xiong, W. Zhouc and S. Saha, *J. Mater. Chem. C,* 2016, **4**, 894-899.

66.	J.-J. Liu, Y.-J. Hong, Y.-F. Guan, M.-J. Lin, C.-C. Huang and W.-X. Dai, *Dalton Trans.,* 2015, **44**, 653-658

67.	J.-J. Liu, Y.-B. Shan, C.-R. Fan, M.-J. Lin, C.-C. Huang and W-X Dai, *Inorg. Chem.,* 2016, **55**, 3680−3684.

68.	C. R. Pfeiffer, N. Biggins, W. Lewis and N.R. Champness, *CrystEngComm*, 2017, **19**, 5558–5564.

69.	G.-B. Li, J.-M. Liu, Y.-P. Cai and C.-Y. Su, *Cryst. Growth Des.,* 2011, **11**, 2763–2772.

70.	C. Li, Z. Wei, M. Pan, H. Deng, J. Jiang, C. Su, *Chin. Chem. Lett.*, 2019, **30**, 1297–1301.

71.	T. Liu, Y. Chen, Z.-L. Sun, J. Liu, J.-J. Liu, *J. Solid State Chem.,* 2019, **277,** 216–220.

72.	J.-J. Liu, Y.-F. Guan, Y. Chen, M.-J. Lin, C.-C. Huang and W.-X. Dai, *Dalton Trans*., 2015, **44**, 17312–17317.

73.	C. R. Wade, M. Li and M. Dinca, *Angew. Chem. Int. Ed*. 2013, **52**, 13377–13381.

74.	C. R. Wade, T. Corrales-Sanchez, T. C. Narayan and M. Dinca, *Energy Environ. Sci.,* 2013, **6**, 2172–2177.

75. Z. Li, J. Guo, F. Xiang, Q. Lin, Y. Ye, J. Zhang, S. Chen, Z. Zhang and S. Xiang, *CrystEngComm*, 2018, **20**, 7567–7573.

76. Y.-X. Xie, W.-N. Z. G.-C. Li, P.-F. Liu and L. Han, *Inorg. Chem.,* 2016, **55,** 549−551.

77. T.-T. Li, Y.-M. Liu, T. Wang and S.-R. Zheng, *Inorg. Chem. Commun.,* 2017, 84, 5–9.

78. Z. Xiang, Y.-B. Shan, T. Li, C.-C. Huang, X.-H. Huang and M.-J. Lin, *Acta Cryst.,* 2019, C**75**, 38–45.

79. O.V.Dolomanov, L. J. Bourhis, R. J. Gildea, J. A. K. Howard and H. Puschmann, *J. Appl. Cryst.,* 2009, **42**, 339-341.

80. G. M. Sheldrick, *Acta Cryst. A*, 2015, **71**, 3-8.

81. G. M. Sheldrick, *Acta Cryst. C*, 2015, **71**, 3-8.

82. A. L. Spek, *Acta Cryst. C.*, 2015, **71**, 9-18.

83. C. F. Macrae, I. Sovago, S. J. Cottrell, P. T. A. Galek, P. McCabe, E. Pidcock, M. Platings, G. P. Shields, J. S. Stevens, M. Towler and P. A. Wood, *J. Appl. Cryst.*, 2020, **53**, 226-235.

84. V. A. Blatov, A. P. Shevchenko and D. M. Proserpio, *Cryst. Growth Des.,* 2014, **14**, 3576–3586.

85. V. Guillerm, D. Kim, J. F. Eubank, R. Luebke, X. Liu, K. Adil, M. S. Lah and M. Eddaoudi, *Chem. Soc. Rev.*, 2014, **43**, 6141-6172

86. P. Hao, H. Zhu, Y. Pang, J. Shena and Y. Fu, *CrystEngComm*, 2020, **22**, 3371-3377.

87. E. V. Alexandrov, A. P. Shevchenko and V. A. Blatov, *Cryst. Growth Des.,* 2019, **19**, 2604-2614.

88. H. Li, M. Eddaoudi, T. L. Groy and O. M. Yaghi, *J. Am. Chem. Soc.,* 1998, **120**, 8571-8572.

89. J. Martí-Rujas, Dalton Trans., 2020, **49**, 13897-13916.

90. S. Rajendran, M. R. Prabhu, M. U. Rani, *Int. J. Electrochem. Sci.*, 2008, **3**, 282-290.

91. R. H. Palmer, J. Liu, C.-W. Kung, I. Hod, O. K. Farha and J. T. Hupp, *Langmuir*, 2018, **34**, 4707−4714.

92. S. Brochsztain, M. A. Rodrigues, G. J. F. Demets and M. J. Politi, *J. Mater. Chem.,* 2002, **12**, 1250–1255

93. H. G. Hong and T. E. Mallouk, *Langmuir*, 1991, **7**, 2362.

94. C. R. DeBlase, K. Hernández-Burgos, J. M. Rotter, D. J. Fortman, D. dos S. Abreu, R. A. Timm, I. C. N. Diógenes, L. T. Kubota, H. D. Abruña and W. R. Dichtel, Angew.Chem. Int.Ed. 2015, 54, 13225–13229].

95. S. Roy, Z. Huang, A. Bhunia, A. Castner, A. K. Gupta, X. Zou and S. Ott, *J. Am. Chem. Soc*. 2019, **141**, 15942−15950.

96. J. H. Lim, J. W. Leem and J. S. Yu, *RSC Adv*., 2015, **5**, 61284–61289.

Chapter Four   Nicotinic Acid NDI Metal-organic Frameworks

4.1 Introduction

In addition to the NDI- and PDI-based MOFs discussed in chapter three, seven novel isostructural lanthanoid framework materials (Lanthanide = La **13**, Ce **9**, Pr **10**, Nd **14**, Gd **11**, Dy **8** and Ho **12**) based on a nicotinic acid NDI, **DNNDI** have been made. Recall that the **DNNDI** linker has been discussed in chapter two. While there have been many reports on NDI MOFs on the one hand as well as nicotinic acid MOFs on the other hand, there is a drought on information regarding the combination of these two units into one ligand for the purpose of MOF synthesis.

Nicotinic acid and its isomer, isonicotinic acid, have been extensively used to make various coordination polymers with unique connectivity occasioned by the availability of both the pyridyl nitrogen and the carboxyl group.[1] These acids can also be further functionalised by the incorporation of substituent groups which, depending on the nature of the latter can act as coordinative sites.[2-5] Scheme 4.1 illustrates some nicotinic acids that have been employed in MOF syntheses. In terms of applications, nicotinic acid containing MOFs have been employed as a biodegradable therapeutic material for the delivery of bioactive molecules.[6] They have also been applied in sensing of trace proteins,[7] Cr(VI)[2] and Mn(VII).[2,3]

(a)

(b)

(c)

(d)
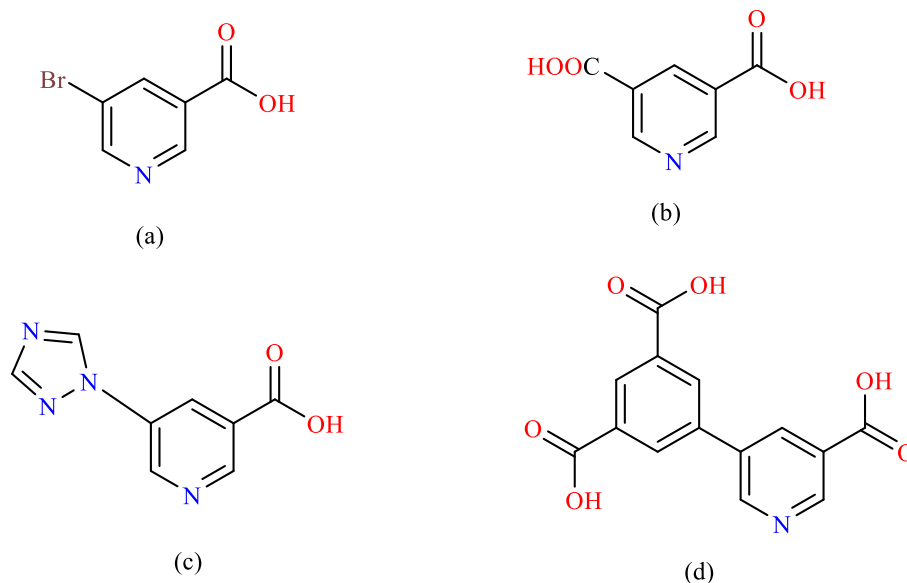
Scheme 4.1: Some nicotinic acids that have been used to construct MOFs; (a) and (b) from ref. 1, (c) from ref. 2 and (d) from ref. 3

4.2 Results and discussion

The synthetic procedures for all the **DNNDI** based MOFs discussed here are similar differing only in the metal ions employed therein. Similarly, all the MOFs are highly similar, forming the same framework structure. Of the seven MOFs, five – Ce **9**, Pr **10**, Gd **11**, Dy **8** and Ho **12** – crystalised in the tetragonal space group $I4_1/a$ while La **13** and Nd **14** adopted the monoclinic space group C2/c. Owing to these different crystal systems, two MOFs, each representing those belonging to one system, will be selected and discussed in detail.

4.2.1 Synthesis and crystal structure of [Dy(DNNDI)$_{1.5}$.DMF].DMF, 8

Crystals of **8** suitable for single crystal X-ray diffraction experiments were prepared through the solvothermal reaction of Dy(NO$_3$)$_3$.5H$_2$O with **DNNDI** in a 20 mL scintillation vial using DMF as the reaction solvent. The reaction lasted for 24 h in an oven whose temperature was set to 100 ^{o}C. The crystal was kept at 120 K during data collection on a single crystal X-ray diffractometer. Using

185

Olex-2,[8] the structure was solved with the SHELXT[9] structure solution program using Intrinsic Phasing and refined with the SHELXL[10] refinement package using Least Squares minimisation. The crystal data and refinement parameters for **8** are given in Table 4.1.

Table 4.1: Crystallographic data and refinement parameters for 8 (Note: the empirical formula in this table was obtained after a solvent mask has been applied).

Empirical formula	$C_{43.5}H_{25.5}DyN_{7.5}O_{13.5}$
Formula weight	1031.71
Temperature/K	120(2)
Crystal system	tetragonal
Space group	$I4_1/a$
a/Å	38.6806(3)
b/Å	38.6806(3)
c/Å	16.10120(10)
α/°	90
β/°	90
γ/°	90
Volume/Å³	24090.4(4)
Z	16
ρ_{calc}g/cm³	1.138
μ/mm⁻¹	7.108
F(000)	8208.0
Crystal size/mm³	$0.281 \times 0.044 \times 0.044$
Radiation	Cu Kα (λ = 1.54184)
2θ range for data collection/°	7.5 to 145.606
Index ranges	$-47 \leq h \leq 47, -47 \leq k \leq 43, -19 \leq l \leq 19$
Reflections collected	196799
Independent reflections	11961 [R_{int} = 0.0749, R_{sigma} = 0.0271]
Data/restraints/parameters	11961/117/618
Goodness-of-fit on F²	1.129
Final R indexes [I>=2σ (I)]	R_1 = 0.0637, wR_2 = 0.1763
Final R indexes [all data]	R_1 = 0.0671, wR_2 = 0.1783
Largest diff. peak/hole / e Å⁻³	1.10/-0.73

Analysis of the single crystal data reveals that **8** crystallises in the tetragonal centrosymmetric space group $I4_1/a$. The asymmetric unit comprises a dysprosium atom, a full, and a half **DNNDI** ligand both of which are coordinated to Dy(III) in a monodentate fashion, one metal-coordinated DMF and a half-occupied solvate DMF as shown in Figure 4.1.
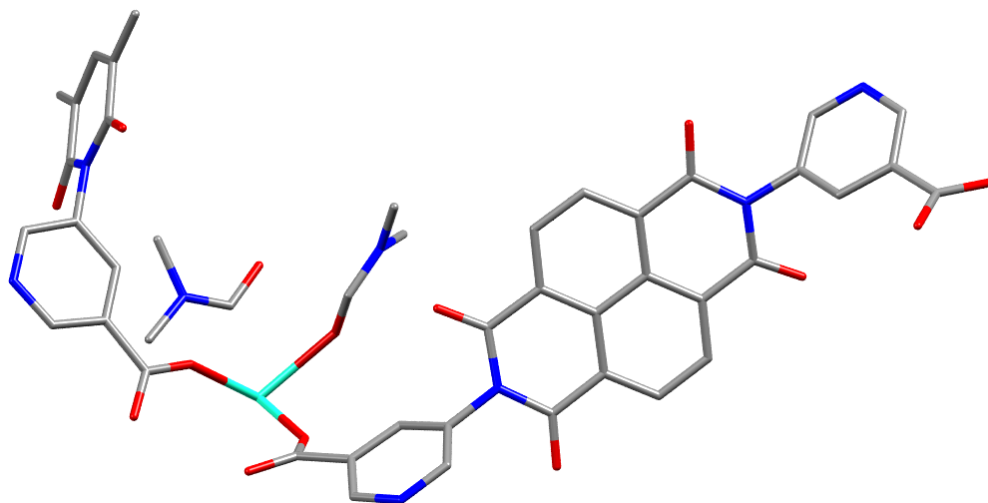
Figure 4.1: Asymmetric unit of **8** (grey = C, cyan = Dy, blue = N and red = O; hydrogen atoms have been removed for clarity)

The extended structure of **8** is a three-dimensional periodic framework with Dy-O-C rod SBUs[11] composed of 8-coordinated Dy(III) with a distorted bicapped trigonal prism geometry[12] around the metal centre (Figure 4.2). Each dysprosium atom is bonded to six carboxylates, each from a different **DNNDI** ligand and a terminal DMF guest. Four of the carboxyl groups are coordinated to the metal in a bridging bis-bidentate fashion as in mode A (Scheme 4.2) in which two of the carboxylates are shared with adjacent dysprosium neighbours on either side of the dysprosium atom in question. The remaining two carboxylates are bonded to the metal centre in a chelating/bridging bidentate mode at one end and bridging bidentate mode at the other end as in modes B and B' respectively (Scheme 4.2). Each rod is joined at the corner and edge forming DyO_8 polyhedra. The **DNNDI** units, which exhibit an *anti* conformation,[14] connect each rod to four neighbouring rods, producing an unprecedented topological net with the Schlafli symbol $\{4^2.6^2.8^2\}\{4^3.6^3\}2\{4^7.6^8\}2$ (Figure 4.2d). The metal-metal distance in the one-dimensional rod is 4.370 Å. This value is close to 4.249 Å for a samarium-nicotinic acid MOF reported by Goldberg *et al*[1] and 4.390 Å for a

lanthanum-nicotinic acid MOF studied by Du and co-workers.[7] Details of the

metal-oxygen bond lengths and angles will be presented later in the chapter and

can be found in the appendix section.
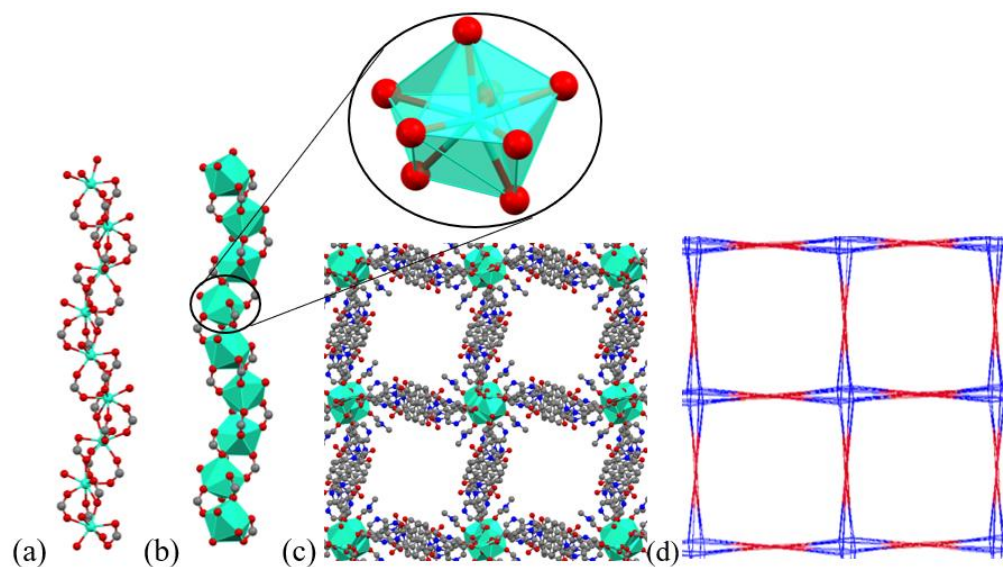
Figure 4.2: SBU of **8** shown using (a) ball and stick representation and (b) polyhedra, both of which are viewed alon the crystallographic *a*-axis. (c) Packed structure of **8** demonstrating how the SBUs are linked together, viewed along the *c*-axis i.e. along the direction of the SBU chain. (Cyan = dysprosium, grey = carbon, blue = nitrogen and red = oxygen)
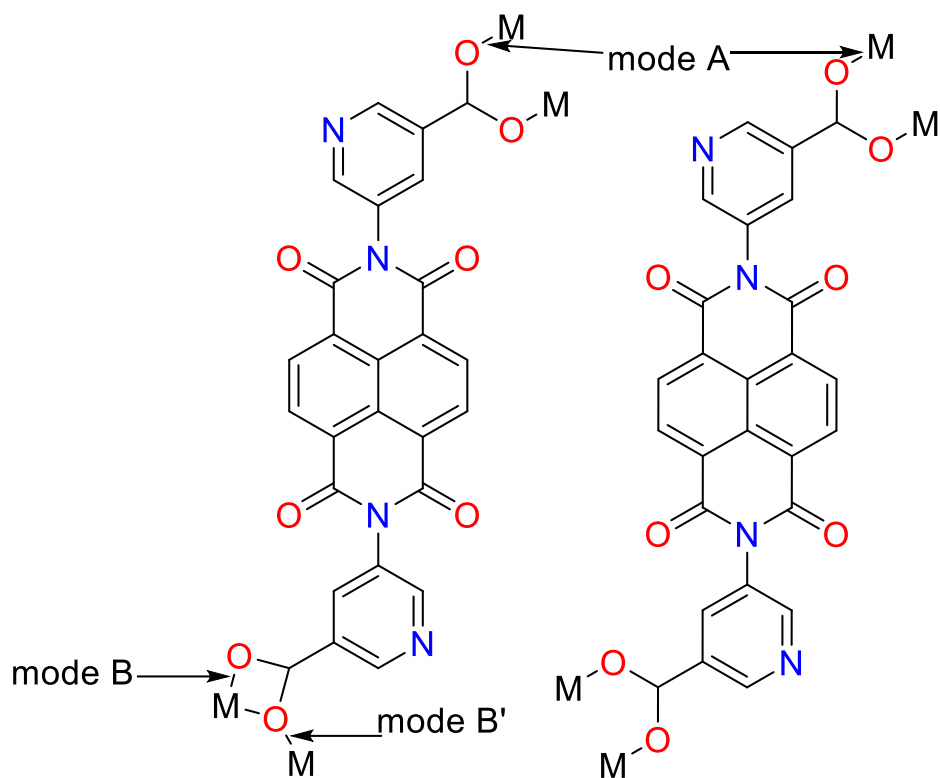
Scheme 4.2: Coordination modes of DNNDI ligand in 8 showing the anti-conformation.

Close inspection of the structure of **8** unveils two types of interaction exhibited by the framework. One of the interactions is a π-π stacking interaction between two (NDI) napthalene units with a stacking distance of 3.418 Å (see Figure 4.3). The second interaction is a lone pair-π interaction with a distance of 3.424 Å resulting from a much twisted naphthalene unit with respect to the plane of the nicotinic acid rings. This twist, with a dihedral angle of 81.1° between the pyridyl ring of the nicotinic acid and the naphthalene plane, has the overall consequence of aligning the carboxy groups of the naphthalene core such that lone pair-π interaction with the adjacent naphthalene core is made possible; thereby acting to stabilise the overall structure. However, for the pair of NDI units that π-stack, the dihedral angles made by the two nicotinic acid rings with the naphthalene core are 53.26° and 68.89°, significantly smaller than that discussed above.

Further inspection of Figure 4.3 shows that the **DNNDI** units that exhibit the high dihedral angle of 81.1^o coordinate to the metal through mode A only (Scheme 4.2) while those that are less twisted, and which exhibit π-π stacking, are bonded to the metal centres through all the modes – mode A at one end, and modes B and B' at the other end. It is also clear, when analysing the structure, that the pyridyl nitrogen of the nicotinic acid moiety is not involved in coordination to the metal and could be useful for some post-synthetic modification and, in general, the behaviour of **8** towards guest species.
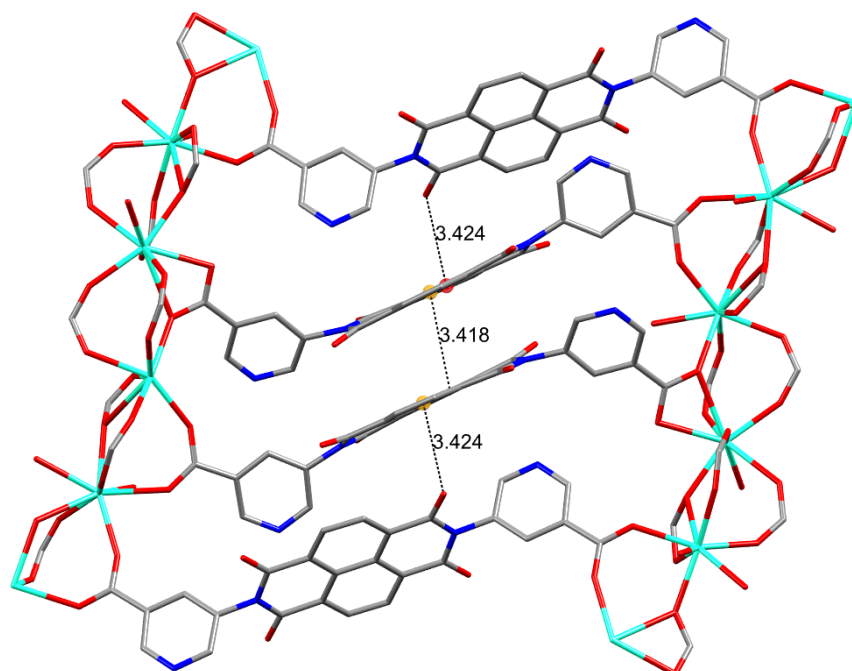
Figure 4.3: Packing motif of DNNDI ligands in **8** along the a-c plane. (Cyan = dysprosium, grey = carbon, blue = nitrogen and red = oxygen, hydrogen atoms, chelating DMF and occluded DMF have been removed for clarity)

As the analogues of **8** based on Ce **9**, Pr **10**, Gd **11** and Ho **12** all crystallised in the same tetragonal centrosymmetric spacegroup I4$_1$/a, the crystal structures are all highly similar; hence these will not be discussed on an individual basis. However, a comparison will be made across all the structures below. Because the frameworks containing La **13** and Nd **14** adopt the same framework but

crystallise in the monoclinic space group C2/c, different to the I4$_1$/a tetragonal space group for **8 – 12**, only the structure of **14** will be described in detail.

4.2.2 Synthesis and crystal structure of [Nd$_2$(DNNDI)$_3$(DMF)$_2$].9.5DMF, 14

Compound **14** was synthesised solvothermally by the reaction of a mixture of Nd(NO$_3$)$_3$.6H$_2$O with **DNNDI** in a 20 mL scintillation vial using DMF as the reaction solvent. The solution in the vial was stirred for 5 mins, the vial tightly capped and transferred into an oven whose temperature was set to 100 ^{o}C. The reaction was stopped after 24 h and bunches of needle-like crystals suitable for SCXRD were observed. A crystal of **14** was selected and kept at 100 K during data collection on a single crystal X-ray diffractometer. Using Olex-2,[8] the structure was solved with the SHELXT[9] structure solution program using Intrinsic Phasing and refined with the SHELXL[10] refinement package using Least Squares minimisation. The crystal data and refinement parameters for **14** are presented in Table 4.2.

Table 4.2: Crystallographic data and refinement parameters for **14**.

Empirical formula	$C_{94.5}H_{68.5}N_{17.5}Nd_2O_{29.5}$
Formula weight	2209.64
Temperature/K	100(2)
Crystal system	monoclinic
Space group	C2/c
a/Å	52.2286(4)
b/Å	16.40470(10)
c/Å	38.9362(3)
α/°	90
β/°	131.8240(10)
γ/°	90
Volume/Å³	24860.0(4)
Z	8
ρ_{calc}g/cm³	1.181
μ/mm⁻¹	0.830
F(000)	8912.0
Crystal size/mm³	-
Radiation	Synchrotron ($\lambda = 0.6889$)
2Θ range for data collection/°	2.028 to 49.038
Index ranges	$-62 \le h \le 62, -18 \le k \le 19, -46 \le l \le 46$
Reflections collected	113689
Independent reflections	22647 [$R_{int} = 0.0610$, $R_{sigma} = 0.0550$]
Data/restraints/parameters	22647/114/1374
Goodness-of-fit on F²	1.065
Final R indexes [I>=2σ (I)]	$R_1 = 0.0506$, $wR_2 = 0.1469$
Final R indexes [all data]	$R_1 = 0.0572$, $wR_2 = 0.1504$
Largest diff. peak/hole / e Å⁻³	2.48/-1.69

The asymmetric unit of **14** consists of two neodymium atoms, a total of three molecules of **DNNDI**, two molecules of metal-coordinated DMF and three and a half ordered free DMF molecules and 6 molecules of disordered DMF molecules. The disordered DMF molecules were removed using Olex-2 feature called Mask[8] which is a semblance of PLATON SQUEEZE.[14] Each Nd(III) is bound by two carboxylic groups – one from a molecule of the **DNNDI** ligand and the other from half a molecule of **DNNDI** – in a bridging isomonodentate fashion. Each Nd(III) is also coordinated to a DMF molecule as shown in Figure 4.4.
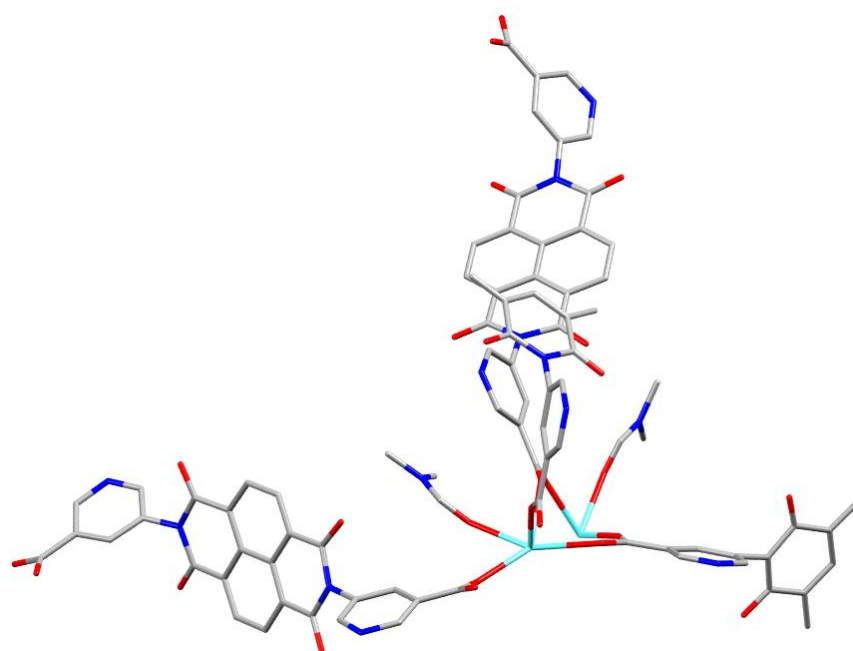
Figure 4.4: Asymmetric unit of **14** viewed along the crystallographic *b*-axis. (Cyan = Neodymium, grey = carbon, blue = nitrogen and red = oxygen, hydrogen atoms, coordinated DMF and occluded DMF have been removed for clarity).

The extended structure (Figure 4.5a) reveals that indeed **14** adopts an analogous framework to the dysprosium MOF **8** discussed above; similar SBUs and connectivity around the metal centres. It could be seen, on careful analysis of the structure of **14**, that the DMF molecules coordinated to the metal centres point diagonally into the somewhat distorted squared pore from each of the four corners – again this is similar to what is found in **8**. The π-π stacking interaction and the lone pair-π interactions found in **8** are also present in the rest of the frameworks within similar distance. After removal of all the free solvent molecules in the pore, the solvent accessible void was visualised with the aid of Mercury crystal software[15]. This revealed that for **14** 6652.02 Å^3/unit cell (i.e., 26.8%) is accessible to solvent (Figure 4.5b and Table 4.3).
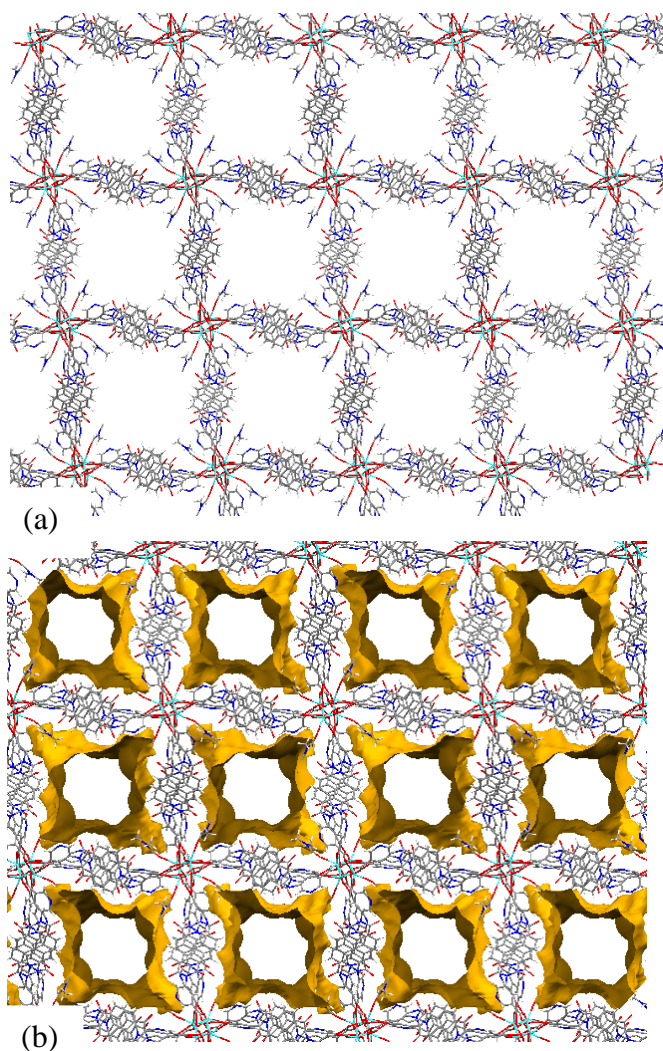
Figure 4.5: Structure of **14** showing the (a) grown structure; and (b) solvent accessible void. (Cyan = Neodymium, grey = carbon, blue = nitrogen and red = oxygen, hydrogen atoms and occluded DMF have been removed for clarity).

For the purpose of comparison, some crystallographic data and refinement parameters for each of the MOFs are presented in Table 4.3. It is worthy of note that the voids are quite similar for all the frameworks irrespective of the crystal system in which they crystallised.

Table 4.3 Key crystallographic data for 8 – 14

	Dy(III) 8	Ce(III) 9	Pr(III) 10	Gd(III) 11	Ho(III) 12	La(III) 13	Nd(III) 14
Crystal system	Tetragonal	Tetragonal	Tetragonal	Tetragonal	Tetragonal	Monoclinic	Monoclinic
Space group	$I4_1/a$	$I4_1/a$	$I4_1/a$	$I4_1/a$	$I4_1/a$	C2/c	C2/c
Temp /K	120(2)	120(2)	120(2)	120(2)	120(2)	100(2)	100(2)
a/Å	38.6806 (3)	38.3333 (6)	38.5013 (8)	38.6994 (3)	38.5579 (6)	51.7695 (4)	52.2286 (4)
b/Å	38.6806 (3)	38.3333 (6)	38.5013 (8)	38.6994 (3)	38.5579(6)	16.57240 (10)	16.40470 (10)
c/Å	16.10120 (10)	16.3408 (4)	16.3519 (5)	16.1696 (2)	16.0368 (4)	39.0913 (3)	38.9362 (3)
α/°	90	90	90	90	90	90	90
β/°	90	90	90	90	90	131.2180 (10)	131.8240 (10)
γ/°	90	90	90	90	90	90	90
Volume/Å³	24090.4 (4)	24011.9 (10)	24239.2 (13)	24216.3 (5)	23842.1(10)	25227.7 (4)	24860.0 (4)
Solvent accessible void/unit cell/ Å³	6107.11 (25.4%)	5802.53 (24.2%)	6059.81 (25.0%)	6128.72 (25.3%)	5909.62 (24.8%)	6689.44 (26.5%)	6652.02 (26.8%)
Z	16	16	16	16	16	8	8
ρ_{calc}g/cm³	1.138	1.118	1.106	1.087	1.216	1.14	1.181
μ/mm⁻¹	7.108	6.332	6.636	7.529	2.993	0.681	0.83
F(000)	8208	8096	8072	7872	8736	8736	8912
Crystal size/mm³	0.281 × 0.044 × 0.044	0.143 × 0.049 × 0.026	0.103 × 0.057 × 0.043	0.245 × 0.057 × 0.041	0.125 × 0.078 × 0.046	-	-
Radiation	Cu Kα (λ = 1.54184)	Cu Kα (λ = 1.54184)	Cu Kα (λ = 1.54184)	Cu Kα (λ = 1.54184)	Cu Kα (λ = 1.54184)	Synchrotron (λ = 0.6889)	Synchrotron (λ = 0.6889)
2Θ range for data collection/°	7.5 to 145.606	6.522 to 102.28	7.456 to 102.014	7.482 to 104.436	7.528 to 101.888	2.028 to 49.038	2.028 to 49.038
Reflections collected	196799	63739	104370	106736	99995	116019	113689
Independent reflections	11961	6487	6448	6796	6341	23006	22647
Data/restraints/ parameters	11961/117/618	6487/501/592	6448/925/591	6796/918/571	6341/0/639	23006/2063/1327	22647/114/1374
Goodness-of-fit on F²	1.129	1.091	1.078	1.088	1.11	1.133	1.065
Final R indexes [I>=2σ (I)]	$R_1 =$ 0.0637, $wR_2 =$ 0.1763	$R_1 =$ 0.0676, $wR_2 =$ 0.2031	$R_1 =$ 0.1012, $wR_2 =$ 0.2616	$R_1 =$ 0.1267, $wR_2 =$ 0.3090	$R_1 =$ 0.0811, $wR_2 =$ 0.2399	$R_1 =$ 0.1678, $wR_2 =$ 0.4310	$R_1 =$ 0.0506, $wR_2 =$ 0.1469
Final R indexes [all data]	$R_1 =$ 0.0671, $wR_2 =$ 0.1783	$R_1 =$ 0.0823, $wR_2 =$ 0.2113	$R_1 =$ 0.1117, $wR_2 =$ 0.2675	$R_1 =$ 0.1276, $wR_2 =$ 0.3094	$R_1 =$ 0.0983, $wR_2 =$ 0.2526	$R_1 =$ 0.1778, $wR_2 =$ 0.4351	$R_1 =$ 0.0572, $wR_2 =$ 0.1504
Largest diff. peak/hole / e Å⁻³	1.10/-0.73	1.36/-0.75	1.65/-1.05	2.25/-2.71	1.54/-0.48	3.68/-3.52	2.48/-1.69

The metal-oxygen (M-O) bond lengths are shown in Scheme 4.3 and Table 4.4. It could be deduced on careful examination of Table 4.4 that the M-O bond length decreases as the atomic number of the lanthanide increases. This trend can be attributed to lanthanide contraction. The metal-metal (M-M) bond lengths (Table 4.4 and bar chart) also show steady decrease from La(III)- to Ho(III)-based system. This trend is consistent with those reported for lanthanoid MOFs.[7] Tables containing important bond angles can be found in the appendix section. An important observation in all seven MOFs reported in this chapter is the fact that the pyridyl nitrogen of the nicotinic acid moiety was not involved in any form of coordination; hence some post-synthetic modification could be performed on these sites. The presence of this Lewis basic pyridyl site can also enhance the sensing ability of these MOFs.[16]
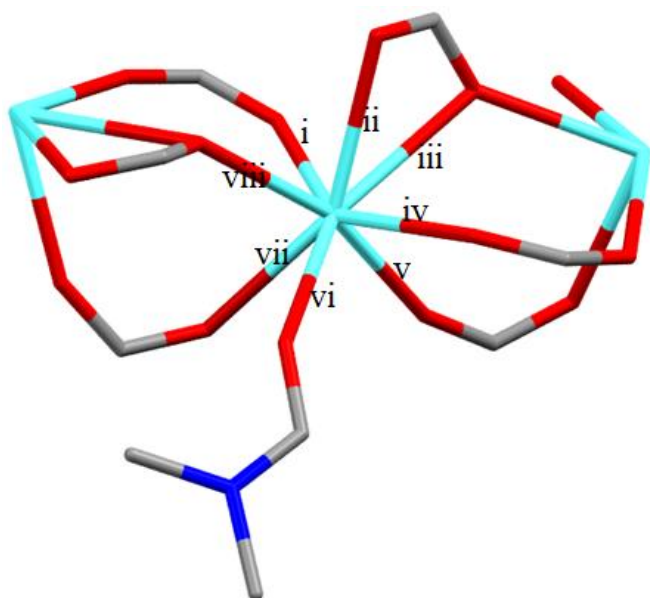
Scheme 4.3: Metal-oxygen (M-O) bond lengths in 8 – 14; (for actual values, see Table 4.4)

Table 4.4: Metal-oxygen (M-O) and metal-metal (M-M) bond lengths in **8 – 14**. [a]The lanthanides have been arranged in order of increasing atomic number from top to bottom. [b]La(III) and Nd(III) systems exhibit two unequal but similar M-O and M-M bond lengths. The esds are in parenthesis. The bar chart showing this steady decrease in M-O and M-M average bond lengths is shown below the table.

compound/ system	Bond lengths (Å)									
	i	ii	iii	iv	v	vi	vii	viii	Average M-O	Average M-M
La(III) 13[a,b]	2.438 (14); 2.465 (15)	2.580 (12); 2.580 (12)	2.689 (10); 2.703 (10)	2.419 (13); 2.404 (15)	2.391 (12); 2.351 (13)	2.510 (13); 2.522 (16)	2.482 (14); 2.493 (12)	2.473 (10); 2.474 (9)	2.509	4.493
Ce III) 9[a]	2.422 (7)	2.554 (6)	2.695 (5)	2.391 (7)	2.327 (6)	2.466 (7)	2.469 (6)	2.437 (6)	2.470	4.458
Pr(III) 10[a]	2.434 (11)	2.489 (10)	2.695 (9)	2.358 (11)	2.339 (10)	2.443 (10)	2.463 (10)	2.426 (10)	2.456	4.453
Nd(III) 14[a,b]	2.420 (3); 2.421 (3)	2.532 (3); 2.520 (3)	2.622 (3); 2.660 (3)	2.348 (3); 2.333 (3);	2.365 (3); 2.365 (3)	2.450 (3); 2.443 (3)	2.443 (3); 2.456 (3)	2.415 (3); 2.416 (3)	2.451	4.444
Gd(III) 11[a]	2.365 (12)	2.453 (11)	2.634 (10)	2.266 (12)	2.317 (12)	2.416 (11)	2.418 (11)	2.349 (10)	2.402	4.390
Dy(III) 8[a]	2.317 (4)	2.438 (4)	2.609 (3)	2.281 (4)	2.258 (4)	2.373 (4)	2.371 (4)	2.329 (3)	2.372	4.370
Ho(III) 12[a]	2.303 (7)	2.423 (7)	2.604 (6)	2.267 (8)	2.232 (7)	2.356 (8)	2.375 (7)	2.303 (7)	2.358	4.355
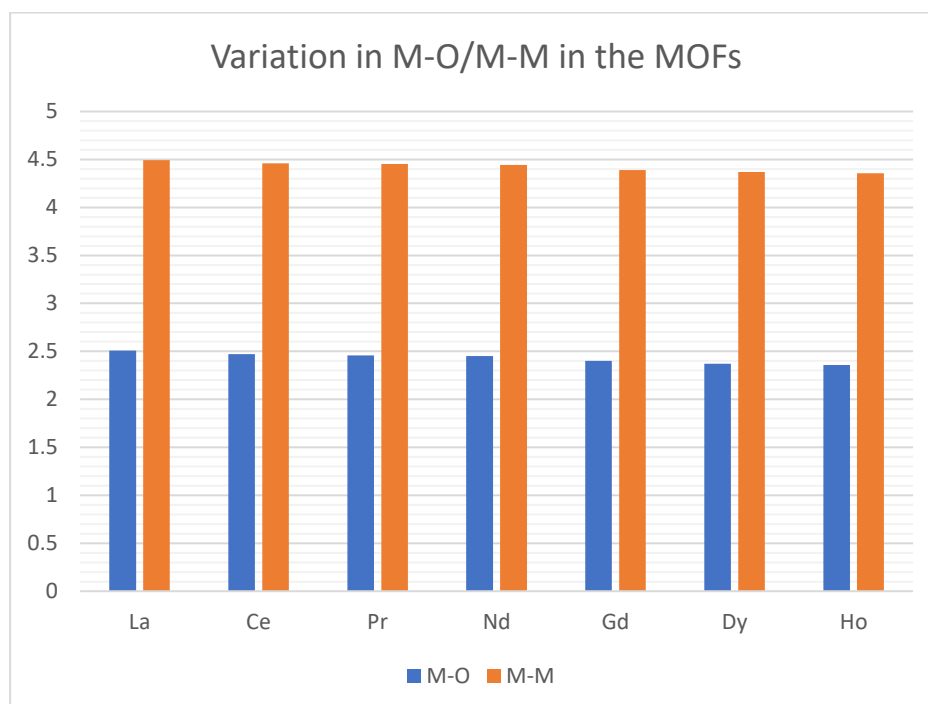
4.2.4 Powder X-ray diffraction experiment

Since compounds **8 – 12** crystallised in the same crystal system and show similar PXRD patterns, only that of **8** (Figure 4.6) will be presented here and the rest can be found in the appendix section. In the same vein, that of **14** (Figure 4.7) is used to represent **13**. From these figures it can be seen that the experimental powder patterns match well with the simulated patterns for the major peaks. However, like the case in **1-7**, there are a couple of low intensity peaks that do not agree which could be due to the presence of impurity in the sample.
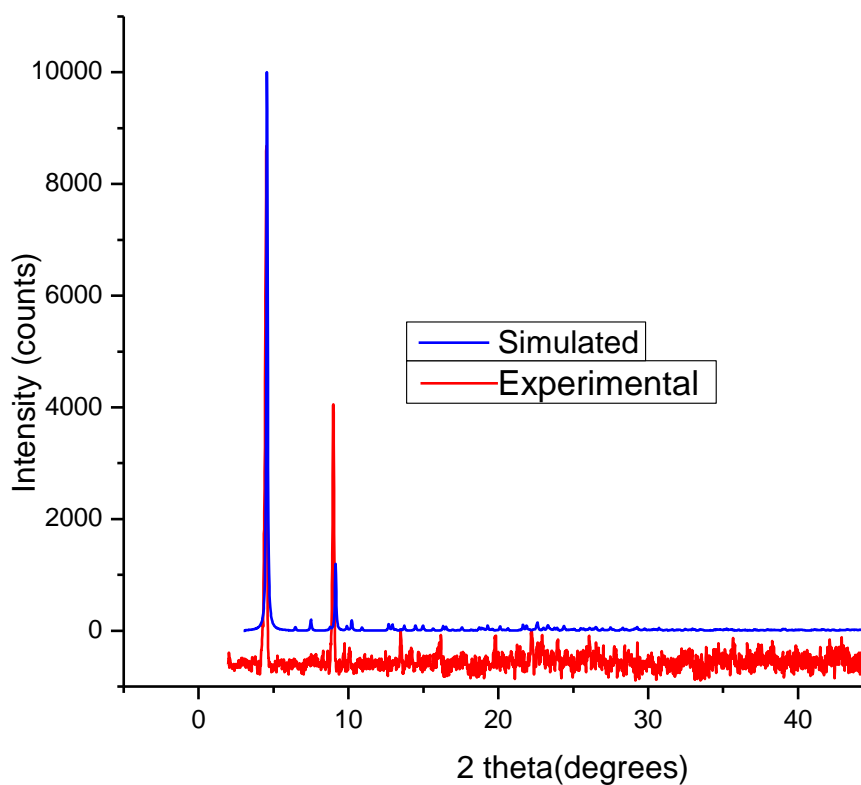
Figure 4.6: PXRD pattern of **8**.
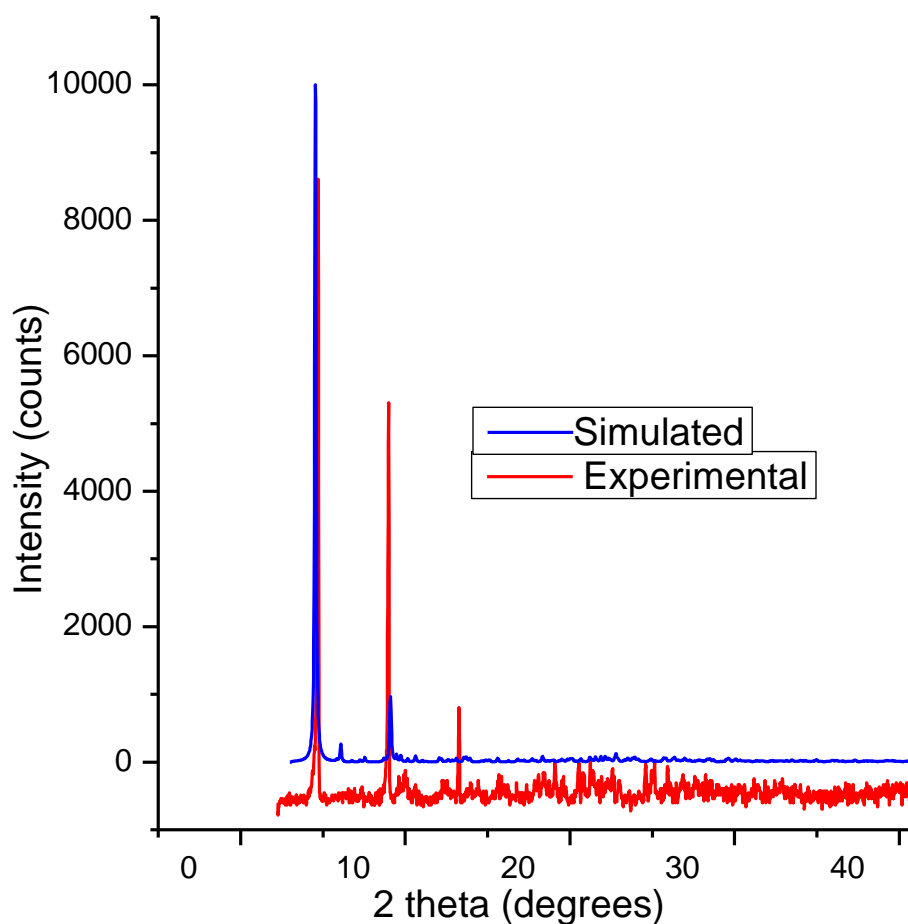
Figure 4.7: PXRD pattern of **14**.

4.2.5 Thermogravimetric analysis (TGA).

The thermal stability of the MOFs was assessed through TGA. Just as with the case of **1** – **7** reported in chapter 3, the TGA of **8** – **14** were recorded using samples that the original reaction solvent (DMF) had been exchanged with acetone. As could be seen in Figure 4.8, all the framework structures **8** – **14** are stable up to about 460 °C after which there is a steep slope which indicates the total collapse of the materials. A careful look at the curve reveals that the Nd(III) system shows a slightly different profile. This is most likely due to the fact that during the solvent exchange procedure, all the DMF molecules in the pore were completely exchanged with acetone molecules.
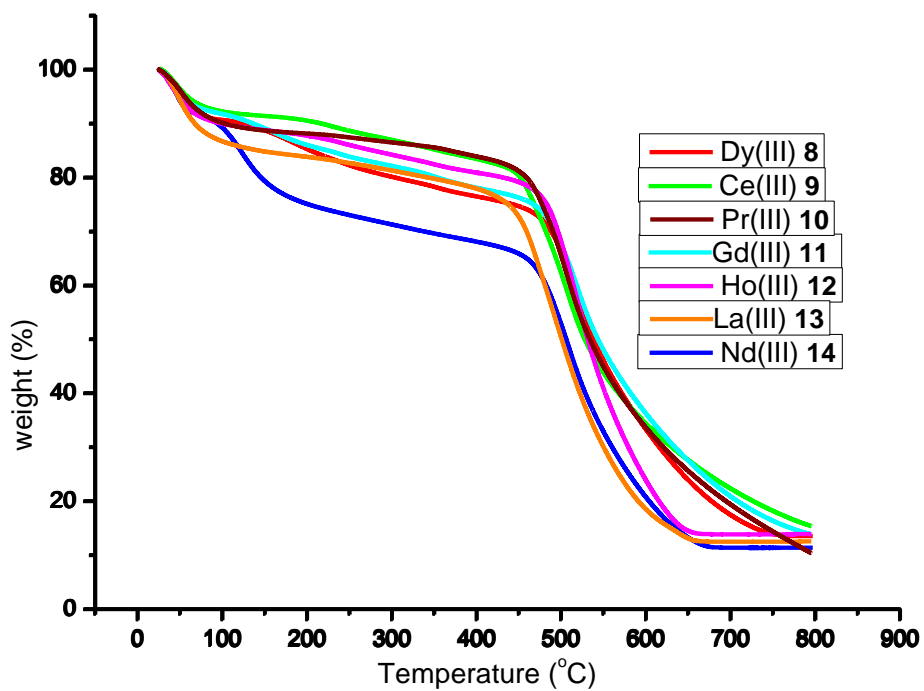
Figure 4.8: TGA curves of **8 – 14**

4.2.6 Scanning Electron Microscopy (SEM)/ Energy Dispersive X-Ray Analysis (EDX).

The micrographs of all the MOFs **8 –14** show similar morphology. The materials

could be described as bunches of needle-shaped crystals (Figure 4.9).
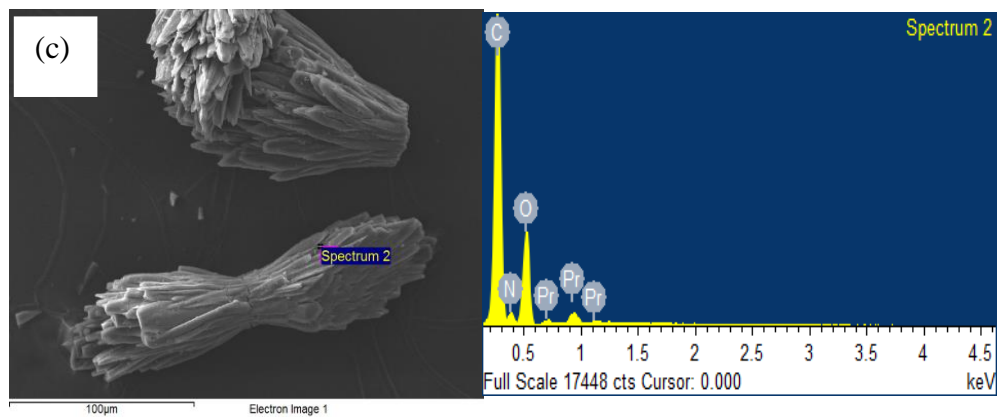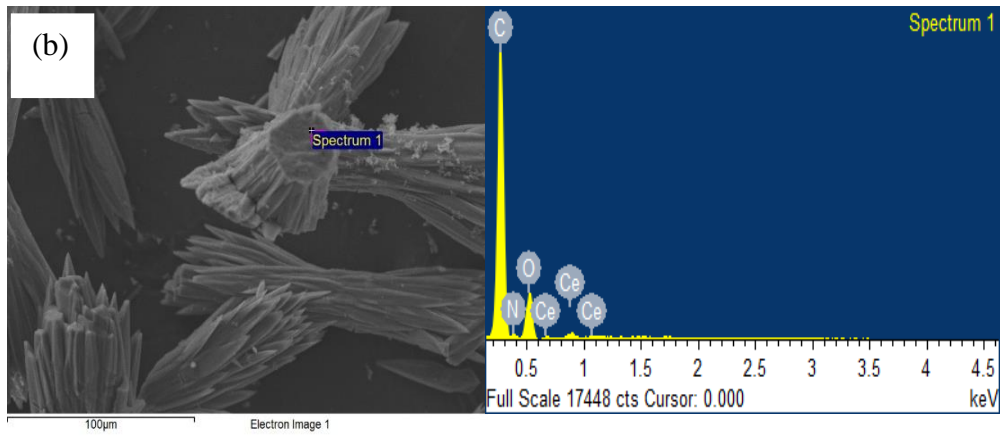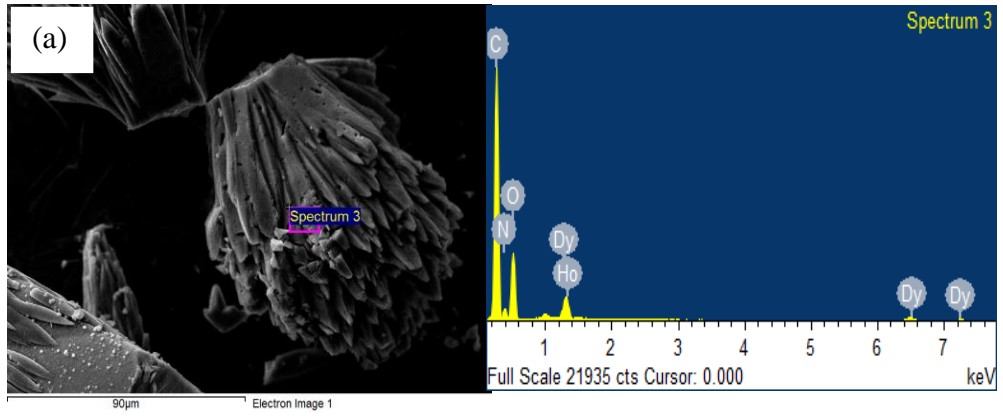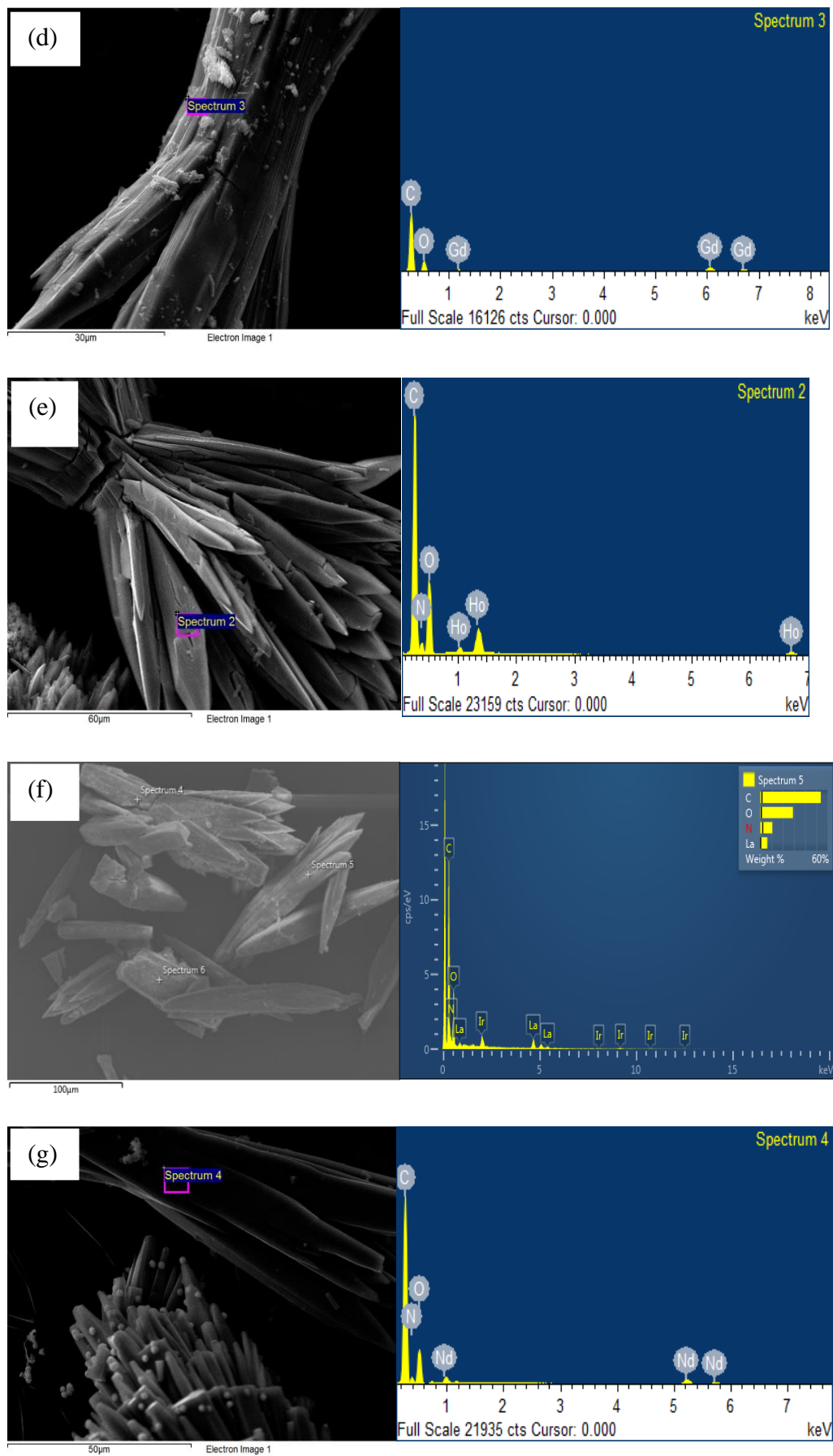
Figure 4.9: SEM images(left)/EDX (right) of (a) Dy **8**, (b) Ce **9**, (c) Pr **10**, (d) Gd **11**, (e) Ho **12**, (f) La **13**, (g) Nd **14**.

4.2.7: Electrochemistry

4.2.7.1 Solid state cyclic voltammetry

The solid state CV was carried out on **8 – 14**, trapped on the surface of a glassy carbon electrode by a $LiClO_4$ intercalated polyvinylchloride (PVC) matrix.[17,18] The results of the CV experiments are presented in Table 4.5. Each of the MOFs undergoes two one-electron reductions typical of **DPNDI** systems as seen in the CVs of **1** and **2** (chapter 3).[19] While the first is fully reversible, the second is not under the conditions of the experiment. The first reduction for **8 – 14** occurs at ca. -0.88 V while the second reduction takes place at ca. -1.29 V. These values are within the range seen for **1** and **2**. The first reduction leads to the formation of the radical monoanions while the second reduction gives rise to dianions. It can be seen from Table 4.5 that the values obtained from the CV experiments are further validated by the square wave (SW) values showing strong agreement. The difference between the first and second reduction potentials, $\Delta E_{1/2}$ can be calculated using the equation: $\Delta E_{1/2} = E_{1/2 \text{ (1st red)}} - E_{1/2 \text{ (2nd red)}}$. The value of $\Delta E_{1/2}$ are also consistent with those of **1** and **2**. The cyclic voltammograms of **8 – 14** have similar profile; therefore, only that of **8** is shown here (Figure 4.10) while the rest can be found in a table in the appendix.

Table 4.5: Solid state cyclic voltammetry on a glassy carbon electrode using LiClO$_4$ intercalated PVC as supporting matrix, in DMF/[Bu$_4$N][BF$_4$] (0.2 M) at 0.1 Vs^{-1}. Potentials are quoted versus E$_{1/2}$ Fc$^+$/Fc used as an internal standard.

Compound	1st reduction		2nd reduction		ΔE$_{1/2}$
	CV, $E_{1/2}$/V	SW/V	CV, $E_{1/2}$/V	SW/V	
8	-0.89	-0.91	-1.32	-1.30	0.43
9	-0.90	-0.93	-1.29	-1.32	0.39
10	-0.88	-0.90	-1.30	-1.27	0.42
11	-0.87	-0.90	-1.28	-1.29	0.41
12	-0.86	-0.89	-1.26	-1.25	0.40
13	-0.86	-0.92	-1.30	-1.31	0.44
14	-0.88	-0.93	-1.31	-1.32	0.43

(a)　　　　　　　　　　　　　　　　(b)
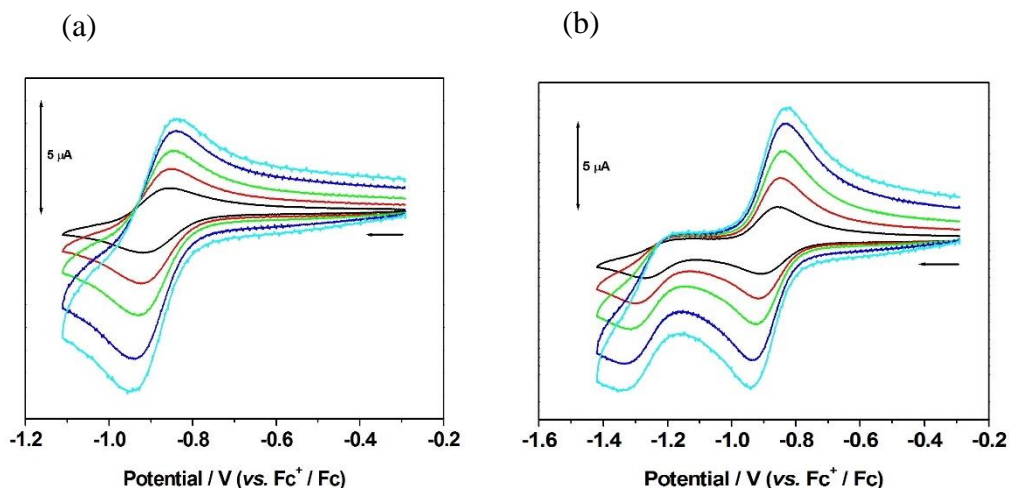
Figure 4.10: Solid state cyclic voltammetry of 8 on a glassy carbon electrode using LiClO$_4$ intercalated PVC as supporting matrix in dmf/[Bu$_4$N][BF$_4$] (0.2 M) for the first reduction (a) and second reduction (b) at scan rates of 0.02 (black), 0.05 (red), 0.10 (green), 0.20 (blue) and 0.30 (cyan) Vs^{-1}.

4.2.7.2 Solid state UV-Vis spectroelectrochemistry (SEC)

The solid state SEC of **8** was carried out using the method described in section 2.3.3.2 of chapter three. While no reasonable data could be obtained for **9 – 14** due to poor film formation, **8** readily forms uniform films; hence the SEC data was successfully obtained.

The UV-Vis SEC spectrum of **8** looks like that of **3** (Figure 4.11). Just as in **3**, only the spectrum for the radical monoanion of **8** (i.e. **8·⁻**) with the characteristic bands at 470 nm, 610nm, 710 nm and 795 nm could be visualised. That does not, however, imply that the neutral and the dianion species do not exist. Rather it is largely due to the experimental conditions viz; the use of FTO glass instead of FTO quartz. The working range of FTO glass does not support the observation of the spectra for the other two species. However, from the CV data, we know that they, indeed, exist.
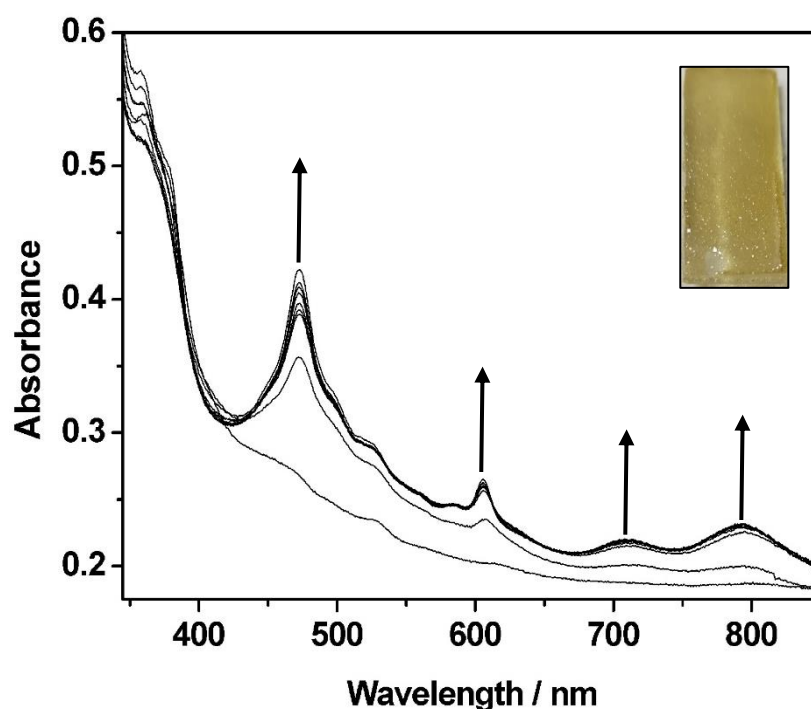
Figure 4.11: UV-vis absorption spectra of **8** showing the formation of **8·⁻**; Arrows indicate the progress of the stated inter-conversion. (Inset is the thin film on FTO glass used for the measurement).

4.8 Conclusion

Seven new lanthanoid MOFs based on a novel NDI, **DNNDI**, have been successfully synthesised and characterised chiefly by single crystal X-ray crystallography (SCRD). The lanthanides employed include lanthanum, cerium, praseodymium, neodymium, gadolinium, dysprosium and holmium. The

frameworks based on Nd(III) and La(III) crystallised in the monoclinic space group C2/c, the rest adopting the tetragonal crystal system I4$_1$/a space group. In general, all the MOFs are isostructural with similar rod SBUs and connectivity. The M-O and the M-M bond lengths decrease steadily from La(III) through Ho(III) which is a direct consequence of lanthanide contraction. The phase purity of the bulk samples were ascertained by comparing the experimental PXRD patterns with those simulated from the SCXRD data. All the MOFs have an unprecedented topological net with Schlafli symbol $\{4^2.6^2.8^2\}\{4^3.6^3\}2\{4^7.6^8\}2$. The cyclic voltammetry data of the MOFs are in line with those for NDI-based MOF systems. Owing to the inability of most of the materials to form uniform thin film on FTO substrate suitable for solid state UV-Vis SEC, only that of dysprosium containing MOF was studied. This however could be used to infer the likely UV-Vis spectroeletrochemical behaviour for the rest of the MOFs since they are isostructural.

4.9 Materials and methods
4.9.1 Synthesis of [Dy(DNNDI)$_{1.5}$.DMF].DMF, 8

A 20 mL scintillation vial was charged with Dy(NO$_3$)$_3$.5H$_2$O (15 mg, 0.032 mmol), **DNNDI** (17 mg, 0.033 mmol) and DMF (1.5 mL). The mixture was stirred for 10 minutes after which the vial was tightly capped and transferred into an oven at 100 ^{o}C. The reaction was stopped after 24 h and needle-like colourless crystals of **8** were obtained. Scanning electron micrographs of **8** are shown in Figure 4.12.
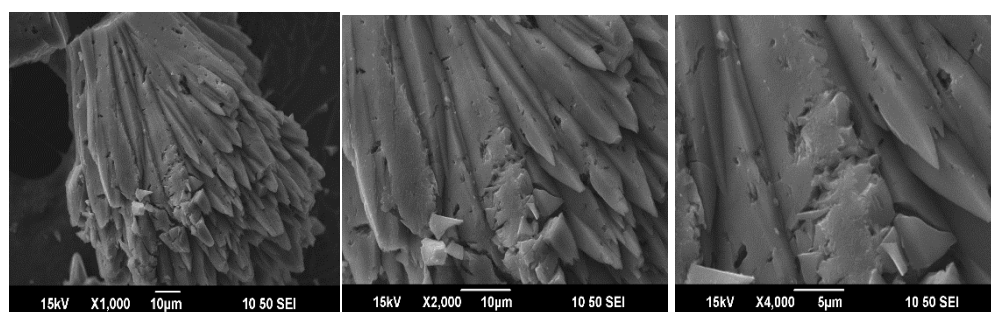
Figure 4.12: SEM images of **8** at different magnifications

4.9.2 Synthesis of [Ce(DNNDI)$_{1.5}$.DMF].DMF, 8

A 20 mL scintillation vial was charged with Ce(NO$_3$)$_3$.6H$_2$O (15 mg, 0.032 mmol), **DNNDI** (17 mg, 0.033 mmol) and DMF (1.5 mL). The mixture was stirred for 10 minutes after which the vial was tightly capped and transferred into an oven at 100 ^{o}C. The reaction was stopped after 24 h and needle-like colourless crystals of **9** were obtained. Scanning electron micrographs of **9** are shown in Figure 4.13.
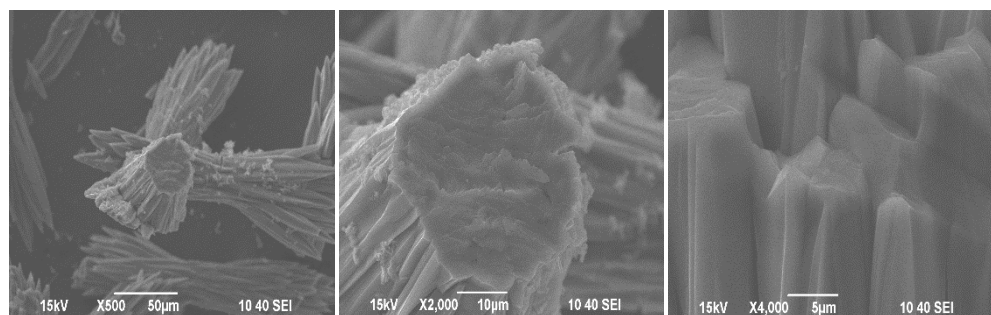
Figure 4.13: SEM images of **9** at different magnifications

4.9.3 Synthesis of [Pr(DNNDI)$_{1.5}$.DMF].DMF, 8

A 20 mL scintillation vial was charged with Pr(NO$_3$)$_3$.6H$_2$O (15 mg, 0.032 mmol), **DNNDI** (17 mg, 0.033 mmol) and DMF (1.5 mL). The mixture was stirred for 10 minutes after which the vial was tightly capped and transferred into an oven at 100 °C. The reaction was stopped after 24 h and needle-like colourless crystals of **10** were obtained. Scanning electron micrographs of **10** are shown in Figure 4.14.
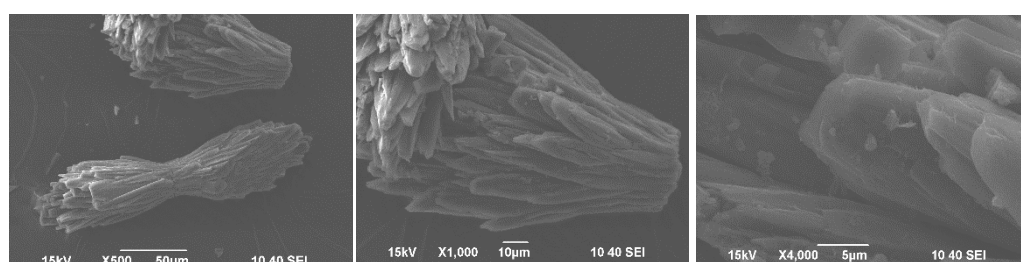
Figure 4.14: SEM images of **10** at different magnifications

4.9.4 Synthesis of compound [Gd(DNNDI)$_{1.5}$.DMF].DMF, 8

A 20 mL scintillation vial was charged with Gd(NO$_3$)$_3$.6H$_2$O (12 mg, 0.032 mmol), **DNNDI** (17 mg, 0.033 mmol) and DMF (1.5 mL). The mixture was stirred for 10 minutes after which the vial was tightly capped and transferred into an oven at 100 °C. The reaction was stopped after 24 h and needle-like colourless crystals of **11** were obtained. Scanning electron micrographs of **11** are shown in Figure 4.15.
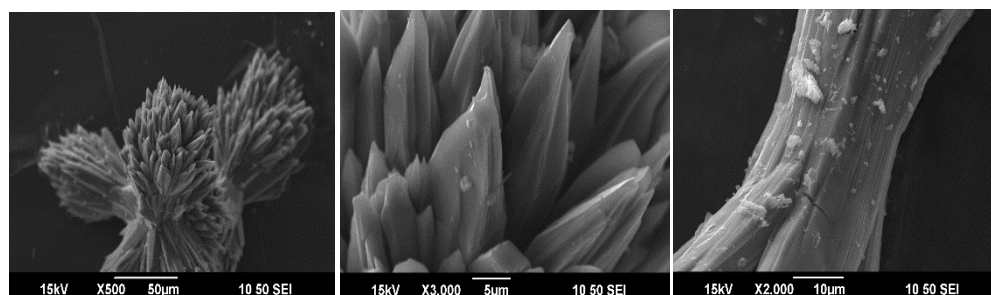
Figure 4.15: SEM images of **11** at different magnifications

4.9.5 Synthesis of [Ho(DNNDI)$_{1.5}$.DMF].DMF, 8

A 20 mL scintillation vial was charged with Ho(NO$_3$)$_3$.6H$_2$O (15 mg, 0.032 mmol), **DNNDI** (17 mg, 0.033 mmol) and DMF (1.5 mL). The mixture was stirred for 10 minutes after which the vial was tightly capped and transferred into an oven at 100 °C. The reaction was stopped after 24 h and needle-like colourless crystals of **12** were obtained. Scanning electron micrographs of **12** are shown in Figure 4.16.
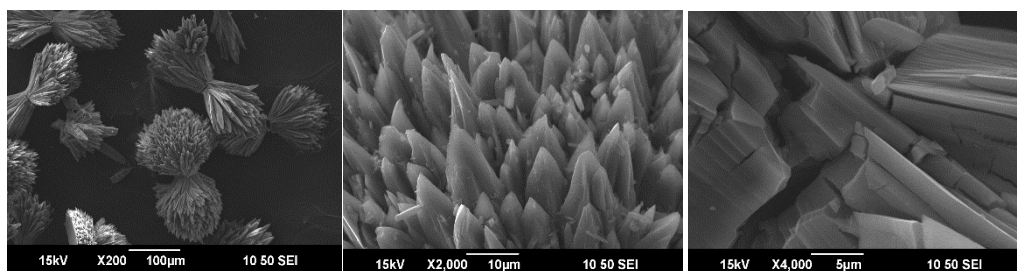
Figure 4.16: SEM images of 12 at different magnifications

4.9.6 Synthesis of [La$_2$(DNNDI)$_3$(DMF)$_2$].9.5DMF, 13

A 20 mL scintillation vial was charged with La(NO$_3$)$_3$.6H$_2$O (15 mg, 0.032 mmol), **DNNDI** (17 mg, 0.033 mmol) and DMF (1.5 mL). The mixture was stirred for 10 minutes after which the vial was tightly capped and transferred into an oven at 100 °C. The reaction was stopped after 24 h and needle-like colourless crystals of **13** were obtained. Scanning electron micrographs of **13** are shown in Figure 4.17
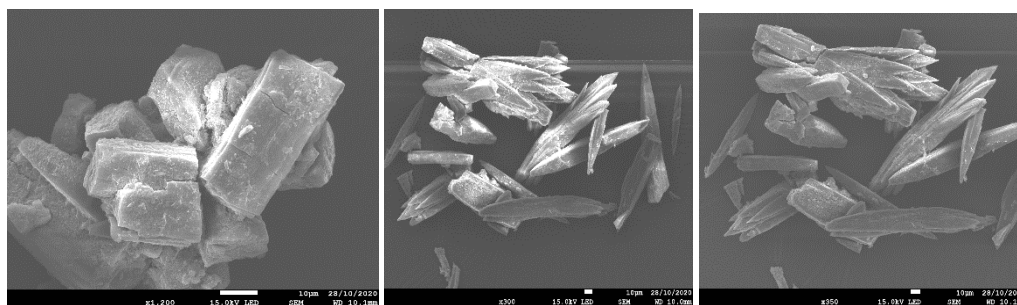
Figure 4.17: SEM images of 13 at different magnifications

4.9.7 Synthesis of [Nd$_2$(DNNDI)$_3$(DMF)$_2$].9.5DMF, 14

A 20 mL scintillation vial was charged with Nd(NO$_3$)$_3$.6H$_2$O (15 mg, 0.032 mmol), **DNNDI** (17 mg, 0.033 mmol) and DMF (1.5 mL). The mixture was stirred for 10 minutes after which the vial was tightly capped and transferred into an oven at 100 °C. The reaction was stopped after 24 h and needle-like colourless crystals of **14** were obtained. Scanning electron micrographs of **14** are shown in Figure 4.18. Scanning electron micrographs of **14** are shown in Figure 4.18.
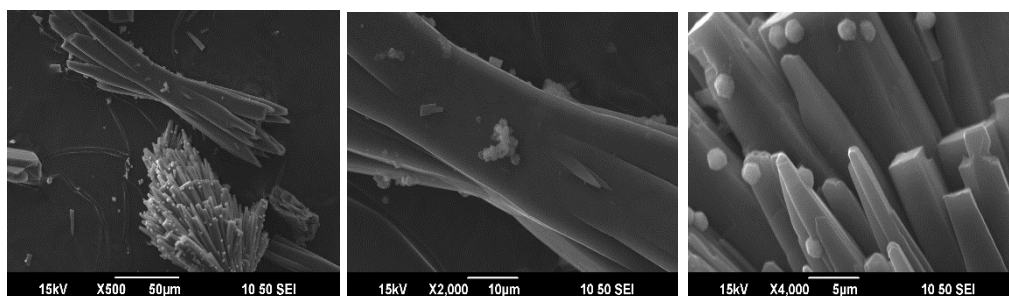
Figure 4.18: SEM images of **14** at different magnifications

4.10 References

1. G. Nandi, R. Thakuria, H. M. Titi, R. Patra and I. Goldberg, *CrystEngComm*, 2014, **16**, 5244–5256.
2. Y.-T. Yan, F. Cao, W.-Y. Zhang, S.-S. Zhang, F. Zhang and Y.-Y. Wang, *New J. Chem*., 2018, **42**, 9865-9875.
3. Z.-P. Dong, F. Zhao, L. Zhang, Z.-L. Liu and Y.-Q. Wang, *New J. Chem*., 2020, **44**, 10239-10249.
4. Y. Shia, X.-Y. Rena, M. Gaoa, Y.-L. Houc, J. Jic, Z.-L. Wub, W.-M. Wang, *Inorg. Chim. Acta*, 2020, **506**, 119536.
5. L. Fu, Q. Yang, D. Li and J.Y. Lu, *Mendeleev Commun.,* 2020, **30**, 589–591.
6. S. R. Miller, D. Heurtaux, T. Baati, P. Horcajada, J.-M Greneche and C. Serre, *Chem. Commun*., 2010, **46**, 4526–4528.
7. X.-L. Sun, B.-X. Shen, S.-Q. Zang and C.-X. Du, *CrystEngComm,* 2013, **15,** 5910–5918.
8. O.V.Dolomanov, L. J. Bourhis, R. J. Gildea, J. A. K. Howard and H. Puschmann, *J. Appl. Cryst.,* 2009, **42**, 339-341.
9. G. M. Sheldrick, *Acta Cryst. A,* 2015, **71**, 3-8.
10. G. M. Sheldrick, *Acta Cryst. C,* 2015, **71**, 3-8.
11. N. L. Rosi, J. Kim, M. Eddaoudi, B. Chen, M. O'Keeffe and O. M. Yaghi, *J. Am. Chem. Soc*. 2005, **127**, 1504-1518.

12. F. G. Chavez and H. I. Beltran, *New J. Chem.*, 2021, **45**, 6600-6610.

13. X. He, X.-P. Lu, Y.-Y. Tian, M.-X. Li, S. Zhu, F. Xing, R. E. Morris, *CrystEngComm*, 2013, **15**, 9437-9443.

14. A. L. Spek, *Acta Cryst. C.,* 2015, **71**, 9-18.

15. C. F. Macrae, I. Sovago, S. J. Cottrell, P. T. A. Galek, P. McCabe, E. Pidcock, M. Platings, G. P. Shields, J. S. Stevens, M. Towler and P. A. Wood, *J. Appl. Cryst.*, 2020, **53**, 226-235.

16. Y.-Q. Wang, Q.-H. Tan H.-T. Liu, W. -S. and Z.-L. Liu, *RSC Adv*., 2015, **5**, 86614-86619.

17. P. M. Usov, C. Fabian and D. M. D'Alessandro, *Chem. Commun*. 2012, **48,** 3945-3947.

18. S. Rajendran, M. R. Prabhu, M. U. Rani, *Int. J. Electrochem. Sci.*, 2008, **3**, 282-290

19. C. F. Leong, B. Chan, T. B. Faust, P. Turner and D. M. D'Alessandro, *Inorg. Chem.* 2013, **52**, 14246−14252.

Chapter Five   Host-guest Experiments

5.1 Introduction

In this chapter, the host-guest chemistry involving molecular ferrocene encapsulation will be reported. Particular attention will be paid to the crystal structures and electrochemistry of the ferrocene-trapped MOFs.

The incorporation of ferrocene and its derivatives in MOFs have been studied to a limited extent.[1] While some researchers have used ferrocene derivatives as ligands,[2-7] others have added them to framework structure as guest species[8-13]in which case the formula of the resulting MOF becomes Fc@MOF (where Fc stands for ferrocene). What is common to both scenarios – whether it is used as a ligand or guest – is the fact that the ferrocene plays a key role in the electrochemical behaviour of the MOF. The preparation of Fc@MOFs can be achieved using different approaches which include vapour-assisted,[14] one-pot,[15] electrodeposition[16] and low diffusion[17] methods. In most cases, the MOFs are constructed first; thereafter, ferrocene is post-synthetically encapsulated into the framework materials. Fc@MOFs have been employed in sensing, gas separation, catalysis, adsorption, amongst other applications.[1]

The rylene diimides are mostly studied for their redox activity. This redox activity stems from the electron-deficient nature of the compounds. For instance, the map of the electrostatic potential for **DPNDI** – a classic example of NDI – (Figure 5.1) reveals that the regions of the molecule with the least electron density (most electron-deficient) are the two imide rings while the four carbonyl oxygen atoms have the highest electron density.[18]

In this study, we sought to take and advantage of this electron deficiency of the NDI by post-synthetically incorporating electron-rich ferrocene in NDI-based

MOFs, **1** and **2,** with the aim of understanding any structural changes that might result in the host network. Also, the electrochemistry of the Fc@**2** will be reported to gain insight into the electrochemical behaviour.
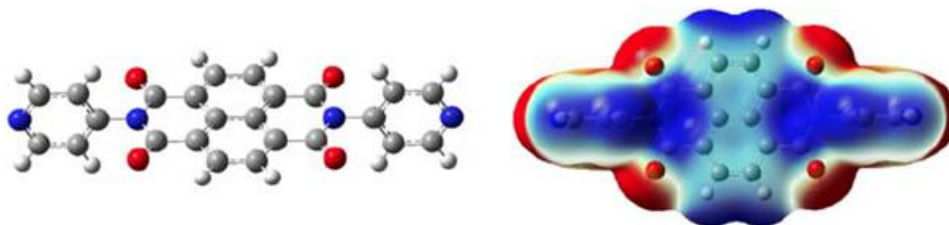
Figure 5.1 Structure of DPNDI (left) showing the electrostatic potential map. The red areas indicate the electron-rich section of the molecule while the blue regions are electron-deficient.[18]

5.2 Results and discussion.

5.2.1 Preparation and crystal structure of Fc@1

Prior to the host-guest experiment, the as-synthesised sample of framework **1** (details of synthesis is contained in chapter three) was subject to solvent exchange. The mother liquor was carefully decanted from the scintillation vial used for the synthesis. Crystals of **1** were then washed three times with acetone (2 mL per washing) and soaked in 2 mL acetone for three further days. Thereafter, the crystals were once again washed with 2 mL acetone before soaking in 2 mL of 0.10 M acetone solution of ferrocene for 10 d. The change in the colour of the crystals from pale pink to orange/yellow signalled the successful inclusion of ferrocene in the framework of **1** to yield **Fc@1**.

As the crystals of **1** remained single with no apparent damage to the crystallinity after the experiment, one of the crystals was selected and mounted on a single crystal X-ray diffractometer. The data was collected at 120 K. Using Olex-2,[19] the structure was solved with the SHELXT[20] structure solution program using Intrinsic Phasing and refined with the SHELXL[21] refinement package using

Least Squares minimisation. The crystal data and refinement parameters for **Fc@1** are given in Table 5.1. Analysis of the SCXRD data reveals that **Fc@1** crystallised in the same triclinic space group P-1 as **1**.

Table 5.1 Summary of crystal data and structure refinements of Fc@1

Empirical formula	$C_{36.5}H_{23}CoFe_{0.5}N_5O_{9.5}$
Formula weight	770.45
Temperature/K	120(2)
Crystal system	triclinic
Space group	P-1
a/Å	11.6456(9)
b/Å	12.4469(8)
c/Å	14.4300(7)
α/°	96.162(5)
β/°	97.751(5)
γ/°	109.602(7)
Volume/Å^3	1926.2(2)
Z	2
ρ_{calc}g/cm^3	1.328
μ/mm^{-1}	5.446
F(000)	786.0
Crystal size/mm^3	$0.185 \times 0.116 \times 0.077$
Radiation	Cu Kα (λ = 1.54184)
2θ range for data collection/°	7.642 to 149.188
Index ranges	$-12 \leq h \leq 14, -15 \leq k \leq 13, -13 \leq l \leq 17$
Reflections collected	13739
Independent reflections	7566 [R_{int} = 0.0361, R_{sigma} = 0.0471]
Data/restraints/parameters	7566/600/543
Goodness-of-fit on F^2	1.260
Final R indexes [I>=2σ (I)]	R_1 = 0.0970, wR_2 = 0.2887
Final R indexes [all data]	R_1 = 0.1075, wR_2 = 0.3022
Largest diff. peak/hole / e Å^{-3}	2.72/-0.72

The asymmetric unit of **Fc@1** (Figure 5.2) comprises one Co(II) cation which is coordinated to one molecule of **DPNDI**, half of naphthalene dicarboxylate linker and a terminal k^2-nitrate moiety. The asymmetric unit also contains a half-occupied acetone molecule and a half-occupied ferrocene molecule, both of which are present as guest molecules. Inspection of the of the unit cell parameters for **Fc@1** points to the fact that its unit cell lengths and by extension

the volume are slightly higher than those of **1**. For instance, the unit cell volume

of **1** is 1869.9(3) Å^3 while that of **Fc@1** is 1926.2(2) Å^3. This gives an early

indication that the pore and indeed the overall structure of **Fc@1** had been

extended through the inclusion of ferrocene. Such expansion and distortion upon

guest inclusion in MOFs have been previously reported for Fc@MOF-5.[22]
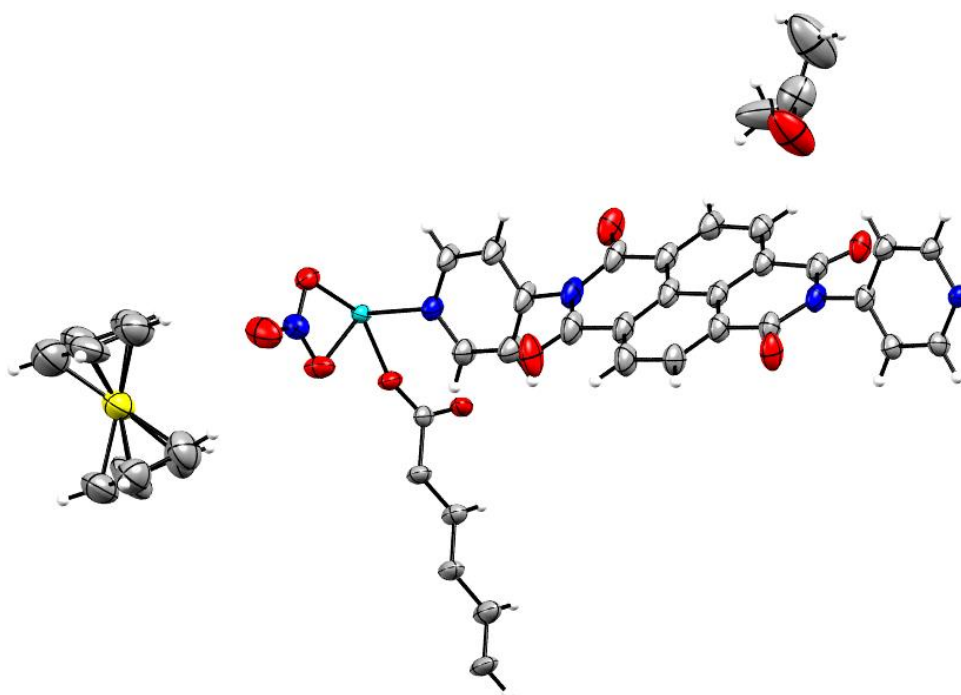
Figure 5.2 ORTEP representation of the asymmetric unit of **Fc@1** with 50% ellipsoid. (grey = C, turquoise = Co, yellow = Fe, red = O, blue = N and white = H).

This elongation is confirmed by the longer pore dimension of 12.4469(8) Å x

19.7275(11) Å exhibited by **Fc@1** compared to 12.4313(17) Å x 19.698(13) Å

for framework **1**.

The framework structure shows that **Fc@1** exhibits similar connectivity to that

of **1**, differing mainly in the materials contained in the channels. While the pore

of **1** contains disordered DMF molecules, which were removed during

refinement using SQUEEZE,[23] that of **Fc@1** plays host to acetone and ferrocene molecules (Figure 5.3a). Further analysis of the structure reveals that the ferrocene molecules are located within the channel close to the pyridyl rings of the **DPNDI** moiety. In this position, there exists one ferrocene molecule below and another above the plane of naphthalene moiety of the carboxylate linker. The location may be influenced by the CH/π interactions as shown in Figure 5.3b. The interactions between the CH of ferrocene with the naphthalene rings have CH…centroid distances of 2.972 Å and 3.305 Å while that between the centroid of the cyclopentadienyl ring and the CH of the pyridyl ring of **DPNDI** has a distance of 2.816 Å. More details on the bond lengths and angles can be found in the appendix crystallographic section.
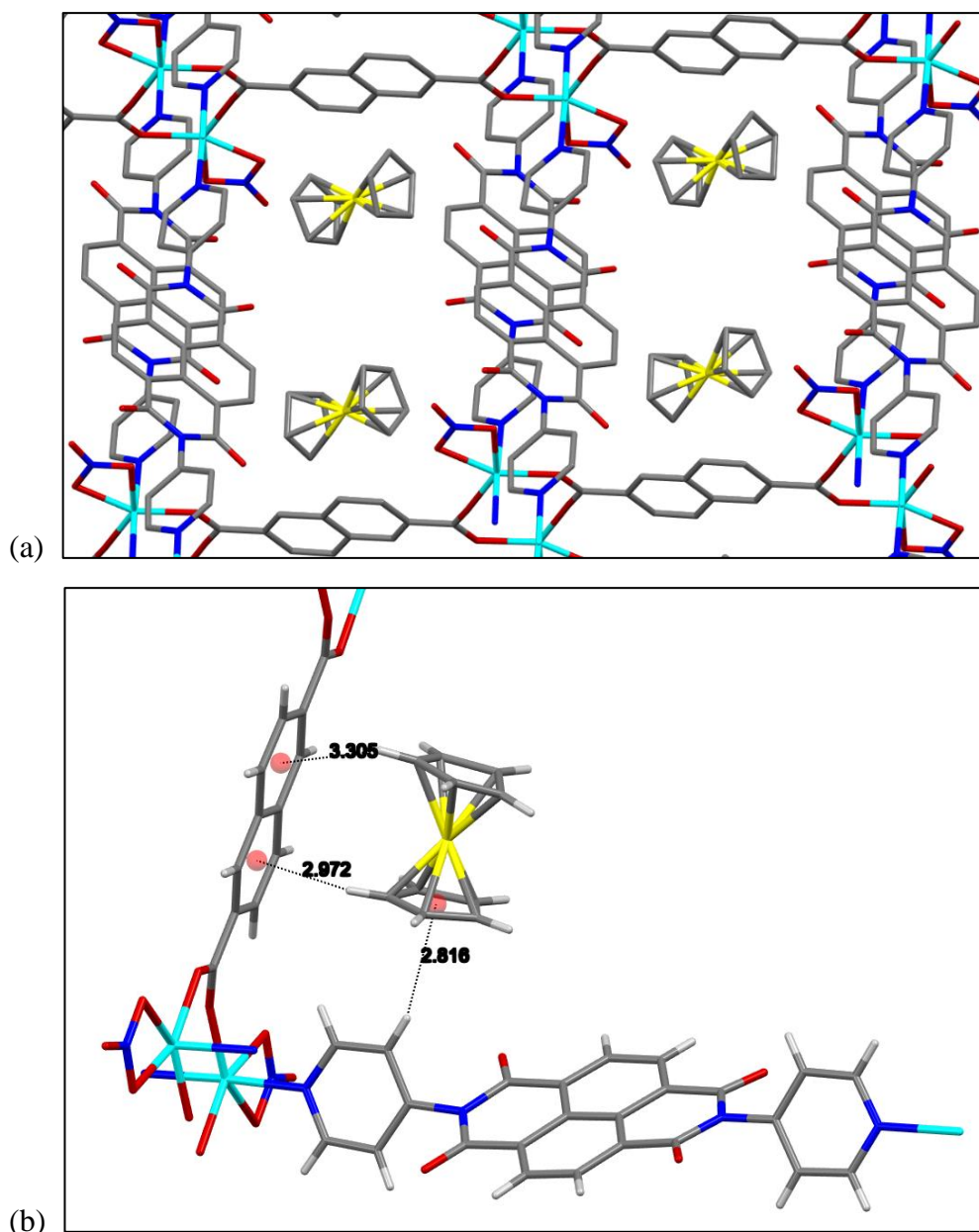
Figure 5.3 Packing view of **Fc@1** along the crystallographic *a*-axis (a) and structure of **Fc@1** showing the location of ferrocene (b). (grey = C, turquoise = Co, yellow = Fe, red = O, blue = N and white = H; pore acetone molecules have been omitted for clarity).

5.2.2 Preparation and crystal structure of Fc@2

The experiment was performed in similar way to that of **Fc@1** described above. The mother liquor was carefully decanted from the scintillation vial used for the synthesis. Crystals of **2** were then washed three times with acetone and soaked in 2 mL acetone for further three days after which the crystals were once again

washed with acetone before soaking in 2 mL of 0.10 M acetone solution of ferrocene for 10 d. Unlike in **Fc@1** in which the encapsulation of ferrocene could easily be seen by colour change, it was not so easily noticeable for **Fc@2** as the crystals of **2** were dark green. However, SCXRD provided evidence of successful inclusion of ferrocene in **2**.

Owing to the fact that this experiment does not affect the integrity of the crystals of **2**, a crystal suitable for SCXRD experiment was selected and mounted on a diffractometer that had been cryo-cooled to 120 K. Upon successfully collecting the data, the structure of **Fc@2** was solved using Olex-2,[19] using the SHELXT[20] structure solution program which uses Intrinsic Phasing and refined with the SHELXL[21] refinement package using Least Squares minimisation. The crystal data and refinement parameters for Fc@**2** are given in Table 5.2. Analysis of the SCXRD data reveals that **Fc@2** crystallised in the same crystal system. However, the space groups are different with **Fc@2** being in P-1 and **2** in P2$_1$. Crystal structure data and refinement parameters for **Fc@2** can be found in Table 5.2.

Table 5.2 Summary of crystal data and structure refinements of Fc@1

Empirical formula	$C_{64}H_{46}Co_2FeN_4O_{14}$
Formula weight	1268.76
Temperature/K	120(2)
Crystal system	triclinic
Space group	P-1
a/Å	12.7200(10)
b/Å	12.9047(14)
c/Å	18.1638(16)
α/°	103.605(8)
β/°	91.918(7)
γ/°	102.098(8)
Volume/Å^3	2822.8(5)
Z	2
ρ_{calc}g/cm^3	1.493
μ/mm^{-1}	7.194
F(000)	1300.0
Crystal size/mm^3	$0.352 \times 0.076 \times 0.049$
Radiation	Cu Kα (λ = 1.54184)
2θ range for data collection/°	7.134 to 145.83
Index ranges	$-9 \leq h \leq 15, -15 \leq k \leq 15, -22 \leq l \leq 22$
Reflections collected	20492
Independent reflections	10871 [R_{int} = 0.0789, R_{sigma} = 0.1125]
Data/restraints/parameters	10871/28/779
Goodness-of-fit on F^2	1.054
Final R indexes [I>=2σ (I)]	R_1 = 0.0986, wR_2 = 0.2537
Final R indexes [all data]	R_1 = 0.1284, wR_2 = 0.2804
Largest diff. peak/hole / e Å^{-3}	1.29/-1.24

The asymmetric unit of **Fc@2** (Figure 5.4) contains structural units similar to the asymmetric unit of **2** discussed in chapter three. One key difference between **2** and **Fc@2** is in the guest species. Whereas the asymmetric unit of **2** has seven solvate DMF molecules, in **Fc@2**, the guest molecules are a ferrocene and two acetone molecules. The ferrocene and acetone molecules were modelled with full occupancy. The structural deformation which accompanied the formation of **Fc@2** resulted in a different coordination motif for the carboxylate ligands

which is clearly absent in **2** Figure 5.4. Details on bond lengths and angles can be found in the appendix crystallographic section.
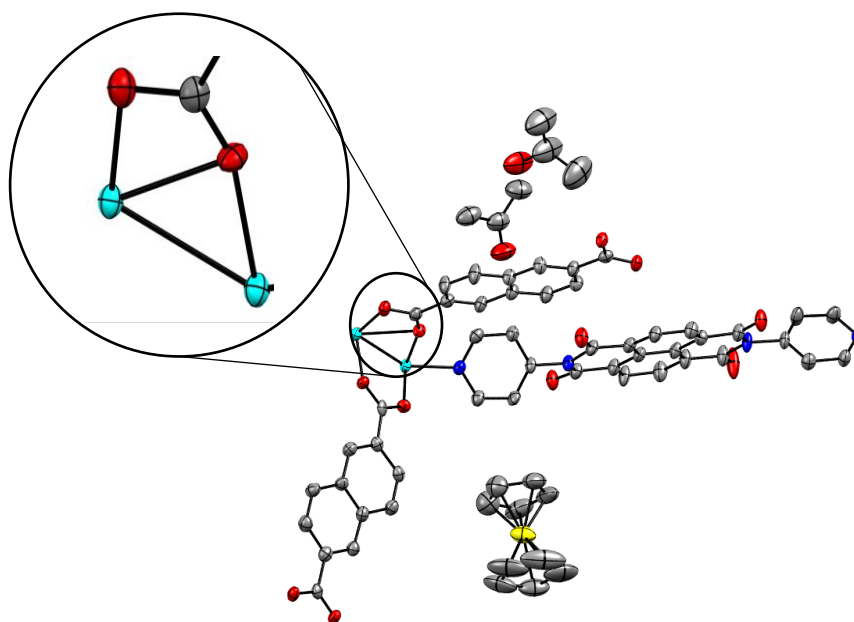
Figure 5.4 Asymmetric unit of **Fc@2**. The zoomed in section highlights the new coordination mode adopted by NDC^{2-}. (grey = C, turquoise = Co, yellow = Fe, red = O and blue = N; hydrogen atoms pore acetone molecules have been omitted for clarity).

Consequently, the once rectangular channels (in **2**) have become distorted into parallelogram-shaped channels (in **Fc@2**) as illustrated in Figure 5.5. A careful examination of the structure of **Fc@2** shows that the encapsulated ferrocene is situated at the corner near the pyridyl ring of the **DPNDI** ligand, close to the metal centre. There is one ferrocene per cavity when individual lattice of the two-fold network is analysed separately, giving a total of two ferrocene molecules per channel created by doubly interpenetrated networks as could be seen in Figure 5.6.

(a)   **(b)**
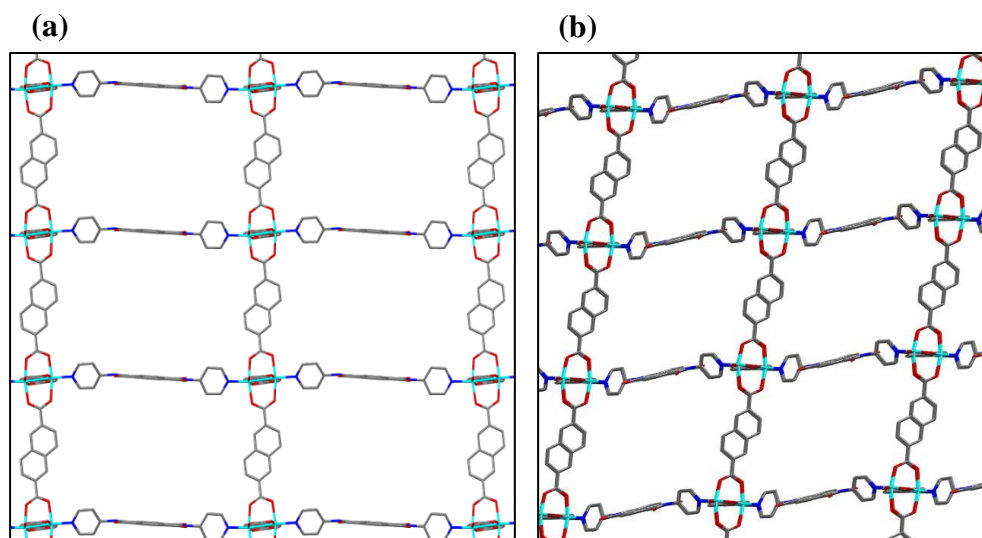
Figure 5.5 Extended framework structures of (a) framework **2** and (b) **Fc@2** revealing the structural deformation in the ferrocene-contained framework. (grey = C, turquoise = Co, red = O and blue = N; hydrogen atoms, guest solvents and ferrocene have been removed for clarity).

The ferrocene molecules are arranged in a somewhat zig-zag pattern along the 1D channels, presumably maximising space filling and intermolecular interactions.
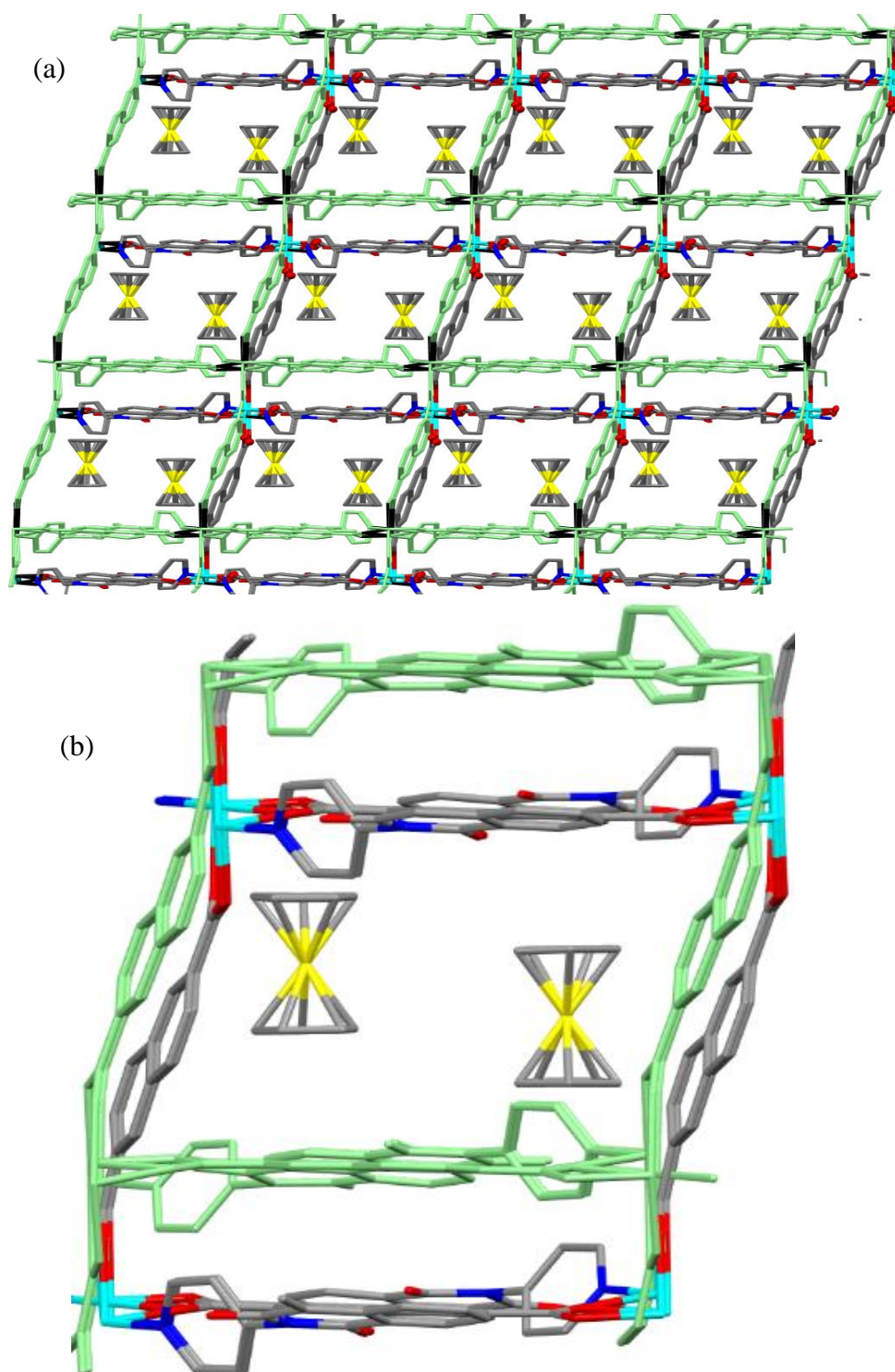
Figure 5.6 (a) Packing view of **Fc@2** along the crystallographic *c*-axis showing the location and arrangement of ferrocene moieties in the channels. The second lattice of the two-fold interpenetrated network is shown in green. (b) A closer view of the channel where the ferrocene molecules sit. (grey = C, turquoise = Co, red = O and blue = N; hydrogen atoms and guest solvents have been removed for clarity.

224

5.2.3 Solid state electrochemistry of Fc@MOFs

5.2.3.1 Cyclic voltammetry of Fc@2

Upon successful inclusion of ferrocene in the framework, we sought to investigate its effect on the electrochemical behaviour of the host. The CV experiment was performed using similar set up as reported for the solid state CVs in chapter three. The data obtained are presented side by side those of **2** in Table 5.3 for easy comparison. Analysis of the data shows no significant changes to the potentials in which the first and second reduction occurred in the host framework. However, the ferrocene oxidation peak could be seen (Figure 5.7), implying **Fc@2** can undergo both reduction and oxidation. The observed oxidation potential can be attributed to the encapsulated ferrocene species since the reference used was ferrocene. The lack of the expected reversibility for a ferrocene species under diffusion control might suggest that the molecule is somehow restricted in its ability to move within the pore. It is important to point out that the return wave for the second reduction peak is clearly smaller than expected indicating that the process is quasi-reversible with respect to the second reduction. The current response to reduction and re-oxidation appears to correlate with the square root of scan rate and this may result from slow electron hopping between NDI units separated by insulating 'metal' layers (Figure 5.7c-d).[24]

Table 5.3 Comparison of CVs of **2** and **Fc@2**

| Compound	1st reduction		2nd reduction		$\Delta E_{1/2}$
	CV, $E_{1/2}$/V	SW/V	CV, $E_{1/2}$/V	SW/V	
2	-0.87	-0.89	-1.32	-1.34	0.45
Fc@2	-0.86	-0.90	-1.32	-1.33	0.44
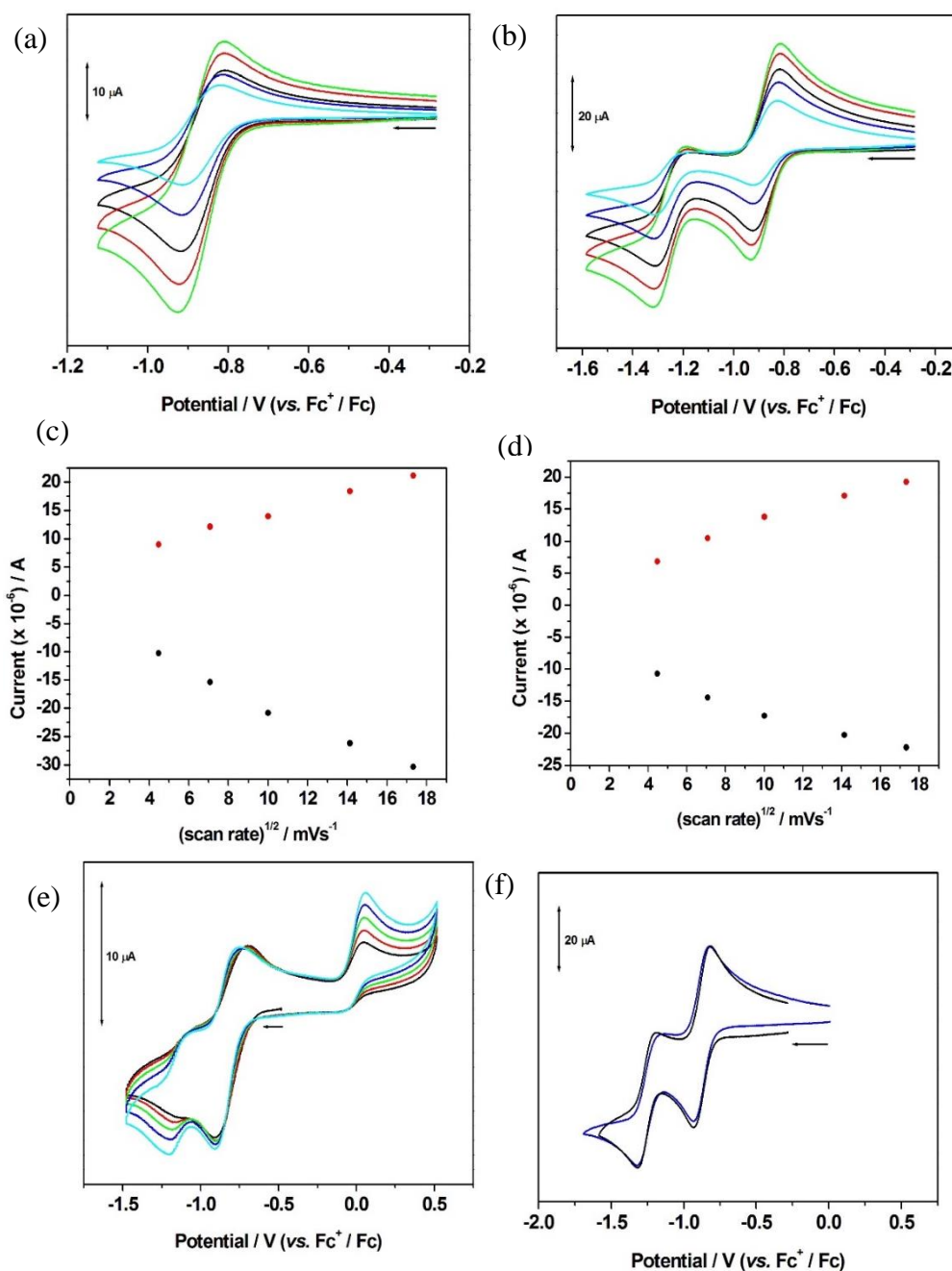
Figure 5.7 Solid state cyclic voltammetry of **Fc@2** on a glassy carbon electrode using LiClO$_4$ intercalated PVC as supporting matrix in DMFf/[Bu$_4$N][BF$_4$] (0.2 M) for the first reduction (a) and second reduction (b) at scan rates of 0.02 (black), 0.05 (red), 0.10 (green), 0.20 (blue) and 0.30 (cyan) Vs^{-1}; plots of the peak anodic current (I$_p^a$) (red dots) and peak cathodic current (I$_p^c$) (black dots) versus the square root of scan rate for the first reduction (c) and the second reduction (d); (e) effect of multiple scans, at 0.10 Vs^{-1}, on the CV response (black, red, green, blue and cyan lines correspond to scans 1, 2, 3, 4 and 5, respectively); (f) comparison between CV profile of **Fc@2** (black) and host molecule **2** (blue) at 0.10 Vs^{-1}

5.3 Conclusion

Ferrocene encapsulation experiments have been successfully performed and characterised crystallographically for frameworks **1** and **2**. Analysis of the single crystal data reveals that the ferrocene is located around the corner of the channel in a ziz-zag fashion. This arrangement has been attributed to favourable π interactions and avoidance of unfavourable clashing of guests in the frameworks. The inclusion of the guest molecules is accompanied by a slight distortion of the framework with **Fc@2** adopting a different crystal system and space group to that of **2** (triclinic P-1 vs monoclinic P2$_1$).

The cyclic voltammetry data of **Fc@2** indicates that the electrochemical behaviour, in terms of reduction, of the host framework remains unaffected in the presence of the guest molecules. Nonetheless, the inclusion of ferrocene in the MOF makes the latter both oxidizing and reducing. This study has provided insight into the solid state electrochemical behaviour of redox-active MOFs containing electron rich species in the pores.

5.4 Materials and methods

5.4.1 Preparation of Fc@1

As-synthesised sample of framework **1** (details of synthesis are contained in chapter three) was subject to solvent exchange. The mother liquor was carefully decanted from the scintillation vial used for the synthesis. Crystals of **1** were then washed three times with 2 mL acetone each time and soaked in 2 mL acetone for further three days. Thereafter, the crystals were once again washed with 2 mL acetone before soaking in 2 mL of 0.10 M solution of ferrocene for 10 d. The change in the colour of the crystals from pale pink to orange/yellow signalled the successful inclusion of ferrocene in the framework of **1** to yield **Fc@1**.

5.4.2 Preparation of Fc@2

As-synthesised sample of framework **2** (details of synthesis are contained in chapter three) was subject to solvent exchange. The mother liquor was carefully decanted from the scintillation vial used for the synthesis. Crystals of **2** were then washed three times with 2 mL acetone each time and soaked in 2 mL acetone for further three days. Thereafter, the crystals were once again washed with 2 mL acetone before soaking in 2 mL of 0.10 M solution of ferrocene for 10 d to yield **Fc@2**.

5.5 References

1. Z. Huang, H. Yu, L. Wang, X. Liu, T. Lin, F. Haq, S. Z. Vatsadze, D. A. Lemenovskiy, *Coord. Chem. Rev.,* 2021, **430**, 213737.

2. M.-W. Zhang, M.-T. Yang, S. Tong, K.-Y. A. Lin, *Chemosphere*, 2018, **213**, 295-304.

3. R. Rajak, M. Saraf, A. Mohammad, S. M. Mobin, *J. Mater. Chem. A,* 2017, **5**, 17998–18011.

4. R. Horikoshi, T. Mochida, H. Moriyama, *Inorg. Chem.,* 2002, **41**, 3017–3024.

5. H. W. Hou, G. Li, L. K. Li, Y. Zhu, X. R. Meng, Y. T. Fan, *Inorg. Chem.*, 2003, **42**, 428– 435.

6. G. Li, H. W. Hou, L. K. Li, X. R. Meng, Y. T. Fan, Y. Zhu, *Inorg. Chem.*, 2003, **42**, 4995–5004.

7. C. Fang, Z. Deng, G. D. Cao, Q. Chu, Y. L. Wu, X. Li, X. S. Peng, G. R. Han, *Adv. Funct. Mater.*, 2020, **30**, 1910085

8. H. Kim, H. Chun, G. H. Kim, H. S. Lee, K. Kim*, Chem. Commun.*, 2006, **26**, 2759– 2761.

9. J. L. Qin, M. Cho, Y. Lee, *ACS Appl. Mater. Interfaces*, 2019, **11**, 743–11748.

10. J. P. Wang, G. K. Han, L. G. Wang, L. Du, G. Y. Chen, Y. Z. Gao, Y. L. Ma, C. Y. Du, X. Q. Cheng, P. J. Zuo, G. P. Yin, *Small,* 2018, **14**, 1704282.

11. G. Y. Ye, Q. He, S. Q. Liu, K. M. Zhao, Y. K. Su, W. W. Zhu, R. J. Huang, Z. He, *J. Mater. Chem. A,* 2019, **7**, 16508–16515.

12. W. Zhang, D. Banerjee, J. Liu, H. T. Schaef, J. V. Crum, C. A. Fernandez, R. K. Kukkadapu, Z. M. Nie, S. K. Nune, R. K. Motkuri, K. W. Chapman, M. H. Engelhard, J. C. Hayes, K. L. Silvers, R. Krishna, B. P. McGrail, J. Liu, P. K. Thallapally, *Adv. Mater.*, 2016, **28**, 3572–3577.

13. Q. Wei, H. W. Xu, X. H. Yu, T. Shimada, M. S. Rearick, D. D. Hickmott, Y. S. Zhao, S. N. Luo, *J. Appl. Phys.*, 2011, **110**, 056102.

14. M. Meilikhov, K. Yusenko, R. A. Fischer*, Dalton Trans.*, 2010, **39**, 10990–10999.

15. P. P. Mazzeo, L. Maini, D. Braga, G. Valenti, F. Paolucci, M. Marcaccio, A. Barbieri, B. Ventura, *Eur. J. Inorg. Chem.*, 2013, **25**, 4459–4465.

16. Y. J. Sun, H. Jin, X. W. Jiang, R. J. Gui, *Anal. Chem.*, 2020, **92**, 2866–2875.

17. J. Y. Li, C. T. He, Y. C. Chen, Z. M. Zhang, W. Liu, Z. P. Ni, M. L. Tong*, J. Mater. Chem. C*, 2015, **3**, 7830–7835.

18. A. Mitra, R. J. Clark, C. T. Hubley and S. Saha, *Supramol. Chem.*, 2014, **26**, 296–301.

19. O.V.Dolomanov, L. J. Bourhis, R. J. Gildea, J. A. K. Howard and H. Puschmann, *J. Appl. Cryst.,* 2009, **42**, 339-341.

20. G. M. Sheldrick, *Acta Cryst. A*, 2015, **71**, 3-8.

21. G. M. Sheldrick, *Acta Cryst. C*, 2015, **71**, 3-8.

22. H. Kim, H. Chun, G.-H. Kim, H.-S. Leeb and Kimoon Kim*, Chem. Commun*., 2006, **26**, 2759-2761.

23. A. L. Spek, *Acta Cryst. C*, 2015, **71**, 9-18.

Chapter Six   Materials and Methods

6.1. Reagents and Purification

All chemicals and dry solvents were sourced from Fluorochem, Alfa Aesar, Fisher Scientific, Sigma-Aldrich, or VWR International and used without further purification. Column chromatography was performed on silica gel 60A. Ferrocene was purchased from Sigma-Aldrich and used as received. Alconox detergent was purchased from Alconox Critical Cleaning Experts and used as received. Preparative thin layer chromatography was also employed, using silica gel as the stationary phase on plates purchased from AnalTech. Ferrocene was purchased from Aldrich and used as received. $[nBu_4N][BF_4]$ was prepared by the reaction of a 14 % aqueous solution of sodium tetrafluoroborate with a 13 % aqueous solution of tetrabutylammonium hydrogen sulfate and crystallised by dropwise addition of a dichloromethane solution of the compound into diethyl ether. Air- and moisture-sensitive reactions were performed using a standard Schlenk line, using dinitrogen as the inert atmosphere. Glassware used were flame-dried under vacuum and backfilled with dinitrogen. FTO glass slides were purchased from Sigma-Aldrich and washed using Alconox solution, and rinsed with acetone and ethanol before use.

6.2 General Equipment

6.2.1 NMR spectroscopy

Proton (^{1}H) and carbon-13 (^{13}C) NMR spectra were recorded using either a Bruker AV(III)400, AV(III)500, AV400 or DPX400 machines at room

temperature. Deuterated solvents were used as specified and chemical shifts were recorded with respective solvent residue peaks.

6.2.2 Mass Spectrometry

The ESI mass spectrometry (MS) spectra were recorded with Bruker MicroTOF using acetonitrile or methanol as the solvent. MALDI-TOF M/S spectra were recorded with a Bruker Ultraflex III mass spectrometer using trans-2-[3-(4-tert-butylphenyl)-2-methyl-2-propenylidene]-malononitrile as the matrix.

6.2.3 Infrared Spectroscopy

The Attenuated Total Reflectance Fourier Transform Infrared (ATR-FTIR) spectra were obtained between 400-4000 cm^{-1} using a Bruker Tensor 27 spectrometer with an ATR attachment.

6.2.4 Thermogravimetric analysis (TGA)

The TGA experiments were performed on TGA Q500 V20.13 Build 39 under an argon atmosphere from 0 to 1000 ^{o}C with a ramp of 10 ^{o}C/min and argon flow rate of 60 mL/min.

6.2.5 Absorbance/Emission/ Spectroscopy

Standard UV-Vis spectra were collected on a Perkin Elmer Lambda 16 spectrophotometer using a 1 cm path length quartz cuvette. Fluorescence spectra were recorded as aerated solutions using a Jobin Yvon Horiba FluoroMax-3 spectrometer at ambient temperature in a 1 cm path length quartz cuvette. Quantum yields were measured using a standard method published by Williams *et al.*[1]

6.2.6 Scanning electron microscopy (SEM)

SEM images were acquired using a JEOL 7100F field emission gun scanning electron microscope. Samples were prepared on 10 mm aluminium with an adhesive carbon tab and coated with 8 nm layer of Iridium using a QUORUM QISOT ES coater. Imaging was conducted at a working distance of 10 mm and an electron gun accelerating potential of 15 kV.

6.3 Electrochemistry

All the electrochemistry measurements were performed by Dr Stephen Davies in my presence for the most part.

6.3.1 Cyclic Voltammetry

Cyclic voltammetry was carried out using an Autolab PGSTAT20 potentiostat under an argon atmosphere using a three-electrode arrangement in a single compartment cell. Glassy carbon was used as the working electrode, platinum wire as the secondary electrode and a silver/silver chloride reference electrode, chemically isolated from the test solution via a fritted bridge tube containing electrolyte solution, in the cell. An analyte concentration of 1 mM was used with $[nBu_4N][BF_4]$ (400 mM) as a supporting electrolyte. Redox potentials are referenced to the ferrocenium/ferrocene couple, which was implemented as an internal reference.[2] Solid state cyclic voltammetry of the MOFs was recorded on a glassy carbon electrode using $LiClO_4$ intercalated PVC as supporting matrix in DMF/$[Bu_4N][BF_4]$ (0.2 M).[3,4]

6.3.2 Spectroelectrochemistry

UV/vis spectroelectrochemical measurements were performed using an optically transparent quartz electrochemical cell, with a 0.5 mm path length. A three-electrode configuration of a platinum/rhodium gauze working electrode,

platinum wire secondary electrode and a silver/silver chloride reference electrode (chemically isolated via a fritted bridge tube) were used in the cell. The potential at the working electrode was regulated with a Sycopel Scientific Ltd DD10M potentiostat and the spectra recorded with a Perkin Elmer 16 spectrophotometer. Temperature control was achieved with a stream of chilled nitrogen gas (cooled by passing through a tube submerged in liquid nitrogen) across the surface of the cell, adjusting the flow rate as necessary in response to a temperature sensor (± 0.1 °C). $[nBu_4N][BF_4]$ (400 mM) was used as the supporting electrolyte for the experiments. For the solid state measurement, samples were grown on the surface of FTO glass slide.

6.3.3 Bulk electrolysis and X-band EPR spectroscopy

X-band EPR spectroscopic data were recorded on a Bruker EMX spectrometer as fluid (ambient temperature) or frozen (77 K) solutions in quartz tubes. Spectra were simulated by Dr Stephen Davies using WINEPR SimFonia software. Bulk electrolysis was performed to generate samples for study by FT-IR, NIR and EPR spectroscopies. Samples were prepared under an argon atmosphere at 0 °C in a two-component cell: a platinum/rhodium gauze working electrode and secondary electrode were separated by a glass frit. A saturated calomel reference electrode was bridged to the test solution through a Vycor frit, oriented at the center of the working electrode. The working electrode compartment, containing analyte (1 mM), was stirred rapidly with a magnetic stirrer bar during electrolysis. $[nBu_4N][BF_4]$ (0.4 M) was used as the supporting electrolyte for the experiments. After electrolysis was completed, the prepared solution was transferred by Teflon cannula for analysis.

6.4 Crystallography

Single crystal X-ray diffraction experiments were performed on an Oxford Diffraction SuperNova CCD area detector diffractometer at 120 K using monochromated Cu Kα radiation (λ = 1.54184 Å); on Agilent GV1000 AtlasS2 or TitanS2 CCD area detector diffractometers at 120 K using monochromated CuKα radiation (λ = 1.54184 Å); or at the UK Diamond Light Source I19-1 3-circle diffractometer4 (λ = 0.6889 Å). Absorption corrections were applied using analytical numerical methods using CrysAlisPro software.[5] Using Olex-2,[6] the structures were solved by direct methods using ShelXT[7] and refined with ShelXL[8] using a least squares method. All hydrogen atoms were placed in geometrically calculated positions; non-hydrogen atoms were refined with anisotropic displacement parameters. CIF checks were performed by Dr. Stephen Argent. In specific cases, geometric restraints were applied. Details of crystal data can be found in the appendix section.

The powder X-ray diffraction data were obtained using PANalytical MPD diffractometer, equipped with a Cu anode X-ray tube, Kα1 monochromator (λ = 1.54184 Å), step size of 0.026 and 2-theta range of 3 to 70°.

6.5 References

1. A. T. R. Williams, S. A. Winfield and J. N. Miller, *Analyst*, 1983, **108**, 1067-1071.
2. R. R. Gagne, C. A. Koval and G. C. Lisensky, *Inorg. Chem.*, 1980, **19**, 2854-2855.

3. S. Rajendran, M. R. Prabhu, M. U. Rani, *Int. J. Electrochem. Sci.*, 2008, **3**, 282-290.

4. P. M. Usov, C. Fabian and D. M. D'Alessandro, *Chem. Commun.* 2012, **48,** 3945-3947.

5. CrysAlisPro, 2013, Agilent Technologies UK Ltd. Oxford, UK.

6. O.V.Dolomanov, L. J. Bourhis, R. J. Gildea, J. A. K. Howard and H. Puschmann, *J. Appl. Cryst.,* 2009, **42**, 339-341.

7. G. M. Sheldrick, *Acta Cryst. A*, 2015, **71**, 3-8.

8. G. M. Sheldrick, *Acta Cryst. C,* 2015, **71**, 3-8.

Appendix

Appendix I Crystallographic information for 2,6-diisopropyl-4-(pyridin-4-yl)aniline.
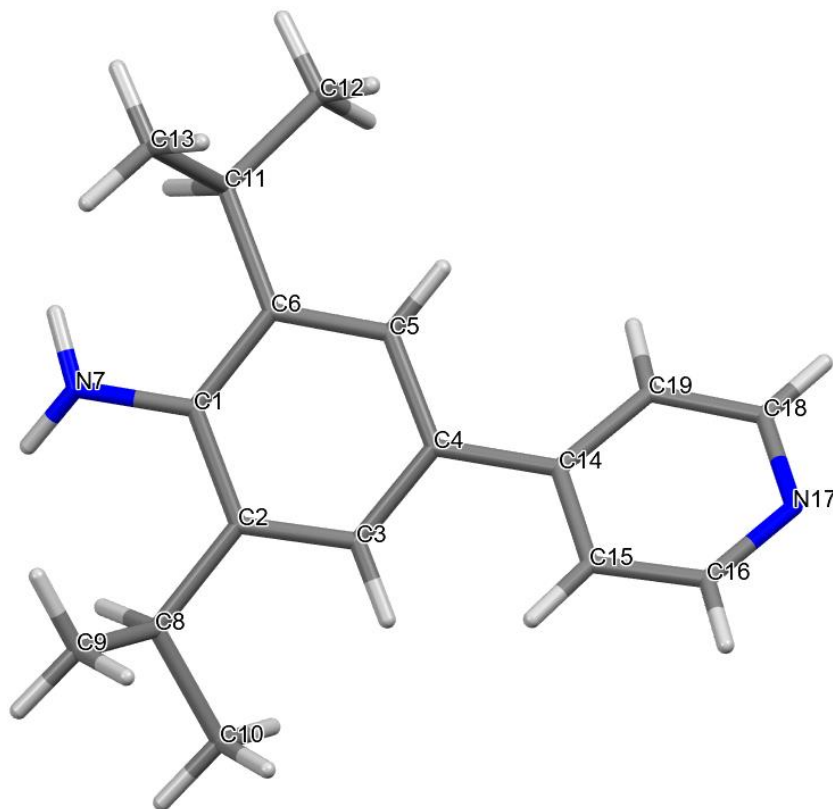
Table of Bond Lengths for 2,6-diisopropyl-4-(pyridin-4-yl)aniline.

Atom	Atom	Length/Å	Atom	Atom	Length/Å
N7	C1	1.383(2)	C5	C6	1.394(2)
N17	C16	1.335(2)	C6	C11	1.521(2)
N17	C18	1.339(3)	C8	C9	1.528(3)
C1	C2	1.413(2)	C8	C10	1.526(3)
C1	C6	1.415(2)	C11	C12	1.529(3)
C2	C3	1.392(2)	C11	C13	1.533(3)
C2	C8	1.520(2)	C14	C15	1.394(2)
C3	C4	1.396(2)	C14	C19	1.389(2)
C4	C5	1.393(2)	C15	C16	1.389(2)
C4	C14	1.484(2)	C18	C19	1.388(3)

Table of Bond angles for 2,6-diisopropyl-4-(pyridin-4-yl)aniline.

Atom	Atom	Atom	Angle/°	Atom	Atom	Atom	Angle/°
C16	N17	C18	116.24(15)	C5	C6	C11	121.50(16)
N7	C1	C2	120.05(16)	C2	C8	C9	111.16(16)
N7	C1	C6	119.58(16)	C2	C8	C10	113.57(15)
C2	C1	C6	120.37(14)	C10	C8	C9	110.07(18)
C1	C2	C8	120.09(15)	C6	C11	C12	114.19(15)
C3	C2	C1	118.44(16)	C6	C11	C13	112.52(15)
C3	C2	C8	121.47(16)	C12	C11	C13	109.79(17)
C2	C3	C4	122.23(16)	C15	C14	C4	121.24(14)
C3	C4	C14	120.80(15)	C19	C14	C4	122.32(15)
C5	C4	C3	118.20(15)	C19	C14	C15	116.43(15)
C5	C4	C14	120.99(15)	C16	C15	C14	120.09(15)
C4	C5	C6	121.99(15)	N17	C16	C15	123.52(16)
C1	C6	C11	119.89(14)	N17	C18	C19	124.16(17)
C5	C6	C1	118.61(15)	C18	C19	C14	119.55(17

Appendix II Crystallographic information for DPPNDI

240
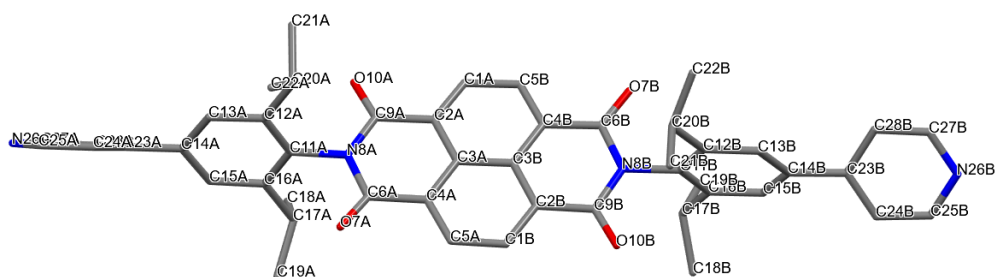
Table of Bond Lengths for DPPNDI

Atom	Atom	Length/Å	Atom	Atom	Length/Å
O7B	C6B	1.211(5)	C14B	C15B	1.386(5)
O7A	C6A	1.193(5)	C14B	C13B	1.391(5)
O10A	C9A	1.233(5)	C14B	C23B	1.486(4)
N8B	C9B	1.373(5)	C15A	C16A	1.397(4)
N8B	C11B	1.463(4)	C12B	C11B	1.393(5)
N8B	C6B	1.407(5)	C12B	C13B	1.402(4)
O10B	C9B	1.218(5)	C12B	C20B	1.522(5)
N8A	C6A	1.412(4)	C16B	C15B	1.393(4)
N8A	C9A	1.374(5)	C16B	C11B	1.392(5)
N8A	C11A	1.457(4)	C16B	C17B	1.527(5)
N26B	C25B	1.340(6)	C1A	C5B	1.417(5)
N26B	C27B	1.338(6)	C12A	C13A	1.400(4)
N26A	C27A	1.338(6)	C12A	C20A	1.514(5)
N26A	C25A	1.350(6)	C1B	C5A	1.399(5)
C3B	C3A	1.424(5)	C16A	C17A	1.528(5)
C3B	C2B	1.423(5)	C23B	C24B	1.391(5)
C3B	C4B	1.385(5)	C23B	C28B	1.390(6)
C2A	C3A	1.419(5)	C23A	C28A	1.395(5)
C2A	C9A	1.487(4)	C23A	C24A	1.382(6)
C2A	C1A	1.348(6)	C17A	C19A	1.508(6)
C3A	C4A	1.392(5)	C17A	C18A	1.511(7)
C6A	C4A	1.501(4)	C17B	C19B	1.512(7)
C2B	C9B	1.487(4)	C17B	C18B	1.519(7)
C2B	C1B	1.370(6)	C24B	C25B	1.387(5)
C4B	C6B	1.479(4)	C28A	C27A	1.389(5)
C4B	C5B	1.383(5)	C20A	C22A	1.499(7)
C4A	C5A	1.379(5)	C20A	C21A	1.543(8)
C11A	C12A	1.394(5)	C20B	C22B	1.514(6)
C11A	C16A	1.398(5)	C20B	C21B	1.519(7)
C14A	C15A	1.389(5)	C24A	C25A	1.386(5)
C14A	C13A	1.389(5)	C27B	C28B	1.391(5)
C14A	C23A	1.487(4)			

Table of Bond angles for DPPNDI

Atom	Atom	Atom	Angle/°	Atom	Atom	Atom	Angle/°
C9B	N8B	C11B	118.4(3)	C15B	C16B	C17B	119.9(3)
C9B	N8B	C6B	125.6(3)	C11B	C16B	C15B	117.2(3)
C6B	N8B	C11B	116.1(3)	C11B	C16B	C17B	122.9(3)
C6A	N8A	C11A	116.1(3)	C14B	C15B	C16B	121.7(3)
C9A	N8A	C6A	126.5(3)	C2A	C1A	C5B	121.4(3)
C9A	N8A	C11A	117.4(3)	C12B	C11B	N8B	118.4(3)
C27B	N26B	C25B	116.4(3)	C16B	C11B	N8B	118.2(3)
C27A	N26A	C25A	116.7(3)	C16B	C11B	C12B	123.4(3)
C2B	C3B	C3A	117.9(3)	O7B	C6B	N8B	120.8(3)
C4B	C3B	C3A	120.2(3)	O7B	C6B	C4B	122.7(3)
C4B	C3B	C2B	121.9(3)	N8B	C6B	C4B	116.5(3)
C3A	C2A	C9A	118.1(3)	C14B	C13B	C12B	121.0(3)
C1A	C2A	C3A	120.9(3)	C11A	C12A	C13A	116.8(3)
C1A	C2A	C9A	121.0(3)	C11A	C12A	C20A	122.6(3)
C2A	C3A	C3B	117.8(4)	C13A	C12A	C20A	120.5(3)
C4A	C3A	C3B	120.0(3)	C2B	C1B	C5A	120.2(3)
C4A	C3A	C2A	122.3(3)	C14A	C13A	C12A	121.6(3)
O7A	C6A	N8A	122.0(3)	C11A	C16A	C17A	123.1(3)
O7A	C6A	C4A	123.4(3)	C15A	C16A	C11A	117.0(3)
N8A	C6A	C4A	114.6(3)	C15A	C16A	C17A	119.9(3)
C3B	C2B	C9B	118.8(3)	C4B	C5B	C1A	118.7(4)
C1B	C2B	C3B	121.0(3)	C24B	C23B	C14B	121.7(4)
C1B	C2B	C9B	120.2(3)	C28B	C23B	C14B	121.4(4)
C3B	C4B	C6B	119.9(3)	C28B	C23B	C24B	116.8(3)
C5B	C4B	C3B	121.1(3)	C28A	C23A	C14A	121.3(4)
C5B	C4B	C6B	119.1(3)	C24A	C23A	C14A	121.5(3)
C3A	C4A	C6A	120.5(3)	C24A	C23A	C28A	117.1(3)
C5A	C4A	C3A	120.6(3)	C19A	C17A	C16A	111.0(3)
C5A	C4A	C6A	118.9(3)	C19A	C17A	C18A	112.5(4)
O10A	C9A	N8A	121.9(3)	C18A	C17A	C16A	111.2(3)
O10A	C9A	C2A	120.2(4)	C19B	C17B	C16B	111.7(4)
N8A	C9A	C2A	117.8(3)	C19B	C17B	C18B	111.1(4)
C12A	C11A	N8A	118.4(3)	C18B	C17B	C16B	110.8(3)
C12A	C11A	C16A	123.6(3)	C4A	C5A	C1B	120.3(4)
C16A	C11A	N8A	117.9(3)	C25B	C24B	C23B	120.0(4)
C15A	C14A	C13A	119.4(3)	C27A	C28A	C23A	119.9(4)
C15A	C14A	C23A	120.4(3)	N26B	C25B	C24B	123.4(4)
C13A	C14A	C23A	120.1(3)	C12A	C20A	C21A	110.8(4)
C15B	C14B	C13B	119.4(3)	C22A	C20A	C12A	112.8(4)
C15B	C14B	C23B	120.3(3)	C22A	C20A	C21A	110.2(5)
C13B	C14B	C23B	120.2(3)	N26A	C27A	C28A	123.1(4)
N8B	C9B	C2B	117.1(3)	C22B	C20B	C12B	113.0(4)
O10B	C9B	N8B	121.1(3)	C22B	C20B	C21B	111.3(4)
O10B	C9B	C2B	121.7(3)	C21B	C20B	C12B	110.2(4)
C14A	C15A	C16A	121.5(3)	C23A	C24A	C25A	119.7(4)
C11B	C12B	C13B	117.3(3)	N26B	C27B	C28B	124.0(4)
C11B	C12B	C20B	123.0(3)	N26A	C25A	C24A	123.5(4)
C13B	C12B	C20B	119.7(3)	C23B	C28B	C27B	119.3(4)
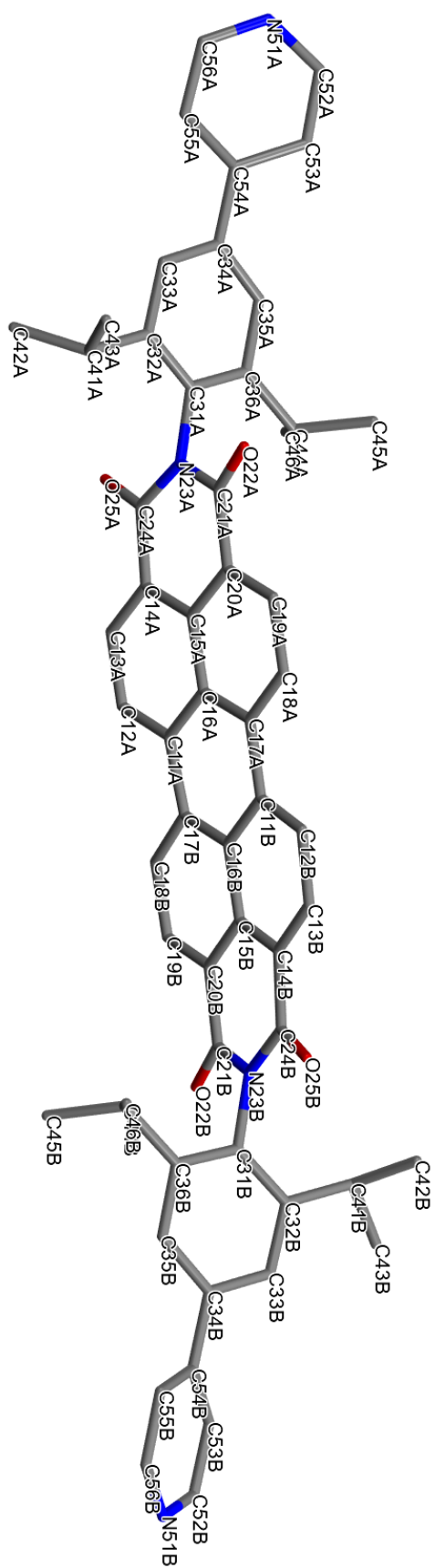
Table of Bond Lengths for DPPPDI

Atom	Atom	Length/Å	Atom	Atom	Length/Å
C11A	C12A	1.385(6)	C55A	C56A	1.389(7)
C11A	C16A	1.410(6)	C11B	C12B	1.389(6)
C11A	C17B	1.477(6)	C11B	C16B	1.415(6)
C12A	C13A	1.383(6)	C12B	C13B	1.392(6)
C13A	C14A	1.371(6)	C13B	C14B	1.373(6)
C14A	C15A	1.398(6)	C14B	C15B	1.410(6)
C14A	C24A	1.489(6)	C14B	C24B	1.471(6)
C15A	C16A	1.434(6)	C15B	C16B	1.440(6)
C15A	C20A	1.397(6)	C15B	C20B	1.391(6)
C16A	C17A	1.413(6)	C16B	C17B	1.402(6)
C17A	C18A	1.383(6)	C17B	C18B	1.377(6)
C17A	C11B	1.467(6)	C18B	C19B	1.403(6)
C18A	C19A	1.397(6)	C19B	C20B	1.370(6)
C19A	C20A	1.371(6)	C20B	C21B	1.490(6)
C20A	C21A	1.495(6)	C21B	O22B	1.208(5)
C21A	O22A	1.203(5)	C21B	N23B	1.391(6)
C21A	N23A	1.408(6)	N23B	C24B	1.387(6)
N23A	C24A	1.365(6)	N23B	C31B	1.466(5)
N23A	C31A	1.456(5)	C24B	O25B	1.226(5)
C24A	O25A	1.204(5)	C31B	C32B	1.394(6)
C31A	C32A	1.387(6)	C31B	C36B	1.382(6)
C31A	C36A	1.388(6)	C32B	C33B	1.384(6)
C32A	C33A	1.395(6)	C32B	C41B	1.501(6)
C32A	C41A	1.504(6)	C33B	C34B	1.375(6)
C33A	C34A	1.378(6)	C34B	C35B	1.394(6)
C34A	C35A	1.377(6)	C34B	C54B	1.485(6)
C34A	C54A	1.491(6)	C35B	C36B	1.397(6)
C35A	C36A	1.389(6)	C36B	C44B	1.512(6)
C36A	C44A	1.515(6)	C41B	C42B	1.504(6)
C41A	C42A	1.513(6)	C41B	C43B	1.498(6)
C41A	C43A	1.517(6)	C44B	C45B	1.521(6)
C44A	C45A	1.519(6)	C44B	C46B	1.517(7)
C44A	C46A	1.517(6)	N51B	C52B	1.326(6)
N51A	C52A	1.320(6)	N51B	C56B	1.307(6)
N51A	C56A	1.286(6)	C52B	C53B	1.380(6)
C52A	C53A	1.398(7)	C53B	C54B	1.377(6)
C53A	C54A	1.407(7)	C54B	C55B	1.377(6)
C54A	C55A	1.336(6)	C55B	C56B	1.388(6)

Table of Bond angles for DPPPDI

Atom	Atom	Atom	Angle/°	Atom	Atom	Atom	Angle/°
C12A	C11A	C16A	119.9(4)	C12B	C11B	C17A	121.4(4)
C12A	C11A	C17B	121.6(5)	C12B	C11B	C16B	119.5(4)
C16A	C11A	C17B	118.5(4)	C16B	C11B	C17A	119.1(4)
C13A	C12A	C11A	120.6(5)	C11B	C12B	C13B	121.4(5)
C14A	C13A	C12A	121.0(5)	C14B	C13B	C12B	120.6(5)
C13A	C14A	C15A	120.4(4)	C13B	C14B	C15B	120.3(4)
C13A	C14A	C24A	120.0(4)	C13B	C14B	C24B	119.9(4)
C15A	C14A	C24A	119.4(5)	C15B	C14B	C24B	119.6(4)
C14A	C15A	C16A	119.2(5)	C14B	C15B	C16B	119.3(4)
C20A	C15A	C14A	121.3(4)	C20B	C15B	C14B	121.0(4)
C20A	C15A	C16A	119.4(4)	C20B	C15B	C16B	119.6(4)
C11A	C16A	C15A	118.8(4)	C11B	C16B	C15B	118.8(4)
C11A	C16A	C17A	122.7(4)	C17B	C16B	C11B	122.4(4)
C17A	C16A	C15A	118.5(4)	C17B	C16B	C15B	118.8(4)
C16A	C17A	C11B	118.4(4)	C16B	C17B	C11A	118.7(4)
C18A	C17A	C16A	119.9(4)	C18B	C17B	C11A	121.6(4)
C18A	C17A	C11B	121.7(4)	C18B	C17B	C16B	119.6(4)
C17A	C18A	C19A	121.1(5)	C17B	C18B	C19B	121.5(5)
C20A	C19A	C18A	119.9(5)	C20B	C19B	C18B	119.7(5)
C15A	C20A	C21A	120.0(4)	C15B	C20B	C21B	120.3(5)
C19A	C20A	C15A	121.1(4)	C19B	C20B	C15B	120.8(4)
C19A	C20A	C21A	119.0(5)	C19B	C20B	C21B	118.9(5)
O22A	C21A	C20A	122.9(5)	O22B	C21B	C20B	122.3(5)
O22A	C21A	N23A	121.5(4)	O22B	C21B	N23B	121.7(5)
N23A	C21A	C20A	115.6(5)	N23B	C21B	C20B	115.9(5)
C21A	N23A	C31A	115.8(4)	C21B	N23B	C31B	116.6(4)
C24A	N23A	C21A	125.2(4)	C24B	N23B	C21B	125.3(4)
C24A	N23A	C31A	118.7(4)	C24B	N23B	C31B	117.3(4)
N23A	C24A	C14A	117.4(4)	N23B	C24B	C14B	117.2(4)
O25A	C24A	C14A	121.4(5)	O25B	C24B	C14B	122.4(5)
O25A	C24A	N23A	121.1(4)	O25B	C24B	N23B	120.3(4)
C32A	C31A	N23A	120.1(4)	C32B	C31B	N23B	121.1(5)
C32A	C31A	C36A	123.2(4)	C36B	C31B	N23B	115.0(4)
C36A	C31A	N23A	116.8(4)	C36B	C31B	C32B	124.0(4)
C31A	C32A	C33A	116.4(4)	C31B	C32B	C41B	121.8(4)
C31A	C32A	C41A	122.6(4)	C33B	C32B	C31B	116.6(5)
C33A	C32A	C41A	121.0(5)	C33B	C32B	C41B	121.6(5)
C34A	C33A	C32A	122.4(5)	C34B	C33B	C32B	122.2(5)
C33A	C34A	C54A	120.7(5)	C33B	C34B	C35B	119.2(5)
C35A	C34A	C33A	118.9(4)	C33B	C34B	C54B	120.2(5)
C35A	C34A	C54A	120.4(5)	C35B	C34B	C54B	120.6(5)
C34A	C35A	C36A	121.4(5)	C34B	C35B	C36B	121.2(5)
C31A	C36A	C35A	117.7(5)	C31B	C36B	C35B	116.8(5)
C31A	C36A	C44A	123.5(4)	C31B	C36B	C44B	124.7(5)
C35A	C36A	C44A	118.8(5)	C35B	C36B	C44B	118.5(5)

C32A	C41A	C42A	112.5(4)	C32B	C41B	C42B	113.2(4)
C32A	C41A	C43A	111.2(4)	C43B	C41B	C32B	113.0(5)
C42A	C41A	C43A	111.7(5)	C43B	C41B	C42B	108.5(5)
C36A	C44A	C45A	111.2(4)	C36B	C44B	C45B	112.7(4)
C36A	C44A	C46A	112.0(4)	C36B	C44B	C46B	110.5(4)
C46A	C44A	C45A	113.1(5)	C46B	C44B	C45B	111.9(5)
C56A	N51A	C52A	116.7(5)	C56B	N51B	C52B	115.1(5)
N51A	C52A	C53A	123.4(6)	N51B	C52B	C53B	123.9(5)
C52A	C53A	C54A	119.1(6)	C54B	C53B	C52B	120.5(5)
C53A	C54A	C34A	121.4(5)	C53B	C54B	C34B	121.0(5)
C55A	C54A	C34A	123.5(5)	C53B	C54B	C55B	115.9(5)
C55A	C54A	C53A	115.0(5)	C55B	C54B	C34B	123.0(5)
C54A	C55A	C56A	122.0(6)	C54B	C55B	C56B	118.9(5)
N51A	C56A	C55A	123.8(6)	N51B	C56B	C55B	125.6(5

Appendix IV Crystallographic information for 1
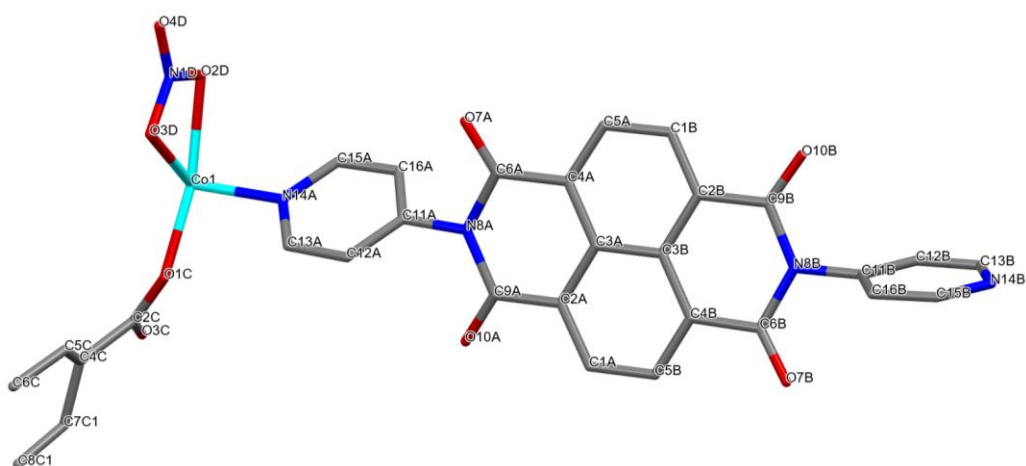
Table of Bond Lengths around Co(II) in 1

Atom	Atom	Length/Å
Co1	N14A	2.137(4)
Co1	N14B[1]	2.148(4)
Co1	O1C	1.997(3)
Co1	O3C[2]	2.000(3)
Co1	O2D	2.198(4)
Co1	O3D	2.192(3)

Table of Bond Angles around Co(II) in 1

Atom	Atom	Atom	Angle/°	Atom	Atom	Atom	Angle/°
N14A	Co1	N14B[1]	173.65(14)	O1C	Co1	O2D	155.59(15)
N14A	Co1	O2D	89.57(15)	O1C	Co1	O3D	97.20(16)
N14A	Co1	O3D	87.83(14)	O3C[2]	Co1	N14A	88.90(15)
N14B[1]	Co1	O2D	92.16(15)	O3C[2]	Co1	N14B[1]	97.29(15)
N14B[1]	Co1	O3D	87.87(13)	O3C[2]	Co1	O2D	86.99(15)
O1C	Co1	N14A	88.40(14)	O3C[2]	Co1	O3D	145.25(15)
O1C	Co1	N14B[1]	87.49(14)	O3D	Co1	O2D	58.40(15)
O1C	Co1	O3C[2]	117.28(15)				

Appendix V Crystallographic information for 2

Table of Bond Lengths around Co (II) in 2

Atom	Atom	Length/Å
Co2	Co1	2.6671(7)
Co2	O2C	2.033(3)
Co2	O16D[1]	2.022(3)
Co2	O1D	2.005(3)
Co2	O15C[2]	2.003(4)
Co2	N14A[3]	2.051(4)
Co1	O15D[1]	2.000(3)
Co1	N14B	2.047(4)
Co1	O2D	2.019(3)
Co1	O1C	2.020(3)
Co1	O16C[2]	2.030(3)

Table of Bond angles around Co(II) in 2

Atom	Atom	Atom	Angle/°	Atom	Atom	Atom	Angle/°
O2C	Co2	Co1	80.34(11)	O2D	Co1	Co2	82.05(11)
O2C	Co2	N14A[1]	93.68(16)	O2D	Co1	N14B	95.81(16)
O16D[2]	Co2	Co1	81.98(11)	O2D	Co1	O1C	87.71(15)
O16D[2]	Co2	O2C	89.19(15)	O2D	Co1	O16C[3]	88.42(14)
O16D[2]	Co2	N14A[1]	89.26(16)	O1C	Co1	Co2	87.40(10)
O1D	Co2	Co1	85.65(10)	O1C	Co1	N14B	96.40(15)
O1D	Co2	O2C	87.51(15)	O1C	Co1	O16C[3]	168.68(15)
O1D	Co2	O16D[2]	167.56(15)	O16C[3]	Co1	Co2	81.53(11)
O1D	Co2	N14A[1]	102.91(15)	O16C[3]	Co1	N14B	94.57(16)
O15C[3]	Co2	Co1	86.22(10)	C3C	O2C	Co2	127.1(3)
O15C[3]	Co2	O2C	166.56(15)	C14D	O15D	Co1[4]	121.5(3)
O15C[3]	Co2	O16D[2]	88.95(15)	C15B	N14B	Co1	122.9(3)
O15C[3]	Co2	O1D	91.47(16)	C15B	N14B	C13B	118.0(5)
O15C[3]	Co2	N14A[1]	99.60(15)	C13B	N14B	Co1	119.1(4)
N14A[1]	Co2	Co1	169.42(12)	C3D	O2D	Co1	124.8(3)
O15D[2]	Co1	Co2	85.78(10)	C14D	O16D	Co2[4]	124.5(3)
O15D[2]	Co1	N14B	96.25(15)	C3D	O1D	Co2	121.4(3)
O15D[2]	Co1	O2D	167.79(15)	C14C	O15C	Co2[5]	121.2(3)
O15D[2]	Co1	O1C	92.81(15)	C3C	O1C	Co1	119.4(3)
O15D[2]	Co1	O16C[3]	88.74(15)	C14C	O16C	Co1[5]	
N14B	Co1	Co2	175.58(12)				

Appendix VI Crystallographic information for 3

Table of Bond Lengths around Co(II) in 3

Atom	Atom	Length/Å	Atom	Atom	Length/Å
Co1	Co2	2.7740(5)	C23A	C24A	1.395(5)
Co1	O15D[1]	2.0213(18)	C11C	C10C	1.362(5)
Co1	O15C[2]	2.028(2)	C25A	C24A	1.378(4)
Co1	O1D	2.0090(18)	C15A	C16A	1.406(5)
Co1	O1C	2.097(2)	N8B	C9B	1.420(8)
Co1	N26A	2.050(2)	N8B	C11B	1.468(5)
Co2	O16D[1]	2.0202(18)	N8B	C6B	1.390(8)
Co2	O16C[2]	2.103(2)	C23B	C14B	1.489(4)
Co2	O3C	2.018(2)	C23B	C28B	1.411(7)
Co2	O2D	2.0156(19)	C23B	C24B	1.353(7)
Co2	N26B[3]	2.059(2)			

Table of Bond angles around Co(II) in 3

Atom	Atom	Atom	Angle/°	Atom	Atom	Atom	Angle/°
O15D[1]	Co1	Co2	84.05(5)	O3C	Co2	N26B[3]	102.67(10)
O15D[1]	Co1	O15C[2]	90.49(8)	O2D	Co2	Co1	82.70(6)
O15D[1]	Co1	O1C	85.75(8)	O2D	Co2	O16D[1]	163.53(8)
O15D[1]	Co1	N26A	94.37(8)	O2D	Co2	O16C[2]	85.67(9)
O15C[2]	Co1	Co2	97.04(6)	O2D	Co2	O3C	90.84(9)
O15C[2]	Co1	O1C	164.40(8)	O2D	Co2	N26B[3]	102.75(9)
O15C[2]	Co1	N26A	102.45(9)	N26B[3]	Co2	Co1	158.93(8)
O1D	Co1	Co2	81.93(6)	N26B[3]	Co2	O16C[2]	91.75(10)
O1D	Co1	O15D[1]	165.97(8)	C14D	O15D	Co1[4]	122.78(17)
O1D	Co1	O15C[2]	91.47(8)	C14C	O15C	Co1[5]	109.15(19)
O1D	Co1	O1C	88.66(9)	C3D	O1D	Co1	125.91(17)
O1D	Co1	N26A	98.77(8)	C14D	O16D	Co2[4]	126.85(17)
O1C	Co1	Co2	67.53(6)	C14C	O16C	Co2[5]	141.30(19)
N26A	Co1	Co2	160.46(7)	C2C	O3C	Co2	108.4(2)
N26A	Co1	O1C	92.94(9)	C2C	O1C	Co1	141.6(2)
O16D[1]	Co2	Co1	80.85(5)	C3D	O2D	Co2	124.58(18)
O16D[1]	Co2	O16C[2]	87.53(9)	C27A	N26A	Co1	123.54(18)
O16D[1]	Co2	N26B[3]	92.42(9)	C27A	N26A	C25A	117.3(2)
O16C[2]	Co2	Co1	68.17(6)	C25A	N26A	Co1	119.15(19)
O3C	Co2	Co1	97.52(7)	C25B	N26B	Co2[6]	123.0(3)
O3C	Co2	O16D[1]	92.05(9)	C25B	N26B	C27B	116.6(3)
O3C	Co2	O16C[2]	165.58(9)	C27B	N26B	Co2[6]	120.3(2)

Appendix VII Crystallographic information for 4

Bond Lengths around Co(II) in 4

Atom	Atom	Length/Å	Atom	Atom	Length/Å
Co1	Co2[1]	2.7647(6)	Co2	N26A[3]	2.057(2)
Co1	N26B	2.052(3)	Co2	O9C[4]	2.026(2)
Co1	O8C	2.008(2)	Co2	O8D	2.029(2)
Co1	O9D[1]	2.002(2)	Co2	O8E	2.020(2)
Co1	O9E[1]	2.121(2)	Co2	O9F[5]	2.121(2)
Co1	O8F[2]	2.015(2)			

Bond Angles around Co(II) in 4

Atom	Atom	Atom	Angle/°	Atom	Atom	Atom	Angle/°
N26B	Co1	Co2[1]	155.11(8)	N26A[3]	Co2	Co1[4]	158.67(8)
N26B	Co1	O9E[1]	89.35(11)	N26A[3]	Co2	O9F[5]	93.01(11)
O8C	Co1	Co2[1]	82.07(6)	O9C[4]	Co2	Co1[4]	82.99(6)
O8C	Co1	N26B	98.41(10)	O9C[4]	Co2	N26A[3]	96.53(10)
O8C	Co1	O9E[1]	85.55(10)	O9C[4]	Co2	O8D	165.23(9)
O8C	Co1	O8F[2]	91.44(10)	O9C[4]	Co2	O9F[5]	84.39(10)
O9D[1]	Co1	Co2[1]	81.53(6)	O8D	Co2	Co1[4]	82.92(6)
O9D[1]	Co1	N26B	95.78(11)	O8D	Co2	N26A[3]	95.00(10)
O9D[1]	Co1	O8C	163.53(9)	O8D	Co2	O9F[5]	85.82(10)
O9D[1]	Co1	O9E[1]	86.29(11)	O8E	Co2	Co1[4]	99.17(7)
O9D[1]	Co1	O8F[2]	92.79(11)	O8E	Co2	N26A[3]	102.16(11)
O9E[1]	Co1	Co2[1]	65.82(7)	O8E	Co2	O9C[4]	92.12(11)
O8F[2]	Co1	Co2[1]	99.35(8)	O8E	Co2	O8D	94.44(11)
O8F[2]	Co1	N26B	105.50(11)	O8E	Co2	O9F[5]	164.73(10)
O8F[2]	Co1	O9E[1]	165.13(11)	O9F[5]	Co2	Co1[4]	65.68(7)

Appendix VIII Crystallographic information for 5

Bond Lengths around Ni(II) in 5

Atom	Atom	Length/Å
Ni1	Ni2	2.6671(15)
Ni1	N36A	1.947(6)
Ni1	O97A	1.986(5)
Ni1	O53A	2.010(5)
Ni1	O1[1]	2.008(5)
Ni1	O2[2]	2.060(5)
Ni2	O98A	1.984(5)
Ni2	O94A[1]	1.986(5)
Ni2	O55A	2.053(5)
Ni2	O58A[2]	2.019(5)
Ni2	N76A[3]	1.962(6)

Bond angles around Ni(II) in 5

Atom	Atom	Atom	Angle/°	Atom	Atom	Atom	Angle/°
N36A	Ni1	Ni2	159.84(19)	O58A^2	Ni2	Ni1	102.06(18)
N36A	Ni1	O97A	94.1(2)	O58A^2	Ni2	O55A	167.4(2)
N36A	Ni1	O53A	98.2(3)	N76A^3	Ni2	Ni1	156.4(2)
N36A	Ni1	O1^1	96.7(2)	N76A^3	Ni2	O98A	94.6(2)
N36A	Ni1	O2^2	95.1(2)	N76A^3	Ni2	O94A^1	97.3(2)
O97A	Ni1	Ni2	84.24(14)	N76A^3	Ni2	O55A	91.0(2)
O97A	Ni1	O53A	92.3(2)	N76A^3	Ni2	O58A^2	101.5(3)
O97A	Ni1	O1^1	168.4(2)	C96A	O98A	Ni2	123.7(4)
O97A	Ni1	O2^2	88.0(2)	C93A	O94A	Ni2^4	123.9(4)
O53A	Ni1	Ni2	101.94(17)	C54A	O55A	Ni2	144.9(5)
O53A	Ni1	O2^2	166.6(2)	C21A	N13A	C14A	119.9(6)
O1^1	Ni1	Ni2	84.12(14)	C12A	N13A	C21A	117.3(6)
O1^1	Ni1	O53A	90.6(2)	C12A	N13A	C14A	122.6(6)
O1^1	Ni1	O2^2	86.7(2)	C37A	N36A	Ni1	123.4(5)
O2^2	Ni1	Ni2	64.79(16)	C37A	N36A	C35A	114.4(6)
O98A	Ni2	Ni1	84.16(14)	C35A	N36A	Ni1	122.2(5)
O98A	Ni2	O94A^1	167.8(2)	C96A	O97A	Ni1	123.1(4)
O98A	Ni2	O55A	89.7(2)	C54A	O53A	Ni1	103.5(5)
O98A	Ni2	O58A^2	90.3(2)	C56A	O58A	Ni2^5	102.8(5)
O94A^1	Ni2	Ni1	83.99(15)	C77A	N76A	Ni2^6	122.7(5)
O94A^1	Ni2	O55A	87.9(2)	C77A	N76A	C75A	115.8(6)
O94A^1	Ni2	O58A^2	89.4(2)	C75A	N76A	Ni2^6	121.1(5)
O55A	Ni2	Ni1	65.43(15)				

Appendix IX Crystallographic information for 6

Bond lengths around Co(II) in 6

Atom	Atom	Length/Å
Co1	Co2	2.651(4)
Co1	O18A	2.021(15)
Co1	O18C	2.051(15)
Co1	O18D	2.039(15)
Co1	O29D[1]	2.057(16)
Co1	N61F	2.083(16)
Co2	O19A	2.042(17)
Co2	O19C	2.062(16)
Co2	O19D	1.991(15)
Co2	O28D[1]	1.980(16)
Co2	N61G[2]	2.061(17)
Co3	Co4	2.654(5)
Co3	O28A	2.014(16)
Co3	O19B	2.041(15)
Co3	O19E	2.043(16)
Co3	O28E[3]	2.003(15)
Co3	N61H	2.049(18)
Co4	O29A	2.056(17)
Co4	O18B	2.067(16)
Co4	O18E	1.992(16)
Co4	O29E[3]	1.978(15)
Co4	N61I[4]	2.071(18)

Bond angles in 6

Atom	Atom	Atom	Angle/°	Atom	Atom	Atom	Angle/°
O18A	Co1	Co2	82.2(4)	C15F	C20F	C19F	119.0(14)
O18A	Co1	O18C	167.6(6)	C15F	C20F	C21F	121.9(14)
O18A	Co1	O18D	89.4(6)	C19F	C20F	C21F	119.0(14)
O18A	Co1	O29D[1]	86.3(6)	O22F	C21F	C20F	123.8(15)
O18A	Co1	N61F	92.8(7)	O22F	C21F	N23F	120.0(15)
O18C	Co1	Co2	85.9(4)	N23F	C21F	C20F	116.2(15)
O18C	Co1	O29D[1]	89.2(6)	C21F	N23F	C24F	125.4(16)
O18C	Co1	N61F	99.2(7)	C21F	N23F	C31F	116.5(12)
O18D	Co1	Co2	82.8(4)	C24F	N23F	C31F	117.7(12)

O18D	Co1	O18C	92.3(6)	N23F	C24F	C14F	116.1(14)
O18D	Co1	O29D[1]	166.3(6)	O25F	C24F	C14F	122.3(15)
O18D	Co1	N61F	96.0(6)	O25F	C24F	N23F	121.6(15)
O29D[1]	Co1	Co2	83.7(4)	C32F	C31F	N23F	114.6(13)
O29D[1]	Co1	N61F	97.1(6)	C36F	C31F	N23F	115.0(13)
N61F	Co1	Co2	174.9(5)	C36F	C31F	C32F	130.1(17)
O19A	Co2	Co1	85.2(5)	C31F	C32F	C33F	113.7(15)
O19A	Co2	O19C	166.5(6)	C31F	C32F	C51F	127.8(16)
O19A	Co2	N61G[2]	97.1(7)	C33F	C32F	C51F	118.4(15)
O19C	Co2	Co1	81.4(4)	C34F	C33F	C32F	120.0(16)
O19D	Co2	Co1	84.8(4)	C33F	C34F	C64F	118.2(13)
O19D	Co2	O19A	90.7(7)	C35F	C34F	C33F	122.0(17)
O19D	Co2	O19C	89.0(6)	C35F	C34F	C64F	119.8(13)
O19D	Co2	N61G[2]	97.0(7)	C34F	C35F	C36F	120.2(15)
O28D[1]	Co2	Co1	83.6(5)	C31F	C36F	C35F	113.8(15)
O28D[1]	Co2	O19A	90.0(7)	C31F	C36F	C41F	128.5(16)
O28D[1]	Co2	O19C	87.6(7)	C35F	C36F	C41F	117.7(14)
O28D[1]	Co2	O19D	168.3(7)	C36F	C41F	C42F	114.1(17)
O28D[1]	Co2	N61G[2]	94.5(7)	C36F	C41F	C43F	113.7(17)
N61G[2]	Co2	Co1	177.1(5)	C42F	C41F	C43F	112.3(17)
N61G[2]	Co2	O19C	96.4(7)	C32F	C51F	C52F	113.4(16)
O28A	Co3	Co4	81.6(5)	C32F	C51F	C53F	115.3(17)
O28A	Co3	O19B	167.2(6)	C53F	C51F	C52F	110.6(17)
O28A	Co3	O19E	86.2(7)	C62F	N61F	Co1	118.3(13)
O28A	Co3	N61H	93.8(7)	C66F	N61F	Co1	122.6(13)
O19B	Co3	Co4	85.7(4)	C66F	N61F	C62F	118.8(16)
O19B	Co3	O19E	90.6(6)	N61F	C62F	C63F	121.1(16)
O19B	Co3	N61H	98.9(7)	C62F	C63F	C64F	120.1(16)

254

O19E	Co3	Co4	83.7(5)	C63F	C64F	C34F	120.8(13)
O19E	Co3	N61H	98.0(7)	C65F	C64F	C34F	121.7(14)
O28E[3]	Co3	Co4	82.4(5)	C65F	C64F	C63F	117.5(16)
O28E[3]	Co3	O28A	87.6(7)	C66F	C65F	C64F	119.4(16)
O28E[3]	Co3	O19B	92.5(6)	N61F	C66F	C65F	122.7(16)
O28E[3]	Co3	O19E	165.5(7)	C12G	C11G	C17F	121.7(14)
O28E[3]	Co3	N61H	95.5(7)	C12G	C11G	C16G	119.4(14)
N61H	Co3	Co4	175.0(6)	C16G	C11G	C17F	118.9(14)
O29A	Co4	Co3	85.2(5)	C13G	C12G	C11G	121.6(15)
O29A	Co4	O18B	167.6(7)	C12G	C13G	C14G	121.1(15)
O29A	Co4	N61I[4]	94.7(8)	C13G	C14G	C24G	120.1(14)
O18B	Co4	Co3	82.4(5)	C15G	C14G	C13G	118.6(14)
O18B	Co4	N61I[4]	97.6(7)	C15G	C14G	C24G	121.2(14)
O18E	Co4	Co3	84.3(5)	C14G	C15G	C16G	120.6(12)
O18E	Co4	O29A	90.1(7)	C14G	C15G	C20G	117.9(15)
O18E	Co4	O18B	87.2(7)	C20G	C15G	C16G	121.5(12)
O18E	Co4	N61I[4]	94.5(7)	C15G	C16G	C11G	118.3(13)
O29E[3]	Co4	Co3	85.2(5)	C15G	C16G	C17G	118.8(12)
O29E[3]	Co4	O29A	91.3(7)	C17G	C16G	C11G	122.8(16)
O29E[3]	Co4	O18B	89.3(7)	C16G	C17G	C11F	118.6(14)
O29E[3]	Co4	O18E	169.3(7)	C18G	C17G	C11F	123.4(14)
O29E[3]	Co4	N61I[4]	96.0(7)	C18G	C17G	C16G	118.0(14)
N61I[4]	Co4	Co3	178.8(6)	C19G	C18G	C17G	123.0(16)
C12A	C11A	C16A	114.6(15)	C18G	C19G	C20G	120.4(15)
C12A	C11A	C17A	124.4(15)	C15G	C20G	C21G	122.3(14)
C16A	C11A	C17A	120.9(14)	C19G	C20G	C15G	118.0(13)
C13A	C12A	C11A	124.9(16)	C19G	C20G	C21G	119.7(14)
C12A	C13A	C14A	120.6(16)	O22G	C21G	C20G	124.3(15)

C13A	C14A	C24A	121.4(18)	O22G	C21G	N23G	119.6(15)
C15A	C14A	C13A	114.4(16)	N23G	C21G	C20G	116.1(14)
C15A	C14A	C24A	124.2(18)	C21G	N23G	C31G	115.5(12)
C16A	C15A	C14A	124.4(16)	C24G	N23G	C21G	124.7(16)
C15A	C16A	C11A	120.9(15)	C24G	N23G	C31G	119.4(12)
O18A	C17A	C11A	119.2(15)	N23G	C24G	C14G	117.4(14)
O18A	C17A	O19A	121.8(16)	O25G	C24G	C14G	122.4(15)
O19A	C17A	C11A	119.0(14)	O25G	C24G	N23G	120.2(15)
C17A	O18A	Co1	127.9(13)	C32G	C31G	N23G	112.9(13)
C17A	O19A	Co2	122.9(13)	C36G	C31G	N23G	115.2(13)
C22A	C21A	C26A	116.6(15)	C36G	C31G	C32G	131.4(17)
C22A	C21A	C27A	123.3(15)	C31G	C32G	C33G	112.6(14)
C26A	C21A	C27A	120.2(15)	C31G	C32G	C51G	129.9(16)
C23A	C22A	C21A	121.8(16)	C33G	C32G	C51G	117.5(15)
C22A	C23A	C24A	123.0(17)	C34G	C33G	C32G	120.0(16)
C23A	C24A	C14A	123.2(19)	C33G	C34G	C64G	117.9(14)
C23A	C24A	C25A	115.0(16)	C35G	C34G	C33G	122.6(17)
C25A	C24A	C14A	121.8(19)	C35G	C34G	C64G	119.5(13)
C26A	C25A	C24A	120.8(17)	C34G	C35G	C36G	120.5(15)
C25A	C26A	C21A	122.9(17)	C31G	C36G	C35G	112.9(15)
O28A	C27A	C21A	118.6(15)	C31G	C36G	C41G	129.2(15)
O28A	C27A	O29A	123.0(17)	C35G	C36G	C41G	117.9(14)
O29A	C27A	C21A	118.5(14)	C36G	C41G	C42G	112.8(17)
C27A	O28A	Co3	128.3(13)	C36G	C41G	C43G	116.8(17)
C27A	O29A	Co4	121.4(13)	C42G	C41G	C43G	110.4(17)
C12B	C11B	C17B	120.5(15)	C32G	C51G	C52G	112.5(17)
C16B	C11B	C12B	117.8(15)	C32G	C51G	C53G	115.4(17)
C16B	C11B	C17B	121.6(14)	C53G	C51G	C52G	110.4(17)

256

C13B	C12B	C11B	123.8(16)	C62G	N61G	Co2[4]	121.3(14)
C12B	C13B	C14B	118.5(16)	C66G	N61G	Co2[4]	120.5(14)
C13B	C14B	C24B	115.4(18)	C66G	N61G	C62G	117.7(17)
C15B	C14B	C13B	116.9(17)	N61G	C62G	C63G	123.5(17)
C15B	C14B	C24B	127.8(19)	C62G	C63G	C64G	119.1(16)
C16B	C15B	C14B	123.3(17)	C63G	C64G	C34G	119.1(14)
C15B	C16B	C11B	119.6(16)	C63G	C64G	C65G	117.8(16)
O18B	C17B	C11B	118.6(15)	C65G	C64G	C34G	123.0(14)
O18B	C17B	O19B	125.5(17)	C66G	C65G	C64G	118.8(16)
O19B	C17B	C11B	115.9(14)	N61G	C66G	C65G	122.9(17)
C17B	O18B	Co4	124.2(13)	C12H	C11H	C16H	118.7(17)
C17B	O19B	Co3	121.4(12)	C12H	C11H	C17I	123.2(17)
C22B	C21B	C27B	120.5(16)	C16H	C11H	C17I	118.0(17)
C26B	C21B	C22B	116.8(16)	C13H	C12H	C11H	123.1(18)
C26B	C21B	C27B	122.7(17)	C12H	C13H	C14H	119.4(17)
C23B	C22B	C21B	122.7(18)	C13H	C14H	C24H	118.4(15)
C22B	C23B	C24B	119.8(18)	C15H	C14H	C13H	119.5(15)
C23B	C24B	C14B	116(2)	C15H	C14H	C24H	122.0(16)
C23B	C24B	C25B	117.6(17)	C14H	C15H	C16H	121.5(14)
C25B	C24B	C14B	126(2)	C14H	C15H	C20H	118.1(17)
C26B	C25B	C24B	121.2(18)	C20H	C15H	C16H	120.4(13)
C25B	C26B	C21B	121.8(18)	C15H	C16H	C11H	117.8(14)
O28B	C27B	C21B	122.3(18)	C15H	C16H	C17H	118.6(14)
O29B	C27B	C21B	115.6(17)	C17H	C16H	C11H	123.6(18)
O29B	C27B	O28B	122(2)	C18H	C17H	C16H	118.6(16)
C12C	C11C	C17C	121.2(15)	C18H	C17H	C11I	123.7(17)
C16C	C11C	C12C	116.7(15)	C11I	C17H	C16H	117.7(17)
C16C	C11C	C17C	121.9(15)	C19H	C18H	C17H	122.9(18)

257

C13C	C12C	C11C	119.8(16)	C18H	C19H	C20H	120.3(17)
C12C	C13C	C14C	124.3(17)	C15H	C20H	C19H	119.1(15)
C13C	C14C	C15C	114.8(17)	C15H	C20H	C21H	121.8(16)
C13C	C14C	C24C	126(2)	C19H	C20H	C21H	119.1(15)
C15C	C14C	C24C	119(2)	O22H	C21H	C20H	123.4(17)
C16C	C15C	C14C	120.2(17)	O22H	C21H	N23H	119.8(17)
C11C	C16C	C15C	124.1(17)	N23H	C21H	C20H	116.7(16)
O18C	C17C	C11C	115.6(14)	C21H	N23H	C24H	124.6(18)
O19C	C17C	C11C	121.6(15)	C21H	N23H	C31H	118.2(14)
O19C	C17C	O18C	122.8(16)	C24H	N23H	C31H	117.0(14)
C17C	O18C	Co1	122.1(12)	N23H	C24H	C14H	116.4(16)
C17C	O19C	Co2	127.6(13)	O25H	C24H	C14H	124.3(18)
C22C	C21C	C26C	118.6(17)	O25H	C24H	N23H	119.3(18)
C22C	C21C	C27C	120.6(17)	C32H	C31H	N23H	115.3(14)
C26C	C21C	C27C	120.8(17)	C36H	C31H	N23H	114.5(14)
C23C	C22C	C21C	120.7(18)	C36H	C31H	C32H	130.2(18)
C22C	C23C	C24C	121.2(18)	C31H	C32H	C33H	114.6(16)
C23C	C24C	C14C	124(2)	C31H	C32H	C51H	127.4(17)
C25C	C24C	C14C	118(2)	C33H	C32H	C51H	117.9(16)
C25C	C24C	C23C	117.3(18)	C34H	C33H	C32H	120.0(17)
C26C	C25C	C24C	120.3(18)	C33H	C34H	C35H	120.7(18)
C25C	C26C	C21C	121.7(18)	C33H	C34H	C64H	119.0(14)
O28C	C27C	C21C	117(2)	C35H	C34H	C64H	120.2(14)
O28C	C27C	O29C	125(2)	C34H	C35H	C36H	122.0(16)
O29C	C27C	C21C	118(2)	C31H	C36H	C35H	112.5(15)
C12D	C11D	C16D	117.4(14)	C31H	C36H	C41H	129.6(17)
C12D	C11D	C17D	121.1(14)	C41H	C36H	C35H	117.9(15)
C16D	C11D	C17D	121.4(14)	C36H	C41H	C42H	115.8(18)

C13D	C12D	C11D	121.5(15)	C36H	C41H	C43H	113.0(18)
C12D	C13D	C14D	122.5(15)	C42H	C41H	C43H	111.8(18)
C13D	C14D	C24D	123.0(18)	C32H	C51H	C52H	109.5(19)
C15D	C14D	C13D	114.5(14)	C32H	C51H	C53H	118(2)
C15D	C14D	C24D	122.5(17)	C53H	C51H	C52H	112(2)
C16D	C15D	C14D	122.8(16)	C62H	N61H	Co3	119.0(15)
C15D	C16D	C11D	121.2(15)	C66H	N61H	Co3	122.0(14)
O18D	C17D	C11D	117.7(14)	C66H	N61H	C62H	118.5(17)
O19D	C17D	C11D	117.1(14)	N61H	C62H	C63H	125.2(18)
O19D	C17D	O18D	125.2(16)	C62H	C63H	C64H	116.9(16)
C17D	O18D	Co1	123.4(12)	C63H	C64H	C34H	120.8(14)
C17D	O19D	Co2	123.6(12)	C65H	C64H	C34H	122.5(15)
C22D	C21D	C26D	115.8(15)	C65H	C64H	C63H	116.7(17)
C22D	C21D	C27D	121.6(14)	C66H	C65H	C64H	123.2(18)
C26D	C21D	C27D	122.6(14)	N61H	C66H	C65H	119.3(17)
C23D	C22D	C21D	122.3(16)	C12I	C11I	C17H	123.0(17)
C22D	C23D	C24D	122.6(16)	C12I	C11I	C16I	116.9(16)
C23D	C24D	C14D	122.9(18)	C16I	C11I	C17H	120.1(17)
C23D	C24D	C25D	115.7(15)	C13I	C12I	C11I	124.6(17)
C25D	C24D	C14D	121.4(18)	C12I	C13I	C14I	119.6(16)
C26D	C25D	C24D	120.2(16)	C13I	C14I	C15I	119.1(15)
C25D	C26D	C21D	123.3(16)	C13I	C14I	C24I	119.2(15)
O28D	C27D	C21D	119.6(15)	C15I	C14I	C24I	121.5(15)
O29D	C27D	C21D	117.5(14)	C14I	C15I	C16I	120.1(13)
O29D	C27D	O28D	122.8(16)	C20I	C15I	C14I	119.1(17)
C27D	O28D	Co2[3]	126.4(13)	C20I	C15I	C16I	120.8(13)
C27D	O29D	Co1[3]	122.6(12)	C11I	C16I	C17I	123.4(18)
C12E	C11E	C16E	116.2(15)	C15I	C16I	C11I	119.6(14)

C12E	C11E	C17E	121.1(14)	C15I	C16I	C17I	116.9(14)
C16E	C11E	C17E	122.6(14)	C16I	C17I	C11H	117.0(16)
C13E	C12E	C11E	124.7(16)	C18I	C17I	C11H	122.6(17)
C12E	C13E	C14E	119.7(16)	C18I	C17I	C16I	120.4(16)
C13E	C14E	C15E	115.2(16)	C19I	C18I	C17I	122.3(17)
C13E	C14E	C24E	120.9(18)	C18I	C19I	C20I	118.7(17)
C15E	C14E	C24E	123.9(18)	C15I	C20I	C19I	120.2(15)
C16E	C15E	C14E	123.6(16)	C15I	C20I	C21I	120.8(15)
C15E	C16E	C11E	120.1(16)	C19I	C20I	C21I	118.0(15)
O18E	C17E	C11E	117.1(14)	O22I	C21I	C20I	120.6(16)
O18E	C17E	O19E	126.4(17)	O22I	C21I	N23I	123.7(17)
O19E	C17E	C11E	116.5(14)	N23I	C21I	C20I	115.7(15)
C17E	O18E	Co4	122.9(13)	C21I	N23I	C24I	126.8(17)
C17E	O19E	Co3	121.2(13)	C21I	N23I	C31I	116.9(14)
C22E	C21E	C26E	116.1(15)	C24I	N23I	C31I	115.6(13)
C22E	C21E	C27E	121.3(14)	N23I	C24I	C14I	115.6(15)
C26E	C21E	C27E	122.5(14)	O25I	C24I	C14I	123.7(16)
C23E	C22E	C21E	122.0(16)	O25I	C24I	N23I	120.7(17)
C22E	C23E	C24E	123.0(16)	C32I	C31I	N23I	114.7(14)
C23E	C24E	C14E	121.6(18)	C36I	C31I	N23I	114.8(14)
C25E	C24E	C14E	124.4(18)	C36I	C31I	C32I	130.3(18)
C25E	C24E	C23E	113.9(15)	C31I	C32I	C33I	114.0(16)
C26E	C25E	C24E	122.6(16)	C31I	C32I	C51I	130.3(17)
C25E	C26E	C21E	122.4(16)	C33I	C32I	C51I	115.5(16)
O28E	C27E	C21E	118.2(14)	C34I	C33I	C32I	119.7(17)
O28E	C27E	O29E	123.8(16)	C33I	C34I	C64I	117.9(14)
O29E	C27E	C21E	118.0(14)	C35I	C34I	C33I	122.5(18)
C27E	O28E	Co3[1]	125.3(12)	C35I	C34I	C64I	119.5(14)

Atom	Atom	Atom	Angle	Atom	Atom	Atom	Angle
C27E	O29E	Co4[1]	123.2(13)	C34I	C35I	C36I	119.8(17)
C12F	C11F	C16F	118.7(14)	C31I	C36I	C35I	113.6(16)
C12F	C11F	C17G	122.1(14)	C31I	C36I	C41I	127.6(17)
C17G	C11F	C16F	119.2(14)	C35I	C36I	C41I	118.8(16)
C13F	C12F	C11F	122.4(15)	C36I	C41I	C43I	111.4(19)
C12F	C13F	C14F	120.1(15)	C42I	C41I	C36I	118(2)
C13F	C14F	C15F	119.7(14)	C42I	C41I	C43I	109.3(19)
C13F	C14F	C24F	119.1(14)	C32I	C51I	C52I	112.3(17)
C15F	C14F	C24F	121.2(14)	C32I	C51I	C53I	113.8(17)
C14F	C15F	C16F	119.6(12)	C53I	C51I	C52I	111.8(18)
C20F	C15F	C14F	118.4(15)	C62I	N61I	Co4[2]	120.2(16)
C20F	C15F	C16F	122.0(12)	C66I	N61I	Co4[2]	121.5(15)
C15F	C16F	C11F	119.5(12)	C66I	N61I	C62I	117.9(18)
C15F	C16F	C17F	117.7(12)	N61I	C62I	C63I	122.5(18)
C17F	C16F	C11F	122.8(16)	C62I	C63I	C64I	120.0(17)
C16F	C17F	C11G	117.7(14)	C63I	C64I	C34I	121.9(15)
C18F	C17F	C16F	118.7(14)	C65I	C64I	C34I	120.9(15)
C18F	C17F	C11G	123.6(14)	C65I	C64I	C63I	117.2(17)
C19F	C18F	C17F	123.4(16)	C66I	C65I	C64I	119.4(17)
C18F	C19F	C20F	119.0(15)	N61I	C66I	C65I	122.5(17)

Appendix X Crystallographic information for 7

Bond lengths around Co(II) in 7					
Atom	Atom	Length/Å	Atom	Atom	Length/Å
Co1	Co2	2.872(3)	Co2	O17A	2.001(9)
Co1	O18A	2.046(10)	Co2	O28A[1]	1.965(9)
Co1	O27A[1]	2.031(9)	Co2	O17B	2.165(9)
Co1	O17B	2.388(8)	Co2	O27B[2]	2.343(8)
Co1	O18B	2.013(9)	Co2	O28B[2]	2.069(10)
Co1	O27B[2]	2.140(10)	Co2	N61D[3]	2.110(13)

| Co1 | N61C | 2.061(10) | C11A | C12A | 1.429(14) |

Bond angles around Co(II) in 7

Atom	Atom	Atom	Angle/°	Atom	Atom	Atom	Angle/°
O18A	Co1	Co2	81.6(2)	O17A	Co2	Co1	81.6(2)
O18A	Co1	O17B	84.9(3)	O17A	Co2	O17B	83.8(4)
O18A	Co1	O27B[1]	85.1(4)	O17A	Co2	O27B[1]	86.2(3)
O18A	Co1	N61C	94.9(4)	O17A	Co2	O28B[1]	94.1(4)
O27A[2]	Co1	Co2	81.5(2)	O17A	Co2	N61D[3]	91.0(5)
O27A[2]	Co1	O18A	163.1(3)	O28A[2]	Co2	Co1	82.2(2)
O27A[2]	Co1	O17B	83.6(3)	O28A[2]	Co2	O17A	162.9(3)
O27A[2]	Co1	O27B[1]	84.9(3)	O28A[2]	Co2	O17B	82.3(3)
O27A[2]	Co1	N61C	99.8(3)	O28A[2]	Co2	O27B[1]	86.8(3)
O17B	Co1	Co2	47.5(2)	O28A[2]	Co2	O28B[1]	96.0(3)
O18B	Co1	Co2	107.6(2)	O28A[2]	Co2	N61D[3]	100.3(5)
O18B	Co1	O18A	90.9(4)	O17B	Co2	Co1	54.4(2)
O18B	Co1	O27A[2]	94.1(3)	O17B	Co2	O27B[1]	101.6(3)
O18B	Co1	O17B	60.1(3)	O27B[1]	Co2	Co1	47.1(2)
O18B	Co1	O27B[1]	160.9(3)	O28B[1]	Co2	Co1	107.5(2)
O18B	Co1	N61C	102.3(4)	O28B[1]	Co2	O17B	161.9(3)
O27B[1]	Co1	Co2	53.3(2)	O28B[1]	Co2	O27B[1]	60.3(3)
O27B[1]	Co1	O17B	100.9(3)	O28B[1]	Co2	N61D[3]	102.6(5)
N61C	Co1	Co2	149.9(4)	N61D[3]	Co2	Co1	149.4(5)
N61C	Co1	O17B	162.4(4)	N61D[3]	Co2	O17B	95.4(5)
N61C	Co1	O27B[1]	96.6(4)	N61D[3]	Co2	O27B[1]	162.4(5)

Appendix XI Crystallographic information for 8

Bond lengths around Dy(III) in 8

Atom	Atom	Length/Å
Dy1	O18A[1]	2.329(3)
Dy1	O18A[2]	2.609(3)
Dy1	O19A[2]	2.438(4)

Atom	Atom	Value
Dy1	O19C	2.258(4)
Dy1	O18B[3]	2.371(4)
Dy1	O18C[3]	2.317(4)
Dy1	O1D	2.373(4)
Dy1	O19B	2.281(4)
Dy1	C17A[2]	2.877(5)

Bond angles around Dy(III) in 8

Atom	Atom	Atom	Angle/°	Atom	Atom	Atom	Angle/°
O18A[1]	Dy1	O18A[2]	119.39(10)	O18C[3]	Dy1	O18B[3]	78.09(15)
O18A[1]	Dy1	O19A[2]	68.97(12)	O18C[3]	Dy1	O1D	144.13(15)
O18A[1]	Dy1	O18B[3]	84.81(13)	O18C[3]	Dy1	C17A[2]	68.42(14)
O18A[1]	Dy1	O1D	74.68(14)	O1D	Dy1	O18A[2]	146.21(13)
O18A[1]	Dy1	C17A[2]	93.77(13)	O1D	Dy1	O19A[2]	123.77(15)
O18A[2]	Dy1	C17A[2]	25.77(12)	O1D	Dy1	C17A[2]	142.40(15)
O19A[2]	Dy1	O18A[2]	51.39(11)	O19B	Dy1	O18A[2]	73.69(13)
O19A[2]	Dy1	C17A[2]	25.83(13)	O19B	Dy1	O18A[1]	107.76(13)
O19C	Dy1	O18A[2]	77.84(12)	O19B	Dy1	O19A[2]	79.30(16)
O19C	Dy1	O18A[1]	159.87(13)	O19B	Dy1	O18B[3]	134.87(16)
O19C	Dy1	O19A[2]	129.22(13)	O19B	Dy1	O18C[3]	143.18(15)
O19C	Dy1	O18B[3]	75.10(14)	O19B	Dy1	O1D	72.69(15)
O19C	Dy1	O18C[3]	88.72(15)	O19B	Dy1	C17A[2]	77.38(15)
O19C	Dy1	O1D	96.76(15)	Dy1[1]	O18A	Dy1[4]	124.39(14)
O19C	Dy1	O19B	86.28(15)	C17A	O18A	Dy1[4]	89.2(3)
O19C	Dy1	C17A[2]	103.53(14)	C17A	O18A	Dy1[1]	135.6(3)
O18B[3]	Dy1	O18A[2]	137.88(13)	C17A	O19A	Dy1[4]	96.9(3)
O18B[3]	Dy1	O19A[2]	143.26(14)	C17C	O19C	Dy1	152.2(4)
O18B[3]	Dy1	O1D	69.30(16)	C17B	O18B	Dy1[5]	134.6(4)
O18B[3]	Dy1	C17A[2]	146.51(15)	C17C	O18C	Dy1[5]	134.1(4)
O18C[3]	Dy1	O18A[2]	69.60(13)	C2D	O1D	Dy1	142.0(4)
O18C[3]	Dy1	O18A[1]	88.18(13)	C17B	O19B	Dy1	143.8(4)
O18C[3]	Dy1	O19A[2]	75.89(15)				

Appendix XII Crystallographic information for 9

Bond lengths around Ce(III) in 9

Atom	Atom	Length/Å
Ce1	O5D	2.466(7)
Ce1	C17A[1]	2.977(9)
Ce1	O18A[1]	2.695(5)
Ce1	O18A[2]	2.437(6)
Ce1	O19A[1]	2.554(7)
Ce1	O18B[3]	2.469(6)
Ce1	O19B	2.391(7)
Ce1	O18C[3]	2.422(7)
Ce1	O19C	2.327(6)

Bond angles around Ce(III) in 9

Atom	Atom	Atom	Angle/°	Atom	Atom	Atom	Angle/°
O5D	Ce1	C17A[1]	139.8(2)	C1B	C2B	C3B	120.6(10)
O5D	Ce1	O18A[1]	144.9(2)	C1B	C2B	C9B	120.4(11)
O5D	Ce1	O19A[1]	121.4(2)	C3B	C2B	C9B	119.0(10)
O5D	Ce1	O18B[2]	70.6(2)	C2B	C3B	C3A	118.3(10)
O18A[3]	Ce1	O5D	74.5(2)	C4B	C3B	C3A	120.5(10)
O18A[1]	Ce1	C17A[1]	24.92(19)	C4B	C3B	C2B	121.0(10)
O18A[3]	Ce1	C17A[1]	91.6(2)	C3B	C4B	C5B	120.2(10)
O18A[3]	Ce1	O18A[1]	116.46(17)	C3B	C4B	C6B	121.1(10)
O18A[3]	Ce1	O19A[1]	68.2(2)	C5B	C4B	C6B	118.6(9)
O18A[3]	Ce1	O18B[2]	88.3(2)	C1A	C5B	C4B	119.8(10)
O19A[1]	Ce1	C17A[1]	24.7(2)	O7B	C6B	C4B	125.1(11)
O19A[1]	Ce1	O18A[1]	49.28(19)	O7B	C6B	N8B	118.6(10)
O18B[2]	Ce1	C17A[1]	148.0(3)	N8B	C6B	C4B	116.1(9)
O18B[2]	Ce1	O18A[1]	138.7(2)	C6B	N8B	C11B	115.4(8)
O18B[2]	Ce1	O19A[1]	146.7(2)	C9B	N8B	C6B	124.4(9)

O19B	Ce1	O5D	73.1(2)	C9B	N8B	C11B	120.1(9)
O19B	Ce1	C17A[1]	76.0(2)	N8B	C9B	C2B	118.1(11)
O19B	Ce1	O18A[3]	108.2(2)	O10B	C9B	C2B	121.3(10)
O19B	Ce1	O18A[1]	71.8(2)	O10B	C9B	N8B	120.5(10)
O19B	Ce1	O19A[1]	77.6(3)	C12B	C11B	N8B	119.1(9)
O19B	Ce1	O18B[2]	134.0(2)	C16B	C11B	N8B	120.9(10)
O19B	Ce1	O18C[2]	139.3(2)	C16B	C11B	C12B	120.0(10)
O18C[2]	Ce1	O5D	147.5(2)	N13B	C12B	C11B	123.1(10)
O18C[2]	Ce1	C17A[1]	67.8(2)	C12B	N13B	C14B	117.9(10)
O18C[2]	Ce1	O18A[3]	91.2(2)	N13B	C14B	C15B	123.6(10)
O18C[2]	Ce1	O18A[1]	67.5(2)	C14B	C15B	C16B	117.2(9)
O18C[2]	Ce1	O19A[1]	77.2(2)	C14B	C15B	C17B	122.7(9)
O18C[2]	Ce1	O18B[2]	80.2(2)	C16B	C15B	C17B	119.8(9)
O19C	Ce1	O5D	99.0(2)	C11B	C16B	C15B	117.7(10)
O19C	Ce1	C17A[1]	102.5(2)	O18B	C17B	C15B	116.2(9)
O19C	Ce1	O18A[1]	77.6(2)	O19B	C17B	C15B	118.0(9)
O19C	Ce1	O18A[3]	163.6(2)	O19B	C17B	O18B	125.8(9)
O19C	Ce1	O19A[1]	126.8(2)	C17B	O18B	Ce1[5]	130.5(6)
O19C	Ce1	O18B[2]	75.2(2)	C17B	O19B	Ce1	148.4(6)
O19C	Ce1	O19B	83.6(2)	C2C	C1C	C1C[6]	118.7(15)
O19C	Ce1	O18C[2]	86.5(2)	C2C	C1C	C5C[6]	119.7(11)
C4D	O5D	Ce1	142.3(8)	C5C[6]	C1C	C1C[6]	121.5(15)
C5B	C1A	C2A	122.3(11)	C1C	C2C	C3C	123.1(12)
C1A	C2A	C3A	117.6(9)	C1C	C2C	C9C[6]	120.0(12)
C1A	C2A	C9A	123.5(10)	C3C	C2C	C9C[6]	116.9(12)
C3A	C2A	C9A	118.9(9)	C2C	C3C	C4C	118.4(12)
C4A	C3A	C2A	121.2(10)	C5C	C4C	C3C	119.0(12)
C4A	C3A	C3B	119.4(10)	C1C[6]	C5C	C4C	119.2(11)

C3B	C3A	C2A	119.4(9)	C1C[6]	C5C	C6C	123.0(13)
C3A	C4A	C6A	119.5(11)	C4C	C5C	C6C	117.7(14)
C5A	C4A	C3A	120.8(10)	O7C	C6C	C5C	126.7(15)
C5A	C4A	C6A	119.6(10)	O7C	C6C	N8C	116.2(12)
C4A	C5A	C1B	121.2(10)	N8C	C6C	C5C	117.1(14)
C4A	C6A	N8A	118.2(9)	C6C	N8C	C9C	124.4(11)
O7A	C6A	C4A	125.0(11)	C6C	N8C	C11C	120.7(11)
O7A	C6A	N8A	116.7(9)	C9C	N8C	C11C	114.9(10)
C9A	N8A	C6A	122.8(9)	N8C	C9C	C2C[6]	115.6(12)
C9A	N8A	C11A	120.4(10)	O10C	C9C	C2C[6]	124.1(13)
C11A	N8A	C6A	116.1(8)	O10C	C9C	N8C	120.2(11)
N8A	C9A	C2A	119.2(11)	C12C	C11C	N8C	118.5(10)
O10A	C9A	C2A	120.6(10)	C16C	C11C	N8C	124.4(10)
O10A	C9A	N8A	120.2(10)	C16C	C11C	C12C	117.0(10)
C12A	C11A	N8A	122.7(9)	N13C	C12C	C11C	125.7(11)
C16A	C11A	N8A	117.2(9)	C14C	N13C	C12C	114.0(10)
C16A	C11A	C12A	120.0(9)	N13C	C14C	C15C	125.3(10)
N13A	C12A	C11A	121.8(9)	C14C	C15C	C16C	116.3(10)
C12A	N13A	C14A	118.8(9)	C14C	C15C	C17C	121.5(9)
N13A	C14A	C15A	123.1(9)	C16C	C15C	C17C	121.8(9)
C14A	C15A	C17A	123.6(8)	C11C	C16C	C15C	121.2(10)
C16A	C15A	C14A	117.9(9)	O18C	C17C	C15C	118.7(9)
C16A	C15A	C17A	118.3(8)	O18C	C17C	O19C	122.6(9)
C11A	C16A	C15A	118.2(9)	O19C	C17C	C15C	118.6(9)
C15A	C17A	Ce1[4]	170.5(7)	C17C	O18C	Ce1[5]	131.0(6)
O18A	C17A	Ce1[4]	64.9(4)	C17C	O19C	Ce1	157.1(6)
O18A	C17A	C15A	118.8(8)	C3D	N2D	C1D	117.1(10)
O19A	C17A	Ce1[4]	58.4(5)	C4D	N2D	C3D	121.2(10)

O19A	C17A	C15A	119.1(8)	C4D	N2D	C1D	121.7(11)
O19A	C17A	O18A	122.0(8)	O5D	C4D	N2D	125.6(12)
Ce1[3]	O18A	Ce1[4]	120.5(2)	C3E	N2E	C1E	104(2)
C17A	O18A	Ce1[3]	137.5(5)	C4E	N2E	C1E	118(3)
C17A	O18A	Ce1[4]	90.2(5)	C4E	N2E	C3E	138(3)
C17A	O19A	Ce1[4]	97.0(5)	N2E	C4E	O5E	128(3)

Appendix XIII Crystallographic information for 10

Bond lengths around Pr(III) in 10

Atom	Atom	Length/Å
Pr1	C17A[1]	2.947(15)
Pr1	O18A[1]	2.695(9)
Pr1	O18A[2]	2.426(9)
Pr1	O19A[1]	2.489(10)
Pr1	O18B[3]	2.463(10)
Pr1	O19B	2.358(11)
Pr1	O18C[3]	2.434(11)
Pr1	O19C	2.339(10)
Pr1	O5D	2.443(10)

Bond angles around Pr(III) in 10

Atom	Atom	Atom	Angle/°	Atom	Atom	Atom	Angle/°
O18A[1]	Pr1	C17A[2]	92.6(4)	C1B	C2B	C9B	118.7(16)
O18A[2]	Pr1	C17A[2]	24.5(3)	C3B	C2B	C9B	117.0(15)
O18A[1]	Pr1	O18A[2]	116.9(3)	C2B	C3B	C3A	115.2(14)
O18A[1]	Pr1	O19A[2]	68.1(3)	C4B	C3B	C3A	121.7(16)
O18A[1]	Pr1	O18B[3]	87.8(3)	C4B	C3B	C2B	122.8(15)
O18A[1]	Pr1	O18C[3]	91.1(3)	C3B	C4B	C6B	120.4(16)

O18A[1]	Pr1	O5D	74.3(3)	C5B	C4B	C3B	118.3(16)
O19A[2]	Pr1	C17A[2]	26.0(4)	C5B	C4B	C6B	121.3(15)
O19A[2]	Pr1	O18A[2]	50.2(3)	C4B	C5B	C1A	122.0(16)
O18B[3]	Pr1	C17A[2]	148.8(4)	O7B	C6B	C4B	123.8(17)
O18B[3]	Pr1	O18A[2]	138.8(3)	O7B	C6B	N8B	119.8(16)
O18B[3]	Pr1	O19A[2]	147.4(4)	N8B	C6B	C4B	116.4(15)
O19B	Pr1	C17A[2]	76.3(4)	C9B	N8B	C6B	123.8(15)
O19B	Pr1	O18A[1]	108.3(3)	C9B	N8B	C11B	119.9(15)
O19B	Pr1	O18A[2]	72.9(3)	C11B	N8B	C6B	116.2(14)
O19B	Pr1	O19A[2]	77.4(5)	N8B	C9B	C2B	118.6(16)
O19B	Pr1	O18B[3]	132.9(4)	O10B	C9B	C2B	121.9(16)
O19B	Pr1	O18C[3]	139.8(4)	O10B	C9B	N8B	119.4(16)
O19B	Pr1	O5D	72.7(4)	N8B	C11B	C12B	120.3(15)
O18C[3]	Pr1	C17A[2]	67.8(4)	N8B	C11B	C16B	123.1(16)
O18C[3]	Pr1	O18A[2]	66.9(3)	C16B	C11B	C12B	116.6(16)
O18C[3]	Pr1	O19A[2]	78.0(4)	N13B	C12B	C11B	123.4(16)
O18C[3]	Pr1	O18B[3]	81.0(4)	C14B	N13B	C12B	119.6(15)
O18C[3]	Pr1	O5D	147.5(4)	N13B	C14B	C15B	123.4(15)
O19C	Pr1	C17A[2]	101.7(4)	C14B	C15B	C17B	122.1(14)
O19C	Pr1	O18A[2]	77.2(3)	C16B	C15B	C14B	117.5(15)
O19C	Pr1	O18A[1]	163.4(3)	C16B	C15B	C17B	120.3(15)
O19C	Pr1	O19A[2]	127.2(4)	C15B	C16B	C11B	119.1(16)
O19C	Pr1	O18B[3]	75.7(4)	O18B	C17B	C15B	118.0(15)
O19C	Pr1	O19B	83.5(4)	O18B	C17B	O19B	125.8(15)
O19C	Pr1	O18C[3]	86.6(4)	O19B	C17B	C15B	116.2(14)
O19C	Pr1	O5D	99.2(4)	C17B	O18B	Pr1[5]	131.6(10)
O5D	Pr1	C17A[2]	140.1(4)	C17B	O19B	Pr1	149.2(10)
O5D	Pr1	O18A[2]	145.6(3)	C5C[6]	C1C	C2C	121(2)
O5D	Pr1	O19A[2]	120.4(4)				

Appendix XIV Crystallographic information for 11

Bond lengths around Gd(III) in 11

Atom	Atom	Length/Å
Gd1	C17A[1]	2.877(15)
Gd1	O18A[2]	2.349(10)
Gd1	O18A[1]	2.634(10)
Gd1	O19A[1]	2.453(11)
Gd1	O18B[3]	2.418(11)
Gd1	O19B	2.317(12)
Gd1	O18C[3]	2.365(12)
Gd1	O19C	2.266(12)
Gd1	O5D	2.416(11)

Bond angles around Gd(III) in 11

Atom	Atom	Atom	Angle/°	Atom	Atom	Atom	Angle/°
O18A[1]	Gd1	C17A[1]	25.5(4)	C2B	C1B	C5A	119(2)
O18A[2]	Gd1	C17A[1]	93.6(4)	C1B	C2B	C3B	119.0(18)
O18A[2]	Gd1	O18A[1]	118.9(3)	C1B	C2B	C9B	122(2)
O18A[2]	Gd1	O19A[1]	68.2(4)	C3B	C2B	C9B	118.7(18)
O18A[2]	Gd1	O18B[3]	85.9(4)	C3A	C3B	C2B	118.6(18)
O18A[2]	Gd1	O18C[3]	89.6(4)	C4B	C3B	C3A	122(2)
O18A[2]	Gd1	O5D	74.8(4)	C4B	C3B	C2B	119.8(18)
O19A[1]	Gd1	C17A[1]	26.8(4)	C3B	C4B	C6B	122(2)
O19A[1]	Gd1	O18A[1]	51.9(4)	C5B	C4B	C3B	117.9(19)
O18B[3]	Gd1	C17A[1]	147.4(4)	C5B	C4B	C6B	120.3(19)
O18B[3]	Gd1	O18A[1]	138.2(4)	C1A	C5B	C4B	122(2)
O18B[3]	Gd1	O19A[1]	145.0(4)	O7B	C6B	C4B	123(2)

O19B	Gd1	C17A[1]	77.1(5)	O7B	C6B	N8B	123.5(19)
O19B	Gd1	O18A[2]	107.6(4)	N8B	C6B	C4B	112.9(18)
O19B	Gd1	O18A[1]	73.5(4)	C6B	N8B	C11B	113.2(17)
O19B	Gd1	O19A[1]	78.1(5)	C9B	N8B	C6B	127.9(18)
O19B	Gd1	O18B[3]	134.0(5)	C9B	N8B	C11B	118.5(19)
O19B	Gd1	O18C[3]	142.2(4)	N8B	C9B	C2B	117.6(19)
O19B	Gd1	O5D	72.6(4)	O10B	C9B	C2B	121.3(19)
O18C[3]	Gd1	C17A[1]	68.3(4)	O10B	C9B	N8B	121.0(18)
O18C[3]	Gd1	O18A[1]	68.7(4)	N8B	C11B	C12B	119.6(17)
O18C[3]	Gd1	O19A[1]	77.6(4)	C16B	C11B	N8B	125.8(18)
O18C[3]	Gd1	O18B[3]	79.1(4)	C16B	C11B	C12B	114.6(18)
O18C[3]	Gd1	O5D	145.2(4)	N13B	C12B	C11B	123.3(18)
O19C	Gd1	C17A[1]	103.1(4)	C14B	N13B	C12B	120.1(18)
O19C	Gd1	O18A[1]	77.7(4)	N13B	C14B	C15B	121.1(18)
O19C	Gd1	O18A[2]	160.8(4)	C14B	C15B	C17B	115.7(16)
O19C	Gd1	O19A[1]	129.5(4)	C16B	C15B	C14B	120.9(17)
O19C	Gd1	O18B[3]	74.9(4)	C16B	C15B	C17B	123.4(17)
O19C	Gd1	O19B	85.7(5)	C15B	C16B	C11B	119.6(18)
O19C	Gd1	O18C[3]	87.8(4)	O18B	C17B	C15B	122.7(17)
O19C	Gd1	O5D	96.9(4)	O18B	C17B	O19B	125.6(16)
O5D	Gd1	C17A[1]	142.0(4)	O19B	C17B	C15B	111.7(15)
O5D	Gd1	O18A[1]	145.9(4)	C17B	O18B	Gd1[5]	134.1(12)
O5D	Gd1	O19A[1]	122.1(4)	C17B	O19B	Gd1	144.7(11)
O5D	Gd1	O18B[3]	69.0(4)	C2C	C1C	C5C[6]	114(2)
C2A	C1A	C5B	120(2)	C3C	C2C	C1C	125(2)

Appendix XV Crystallographic information for 12

Bond lengths around Ho(III) in 12

Atom	Atom	Length/Å
Ho1	C17A[1]	2.865(10)
Ho1	O18A[2]	2.303(7)
Ho1	O18A[1]	2.604(6)
Ho1	O19A[1]	2.423(7)
Ho1	O18B[3]	2.375(7)
Ho1	O19B	2.267(8)
Ho1	O18C[3]	2.304(7)
Ho1	O19C	2.232(7)
Ho1	O5D	2.356(8)

Bond angles around Ho(III) 12

Atom	Atom	Atom	Angle/°	Atom	Atom	Atom	Angle/°
O18A[1]	Ho1	C17A[2]	93.8(3)	C3B	C4B	C6B	119.8(11)
O18A[2]	Ho1	C17A[2]	26.1(2)	C5B	C4B	C3B	120.7(11)
O18A[1]	Ho1	O18A[2]	119.7(2)	C5B	C4B	C6B	119.5(12)
O18A[1]	Ho1	O19A[2]	69.2(2)	C4B	C5B	C1A	119.3(13)
O18A[1]	Ho1	O18B[3]	84.6(2)	O7B	C6B	C4B	122.2(12)
O18A[1]	Ho1	O18C[3]	87.9(2)	O7B	C6B	N8B	120.3(11)
O18A[1]	Ho1	O5D	74.8(3)	N8B	C6B	C4B	117.4(12)
O19A[2]	Ho1	C17A[2]	25.7(3)	C6B	N8B	C11B	119.2(10)
O19A[2]	Ho1	O18A[2]	51.6(2)	C9B	N8B	C6B	124.1(10)
O18B[3]	Ho1	C17A[2]	146.3(3)	C9B	N8B	C11B	116.7(10)
O18B[3]	Ho1	O18A[2]	137.8(2)	N8B	C9B	C2B	118.1(11)
O18B[3]	Ho1	O19A[2]	143.3(3)	O10B	C9B	C2B	121.0(13)
O19B	Ho1	C17A[2]	77.2(3)	O10B	C9B	N8B	120.8(12)

O19B	Ho1	O18A[2]	73.2(2)	C12B	C11B	N8B	118.5(10)
O19B	Ho1	O18A[1]	108.2(2)	C16B	C11B	N8B	121.9(11)
O19B	Ho1	O19A[2]	79.2(3)	C16B	C11B	C12B	119.5(11)
O19B	Ho1	O18B[3]	135.1(3)	N13B	C12B	C11B	122.0(11)
O19B	Ho1	O18C[3]	142.7(3)	C14B	N13B	C12B	118.7(10)
O19B	Ho1	O5D	72.9(3)	N13B	C14B	C15B	123.4(11)
O18C[3]	Ho1	C17A[2]	68.1(3)	C14B	C15B	C16B	118.1(10)
O18C[3]	Ho1	O18A[2]	69.6(2)	C14B	C15B	C17B	122.3(10)
O18C[3]	Ho1	O19A[2]	75.6(2)	C16B	C15B	C17B	119.6(10)
O18C[3]	Ho1	O18B[3]	78.3(3)	C11B	C16B	C15B	118.1(11)
O18C[3]	Ho1	O5D	144.4(3)	O18B	C17B	C15B	117.5(10)
O19C	Ho1	C17A[2]	103.3(3)	O18B	C17B	O19B	126.4(10)
O19C	Ho1	O18A[1]	160.0(3)	O19B	C17B	C15B	116.1(10)
O19C	Ho1	O18A[2]	77.3(2)	C17B	O18B	Ho1[5]	134.0(7)
O19C	Ho1	O19A[2]	128.9(3)	C17B	O19B	Ho1	144.3(7)
O19C	Ho1	O18B[3]	75.4(3)	C2C	C1C	C5C[6]	118.4(13)
O19C	Ho1	O19B	85.9(3)	C1C	C2C	C3C	122.4(12)
O19C	Ho1	O18C[3]	89.0(3)	C1C	C2C	C9C	117.1(14)
O19C	Ho1	O5D	96.9(3)	C3C	C2C	C9C	120.5(13)
O5D	Ho1	C17A[2]	142.4(3)	C2C	C3C	C3C[6]	119.6(16)
O5D	Ho1	O18A[2]	145.9(2)	C2C	C3C	C4C	120.0(12)
O5D	Ho1	O19A[2]	123.8(3)	C4C	C3C	C3C[6]	120.4(15)
O5D	Ho1	O18B[3]	69.4(3)	C3C	C4C	C5C	118.8(12)

Appendix XVI Crystallographic information for 13

Bond lengths around La(III) in 13

Atom	Atom	Length/Å
La1	O18A[1]	2.474(9)
La1	O18B	2.405(15)
La1	C17C[2]	2.998(14)
La1	O18C[2]	2.702(11)
La1	O19C[2]	2.580(12)
La1	O18D[3]	2.493(12)
La1	O17E[3]	2.465(15)
La1	O19F	2.351(13)
La1	O5H	2.522(15)
La2	C17A[4]	2.962(15)
La2	O18A[4]	2.689(10)
La2	O19A[4]	2.580(12)
La2	O19B	2.482(14)
La2	O18C[2]	2.473(10)
La2	O19D	2.419(13)
La2	O18E	2.391(12)
La2	O18F	2.438(14)
La2	O5I	2.510(13)

Bond angles around La(III) in 13

Atom	Atom	Atom	Angle/°	Atom	Atom	Atom	Angle/°
O18A¹	La1	C17C²	91.1(3)	C5C	C4C	C6C	118(2)
O18A¹	La1	O18C²	115.9(3)	C1D	C5C	C4C	118(2)
O18A¹	La1	O19C²	68.1(4)	O7C	C6C	C4C	124.2(19)
O18A¹	La1	O18D³	87.5(4)	O7C	C6C	N8C	119.8(17)
O18A¹	La1	O5H	72.0(5)	N8C	C6C	C4C	115.7(18)
O18B	La1	O18A¹	107.5(4)	C6C	N8C	C9C	124.1(15)
O18B	La1	C17C²	76.5(5)	C6C	N8C	C11C	120.3(16)
O18B	La1	O18C²	72.0(4)	C9C	N8C	C11C	114.9(15)
O18B	La1	O19C²	76.3(6)	C2C	C9C	N8C	117.4(17)
O18B	La1	O18D³	133.7(5)	O10C	C9C	C2C	125(2)
O18B	La1	O17E³	139.5(5)	O10C	C9C	N8C	118.0(17)
O18B	La1	O5H	73.7(6)	C12C	C11C	N8C	121.0(15)
O18C²	La1	C17C²	24.9(2)	C16C	C11C	N8C	119.6(16)
O19C²	La1	C17C²	24.8(3)	C16C	C11C	C12C	119.3(16)
O19C²	La1	O18C²	49.0(3)	N13C	C12C	C11C	121.0(17)
O18D³	La1	C17C²	148.5(5)	C14C	N13C	C12C	116.8(16)
O18D³	La1	O18C²	140.3(4)	N13C	C14C	C15C	124.6(16)
O18D³	La1	O19C²	147.4(5)	C14C	C15C	C17C	122.5(14)
O18D³	La1	O5H	69.9(6)	C16C	C15C	C14C	118.9(16)
O17E³	La1	O18A¹	90.0(4)	C16C	C15C	C17C	118.6(14)
O17E³	La1	C17C²	66.7(5)	C15C	C16C	C11C	118.8(16)
O17E³	La1	O18C²	67.5(4)	C15C	C17C	La1²	169.0(13)
O17E³	La1	O19C²	77.1(5)	O18C	C17C	La1²	64.3(8)
O17E³	La1	O18D³	81.8(5)	O18C	C17C	C15C	119.8(11)
O17E³	La1	O5H	146.7(5)	O18C	C17C	O19C	120.7(14)
O19F	La1	O18A¹	165.1(4)	O19C	C17C	La1²	58.7(8)
O19F	La1	O18B	84.7(6)	O19C	C17C	C15C	119.2(12)
O19F	La1	C17C²	100.3(4)	La2²	O18C	La1²	120.9(4)
O19F	La1	O18C²	75.5(4)	C17C	O18C	La1²	90.8(8)
O19F	La1	O19C²	124.5(4)	C17C	O18C	La2²	137.3(11)
O19F	La1	O18D³	77.7(5)	C17C	O19C	La1²	96.5(9)
O19F	La1	O17E³	85.8(6)	C2D	C1D	C5C	123(2)
O19F	La1	O5H	104.3(6)	C1D	C2D	C3D	120.6(18)
O5H	La1	C17C²	139.0(6)	C1D	C2D	C9D	122.0(19)
O5H	La1	O18C²	145.5(5)	C3D	C2D	C9D	117(2)
O5H	La1	O19C²	118.8(6)	C2D	C3D	C3C	117.0(19)
O18A⁴	La2	C17A⁴	25.2(2)	C4D	C3D	C3C	119.7(17)
O19A⁴	La2	C17A⁴	25.3(3)	C4D	C3D	C2D	123.3(18)
O19A⁴	La2	O18A⁴	49.5(3)	C3D	C4D	C5D	122.9(18)
O19B	La2	C17A⁴	146.4(5)	C3D	C4D	C6D	119.2(18)
O19B	La2	O18A⁴	138.5(4)	C5D	C4D	C6D	118(2)
O19B	La2	O19A⁴	147.4(6)	C4D	C5D	C1C	117(2)
O19B	La2	O5I	69.4(5)	O7D	C6D	C4D	123.5(18)
O18C²	La2	C17A⁴	92.4(3)	O7D	C6D	N8D	119.5(17)
O18C²	La2	O18A⁴	117.5(3)	N8D	C6D	C4D	117.1(19)
O18C²	La2	O19A⁴	69.3(4)	C6D	N8D	C11D	120.2(18)
O18C²	La2	O19B	87.3(4)	C9D	N8D	C6D	124.7(16)
O18C²	La2	O5I	72.6(4)	C9D	N8D	C11D	115.1(17)
O19D	La2	C17A⁴	78.3(5)	N8D	C9D	C2D	117.4(17)
O19D	La2	O18A⁴	73.5(4)	O10D	C9D	C2D	122(2)
O19D	La2	O19A⁴	76.4(6)	O10D	C9D	N8D	120.4(18)
O19D	La2	O19B	133.8(5)	C12D	C11D	N8D	119.1(17)
O19D	La2	O18C²	106.6(4)	C16D	C11D	N8D	123.5(17)
O19D	La2	O18F	141.9(5)	C16D	C11D	C12D	117.3(18)
O19D	La2	O5I	73.3(5)	N13D	C12D	C11D	125(2)
O18E	La2	C17A⁴	102.1(4)	C14D	N13D	C12D	117(2)
O18E	La2	O18A⁴	77.0(4)	N13D	C14D	C15D	125(2)
O18E	La2	O19A⁴	126.3(4)	C14D	C15D	C17D	120.2(16)
O18E	La2	O19B	75.9(5)	C16D	C15D	C14D	119.4(17)
O18E	La2	O18C²	163.1(4)	C16D	C15D	C17D	120.4(16)
O18E	La2	O19D	85.1(6)	C15D	C16D	C11D	116.5(18)
O18E	La2	O18F	86.8(5)	O18D	C17D	C15D	118.7(14)

Atom	Atom	Atom	Angle	Atom	Atom	Atom	Angle
O18E	La2	O5I	100.2(5)	O18D	C17D	O19D	124.3(16)
O18F	La2	C17A[4]	67.1(5)	O19D	C17D	C15D	116.7(13)
O18F	La2	O18A[4]	68.4(4)	C17D	O18D	La1[6]	132.1(12)
O18F	La2	O19A[4]	78.8(6)	C17D	O19D	La2	149.1(13)
O18F	La2	O19B	79.3(5)	C2E	C1E	C5E[7]	119(2)
O18F	La2	O18C[2]	90.8(4)	C1E	C2E	C3E	125.8(19)
O18F	La2	O5I	144.8(5)	C1E	C2E	C9E	118.3(19)
O5I	La2	C17A[4]	142.0(5)	C3E	C2E	C9E	116(2)
O5I	La2	O18A[4]	146.7(4)	C2E	C3E	C3E[7]	112(3)
O5I	La2	O19A[4]	120.9(5)	C4E	C3E	C2E	125(2)

Appendix XVII Crystallographic information for 14

Bond lengths around Nd(III) in 14

Atom	Atom	Length/Å	Atom	Atom	Length/Å
Nd1	O18A[1]	2.660(3)	Nd2	O18A[1]	2.415(2)
Nd1	O18C[2]	2.416(2)	Nd2	O18C[4]	2.622(3)
Nd1	O18F[3]	2.421(3)	Nd2	O19F	2.348(3)
Nd1	O19A[1]	2.520(3)	Nd2	O19C[4]	2.532(3)
Nd1	O19E	2.333(3)	Nd2	O18E	2.420(3)
Nd1	O18B[3]	2.456(3)	Nd2	O5G	2.450(3)
Nd1	O19D	2.365(3)	Nd2	O19B	2.365(3)
Nd1	O5H	2.443(3)	Nd2	O18D	2.443(3)
Nd1	C17A[1]	2.953(4)	Nd2	C17C[4]	2.925(4)

Bond angles around Nd(III) in 14

Atom	Atom	Atom	Angle/°	Atom	Atom	Atom	Angle/°
O18A[1]	Nd1	C17A[1]	25.51(9)	O5G	Nd2	C17C[4]	142.29(11)
O18C[2]	Nd1	O18A[1]	118.08(8)	O19B	Nd2	O18A[1]	107.36(10)
O18C[2]	Nd1	O18F[3]	89.10(9)	O19B	Nd2	O18C[4]	73.85(10)
O18C[2]	Nd1	O19A[1]	68.58(9)	O19B	Nd2	O19C[4]	79.90(12)
O18C[2]	Nd1	O18B[3]	86.15(10)	O19B	Nd2	O18E	142.34(10)
O18C[2]	Nd1	O5H	73.47(10)	O19B	Nd2	O5G	72.78(11)
O18C[2]	Nd1	C17A[1]	92.68(10)	O19B	Nd2	O18D	135.30(12)
O18F[3]	Nd1	O18A[1]	68.16(9)	O19B	Nd2	C17C[4]	78.51(12)
O18F[3]	Nd1	O19A[1]	74.32(11)	O18D	Nd2	O18C[4]	137.67(10)
O18F[3]	Nd1	O18B[3]	80.11(11)	O18D	Nd2	O19C[4]	142.48(11)
O18F[3]	Nd1	O5H	146.15(11)	O18D	Nd2	O5G	70.20(12)

O18F[3]	Nd1	C17A[1]	67.10(11)	O18D	Nd2	C17C[4]	145.04(12)
O19A[1]	Nd1	O18A[1]	50.25(8)	Nd2[1]	O18A	Nd1[1]	122.97(10)
O19A[1]	Nd1	C17A[1]	24.91(10)	C17A	O18A	Nd1[1]	90.2(2)
O19E	Nd1	O18A[1]	77.01(9)	C17A	O18A	Nd2[1]	136.0(2)
O19E	Nd1	O18C[2]	162.21(10)	Nd1[2]	O18C	Nd2[5]	122.93(10)
O19E	Nd1	O18F[3]	88.25(11)	C17C	O18C	Nd1[2]	136.2(2)
O19E	Nd1	O19A[1]	127.26(10)	C17C	O18C	Nd2[5]	90.4(2)
O19E	Nd1	O18B[3]	76.07(11)	C17F	O19F	Nd2	155.2(3)
O19E	Nd1	O19D	84.79(12)	C17F	O18F	Nd1[6]	132.2(3)
O19E	Nd1	O5H	99.58(12)	C17A	O19A	Nd1[1]	97.2(2)
O19E	Nd1	C17A[1]	102.46(11)	C17C	O19C	Nd2[5]	95.3(2)
O18B[3]	Nd1	O18A[1]	138.59(10)	C17E	O18E	Nd2	132.4(3)
O18B[3]	Nd1	O19A[1]	143.87(11)	C17E	O19E	Nd1	157.8(3)
O18B[3]	Nd1	C17A[1]	147.21(12)	C4G	O5G	Nd2	141.6(3)
O19D	Nd1	O18A[1]	73.06(10)	C17B	O19B	Nd2	145.8(3)
O19D	Nd1	O18C[2]	107.92(10)	C17B	O18B	Nd1[6]	132.2(3)
O19D	Nd1	O18F[3]	141.18(10)	C17D	O18D	Nd2	131.7(3)
O19D	Nd1	O19A[1]	79.86(12)	C17D	O19D	Nd1	146.4(3)
O19D	Nd1	O18B[3]	134.13(12)	C6A	N8A	C11A	118.8(4)
O19D	Nd1	O5H	72.61(12)	C9A	N8A	C11A	115.5(4)
O19D	Nd1	C17A[1]	77.24(11)	C9A	N8A	C6A	125.3(4)
O5H	Nd1	O18A[1]	145.67(11)	C4H	O5H	Nd1	148.6(4)
O5H	Nd1	O19A[1]	122.51(12)	C9C	N8C	C11C	118.5(4)
O5H	Nd1	O18B[3]	70.15(12)	C6C	N8C	C9C	125.9(4)
O5H	Nd1	C17A[1]	140.53(12)	C6C	N8C	C11C	115.5(4)
O18A[1]	Nd2	O18C[4]	118.54(9)	C6B	N8B	C11B	117.9(4)
O18A[1]	Nd2	O19C[4]	68.61(9)	C6B	N8B	C9B	125.6(4)
O18A[1]	Nd2	O18E	89.73(9)	C9B	N8B	C11B	116.4(4)
O18A[1]	Nd2	O5G	73.65(10)	C12C	N13C	C14C	117.5(4)
O18A[1]	Nd2	O18D	85.33(10)	C9D	N8D	C11D	117.1(4)
O18A[1]	Nd2	C17C[4]	92.66(10)	C6D	N8D	C11D	117.2(4)
O18C[4]	Nd2	C17C[4]	25.94(9)	C6D	N8D	C9D	125.7(4)
O19F	Nd2	O18A[1]	160.98(10)	C4G	N2G	C1G	121.4(4)
O19F	Nd2	O18C[4]	77.88(9)	C4G	N2G	C3G	121.5(5)

O19F	Nd2	O19C[4]	128.61(10)	C3G	N2G	C1G	117.1(4)
O19F	Nd2	O18E	87.78(11)	C11A	C16A	C15A	119.0(4)
O19F	Nd2	O5G	98.07(11)	C9F	N8F	C11F	117.0(4)
O19F	Nd2	O19B	85.70(11)	C6F	N8F	C9F	125.5(4)
O19F	Nd2	O18D	75.71(11)	C6F	N8F	C11F	117.4(5)
O19F	Nd2	C17C[4]	103.68(10)	C12A	N13A	C14A	117.6(4)
O19C[4]	Nd2	O18C[4]	50.74(8)	N13C	C14C	C15C	123.3(4)
O19C[4]	Nd2	C17C[4]	25.13(10)	C11E	C16E	C15E	117.6(5)
O18E	Nd2	O18C[4]	68.51(9)	C11B	C16B	C15B	117.9(4)
O18E	Nd2	O19C[4]	75.52(11)	O18C	C17C	Nd2[5]	63.7(2)
O18E	Nd2	O5G	144.88(11)	O18C	C17C	C15C	119.1(3)
O18E	Nd2	O18D	77.94(11)	O19C	C17C	Nd2[5]	59.6(2)
O18E	Nd2	C17C[4]	67.14(11)	O19C	C17C	O18C	122.0(4)
O5G	Nd2	O18C[4]	146.59(10)	O19C	C17C	C15C	118.9(4)
O5G	Nd2	O19C[4]	123.29(11)	C15C	C17C	Nd2[5]	165.4(3)

Appendix XVIII Crystallographic information for Fc@1

Bond lengths for Fc@1

Atom	Atom	Length/Å		Atom	Atom	Length/Å
Co1	N14A[1]	2.140(4)		C12B	C13B	1.387(7)
Co1	N14B	2.142(4)		C13B	N14B	1.348(7)
Co1	O2C	2.200(4)		N14B	C15B	1.340(6)
Co1	O3C	2.188(4)		C15B	C16B	1.386(7)
Co1	O1D	1.992(3)		N1C	O2C	1.273(6)
Co1	O3D[2]	2.008(3)		N1C	O3C	1.262(6)
C1A	C2A	1.366(9)		N1C	O4C	1.216(7)
C1A	C5B	1.421(7)		O1D	C2D	1.245(6)
C2A	C3A	1.418(8)		C2D	O3D	1.257(6)
C2A	C9A	1.481(6)		C2D	C4D	1.499(6)
C3A	C4A	1.410(8)		C4D	C5D	1.367(7)

C3A	C3B	1.407(7)	C4D	C8D³	1.422(7)
C4A	C5A	1.366(8)	C5D	C6D	1.425(6)
C4A	C6A	1.488(6)	C6D	C6D³	1.413(10)
C5A	C1B	1.415(7)	C6D	C7D	1.418(7)
C6A	O7A	1.209(7)	C7D	C8D	1.381(7)
C6A	N8A	1.403(7)	Fe1	C1F	1.996(13)
N8A	C9A	1.409(7)	Fe1	C2F	2.013(12)
N8A	C11A	1.439(5)	Fe1	C3F	2.039(12)
C9A	O10A	1.219(7)	Fe1	C4F	2.103(14)
C11A	C12A	1.370(7)	Fe1	C5F	2.043(13)
C11A	C16A	1.388(7)	Fe1	C6F	1.984(13)
C12A	C13A	1.387(6)	Fe1	C7F	1.999(14)
C13A	N14A	1.341(6)	Fe1	C8F	1.991(13)
N14A	C15A	1.344(6)	Fe1	C9F	2.006(12)
C15A	C16A	1.387(6)	Fe1	C10F	2.000(12)
C1B	C2B	1.366(9)	C1F	C2F	1.47(3)
C2B	C3B	1.418(8)	C1F	C5F	1.25(3)
C2B	C9B	1.492(6)	C2F	C3F	1.45(3)
C3B	C4B	1.417(9)	C3F	C4F	1.26(3)
C4B	C5B	1.361(9)	C4F	C5F	1.36(3)
C4B	C6B	1.494(7)	C6F	C7F	1.41(3)
C6B	O7B	1.205(9)	C6F	C10F	1.31(3)
C6B	N8B	1.419(9)	C7F	C8F	1.44(3)
N8B	C9B	1.399(9)	C8F	C9F	1.31(3)
N8B	C11B	1.437(6)	C9F	C10F	1.38(3)
C9B	O10B	1.205(8)	C1E	C2E	1.39(4)
C11B	C12B	1.400(8)	C1E	C3E	1.43(3)
C11B	C16B	1.387(8)	C1E	O4E	1.22(2)

Bond angles in Fc@1

Atom	Atom	Atom	Angle/°	Atom	Atom	Atom	Angle/°
N14A[1]	Co1	N14B	177.36(14)	C5D	C4D	C8D[4]	121.3(4)
N14A[1]	Co1	O2C	87.73(14)	C8D[4]	C4D	C2D	119.5(4)
N14A[1]	Co1	O3C	91.30(16)	C4D	C5D	C6D	120.0(5)
N14B	Co1	O2C	91.05(15)	C6D[4]	C6D	C5D	119.1(5)
N14B	Co1	O3C	90.06(17)	C6D[4]	C6D	C7D	119.8(5)
O3C	Co1	O2C	58.54(13)	C7D	C6D	C5D	121.0(5)
O1D	Co1	N14A[1]	89.04(14)	C8D	C7D	C6D	120.3(5)
O1D	Co1	N14B	93.21(15)	C7D	C8D	C4D[4]	119.5(4)
O1D	Co1	O2C	148.82(15)	C1F	Fe1	C2F	43.1(8)
O1D	Co1	O3C	90.56(14)	C1F	Fe1	C3F	69.3(7)
O1D	Co1	O3D[2]	120.62(15)	C1F	Fe1	C4F	64.4(8)
O3D[2]	Co1	N14A[1]	87.74(14)	C1F	Fe1	C5F	35.9(8)
O3D[2]	Co1	N14B	89.93(15)	C1F	Fe1	C6F	153.4(10)
O3D[2]	Co1	O2C	90.24(14)	C1F	Fe1	C7F	160.7(10)
O3D[2]	Co1	O3C	148.77(15)	C1F	Fe1	C8F	120.4(9)
C2A	C1A	C5B	120.3(6)	C1F	Fe1	C9F	104.2(8)
C1A	C2A	C3A	120.4(5)	C1F	Fe1	C10F	119.1(8)
C1A	C2A	C9A	120.3(5)	C2F	Fe1	C3F	41.9(8)
C3A	C2A	C9A	119.3(5)	C2F	Fe1	C4F	64.1(8)
C4A	C3A	C2A	121.8(4)	C2F	Fe1	C5F	64.3(9)
C3B	C3A	C2A	119.3(5)	C3F	Fe1	C4F	35.4(8)
C3B	C3A	C4A	118.9(5)	C3F	Fe1	C5F	63.3(9)
C3A	C4A	C6A	119.7(5)	C5F	Fe1	C4F	38.2(8)
C5A	C4A	C3A	121.2(5)	C6F	Fe1	C2F	162.8(9)
C5A	C4A	C6A	119.2(5)	C6F	Fe1	C3F	126.2(8)
C4A	C5A	C1B	119.6(6)	C6F	Fe1	C4F	113.9(9)
O7A	C6A	C4A	122.8(5)	C6F	Fe1	C5F	125.8(10)

O7A	C6A	N8A	120.7(4)	C6F	Fe1	C7F	41.4(10)
N8A	C6A	C4A	116.5(5)	C6F	Fe1	C8F	69.4(9)
C6A	N8A	C9A	125.3(4)	C6F	Fe1	C9F	67.2(8)
C6A	N8A	C11A	118.3(4)	C6F	Fe1	C10F	38.3(8)
C9A	N8A	C11A	116.3(4)	C7F	Fe1	C2F	125.0(10)
N8A	C9A	C2A	116.9(5)	C7F	Fe1	C3F	112.7(9)
O10A	C9A	C2A	122.1(5)	C7F	Fe1	C4F	129.0(9)
O10A	C9A	N8A	121.0(5)	C7F	Fe1	C5F	163.1(10)
C12A	C11A	N8A	121.2(4)	C7F	Fe1	C9F	67.5(9)
C12A	C11A	C16A	119.8(4)	C8F	Fe1	C2F	107.6(8)
C16A	C11A	N8A	118.9(4)	C8F	Fe1	C3F	129.0(9)
C11A	C12A	C13A	118.8(4)	C8F	Fe1	C4F	163.6(8)
N14A	C13A	C12A	122.6(4)	C8F	Fe1	C5F	153.5(9)
C13A	N14A	Co1^3	121.3(3)	C8F	Fe1	C7F	42.4(10)
C13A	N14A	C15A	117.9(4)	C8F	Fe1	C9F	38.4(8)
C15A	N14A	Co1^3	120.8(3)	C8F	Fe1	C10F	66.7(9)
N14A	C15A	C16A	123.2(4)	C9F	Fe1	C2F	121.6(8)
C15A	C16A	C11A	117.8(4)	C9F	Fe1	C3F	161.6(9)
C2B	C1B	C5A	120.5(5)	C9F	Fe1	C4F	158.0(9)
C1B	C2B	C3B	120.2(5)	C9F	Fe1	C5F	121.9(9)
C1B	C2B	C9B	120.0(5)	C10F	Fe1	C2F	157.3(8)
C3B	C2B	C9B	119.8(6)	C10F	Fe1	C3F	158.0(9)
C3A	C3B	C2B	119.4(5)	C10F	Fe1	C4F	126.6(9)
C3A	C3B	C4B	118.9(5)	C10F	Fe1	C5F	110.3(10)
C4B	C3B	C2B	121.7(5)	C10F	Fe1	C7F	66.7(9)
C3B	C4B	C6B	120.0(6)	C10F	Fe1	C9F	40.3(8)
C5B	C4B	C3B	121.0(5)	C2F	C1F	Fe1	69.1(7)
C5B	C4B	C6B	118.9(6)	C5F	C1F	Fe1	74.1(8)

C4B	C5B	C1A	119.8(6)	C5F	C1F	C2F	104.9(16)
O7B	C6B	C4B	122.8(6)	C1F	C2F	Fe1	67.8(7)
O7B	C6B	N8B	121.4(5)	C3F	C2F	Fe1	70.0(7)
N8B	C6B	C4B	115.8(6)	C3F	C2F	C1F	103.4(17)
C6B	N8B	C11B	115.3(5)	C2F	C3F	Fe1	68.1(7)
C9B	N8B	C6B	126.1(4)	C4F	C3F	Fe1	75.1(8)
C9B	N8B	C11B	118.5(5)	C4F	C3F	C2F	107.5(17)
N8B	C9B	C2B	116.5(5)	C3F	C4F	Fe1	69.5(8)
O10B	C9B	C2B	122.3(6)	C3F	C4F	C5F	109.8(18)
O10B	C9B	N8B	121.2(5)	C5F	C4F	Fe1	68.5(7)
C12B	C11B	N8B	120.2(5)	C1F	C5F	Fe1	70.0(8)
C16B	C11B	N8B	119.8(5)	C1F	C5F	C4F	114.1(19)
C16B	C11B	C12B	119.9(5)	C4F	C5F	Fe1	73.3(8)
C13B	C12B	C11B	117.7(5)	C7F	C6F	Fe1	69.9(8)
N14B	C13B	C12B	123.2(5)	C10F	C6F	Fe1	71.5(8)
C13B	N14B	Co1	119.3(3)	C10F	C6F	C7F	108.0(19)
C15B	N14B	Co1	123.1(3)	C6F	C7F	Fe1	68.7(8)
C15B	N14B	C13B	117.5(4)	C6F	C7F	C8F	105.0(17)
N14B	C15B	C16B	124.0(5)	C8F	C7F	Fe1	68.5(8)
C11B	C16B	C15B	117.5(5)	C7F	C8F	Fe1	69.1(8)
O3C	N1C	O2C	115.6(4)	C9F	C8F	Fe1	71.4(9)
O4C	N1C	O2C	121.6(5)	C9F	C8F	C7F	107.5(18)
O4C	N1C	O3C	122.8(5)	C8F	C9F	Fe1	70.1(7)
N1C	O2C	Co1	92.5(3)	C8F	C9F	C10F	109.0(18)
N1C	O3C	Co1	93.4(3)	C10F	C9F	Fe1	69.6(8)
C2D	O1D	Co1	159.6(3)	C6F	C10F	Fe1	70.2(8)
O1D	C2D	O3D	124.3(4)	C6F	C10F	C9F	110(2)
O1D	C2D	C4D	118.9(4)	C9F	C10F	Fe1	70.1(7)

O3D	C2D	C4D	116.9(4)	C2E	C1E	C3E	117(2)
C2D	O3D	Co1[2]	122.1(3)	O4E	C1E	C2E	132(2)
C5D	C4D	C2D	119.2(4)	O4E	C1E	C3E	110(2)

Appendix XIX Crystallographic information for Fc@2

Bond lengths in Fc@2

Atom	Atom	Length/Å	Atom	Atom	Length/Å
Co1	Co2	2.8653(14)	C5C	C6C	1.362(10)
Co1	N14B	2.069(5)	C6C	C7C	1.421(9)
Co1	O3C	2.249(4)	C7C	C8C	1.432(9)
Co1	C14C[1]	2.501(6)	C7C	C13C	1.404(9)
Co1	O15C[1]	2.318(4)	C8C	C9C	1.410(9)
Co1	O16C[1]	2.052(5)	C8C	C10C	1.415(9)
Co1	O1D	2.000(4)	C10C	C11C	1.367(10)
Co1	O15D[2]	2.046(4)	C11C	C12C	1.439(9)
Co2	N14A[3]	2.081(5)	C12C	C13C	1.376(9)
Co2	O1C	2.055(5)	C12C	C14C	1.490(9)
Co2	O3C	2.363(4)	C14C	O15C	1.264(8)
Co2	O15C[1]	2.242(4)	C14C	O16C	1.260(8)
Co2	O3D	2.006(4)	O1D	C2D	1.260(8)
Co2	O16D[2]	1.997(4)	C2D	O3D	1.258(8)
C1A	C2A	1.381(9)	C2D	C4D	1.487(9)
C1A	C5B	1.408(9)	C4D	C5D	1.413(9)
C2A	C3A	1.408(9)	C4D	C9D	1.374(9)
C2A	C9A	1.469(9)	C5D	C6D	1.364(10)
C3A	C4A	1.423(9)	C6D	C7D	1.430(9)
C3A	C3B	1.408(9)	C7D	C8D	1.433(9)
C4A	C5A	1.363(10)	C7D	C13D	1.396(9)
C4A	C6A	1.467(9)	C8D	C9D	1.406(9)
C5A	C1B	1.409(10)	C8D	C10D	1.424(9)
C6A	O7A	1.228(9)	C10D	C11D	1.350(10)

C6A	N8A	1.390(9)	C11D	C12D	1.426(10)
N8A	C9A	1.421(8)	C12D	C13D	1.370(9)
N8A	C11A	1.442(8)	C12D	C14D	1.488(9)
C9A	O10A	1.196(8)	C14D	O15D	1.239(8)
C11A	C12A	1.378(10)	C14D	O16D	1.279(8)
C11A	C16A	1.377(10)	Fe1	C1E	2.045(14)
C12A	C13A	1.377(10)	Fe1	C2E	2.016(13)
C13A	N14A	1.331(9)	Fe1	C3E	2.000(14)
N14A	C15A	1.342(9)	Fe1	C4E	2.040(11)
C15A	C16A	1.378(10)	Fe1	C5E	2.023(11)
C1B	C2B	1.382(9)	Fe1	C6E	2.000(10)
C2B	C3B	1.397(9)	Fe1	C7E	2.025(12)
C2B	C9B	1.479(9)	Fe1	C8E	2.059(13)
C3B	C4B	1.427(9)	Fe1	C9E	2.035(12)
C4B	C5B	1.365(10)	Fe1	C10E	2.028(10)
C4B	C6B	1.476(9)	C1E	C2E	1.45(3)
C6B	O7B	1.228(8)	C1E	C5E	1.399(19)
C6B	N8B	1.403(9)	C2E	C3E	1.34(3)
N8B	C9B	1.420(8)	C3E	C4E	1.37(2)
N8B	C11B	1.452(7)	C4E	C5E	1.43(2)
C9B	O10B	1.199(8)	C6E	C7E	1.393(19)
C11B	C12B	1.370(9)	C6E	C10E	1.387(18)
C11B	C16B	1.373(9)	C7E	C8E	1.387(18)
C12B	C13B	1.382(9)	C8E	C9E	1.411(16)
C13B	N14B	1.343(9)	C9E	C10E	1.405(17)
N14B	C15B	1.338(9)	C1F	C2F	1.513(17)
C15B	C16B	1.387(9)	C1F	C3F	1.477(16)
O1C	C2C	1.276(8)	C1F	O4F	1.209(12)
C2C	O3C	1.254(8)	C1G	C2G	1.52(2)
C2C	C4C	1.481(9)	C1G	C3G	1.41(2)
C4C	C5C	1.424(9)	C1G	O4G1	1.298(16)
C4C	C9C	1.377(9)	C1G	O4G2	1.33(2)

Bond angles in Fc@2

Atom	Atom	Atom	Angle/°	Atom	Atom	Atom	Angle/°
N14B	Co1	Co2	141.82(15)	C11C	C10C	C8C	121.2(6)
N14B	Co1	O3C	88.46(19)	C10C	C11C	C12C	119.9(6)
N14B	Co1	C14C^1	137.7(2)	C11C	C12C	C14C	119.6(6)
N14B	Co1	O15C^1	167.61(19)	C13C	C12C	C11C	120.1(6)
O3C	Co1	Co2	53.41(11)	C13C	C12C	C14C	120.3(6)
O3C	Co1	C14C^1	133.12(19)	C12C	C13C	C7C	120.4(6)
O3C	Co1	O15C^1	103.29(15)	C12C	C14C	Co1^5	175.0(5)
C14C^1	Co1	Co2	79.93(16)	O15C	C14C	Co1^5	66.9(3)
O15C^1	Co1	Co2	49.91(11)	O15C	C14C	C12C	118.1(6)
O15C^1	Co1	C14C^1	30.10(18)	O16C	C14C	Co1^5	54.8(3)
O16C^1	Co1	Co2	110.04(13)	O16C	C14C	C12C	120.1(6)
O16C^1	Co1	N14B	107.7(2)	O16C	C14C	O15C	121.7(6)
O16C^1	Co1	O3C	162.70(17)	Co2^5	O15C	Co1^5	77.83(13)
O16C^1	Co1	C14C^1	30.1(2)	C14C	O15C	Co1^5	83.0(4)
O16C^1	Co1	O15C^1	60.21(16)	C14C	O15C	Co2^5	160.2(4)
O1D	Co1	Co2	81.47(13)	C14C	O16C	Co1^5	95.1(4)
O1D	Co1	N14B	99.06(19)	C2D	O1D	Co1	125.2(4)
O1D	Co1	O3C	85.19(17)	O1D	C2D	C4D	117.7(6)
O1D	Co1	C14C^1	92.86(19)	O3D	C2D	O1D	125.2(6)
O1D	Co1	O15C^1	86.02(17)	O3D	C2D	C4D	117.0(6)
O1D	Co1	O16C^1	97.95(18)	C2D	O3D	Co2	126.7(4)
O1D	Co1	O15D^2	159.25(18)	C5D	C4D	C2D	119.9(6)
O15D^2	Co1	Co2	78.40(12)	C9D	C4D	C2D	120.0(6)
O15D^2	Co1	N14B	93.71(19)	C9D	C4D	C5D	120.0(6)
O15D^2	Co1	O3C	78.85(17)	C6D	C5D	C4D	120.0(6)
O15D^2	Co1	C14C^1	88.54(19)	C5D	C6D	C7D	121.5(6)

O15D²	Co1	O15C¹	84.86(17)	C6D	C7D	C8D	118.1(6)
O15D²	Co1	O16C¹	93.62(18)	C13D	C7D	C6D	123.0(6)
N14A³	Co2	Co1	140.88(16)	C13D	C7D	C8D	119.0(6)
N14A³	Co2	O3C	169.05(19)	C9D	C8D	C7D	118.7(6)
N14A³	Co2	O15C¹	88.76(19)	C9D	C8D	C10D	123.2(6)
O1C	Co2	Co1	108.85(13)	C10D	C8D	C7D	118.1(6)
O1C	Co2	N14A³	109.9(2)	C4D	C9D	C8D	121.7(6)
O1C	Co2	O3C	59.21(16)	C11D	C10D	C8D	121.2(7)
O1C	Co2	O15C¹	160.98(17)	C10D	C11D	C12D	120.8(7)
O3C	Co2	Co1	49.81(10)	C11D	C12D	C14D	120.9(6)
O15C¹	Co2	Co1	52.26(11)	C13D	C12D	C11D	118.9(6)
O15C¹	Co2	O3C	102.05(15)	C13D	C12D	C14D	120.2(6)
O3D	Co2	Co1	80.36(13)	C12D	C13D	C7D	122.0(6)
O3D	Co2	N14A³	93.23(19)	O15D	C14D	C12D	118.1(6)
O3D	Co2	O1C	91.77(18)	O15D	C14D	O16D	125.3(6)
O3D	Co2	O3C	86.38(16)	O16D	C14D	C12D	116.5(6)
O3D	Co2	O15C¹	83.24(17)	C14D	O15D	Co1⁶	127.8(4)
O16D²	Co2	Co1	83.65(13)	C14D	O16D	Co2⁶	122.0(4)
O16D²	Co2	N14A³	98.15(19)	C1E	Fe1	C8E	160.9(6)
O16D²	Co2	O1C	94.98(19)	C2E	Fe1	C1E	41.8(8)
O16D²	Co2	O3C	84.58(16)	C2E	Fe1	C4E	68.3(7)
O16D²	Co2	O15C¹	85.67(18)	C2E	Fe1	C5E	68.4(5)
O16D²	Co2	O3D	163.92(19)	C2E	Fe1	C7E	162.6(9)
C2A	C1A	C5B	119.5(6)	C2E	Fe1	C8E	156.2(8)
C1A	C2A	C3A	120.4(6)	C2E	Fe1	C9E	121.0(6)
C1A	C2A	C9A	118.8(6)	C2E	Fe1	C10E	108.1(6)
C3A	C2A	C9A	120.9(6)	C3E	Fe1	C1E	67.1(8)
C2A	C3A	C4A	120.8(6)	C3E	Fe1	C2E	39.0(8)

C2A	C3A	C3B	120.2(6)	C3E	Fe1	C4E	39.7(6)
C3B	C3A	C4A	119.0(6)	C3E	Fe1	C5E	66.5(6)
C3A	C4A	C6A	119.5(6)	C3E	Fe1	C6E	162.3(8)
C5A	C4A	C3A	119.9(6)	C3E	Fe1	C7E	156.6(9)
C5A	C4A	C6A	120.6(6)	C3E	Fe1	C8E	123.6(9)
C4A	C5A	C1B	121.1(7)	C3E	Fe1	C9E	110.1(7)
O7A	C6A	C4A	122.2(7)	C3E	Fe1	C10E	126.7(6)
O7A	C6A	N8A	119.9(6)	C4E	Fe1	C1E	69.0(7)
N8A	C6A	C4A	117.9(6)	C4E	Fe1	C8E	108.2(7)
C6A	N8A	C9A	124.8(6)	C5E	Fe1	C1E	40.2(5)
C6A	N8A	C11A	119.2(5)	C5E	Fe1	C4E	41.1(6)
C9A	N8A	C11A	115.9(5)	C5E	Fe1	C7E	107.8(5)
N8A	C9A	C2A	116.1(6)	C5E	Fe1	C8E	125.4(5)
O10A	C9A	C2A	123.5(6)	C5E	Fe1	C9E	162.1(5)
O10A	C9A	N8A	120.4(6)	C5E	Fe1	C10E	155.9(6)
C12A	C11A	N8A	118.6(6)	C6E	Fe1	C1E	107.4(6)
C16A	C11A	N8A	122.2(6)	C6E	Fe1	C2E	125.7(8)
C16A	C11A	C12A	119.2(6)	C6E	Fe1	C4E	156.2(6)
C13A	C12A	C11A	118.4(7)	C6E	Fe1	C5E	121.1(5)
N14A	C13A	C12A	123.8(6)	C6E	Fe1	C7E	40.5(6)
C13A	N14A	Co2[4]	119.0(4)	C6E	Fe1	C8E	67.1(5)
C13A	N14A	C15A	116.7(6)	C6E	Fe1	C9E	67.8(4)
C15A	N14A	Co2[4]	124.0(5)	C6E	Fe1	C10E	40.3(5)
N14A	C15A	C16A	123.6(7)	C7E	Fe1	C1E	124.3(6)
C11A	C16A	C15A	118.3(6)	C7E	Fe1	C4E	120.8(7)
C2B	C1B	C5A	119.7(6)	C7E	Fe1	C8E	39.7(5)
C1B	C2B	C3B	120.3(6)	C7E	Fe1	C9E	67.9(5)
C1B	C2B	C9B	119.0(6)	C7E	Fe1	C10E	68.0(5)

C3B	C2B	C9B	120.7(6)	C9E	Fe1	C1E	156.6(5)
C3A	C3B	C4B	118.3(6)	C9E	Fe1	C4E	124.8(6)
C2B	C3B	C3A	120.1(6)	C9E	Fe1	C8E	40.3(5)
C2B	C3B	C4B	121.6(6)	C10E	Fe1	C1E	121.1(6)
C3B	C4B	C6B	119.4(6)	C10E	Fe1	C4E	161.8(6)
C5B	C4B	C3B	120.4(6)	C10E	Fe1	C8E	67.5(5)
C5B	C4B	C6B	120.3(6)	C10E	Fe1	C9E	40.4(5)
C4B	C5B	C1A	121.2(6)	C2E	C1E	Fe1	68.0(9)
O7B	C6B	C4B	122.6(6)	C5E	C1E	Fe1	69.0(8)
O7B	C6B	N8B	120.8(6)	C5E	C1E	C2E	105.6(17)
N8B	C6B	C4B	116.6(6)	C1E	C2E	Fe1	70.2(7)
C6B	N8B	C9B	125.5(5)	C3E	C2E	Fe1	69.9(9)
C6B	N8B	C11B	117.3(5)	C3E	C2E	C1E	106.4(14)
C9B	N8B	C11B	116.4(5)	C2E	C3E	Fe1	71.1(9)
N8B	C9B	C2B	115.6(6)	C2E	C3E	C4E	114.1(19)
O10B	C9B	C2B	125.1(6)	C4E	C3E	Fe1	71.7(8)
O10B	C9B	N8B	119.3(6)	C3E	C4E	Fe1	68.6(7)
C12B	C11B	N8B	121.2(6)	C3E	C4E	C5E	103.9(16)
C12B	C11B	C16B	120.5(6)	C5E	C4E	Fe1	68.8(7)
C16B	C11B	N8B	118.3(6)	C1E	C5E	Fe1	70.7(7)
C11B	C12B	C13B	118.2(6)	C1E	C5E	C4E	110.0(13)
N14B	C13B	C12B	122.5(7)	C4E	C5E	Fe1	70.1(7)
C13B	N14B	Co1	124.6(5)	C7E	C6E	Fe1	70.7(7)
C15B	N14B	Co1	117.2(4)	C10E	C6E	Fe1	70.9(6)
C15B	N14B	C13B	118.2(6)	C10E	C6E	C7E	109.3(11)
N14B	C15B	C16B	122.6(6)	C6E	C7E	Fe1	68.8(7)
C11B	C16B	C15B	117.9(6)	C8E	C7E	Fe1	71.5(7)
C2C	O1C	Co2	96.7(4)	C8E	C7E	C6E	107.6(12)

O1C	C2C	C4C	119.4(6)	C7E	C8E	Fe1	68.8(7)
O3C	C2C	O1C	120.7(6)	C7E	C8E	C9E	108.2(12)
O3C	C2C	C4C	119.9(6)	C9E	C8E	Fe1	68.9(7)
Co1	O3C	Co2	76.78(13)	C8E	C9E	Fe1	70.7(7)
C2C	O3C	Co1	159.3(4)	C10E	C9E	Fe1	69.5(6)
C2C	O3C	Co2	83.3(4)	C10E	C9E	C8E	107.5(11)
C5C	C4C	C2C	121.4(6)	C6E	C10E	Fe1	68.8(6)
C9C	C4C	C2C	119.2(6)	C6E	C10E	C9E	107.4(11)
C9C	C4C	C5C	119.4(6)	C9E	C10E	Fe1	70.1(7)
C6C	C5C	C4C	120.4(6)	C3F	C1F	C2F	117.0(10)
C5C	C6C	C7C	121.2(7)	O4F	C1F	C2F	120.0(10)
C6C	C7C	C8C	118.7(6)	O4F	C1F	C3F	123.0(12)
C13C	C7C	C6C	121.3(6)	C3G	C1G	C2G	118.8(13)
C13C	C7C	C8C	119.9(6)	O4G1	C1G	C2G	113.8(17)
C9C	C8C	C7C	118.6(6)	O4G1	C1G	C3G	118.7(16)
C9C	C8C	C10C	122.9(6)	O4G2	C1G	C2G	125.0(17)
C10C	C8C	C7C	118.5(6)	O4G2	C1G	C3G	104.3(18)
C4C	C9C	C8C	121.6(6)				

Appendix XX: PXRD for Lanthanides MOFs

Experimental PXRD pattern for Ho(III)DNNDI MOF **11**
Simulated PXRD pattern

Experimental PXRD pattern for Ho(III)DNNDI MOF **12**
Simulated pattern
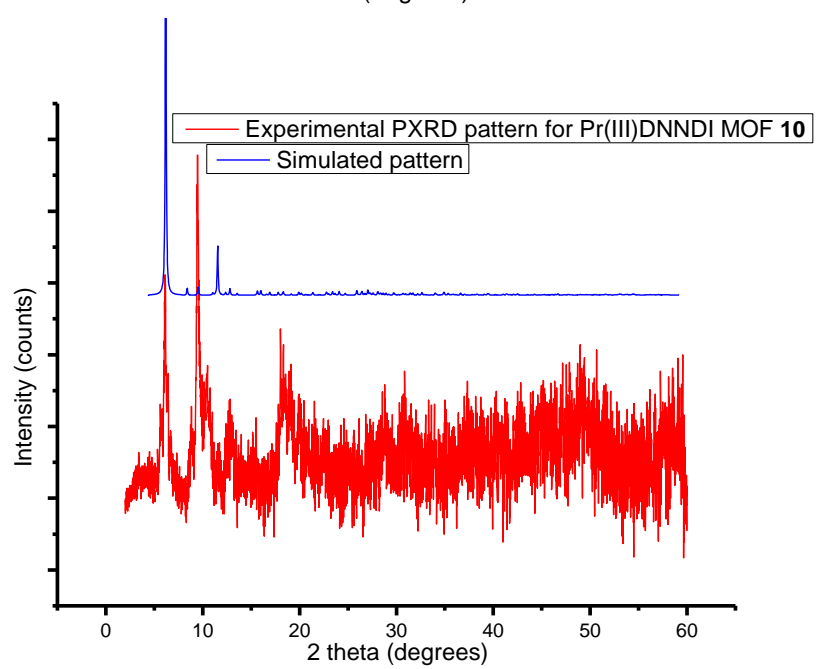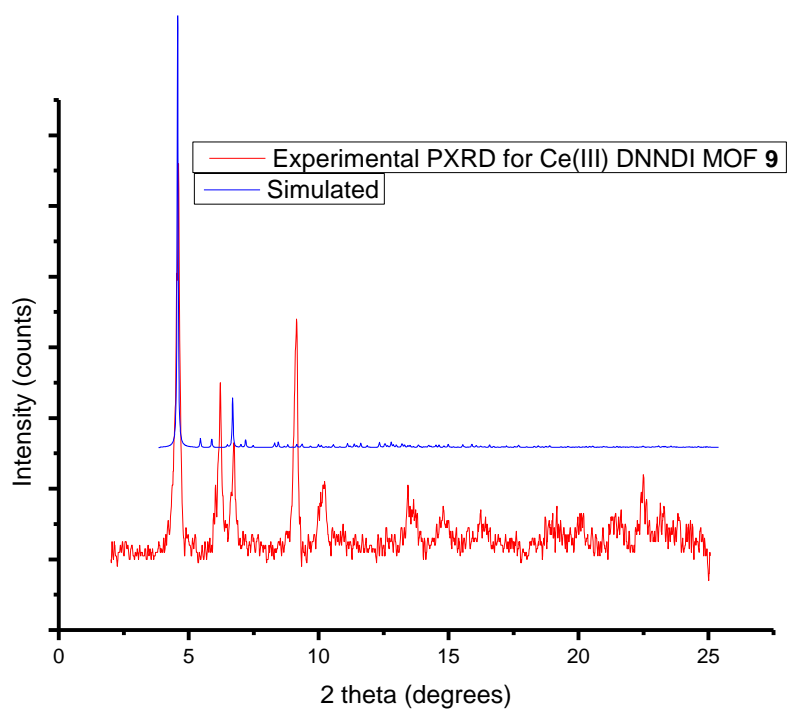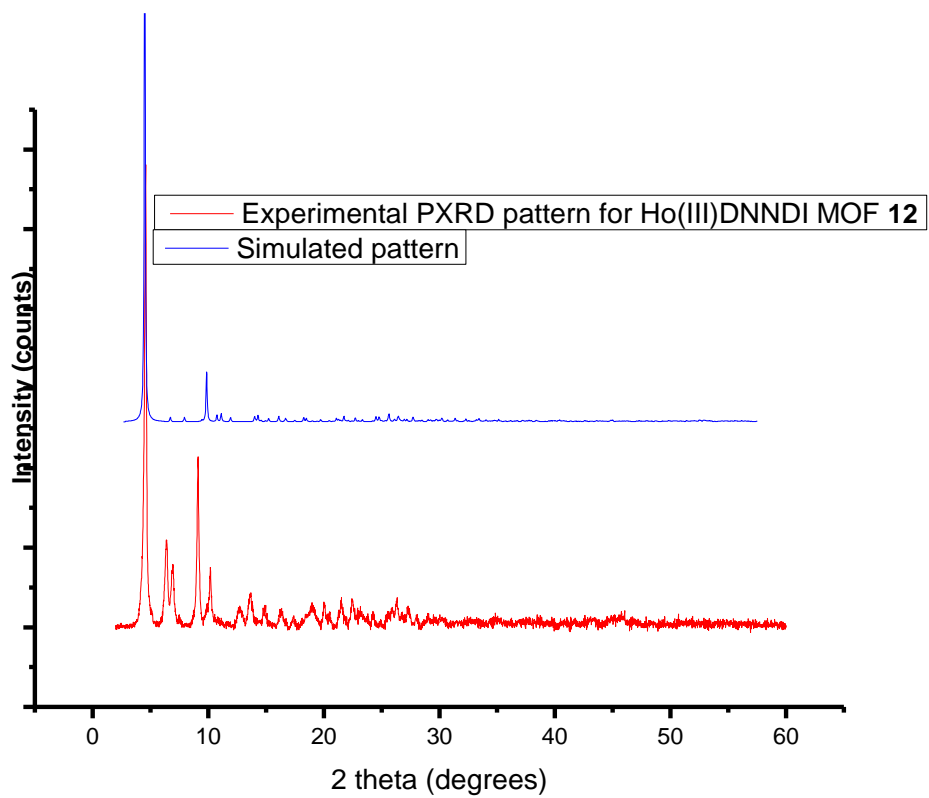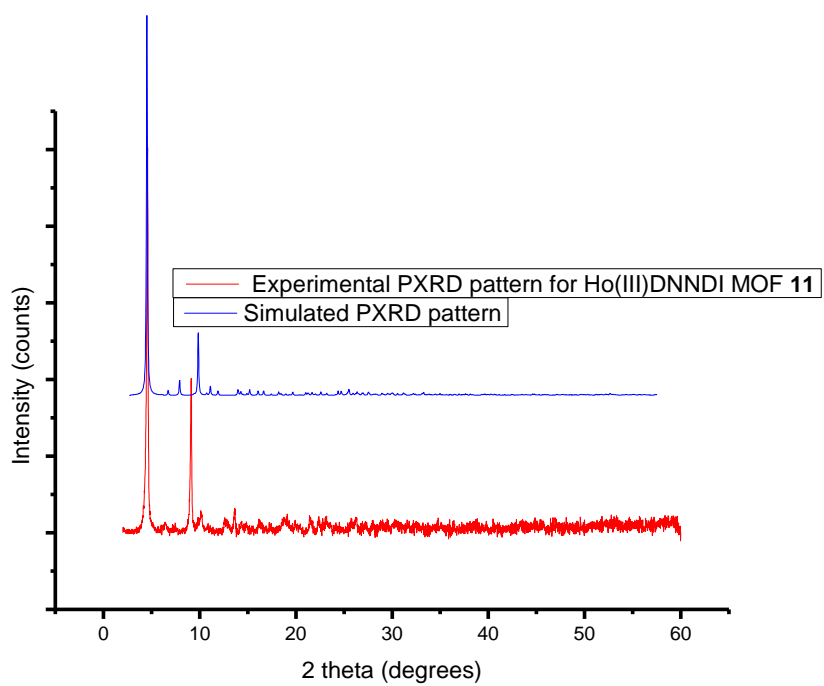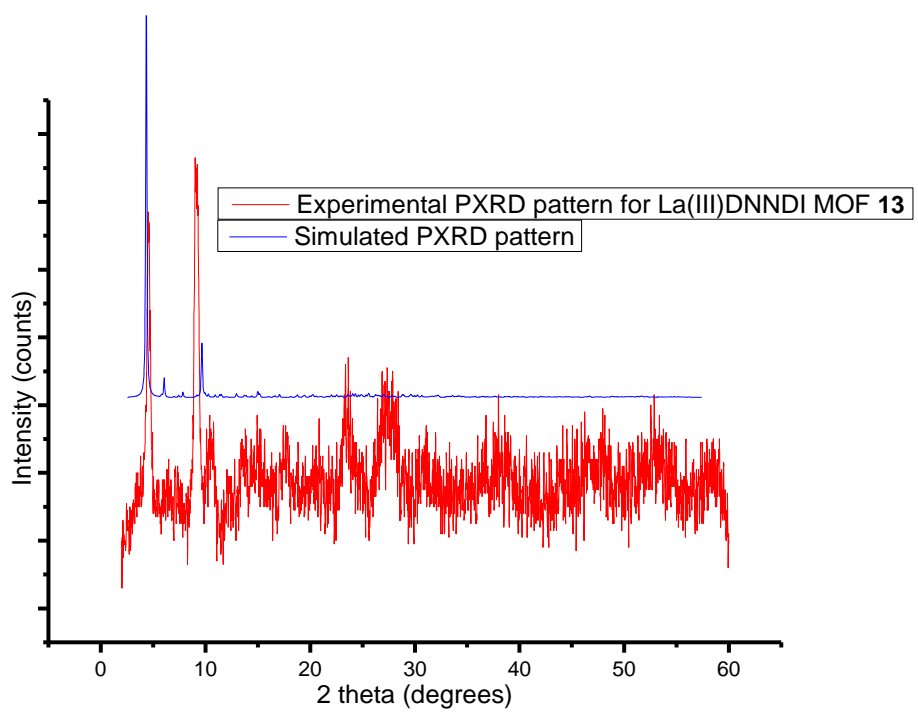
Appendix XXI: Table Cyclic Voltammetry for the MOFs.

Sample	1st reduction E₁/₂ / V	2nd reduction E₁/₂ / V	ΔE (Fc)
1	-0.88 (0.08)	-1.28 (0.10) [-1.32 [a]]	0.07
2	-0.87 (0.13)	-1.32[a]	0.07
3	-0.88 (0.10)	-1.41 (0.11) [-1.47 [a]]	0.07
4	-0.88 (0.08)	-1.44 (0.09) [-1.48 [a]]	0.08
5	-0.88 (0.08)	-1.43 (0.09) [-1.46 [a]]	0.08
6	-0.86 (0.10)	-1.12 (0.12) [-1.18 [a]]	0.09
7	-0.85 (0.08)	-1.11 (0.11) [-1.16 [a]]	0.07
8	-0.89 (0.09)	-1.32[a]	0.07
9	-0.90 (0.12)	-1.29 (0.15) [-1.36 [a]]	0.07
10	-0.88 (0.10)	-1.22 (0.16) [-1.30 [a]]	0.07
11	-0.87 (0.09)	-1.28[a]	0.07
12	-0.86 (0.11)	-1.26[a]	0.07
13	-0.86 (0.15)	-1.21 (0.17) [-1.30[a]]	0.08
14	-0.88 (0.12)	-1.22 (0.19) [-1.31[a]]	0.06

Table of Solid state cyclic voltammetry on a glassy carbon electrode using LiClO₄ intercalated PVC as supporting matrix, in dmf/[Bu₄N][BF₄] (0.2 M) at 0.1 Vs⁻¹. Potentials are quoted versus $E_{1/2}$ Fc⁺/Fc used as an internal standard. Values in brackets are ΔE (=E_p^a – E_p^c). [a] E_p^c; [b] oxidation process at 0.00 V (0.09)